THE UNIVERSITY *of* EDINBURGH

Declaration of Authorship

I, Darren BELLSHAW, declare that this thesis titled, "Theoretical Modelling of Ultrafast Photodynamics" and the work presented in it are my own. I confirm that:

- This work was done wholly or mainly while in candidature for a research degree at this University.
- Where any part of this thesis has previously been submitted for a degree or any other qualification at this University or any other institution, this has been clearly stated.
- Where I have consulted the published work of others, this is always clearly attributed.
- Where I have quoted from the work of others, the source is always given. With the exception of such quotations, this thesis is entirely my own work.
- I have acknowledged all main sources of help.
- Where the thesis is based on work done by myself jointly with others, I have made clear exactly what was done by others and what I have contributed myself.

Signed:

Date:

"Nature isn't classical, dammit, and if you want to make a simulation of nature, you'd better make it quantum mechanical, and by golly it's a wonderful problem, because it doesn't look so easy..."

Richard Phillips Feynman

"Bad times have a scientific value. These are occasions a good learner would not miss."

Ralph Waldo Emerson

Abstract

This thesis presents detailed electronic structure calculations and mixed quantum-classical dynamics simulations of the photodynamics of two small polyatomic molecules using "*on-the-fly*" surface-hopping. Most of the emphasis in this work is on CS_2, which upon absorption of a UV photon undergoes a complex photodissociation process propagating across the potential energy surfaces of multiple singlet and triplet electronic states, under the influence of both nonadiabatic and spin-orbit coupling. Backed by extensive CASSCF and post-CASSCF electronic structure calculations, excitation to the 1^1B_2 state is considered as a first exploration of the dynamics over the first picosecond, accounting for the lowest-lying four singlet and four triplet states. Following this, dynamics occurring after excitation to the 2^1B_2 state, which is the state typically excited in time-resolved experimental studies of this system, are simulated. The additional computational complexity (with dynamics evolving on 19 interacting singlet and triplet states) and the limitations of "*on-the-fly*" techniques for a simulation of this size is discussed. This motivates initial steps towards generating full-dimensional grid-based surfaces for CS_2 on which dynamics could later be simulated. These studies reinforce the importance of spin-orbit coupling in the dynamics and shine a light on the competitive nature of the singlet and triplet dissociation channels.

Secondly, the short-time dynamics of trimethylamine are simulated, also using surface-hopping. Two sets of simulations are compared with regard to their description of the main dynamical features of the system, including dissociation of a methyl fragment and the extensive interplay between the

low-lying $3p_{xyz}$ and $3s$ Rydberg states, behaviour characteristic of tertiary substituted aliphatic amine systems. It is concluded that the sixth singlet state ($3d$) plays a significant role in the dissociation mechanism.

The calculations and simulations here demonstrate the increasing utility of the conceptually intuitive surface-hopping approach in studying two contrasting classes of photochemical reactions, namely over-the-barrier photodissociation in CS_2 and the photodynamics of low-lying Rydberg states in trimethylamine. In both cases, a comparison is made with complementary time-resolved experimental work by collaborators, articulating the need for experiment and theory to work together to provide a complete description of these fundamental chemical processes.

Lay summary

The work in this thesis describes the use of mathematical modelling techniques and specialist computational software to simulate what happens when two small molecules, carbon disulfide (CS_2) and trimethylamine (TMA), absorb pulses of ultraviolet (UV) light; in other words, their photochemistry, which begins when the absorbed photon causes an electron to be excited to a higher energy orbital and puts the molecule in an excited electronic state. This is done using the surface-hopping technique, where the nuclei in each molecule are treated using Newton's classical equations of motion while the electrons are described using more accurate quantum mechanics. This mixture of classical and quantum mechanical descriptions means surface-hopping is computationally cheap compared to fully quantum methods, while still retaining accuracy within certain approximations.

In CS_2, surface-hopping is used to simulate the dissociation of the molecule into CS and S fragments, which can occur by two different mechanistic pathways. The ratio of these pathways is greatly influenced by a quantum mechanical phenomenon called spin-orbit coupling, which arises from the atomic weight of the sulfur atoms. Simulations have been run considering excitation to two different excited states. Beyond the surface-hopping simulations, initial steps have been taken towards the calculation of full-dimensional potential energy surfaces (maps of how the energy of the molecule changes with its geometry) in order that more accurate methods may be used in the future to simulate the dynamics using these surfaces.

In TMA, the photodynamics takes place among Rydberg electronic states — states in which the excited electron may be found a great distance away from the nuclei. Such states are typically found at very high energies, but can be easily reached by a photon of UV light in TMA. As well as interplay between various Rydberg electronic states, the photochemistry of TMA is

intriguing because a methyl (CH_3) fragment will also dissociate by either one of two pathways (one fast, one slow). Two sets of simulations have been run in order to see whether the inclusion of an extra excited state affects the interactions between the Rydberg states and the fast dissociation pathway (the simulations do not cover the the timescale of the slow pathway).

In both cases, comparisons are made to practical experiments by collaborators which have used sophisticated time-resolved techniques to image the dynamics in real time. It is shown that it is necessary for experiment and theory to unite to provide a complete description of how each reaction unfolds.

Acknowledgements

"No one can whistle a symphony."

Halford Edward Luccock

Firstly, I must express my gratitude to my supervisor, Dr. Adam Kirrander, for giving me the opportunity to study with him. Over the course of my PhD studies he has been a continual source of support, advice, and good humour. As well as this, he has demonstrated no small amount of patience towards me during times of frustration, and encouraged the growth of playful scientific curiosity of the most rewarding kind.

Thanks is also due to a number of past and present colleagues in the Kirrander group; Dr. Andrés Moreno Carrascosa, Nikola Zotev, Dr. Mats Simmermacher, Haiwang Yong, Minas Stefanou, Dr. Maria Tudorovskaya, Dr. Thomas Northey and Dr. David Rogers. This academic fellowship did not only create a stimulating environment in which to study through good-natured scientific discourse; they remain firm friends whose regular companionship I shall miss. Particular thanks go to David, who took me under his wing as an inexperienced Hartree-Fock user and mentored me in the intricacies of multireference methods, enduring my impatience with considerable resilience.

All of the work here has been inspired and greatly enhanced by collaborations across both disciplinary and international boundaries. For this, I am thankful to all the members of the groups of Dr. Russell Minns (University of Southampton) and Prof. Peter Weber (Brown University).

I have been blessed by the companionship of my friends here in Edinburgh and beyond, who continue to inspire and encourage me as they have done throughout my PhD. They cannot all be listed here, but include colleagues from my undergraduate studies: Andrew Anderson, Iain McKean,

Nicolle Giuliani, and others, as well as my church family both locally and across the country, without whose support I would not have completed this project.

To Fiona — you came into my life late on in this process, but your timing was faultless. Thank you for your scientific advice, your constant encouragement, and for believing in me.

The final thanks is due to my family; my parents (Alan and Gill), and brothers (Martyn, Jonathan, and Craig), each of whom have expended considerable effort supporting me through difficult times. A special mention is reserved for Mum, who continues to do this while fighting a much larger battle of her own — you inspire me every day.

Contents

List of Figures

List of Tables

List of Abbreviations

AIMS	*Ab Initio* Multiple Spawning
ANN	Artificial neural network
BOA	Born-Oppenheimer approximation
CASPT2	Complete Active Space Perturbation Theory, 2nd order
CASSCF	Complete Active Space Self-Consistent Field
CC	Coupled cluster
CI	Configuration Interaction
CoIn	Conical intersection
CSF	Configuration State Function
DKH	Douglas-Kroll-Hess
DMA	Dimethylamine
FCI	Full Configuration Interaction
FERMI	Free-Electron Radiation for Multidisciplinary Investigations
FLASH	Free-Electron Laser in Hamburg
FMS	Full Multiple Spawning
FSSH	Fewest Switches Surface-Hopping
G-MCTDH	Gaussian Multiconfigurational Time-Dependent Hartree
GTO	Gaussian-type orbitals
HF	Hartree-Fock
IC	Internal conversion
ISC	Intersystem crossing
LCLS	Linac Coherent Light Source
MCE	Multiconfigurational Ehrenfest
MCSCF	Multiconfigurational Self-Consistent Field
MCTDH	Multiconfigurational Time-Dependent Hartree
MD	Molecular dynamics
MP2	Møller-Plesset Perturbation theory, 2nd order

MRCI	Multireference Configuration Interaction
MRPT	Multireference Perturbation theory
MS-CASPT2	Multistate complete active space perturbation theory, 2^{nd} order
NACME	Nonadiabatic coupling matrix element
PAD	Photoelectron angular distribution
PEC	Potential energy cut
PES	Potential energy surface
PT	Perturbation theory
QMD	Quantum molecular dynamics
SA-CASSCF	State-Averaged Complete Active Space Self-Consistent Field
SACLA	Spring-8 Angstrom Compact Free-Electron LAser
SASE	Self-amplified stimulated emission
SCF	Self-Consistent Field
SD	Slater determinant
SH	Surface-hopping
SHARC	Surface-Hopping including Arbitrary Couplings
SLAC	Stanford Linear Accelerator
SOC	Spin-orbit coupling
SwissFEL	Swiss Free-Electron Laser
TAA	Tertiary aliphatic amine
TDM	Transition dipole moment
TDSE	Time-dependent Schrödinger equation
TISE	Time-independent Schrödinger equation
TMA	Trimethylamine
ToF	Time of flight
TR-MS	Time-resolved mass spectrometry
TR-PES	Time-resolved photoelectron spectroscopy
TR-XRD	Time-resolved X-ray diffraction
UED	Ultrafast electron diffraction
vMCG	variational Multiconfigurational Gaussian
VMI	Velocity map imaging
VUV	Vacuum ultraviolet

XFEL	X-ray Free-Electron laser
XMCQDPT2	Extended multiconfiguration quasi-degenerate second-order perturbation theory
XUV	Extreme ultraviolet

List of Publications

Work from this thesis has been published (or soon will be) in the following papers:

Darren Bellshaw, Daniel A. Horke, Adam D. Smith, Hannah M.Watts, Edward Jager, Emma Springate, Oliver Alexander, Cephise Cacho, Richard T. Chapman. Adam Kirrander, and Russell S .Minns. "*Ab-initio* surface hopping and multiphoton ionisation study of the photodissociation dynamics of CS_2." *Chemical Physics Letters* **683**, 383 (2017).

Adam D. Smith, Emily M. Warne, **Darren Bellshaw**, Daniel A. Horke, Maria Tudorovskya, Emma Springate, Alfred J. H. Jones, Cephise Cacho, Richard T. Chapman, Adam Kirrander, and Russell S. Minns. "Mapping the Complete Reaction Path of a Complex Photochemical Reaction." *Physical Review Letters* **120**, 183003 (2018)

Darren Bellshaw, Russell S. Minns, and Adam Kirrander. "Correspondence between electronic structure calculations and simulations: nonadiabatic dynamics in CS_2." *Physical Chemistry Chemical Physics*, (accepted Dec. 2018)

Jennifer M. Ruddock, Nikola Zotev, Brian Stankus, Haiwang Yong, **Darren Bellshaw**, Sébastien Boutet, Thomas J. Lane, Mengning Liang, Sergio Carbajo, Wenpeng Du, Adam Kirrander, Michael P. Minitti and Peter M. Weber. "Simplicity beneath Complexity: Counting Molecular Electrons Reveals Transients and Kinetics of Photodissociation Reactions". *Angewandte Chemie International Edition* (accepted March 2019)

Darren Bellshaw, Jennifer M. Ruddock, Adam Kirrander, Peter M. Weber, *et al. Manuscript in preparation.* Early time Rydberg photodynamics of UV-excited trimethylamine (2019)

Darren Bellshaw, Russell Minns, Adam Kirander *et al. Manuscript in preparation.* Photodynamics of the 2^1B_2 state of CS_2 studied by surface-hopping and time-resolved photoelectron spectroscopy (2019)

Other work not directly related to this thesis has been published (or soon will be) in the following papers:

Haiwang Yong, Nikola Zotev, Brian Stankus, Jennifer M. Ruddock, **Darren Bellshaw**, Sébastien Boutet, Thomas J. Lane, Mengning Liang, Sergio Carbajo, Joseph S. Robinson, Wenpeng Du, Nathan Goff, Yu Chang, Jason E. Koglin, Max D. J. Waters, Theis I. Sølling, Michael P. Minitti, Adam Kirrander and Peter M. Weber. (2018). "Determining Orientations of Optical Transition Dipole Moments using Ultrafast X-Ray Scattering". *The Journal of Physical Chemistry Letters* **9**, 6556 (2018)

Haiwang Yong, Jennifer M. Ruddock, Nikola Zotev, Brian Stankus, Andrés Moreno Carrascosa, Wenpeng Du, Nathan Goff, Yu Chang, **Darren Bellshaw**, Mengning Liang, Sergio Carbajo, Jason Koglin, Joseph S. Robinson, Sébastien Boutet, Michael P. Minitti, Adam Kirrander and Peter M. Weber. "Direct Observation of Excited State Electron Density Using X-Ray Scattering." *Nature*, (submitted March 2019)

Brian Stankus, Haiwang Yong, Nikola Zotev, Jennifer Ruddock, **Darren Bellshaw**, Thomas J. Lane, Mengning Liang, Sébastien Boutet, Sergio Carbajo, Joseph S. Robinson, Wenpeng Du, Nathan Goff, Yu Chang, Jason E. Koglin, Michael P. Minitti, Adam Kirrander and Peter M. Weber. "Ultrafast X-Ray Scattering Reveals Vibrational Coherence Following Rydberg Excitation."

Nature Chemistry, (submitted March 2019)

Jennifer M. Ruddock, Haiwang Yong, Brian Stankus, Wenpeng Du, Nathan Goff, Yu Chang, Andrés Moreno Carrascosa, **Darren Bellshaw**, Nikola Zotev, Mengning Liang, Sergio Carbajo, Jason Koglin, Joseph S. Robinson, Sébastien Boutet, Adam Kirrander, Michael P. Minitti and Peter M. Weber. "The Deep-UV, Photo-Induced Ring-Opening Dynamics of 1,3-Cyclohexadiene." *Journal of the American Chemical Society*, (submitted April 2019)

Emily Warne, Briony Downes-ward, Joanne Woodhouse, Michael Parkes, **Darren Bellshaw**, Emma Springate, Paulina Majchrzak, Yu Zhang, Gabriel Karras, Adam Wyatt, Richard Chapman, Adam Kirrander, and Russell Minns. "Photodissociation dynamics of CH_3I probed via multiphoton ionisation photoelectron spectroscopy." *Physical Chemistry Chemical Physics*, (Accepted May 2019)

Chapter 1

Introduction

In its most general sense, chemistry can be defined as the science of the composition and transformation of matter. Therefore it is inevitable that one of the key goals of chemistry is the detailed study of chemical reactions [1], processes which result in the interconversion of chemical species by the rearrangement of the nuclei and electrons [2]. These rearrangements can be described by quantum mechanics, a branch of physics which describes nature at the molecular, atomic and subatomic levels, and from which concepts such as the quantization of energy levels and the dual wave-particle nature of matter arise. The fundamental steps of chemical reactions, governed by atomic vibrations, occur on a timescale of femtoseconds — Fig. 1.1 shows a broad comparison of this timescale to other fundamental, physical, chemical, and biological processes. Experimentally, one may infer reaction dynamics by the distribution of products at the conclusion of a particular reaction, but over more recent decades the field of time-resolved imaging has seen great advances in our ability to follow the time dependence of chemical reactions; in particular, the introduction of the laser over 50 years ago [3, 4] was essential to the development of methods to map molecular dynamics which can now be imaged in real time [5, 6].

Alongside experimental developments, advances in theoretical techniques [8] and the computational resources to make use of them [9] mean that the modern computational chemist has an extensive arsenal of tools with which to tackle a wide scope of chemical problems: from approximate treatments based on statistical mechanics and force fields, semi-empirical methods incorporating parameters derived from experiment, approaches based

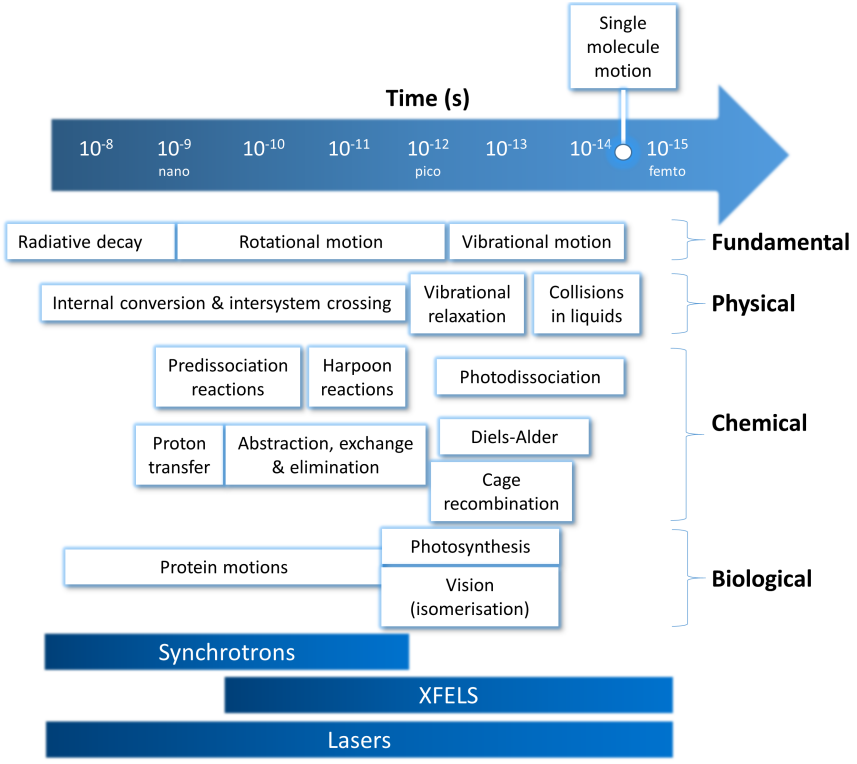

FIGURE 1.1: A broad comparison of the approximate timescales of a number of physical, chemical and biological processes in atoms and molecules, alongside the approximate ranges of pulse duration for lasers, synchrotrons, and X-ray Free-Electron lasers (the latter two are sources of X-rays). Adapted from Ref. [7]

on electron density through to fully quantum multireference *ab initio* descriptions of the electronic structure of a given molecule. For any system a great variety of static properties related to electronic structure can be calculated, including interaction, orbital, and excitation energies, vibrational frequencies, transition moments, dipole and higher-order multiple moments and spectroscopic observables. In this endeavour it is usually the size of the problem, roughly proportional to the number of electrons, which dictates the choice of method. Generally, the larger the system, the greater degree of approximation required in order that calculations can be carried out in a feasible time. A number of standard computational chemistry packages are

available with which one may carry out such electronic structure computations.

The field of *ab initio* quantum molecular dynamics (QMD) extends electronic structure calculations of molecular properties for a specific structure into the time domain, where the structural evolution is governed by the nuclear wavepacket. QMD considers interactions between different electronic states (for example, nonadiabatic or spin-orbit coupling) explicitly[1] and allows dynamics to evolve over coupled potential energy surfaces obtained either by pre-computation or "*on-the-fly*" as the dynamics progress.

1.1 Photochemistry

Ancient civilisations recognized the importance of light to life on Earth — - indeed, the Sun has been worshipped as a deity since antiquity. Photochemistry is ubiquitous in nature, with famous examples include bioluminescence [10], photosynthesis [11], vision [12] and DNA damage mitigation [13] to name but a few. The pervasiveness of photochemistry in nature underlines the need for a complete understanding of the underlying mechanisms. A number of Nobel Prizes have related to photochemistry, notably the 1981 prize concerning the Woodward-Hoffman rules [14] which predict the stereochemical outcome of electrocyclic reactions based on the number of π electrons and whether the reaction takes places under thermal or photochemical conditions.

Important early understanding of photochemical and photophysical processes came from the work of Draper [15], Grotthuss [16], Stark and Einstein [17] in formulating their laws of photochemistry:

- **First (Grotthuss-Draper) law** — Light must be absorbed by a compound in order for a photochemical reaction to occur

[1] This is in contrast to molecular dynamics (MD), where the aim is to reproduce ground state statistical properties by modelling the constituents of an N-body system by classical mechanics with forces most commonly derived from parametrised force fields.

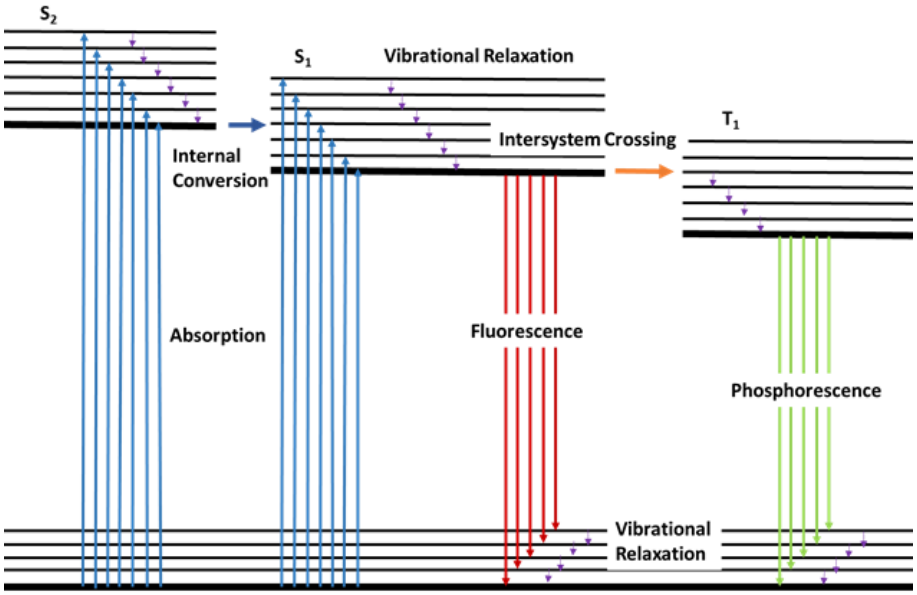

FIGURE 1.2: An example of a Jablonski diagram, demonstrating possible radiative and non-radiative events in a photochemical reaction: absorption, fluorescence, phosphorescence, vibrational relaxation, internal conversion, and intersystem crossing [18].

- **Second (Stark-Einstein) law** — The number of photons absorbed must match the number of molecules which undergo a photochemical reaction

A modern understanding of photochemistry is often summarised in a Jablonski diagram [19] as shown in Fig. 1.2, which schematically details the radiative and non-radiative processes a molecule may undergo after absorbing a photon, all of which lead to a decay of the initially excited electronic state. The example here shows excitation from the ground state to various vibrational levels of the S_2 state, after which the population in S_2 may relax to lower vibrational levels or undergo internal conversion (IC) to the S_1 state. Once in S_1, the system may continue to vibrationally relax, decay directly to the ground state by emitting a photon (fluorescence), or transfer to the T_1 state *via* intersystem crossing (ISC), following which the ground state is reached by phosphorescence (spin-forbidden photon emission). Herein

the focus on nonradiative processes, which occur rapidly compared to the emission of light.

More generally, following absorption the excited molecule[2] evolves along the potential energy surface, dictated by forces exerted on the nuclei by the electrons, where it may encounter regions of strong electronic state coupling and leak population onto other states. Regions where state crossings are found are termed conical intersections (CoIns) [20–23] whose dimensionality in polyatomic systems is given by $N - 2$, where N is the number of internal co-ordinates. An example of such a process is shown in Fig. 1.3 for the case of the excited state dynamics of acetylacetone. CoIns are critical mechanisms by which population is transferred nonradiatively between electronic states. Internal conversion (IC) refers to the spin-allowed population transfer between states of the same spin multiplicity, while intersystem crossing (ISC) occurs between states of different spin multiplicities. ISC is spin-forbidden and is mediated by spin-orbit coupling (SOC), a relativistic effect arising from the coupling between the intrinsic spin and orbital motion of an electron. If sufficiently strong, SOC facilitates the flip of the spin of an electron and thus the transfer to a state of different multiplicity. Because of selection rules governing absorption and nature's favour of stable open-shell systems, SOC typically manifests itself as transitions between singlet and triplet states. Through IC and ISC, the nuclear and electronic motions of a photochemical system are intrinsically coupled together. *Via* traversing through one or more CoIns the wavepacket will either return to the reactant ground state or locate a minimum energy structure corresponding to a chemical reaction product. Crucially, it does so without the need to cross thermal activation barriers, which are insignificant compared to the energy supplied by, for instance, a UV photon. In other words, photochemical reactions offer unique opportunities in the effort to control chemistry.

[2]Or more accurately the *wavepacket*, a superposition of molecular eigenstates whose coherence is governed by the coherence of the pump photons. In other words, incoherent light (e.g. sunlight), whose contributing electromagnetic field components oscillate out of phase, would create an incoherent wavepacket whose behaviour is quasi-statistical. A coherent pulse (e.g. from a laser) would instead produce a coherent wavepacket whose nuclear motion is shot-to-shot reproducible.

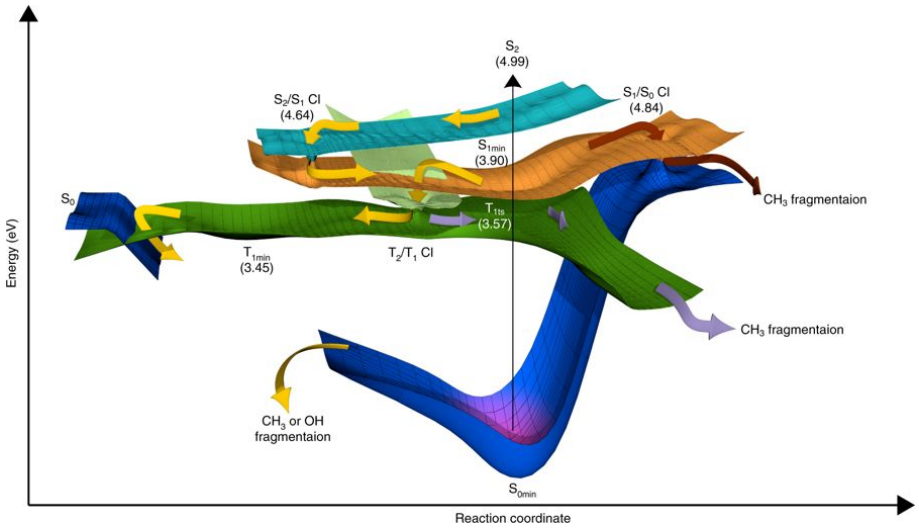

FIGURE 1.3: A schematic overview of the relaxation mechanism of acetylacetone as an illustration of wavepacket evolution. Initial excitation is to S_2 $\pi\pi^*$ state. The wavepacket subsequently passes through several conical intersections and undergoes intersystem crossing to the T_2 and T_1 states as it explores the potential energy landscape, dividing among CH_3 and OH fragmentation pathways as well as leading back to the ground S_0 state. Taken from Ref. [24].

1.2 Experimental methods

Although the focus of this thesis is on computational simulations of interesting photochemical processes, the impetus for these simulations comes from exciting new experimental techniques that study the temporal evolution of such processes. It is therefore useful to give a brief overview of the most relevant experimental techniques.

The dawn of femtochemistry was ushered in almost 20 years ago when the 1999 Nobel Prize in chemistry was awarded to Ahmed Zewail for his pioneering work on capturing the femtosecond scale chemistry of the photodissociation of ICN and NaI [7], work itself underpinned by advances in laser technology recognised by the 2018 Nobel Prize in Physics, which was partially awarded to Donna Strickland for her *"role in the development*

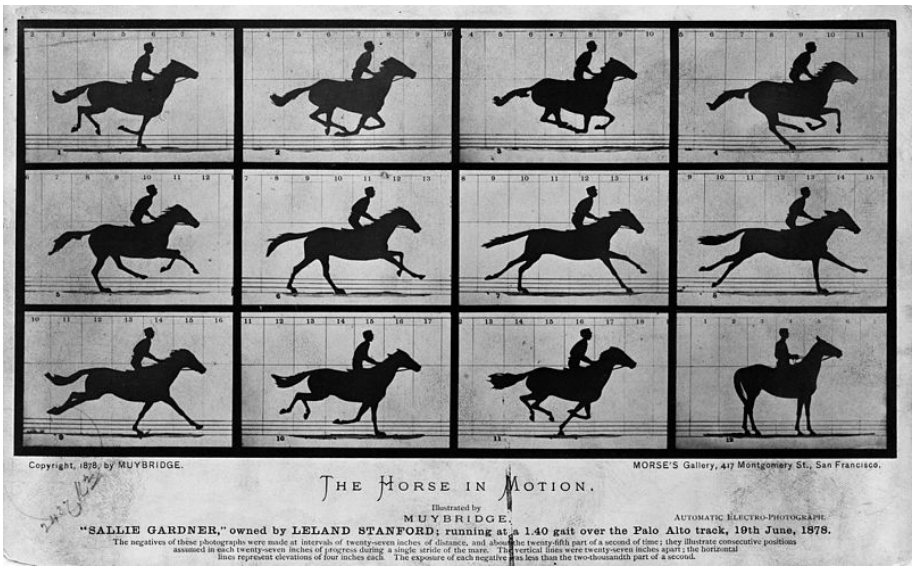

FIGURE 1.4: *"The Horse in Motion"* by Eadweard Muybridge, who in 1872 was hired by American industrialist Leland Stanford to settle a debate: At any point in time, are all four hooves of a trotting horse out of contact with the ground? This sequence of photographs was taken by a series of cameras triggered one after another with a set of strings, and demonstrated conclusively that this was indeed the case. Muybridge spent many years studying humans and animals in motion *via* stop-motion photography [25].

of a method of generating high-intensity, ultra-short optical pulses" [26]. The origins of femtochemistry can be traced to the development of flash photolysis in 1949 [27], which seeded numerous variations of spectroscopy (emission, single-photon, electron spin resonance and others [28]) and latterly the modern framework of high precision, high resolution pump-probe spectroscopy and diffraction experiments made possible with the advent of the femtosecond laser [29].

The importance of short pulses of light for time-resolved imaging can be understood by analogy to the stop-motion photographic experiments of Eadweard Muybridge [25]. In the late 19th century, Muybridge set about answering the question of whether the four hooves of a galloping horse simultaneously left the ground. Because the motion in question was too fast for the naked eye to observe, Muybridge set up a series of cameras, spaced

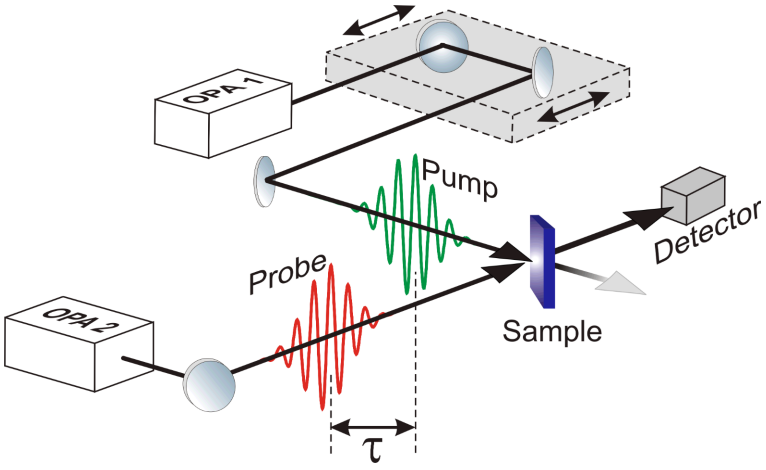

FIGURE 1.5: A simplified schematic representation of a typical pump-probe experimental setup. The reaction is initiated by a pump whose photon energy is tuned to the intended excitation process. Depending on the specified time delay, the reaction is interrogated by the probe pulse and the resultant changes in the probe light (be it scattering or absorption) transmitted to a suitable detector. In this example the pump and probe lasers are generated from OPAs, devices which emit variable wavelengths of laser light *via* nonlinear parametric mixing of input sources. Taken from Ref. [30].

21 inches apart and triggered by tripwire. This setup corresponds to a snapshot taken every 35 milliseconds, with contemporary technology dictating an exposure time of about 1 millisecond. This was sufficient to demonstrate that the four hooves do indeed leave the ground at the same time, as shown in Muybridge's photographs in Fig. 1.4. Notions of spatial and temporal resolution, shutter speed (i.e. pulse length) and time-synchronisation are directly transferable to time-resolved molecular imaging.

Essentially all modern time-resolved experiments rely on pump-probe schemes as shown in Fig. 1.5. The reaction is initialised by a suitable pump laser pulse, establishing a uniform time zero for the creation of a wavepacket from the ensemble of molecules. The wavepacket is probed with a second laser pulse after a variable time delay, with the scattered or emitted light captured on a suitable detector. In Fig. 1.5, the time delay is in fact controlled by the length of the pump laser path, but relative to a fixed probe path length the same effect is achieved. A sequence of such snapshots

can be stitched together to present a so-called *molecular movie* showing the time-evolution of the molecule in terms of the detected signal. The pump and probe lasers here are generated using optical parametric amplification (OPA), which produces the desired wavelengths of light *via* nonlinear parametric mixing of input light sources.

With the probe source, there are a myriad of spectroscopic or diffractive techniques which give complementary information on the internal electronic structure and nuclear motion of the system under study. The resolution of dynamical information a particular method can retrieve is dependent on the temporal resolution of the probe[3]. Femtosecond resolution is necessary to observe vibrational motions and extremely short-lived excited states. Two important time-resolved imaging techniques are discussed below, both of which were used by experimental collaborators to study the molecules of interest in this thesis.

1.2.1 Time-resolved photoelectron spectroscopy

Time-resolved photoelectron spectroscopy (TR-PES) is well-established as a technique to follow dynamics at the molecular scale as it is directly sensitive to changes in the electronic and vibrational structure of a system (but not directly to its geometry). The basis of the method lies in capturing the distribution of kinetic energies E_K of photoelectrons produced by photoionisation of the sample, from which the binding energy of the electron E_B can be inferred by $E_B = h\nu - E_K$ where $h\nu$ is the energy of the incident photons. In the case of aligned molecules, this technique can be expanded to include the photoelectron angular distribution (PAD), which gives information on the angular momentum of the orbitals from which the photoelectrons are ionised [31].

The molecule of interest is excited to a bright state by the pump pulse, and after a variable time delay, the sample is ionised by the probe. Here lies the chief advantage of the method; there are no dark states in photoionisation so signal may generated at every geometry if the probe energy is high

[3]Specifically, the cross-correlation of the pump and probe pulses. In an experiment the pump event is not instantaneous due to the comparative broadness of the pump pulse.

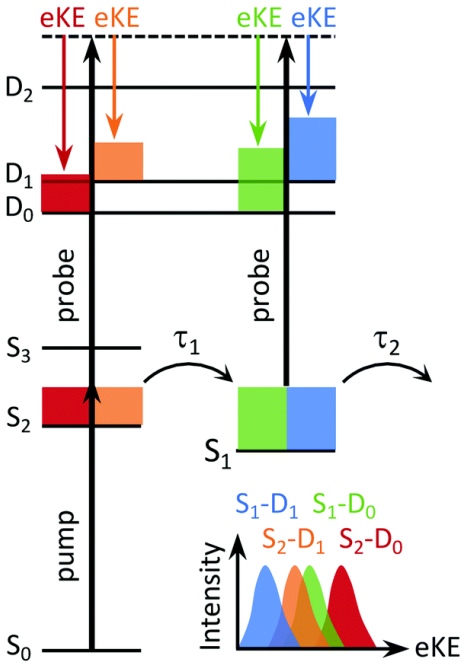

FIGURE 1.6: A schematic energy level diagram demonstrating the typical processes involved in a TR-PES experiment Here, coloured blocks represent excess vibrational energy in the system following photoexcitation from the ground state. The various permutations of ionisation into different cationic states from different neutral states gives rise to a band structure, shown as the photoelectron spectrum in the lower right of the figure. Timescales for internal conversion from $S_2 \rightarrow S_1$ and $S_1 \rightarrow S_0$ are labelled τ_1 and τ_2 respectively. Taken from Ref. [32].

enough. The ejected electrons are dispersed according to their kinetic energy. Sufficient sampling of time points allows experimentalists to build up a picture of the evolving E_K distributions and PADs. A schematic description of the processes in a TR-PES experiment is shown in Fig. 1.6, which demonstrates the various ionisation channels (into states D_0 to D_2) open to a system after excitation from the ground state. Coloured blocks represent excess vibrational energy left in the system after each excitation event, which correspond to the photoelectron spectrum shown in the lower right of the figure.

The photoelectron spectra themselves can be measured by methods based

on velocity map imaging (VMI). In VMI, an electrostatic field is used to accelerate ions onto a detector consisting of a microchannel plate, a phosphor screen and a charge-coupled device. The resultant image separates ions based on their velocities. Such experiments also encompass time-of-flight information, from which the photoelectron spectrum can be inferred by how long it takes photoelectrons to traverse the distance between the interaction region to the detector. The range of molecular motion which can be imaged in these ways is dictated by the energy range of the probe; the lower the energy of the molecule, the more energy is required to ionise it. Recent experiments on the photodynamics of CS_2 has demonstrated the use of a probe covering the entire reaction path [33]. Excellent descriptions of these methods and their applications can be found in Ref. [32] and references therein.

An engineering drawing of Artemis, part of the Central Laser Facility, is shown in Fig. 1.7, showing the high flux XUV line and the tuneable XUV beamline, with their respective coherent XUV imaging and condensed matter end-stations. Artemis uses high harmonics to generate femtosecond pulses for time-resolved imaging studies of solid, condensed and gas-phase matter. Much of the TR-PES experimental work on the photodissociation of CS_2 associated with this thesis was carried out at Artemis in 2017 [33, 34].

1.2.2 Time-resolved X-ray diffraction

While photoelectron spectroscopy is sensitive to the electronic states of the target system, it does not directly give information about the molecular structure. Diffractive techniques rely on the scattering of incoming particles such as electrons or photons to generate a diffraction pattern in reciprocal space which is a function of the charge or electron density [36].

A new X-ray source is the X-ray free-electron laser (XFEL), whose principles were first suggested by Madey [38]. In brief, in an XFEL a beam of free electrons is accelerated to relativistic velocities and passed through long undulators, series of magnets of opposite polarisation, which force the electrons to oscillate and emit radiation perpendicularly. Essential to the function of XFELs is the principle of self-amplified stimulated emission

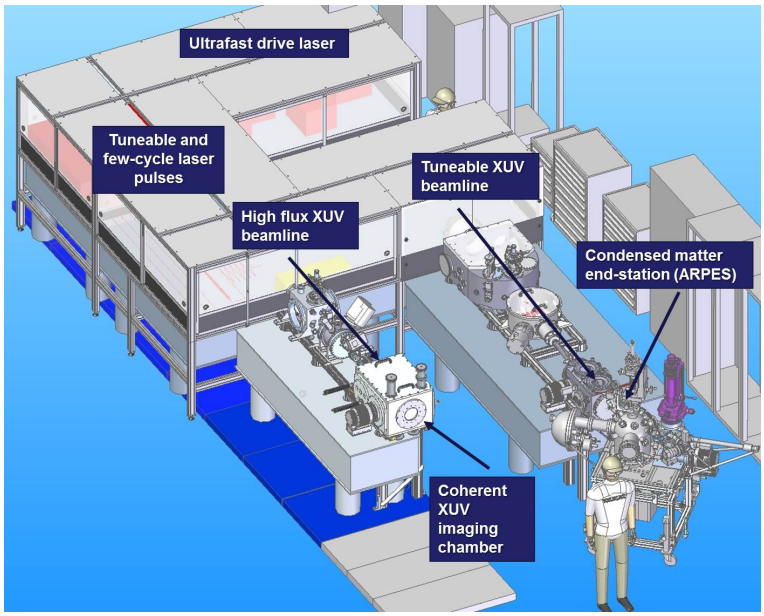

FIGURE 1.7: Engineering drawing of the Artemis setup at the Central Laser Facility, used for ultrafast XUV research. Artemis features two XUV beamlines; a tuneable beamline with monochromator for the generation on 10-50 fs pulses ranging from 12-80 eV, and an imaging beamline with a flat field spectrometer, filters and multilayer mirrors, for experiments requiring higher photon flux. TR-PES work on the photodissociation dynamics of CS_2 forming much of this thesis was carried out at the Artemis facility in 2017. https://www.clf.stfc.ac.uk/Pages/Technical-Specification.aspx (accessed 09-10-2018).

(SASE) [38, 39]; at sufficient beam intensity, the electrons begin to form microbunches which emit coherent radiation as they undulate. This radiation sums constructively to generate tunable, ultrashort pulses of intense, bright, light [40]. This method of coherent pulse generation is quite unlike the population inversion-produced stimulated emission of previous lasers. Before the realisation of practical XFELs, experimentalists made use of radiation from third-generation synchrotron sources [41]. In short, the requirement that the emitted radiation be of immense intensity and brightness, packaged in a very short pulse, puts severe strain on the quality of the electron or positron beam. XFELs overcome these difficulties and allow the generation

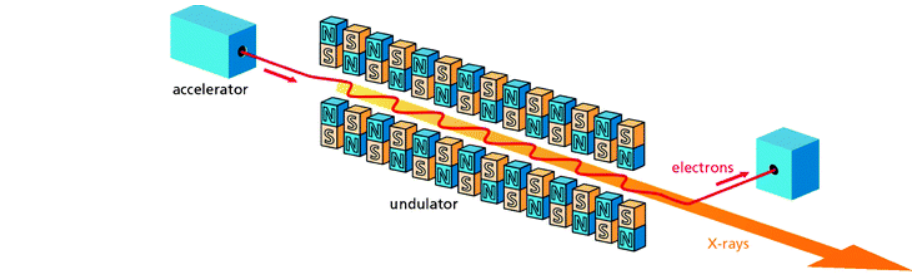

FIGURE 1.8: X-ray free-electron lasers are capable of intense, ultrashort pulses. *Top*: A key component of an XFEL is the undulator, through which electrons are manipulated into coherent bunches by alternating magnetic fields, causing the emission of coherent X-rays (figure adapted from Ref. [35]). *Bottom*: Bird's eye view of LCLS, a hard X-ray source which is part of SLAC National Accelerator Laboratory at Stanford University. The main beam line is approximately 1 km long.

of pulses on the order of 20 fs duration at very high intensities and are ideally suited for the study of chemical reactions which occur on this timescale, mapping out the structural changes as, for instance, a photochemical dissociation progresses [42]. The use of these diffractive techniques in the study of dynamics is termed time-resolved X-ray diffraction (TR-XRD) and has been reviewed extensively [6, 43] (and references therein). A comparison of the peak brilliances (a measure of X-ray beam quality) of a number of synchrotron and XFEL sources is given in Fig. 1.9. The first facility capable of delivering soft X-rays in this way (FLASH) opened in 2005 in Hamburg [44], followed by FERMI [45] (Italy). Currently, the only operational hard X-ray facilities are the Linac Coherent Light Source (LCLS) at Stanford [46] and SACLA [47] in Japan, while the European XFEL in Hamburg [48] began

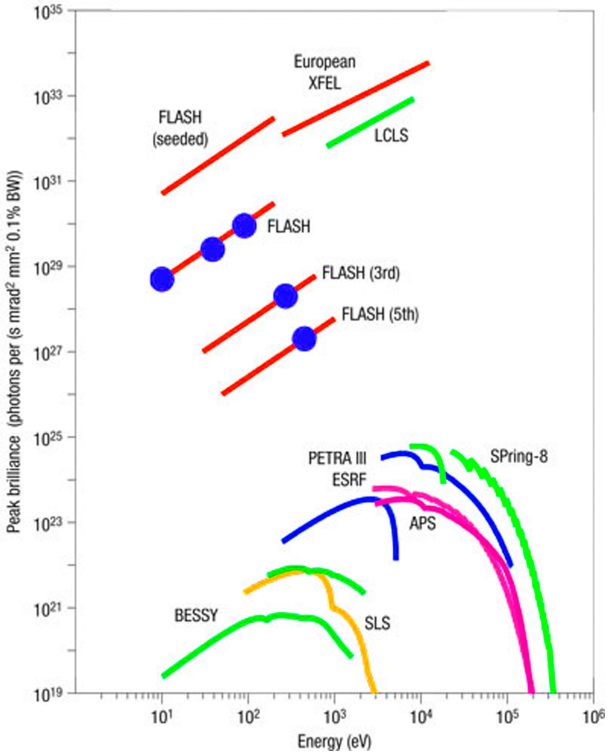

FIGURE 1.9: A comparison between the peak brilliance and photon energy of a number of current synchrotron and X-ray free-electron laser sources. At the top of the figure are XFELs in Hamburg and Stanford, with various synchrotron sources shown at lower peak brilliances. Taken from Ref. [37].

user operation in 2017. Other facilities include Korean XFEL [49] and SwissFEL [50].

Today's sophisticated time-resolved experiments, be they carried out using small tabletop lasers or at large scale national facilities, provide only a partial view of inherently complex processes. Therefore the interpretation of such experiments is greatly assisted by contributions from parallel theoretical work, which often serves to bring out subtleties easily missed otherwise in the assignment of particular features of, for example, a photoelectron spectrum or a diffraction pattern. QMD simulations in particular offer the tantalising prospect of allowing one in principle to study of all features of a chemical reaction in a single production run.

1.3 Overview of thesis

Since the 1950s, the development of ever-more instructive experimental techniques to study molecular motion at atomic spatial and temporal resolution has naturally spurred the parallel evolution of theoretical frameworks, models, codes and software which one can use to help decode the underlying dynamics taking place in a given chemical system, aiding in the interpretation of complex, multi-faceted and at times indirect experimental data — indeed, at times helping to direct experimentalists down viable avenues of future exploration. An overview of the relevant background and methods in electronic structure theory and QMD approaches is given in Chapter 2. Chapter 3 introduces the first simulations of the photodynamics of CS_2 to take account of SOC, analysed alongside new TR-PES experiments. While structurally simple, the dissociation of one of the sulfur atoms after UV photon absorption evolves across a multitude of couple potential energy surfaces, complicated by strong spin-orbit coupling *via* which triplet states strongly participate in the dynamics. Whilst initially intended to map onto new TR-PES experimental results of CS_2 photodissociation, it will be discussed why the results are not comparable despite encouraging similarities between experiment and theory. Chapter 4 details the initial results of more accurate, but much more computationally demanding, simulations of the early stages of the photodynamics studied by the TR-PES experiments, which include many more electronic states. In Chapter 5, a comparison is discussed between reduced-state simulations analogous to those of Chapter 3 with simulations calculated using an enhanced *ab initio* approach. Chapter 6 deals briefly with efforts to move towards the calculation of full-dimensional surfaces of CS_2, demonstrated by examples calculated at low levels of theory. Finally, Chapter 7 features a study of the photodynamics of trimethylamine (TMA), a system featuring the characteristic low-lying valence Rydberg states of tertiary aliphatic amines, and the rapid interplay between the Rydberg manifold of states.

Chapter 2

Theory

2.1 Introduction

This thesis describes applications of quantum molecular dynamics (QMD) methods to chemically-relevant problems. As the name suggests, these problems are fundamentally quantum mechanical in nature; QMD methods and the underlying electronic structure calculations attempt to describe atomic and subatomic particles whose behaviour is not classical. In this chapter an overview is given of the pertinent concepts of quantum mechanics, electronic structure theory, and dynamics approaches with particular emphasis on surface-hopping as implemented in the SHARC code.

2.2 The Schrödinger equation

The fundamental goal of any quantum dynamics method is to solve the time-dependent Schrödinger equation (TDSE),

$$\imath\hbar\frac{\partial}{\partial t}|\Psi(\vec{R},\vec{r},t)\rangle = \hat{H}(\vec{R},\vec{r},t)|\Psi(\vec{R},\vec{r},t)\rangle \tag{2.1}$$

which governs the non-relativistic evolution of a particle or system of particles. In Eq. (2.1) $|\Psi(\vec{R},\vec{r},t)\rangle$ is the wave function, $\imath$ is the complex unit, $\hbar$ is the reduced Planck's constant and $\hat{H}(\vec{R},\vec{r},t)$ is the Hamiltonian operator for the system. Both of these quantities depend on nuclear coordinates $\vec{R}$, electronic coordinates $\vec{r}$ and time t. Any observable property of a system may be calculated from its wave function; the square modulus of the wave

function of a particle is proportional to the probability that the particle will be found at a given point and time.

For eigenstates of this time-dependent Hamiltonian (also called stationary states), the separation of variables technique can be applied to Eq. (2.1) to yield,

$$|\Psi(\vec{R},\vec{r},t)\rangle = |\Psi(\vec{R},\vec{r})\rangle \exp\left(-\imath\frac{E_{\text{total}}}{\hbar}\right), \tag{2.2}$$

where time-dependence is included *via* the complex phase factor in the exponential term. From this separation, the time-independent Schrödinger equation (TISE) [51] may be derived,

$$\hat{H}(\vec{R},\vec{r})|\Psi(\vec{R},\vec{r})\rangle = E_{\text{total}}|\Psi(\vec{R},\vec{r})\rangle, \tag{2.3}$$

where E_{total} is an infinite series of eigenvalues corresponding to the energy levels of the system.

Numerical solutions of the TDSE require further simplification, most notably the Born-Oppenheimer approximation discussed in the next section.

2.3 The molecular Hamiltonian

2.3.1 The Born-Oppenheimer approximation

In atomic units, the molecular Hamiltonian can be defined as,

$$\begin{aligned}\hat{H}_{\text{mol}}(\vec{R},\vec{r}) = &-\sum_A \frac{1}{2M_A}\nabla_A^2 - \sum_i \frac{1}{2}\nabla_i^2 \\ &+ \sum_{A<B}\frac{Z_A Z_B}{|\vec{R}_A - \vec{R}_B|} - \sum_A\sum_i \frac{\vec{R}_A}{|\vec{R}_a - \vec{r}_i|} + \sum_{i<j}\frac{1}{|\vec{r}_i - \vec{r}_j|},\end{aligned} \tag{2.4}$$

where the electrons are indexed by i and nuclei by A (with mass M_a and atomic charge Z_a). The first two terms refer to the nuclear and electronic kinetic energies respectively (T_{n} and $\hat{T}_{\text{e}}$), and the latter three encompass the

Coulombic potentials for the nuclear-nuclear V_{nn}, nuclear-electronic V_{ne} and electronic-electronic V_{ee} interactions respectively.

This non-relativistic Hamiltonian is an example of the many-body problem, and as such cannot at present be solved analytically for even the smallest molecule. Therefore, approximations must be invoked. The first and best known of these is the Born-Oppenheimer approximation (BOA) [52], which states that one may uncouple the nuclear and electronic degrees of freedom in a molecular wave function,

$$|\Psi(\vec{R},\vec{r})\rangle = |\Psi^{\mathrm{e}}(\vec{r},\vec{\vec{R}})\rangle|\Psi^{\mathrm{n}}(\vec{R})\rangle, \tag{2.5}$$

where $\vec{\vec{R}}$ indicates that the electrons depend parametrically on the nuclear positions. Physically, this approximation is derived from the fact the the nuclei are much heavier than the electrons (a proton being a factor of $\sim$1836 heavier than an electron) and thus nuclear kinetic energy can be neglected; in other words the electrons respond practically instantly to any nuclear motion. Applying this approximation leads to the so-called electronic Hamiltonian as the sum of $\hat{T}_{\mathrm{e}}$, V_{ee}, V_{ne} and constant T_{n}. This leaves the electronic Schrödinger equation,

$$\hat{H}^{\mathrm{e}}|\Psi^{\mathrm{e}}(\vec{r},\vec{\vec{R}})\rangle = E^{\mathrm{e}}(\bar{R})|\Psi^{\mathrm{e}}(\vec{r},\vec{\vec{R}})\rangle, \tag{2.6}$$

With this equation, electronic energy levels can be calculated as the eigenvalues $E^{\mathrm{e}}(\vec{\vec{R}})$ of $\hat{H}^{\mathrm{e}}$. These are the adiabatic states, i.e. eigenstates of the electronic Schrödinger equation within the BOA. The dimensionality of this computation scales with the size of the system being calculated as $3N$ where N is the number of particles. By solving this equation for different nuclear positions a multidimensional potential energy surface can be calculated. Before this, further approximations are necessary as the problem is still many-bodied.

2.3.2 Nonadiabatic coupling

As an eigenvalue problem, Eq. (2.6) has an infinite number of solutions $|\Psi^{\mathrm{e}}_{\alpha}(\vec{r},\vec{\vec{R}})\rangle$ and eigenvalues $E^{\mathrm{e}}_{\alpha}(\bar{R})$. The lowest energy solution describes the

ground state of the molecule, and all other solutions giving the electronic excited states. Given this separation, the exact total wave function for a molecule may be expressed by the Born-Huang ansatz [53],

$$|\Psi\rangle = \sum_{\alpha}^{\infty} |\Psi_{\alpha}^{\mathrm{e}}\rangle |\Psi_{\alpha}^{\mathrm{n}}\rangle, \tag{2.7}$$

which is a product of the separated nuclear and electronic wave functions summed over all states, and solves the combined electronic-nuclear wave function. This can be inserted into the TDSE to give,

$$\imath\hbar \frac{\partial}{\partial t} \sum_{\alpha}^{\infty} |\Psi_{\alpha}^{\mathrm{e}}\rangle |\Psi_{\alpha}^{\mathrm{n}}\rangle = \hat{H}(\vec{R}, \vec{r}, t) \sum_{\alpha}^{\infty} |\Psi_{\alpha}^{\mathrm{e}}\rangle |\Psi_{\alpha}^{\mathrm{n}}\rangle. \tag{2.8}$$

Taking solutions to the electronic Schrödinger equation and projecting on $\langle \Psi_{\beta}^{\mathrm{e}}|$ gives,

$$\left[\hat{T}_{\mathrm{n}} + E_{\beta}^{\mathrm{e}}\right] |\Psi_{\beta}^{\mathrm{n}}\rangle + \sum_{\alpha} T_{\beta\alpha}^{\mathrm{NACMEs}} |\Psi_{\alpha}^{\mathrm{n}}\rangle = \imath\hbar \frac{\partial}{\partial t} |\Psi_{\beta}^{\mathrm{n}}\rangle. \tag{2.9}$$

Here, $T_{\beta\alpha}^{\mathrm{NACMEs}}$ is an operator which describes the effect of the nuclear kinetic energy operator $\hat{T}_{\mathrm{n}}$ on the allowed electronic wave functions,

$$T_{\beta\alpha}^{\mathrm{NACMEs}} = -\sum_{A} \frac{1}{2M_A} \left[\langle \Psi_{\beta}^{\mathrm{e}} | \nabla_A^2 | \Psi_{\alpha}^{\mathrm{e}} \rangle\right] + \left[\langle \Psi_{\beta}^{\mathrm{e}} | \boldsymbol{\nabla}_{\boldsymbol{A}} | \Psi_{\alpha}^{\mathrm{e}} \rangle \boldsymbol{\nabla}_A\right]. \tag{2.10}$$

Eq. (2.10) describes the coupling between the electronic wave functions and the nuclear motion in terms of the nonadiabatic coupling matrix elements (NACMEs). If the NACMEs are neglected (i.e. the BOA is applied), Eq. (2.9) is simplified to,

$$\left[\hat{T}_{\mathrm{n}} + E_{\beta}^{\mathrm{e}}\right] |\Psi_{\beta}^{\mathrm{n}}\rangle = \imath\hbar \frac{\partial}{\partial t} |\Psi_{\beta}^{\mathrm{n}}\rangle, \tag{2.11}$$

which is the nuclear Schrödinger equation for only a single, adiabatic electronic state. While significantly simplifying Eq. (2.10), this approximation is not always valid. In regions where electronic states become close in energy, the NACMEs are generally large and cannot be neglected. This is easily

shown by expanding the elements of the derivative coupling terms in Eq. (2.10) (the second term in square brackets) as,

$$d^{A}_{\alpha\beta} = \frac{\langle \Psi^{\mathrm{e}}_{\beta} | \boldsymbol{\nabla}_{\boldsymbol{A}} \hat{H}^{\mathrm{e}} | \Psi^{\mathrm{e}}_{\alpha} \rangle}{E_{\beta} - E_{\alpha}}, \tag{2.12}$$

which become large as E_α and E_β approach each other and singular when $E_\beta = E_\alpha$, demonstrating why the BOA breaks down near degeneracies [54].

All of the above has been discussed in the context of adiabatic states, the physical character of which may change across a reaction co-ordinate in order to ensure they remain eigenstates of the electronic Hamiltonian [55]. Conversely, diabatic states do not change in character as a reaction co-ordinate is scanned. A typical example demonstrating the difference is shown in Fig. 2.1, which shows schematic potential energy cuts of the dissociation co-ordinate in NaCl. The adiabatic states (black curves) feature an avoided crossing between the ionic and covalent states (the green and blue curves respectively). As such, the character of each adiabatic state changes (from ionic to covalent or *vice versa*) as the NaCl bond is extended.

More formally, diabatic states are generated by applying a unitary transform to the adiabatic states, diagonalising $\hat{T}_{\mathrm{n}}$. Strictly speaking, true diabatic states have vanishing derivative coupling between any two states at any geometry,

$$d_{\alpha\beta}(\vec{R}) = \langle \Psi_{\alpha} | \frac{\partial}{\partial \vec{R}} \Psi_{\beta} \rangle = 0 \; \forall \; \alpha, \beta, \vec{R}, \tag{2.13}$$

a condition which simplifies the description of electronic transitions as the coupling is accounted for in the electronic Hamiltonian [56, 57]. In other words, the diabatic states are not coupled by $\hat{T}_{\mathrm{n}}$ and so are not affected by the problem that the couplings can become singular.

Unfortunately it is usually not possible to transform from a given adiabatic basis into a strictly diabatic basis because the curl condition ($\nabla \times \tau = \tau \times \tau$ where τ represents the nonadiabatic coupling matrix elements), derived from Eq. (2.13), cannot be met [58]. However, techniques exist to approximate this transformation, typically by minimising the derivative coupling [58], slowly varying the states by block diagonalisation [59], or by

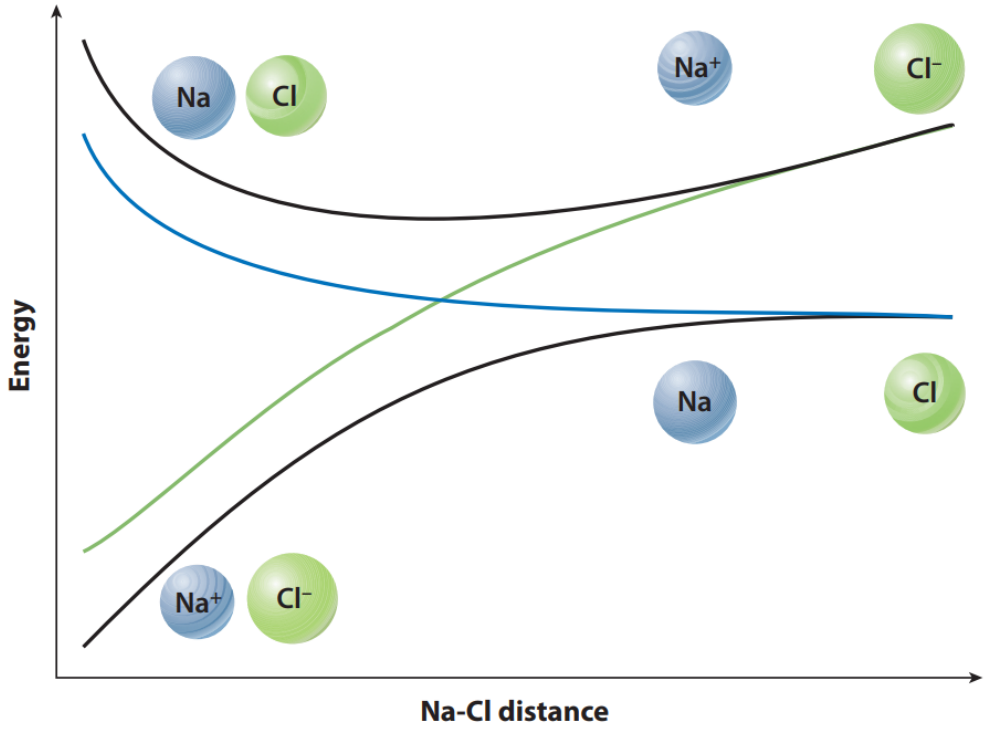

FIGURE 2.1: Schematic potential energy cuts showing the dissociation of NaCl. The diabatic ionic and covalent curves are shown as green and blue respectively, and maintain the same character across the reaction co-ordinate. This is not the case for the adiabatic curves (black). Taken from Ref. [55].

using the eigenstates of experimental observables [60, 61]. Because of the inexactitude of such transformations (which require the calculation of expensive derivative couplings), the difficulties of directly constructing diabatic states [62], and the fact that the adiabatic basis arises naturally from the definition of the electronic Schrödinger equation, electronic structure packages conventionally work in the adiabatic basis. An excellent review of diabatic states and their role in the qualitative understanding of chemical phenomena is given in Ref. [55].

The breakdown of the BOA is, in a way, unnerving; much of modern understanding of physical chemistry is predicated on it, for example fundamental concepts such as molecular structure [8]. The BOA does, however, give the starting point for the simulation of nonadiabatic dynamics, from

which the picture of a single potential energy surface is extended to a multi-surface manifold of coupled electronic states.

2.3.3 Spin-orbit coupling

Relativistic effects such as spin-orbit coupling (SOC) cannot be neglected in heavy atoms or in any instance where one wishes to describe the coupling of electronic states whose spin multiplicity differs. The origin of these effects, a subject spanning textbooks of its own, e.g. [63], lies in the mass increase of particles travelling at a significant fraction of the speed of light,

$$m_{\text{rel}} = \frac{m_{\text{rest}}}{(1 - (v/c))^2}, \tag{2.14}$$

where m_{rest} is the rest mass of the particle (typically an electron in quantum chemical applications), v is its velocity, and c is the speed of light. The Bohr radius a_0 is dependent on the electron mass,

$$a_0 = 4\pi\epsilon_0 \frac{\hbar^2}{m_{\text{e}}}, \tag{2.15}$$

where ϵ_0 is the vacuum permittivity constant. Any increase in mass will decrease the Bohr radius. After some derivation, and simplifying to atomic units, the ratio of the effective Bohr radius to its stationary counterpart can be expressed as,

$$\frac{a_{\text{rel}}}{a_0} = \sqrt{1 - \left(\frac{Z}{nc}\right)^2}, \tag{2.16}$$

where Z is the nuclear charge and n is the principle quantum number of the electron. Thus, for small values of n and large values of Z (i.e. core electrons, which have a high probability density close to large nuclei) relativistic effects are prominent. Such effects are crucial in explaining a variety of phenomena, for example the colour of gold [64], the behaviour of valence electrons in large atoms [65], the stability of Hg^{2+} [66], the crystal structure of lead [67], and a plethora of others [68].

Key to many examples of photochemistry is ISC, the flip of an electron's spin without the emission of any radiation, most commonly seen by the singlet-triplet transitions in closed shell systems. ISC arises from the spin-orbit interaction (the interaction of the spin angular momentum with its orbital angular momentum; in other words, the interaction of the magnetic moments from each angular momenta, μ_s and μ_l). If the total orbital and total spin angular momenta of the electrons in an atom are defined as $\hat{L}$ and $\hat{S}$, an operator describing the energy change due to the spin-orbit interaction may be defined,

$$\hat{H}_{\mathrm{SOC}} = hc\zeta\hat{L}\hat{S}, \tag{2.17}$$

where there is the spin orbit constant ζ (an energy). For hydrogenic systems, it can be shown that ζ depends only on the principle n and orbital l quantum numbers,

$$\zeta_{nl} = \frac{\alpha^2 R_\infty Z^4}{n^3 l(l+1/2)(l+1)}, \tag{2.18}$$

where α is the fine structure constant and Z is the nuclear charge. Here the spin-orbit constant ζ_{nl} scales as the fourth power of Z, but is also inversely dependent on n^3. Thus, as for relative effects in general, SOC is greater in the case of core electrons in heavy nuclei. However, relativistic effects are not merely a curiosity of the extremes of the periodic table. Even in small systems, both natural and artificial (such as photovoltaics and organic light-emitting diodes), relativistic effects can play a role as shall be seen in the case of CS_2.

2.4 Electronic structure theory

In practice, solving the electronic Schrödinger equation defined in Eq. 2.6 requires approximations. The application of such approximations gives rise to electronic structure theory, whose methods are divided into two broad families: semi-empirical, where data derived from experiment is used to parametrise an approach, or *ab initio*, which take as their starting point

only atomic numbers and physical constants (*ab initio* translates into Latin as "from the beginning"). Considered here are *ab initio* approaches only, beginning with multiconfigurational post-Hartree-Fock methods (an introduction to the basic concepts of Hartree-Fock theory, the calculation of electronic properties, and the construction of common basis sets may be found in Appendix A).

2.4.1 Multiconfigurational approaches

In Hartree-Fock (HF) theory, a Slater determinant (see Appendix A) is used as an approximation to the true wave function. This often falls short of reliable chemical accuracy, particularly in the description of excited states, where electron correlation is typically important. This correlation energy is made of up static and dynamical contributions. Static correlation takes into account the contribution of different electronic configurations to the total electronic wave function, whereas dynamic correlation refers to the instantaneous reaction of electrons to the motion of each other [69, 70]. To address this, a series of extensions to HF theory (termed post-HF methods) have been developed in order to better describe the missing correlation energy. These methods typically involve the use of more than one single Slater determinant to construct the wave function. Two of the most common methods are Configuration Interaction (CI) and MultiConfigurational Self-Consistent Field (MCSCF).

2.4.1.1 Configuration Interaction

The HF method represents the wave function with a single Slater determinant. Beginning with a basis of K spatial and $2K$ spin orbitals, of which N are occupied and $2K - N$ are virtual, the Slater determinant,

$$|\Psi_0\rangle = |\chi_1\chi_2, ..., \chi_a\chi_b, ..., \chi_N\rangle, \tag{2.19}$$

is only one of $\binom{2K}{N}$ possible determinants or configurations which could be formed from this set of spin orbitals. Beginning from the ground state

configuration, more determinants can be formed by the excitation of a single electron into a virtual orbital,

$$|\Psi_0^r\rangle = |\chi_1\chi_2, ..., \chi_r\chi_b, ..., \chi_N\rangle, \tag{2.20}$$

Similarly, a doubly-excited determinant is defined in which two electrons have been excited into virtual orbitals,

$$|\Psi_{ab}^{rs}\rangle = |\chi_1\chi_2, ..., \chi_r\chi_s, ..., \chi_N\rangle, \tag{2.21}$$

and so forth into N-tuply excited determinants. The CI method constructs the wave function as a linear combination of all possible Slater determinants within a given set of spin orbitals,

$$|\Psi_{\mathrm{CI}}\rangle = c_o|\Psi_0\rangle + \sum_{r,a} c_a^r|\Psi_a^r\rangle + \sum_{a<b,r<s} c_{ab}^{rs}|\Psi_{ab}^{rs}\rangle + ..., \tag{2.22}$$

where each term contains expansion coefficients, and the orbitals are variationally minimised with respect to the energy to generate optimal expansion coefficients. Taking the wave function as a linear combination of all $\binom{2K}{N}$ possible Slater determinants represents the best possible wave function within the particular basis set used and is termed full configuration interaction (FCI). However, this approach quickly becomes computationally impractical as the number of particles and the size of the basis set increases, quickly running into the billions for medium-sized molecules ($N_{\mathrm{atoms}} = 10 - 15$ broadly) with reasonably-sized basis sets. Thus only very small systems can be treated in this way. To counter this, truncated methods where only certain subsets of excitations are accounted for have been developed — for example, the inclusion of only singly-excited determinants (CIS) or singly- and doubly-excited determinants (CISD), and so forth. A major drawback with the CISD method is that it is not size-extensive [69]; the correlation energy does not scale properly with the size of the system. So even these truncated CI-based methods are suited only to small molecules. Size-extensive methods do exist, commonly based on perturbation theory (PT),

the overarching aim of which is to partition a complex problem into a solvable component plus a small corrective term. In terms of Hamiltonians used in quantum chemistry, this is expressed,

$$\hat{H}^{\mathrm{e}} = \hat{H}_0 + \lambda \hat{H}_1, \tag{2.23}$$

where $\hat{H}^{\mathrm{e}}$ has been separated into a zeroth order $\hat{H}_0$ term and perturbation $\hat{H}_1$. $\hat{H}^{\mathrm{e}}$ has known eigenfunction $|\Psi_0\rangle$ and eigenvalue E_0. These can be expanded in λ,

$$|\Psi^{\mathrm{e}}\rangle = |\Psi_0\rangle + \lambda|\Psi_1\rangle + \lambda^2|\Psi_2\rangle + ...\lambda^N|\Psi_N\rangle, \tag{2.24}$$

$$E^{\mathrm{e}} = E_0 + \lambda E_1 + \lambda^2 E_2 + ...\lambda^N E_N, \tag{2.25}$$

These expressions can be inserted into the electronic Schrödinger equation to derive a mathematical framework from which molecular properties can be calculated. Differing flavours of this general method generally consist of choices in the partition schemes for $\hat{H}^{\mathrm{e}}$. The most common is Møller-Plesset PT [71], implemented in many quantum chemistry programs for second order and higher (for example, Møller-Plesset PT second order is notated MP2). Another popular scheme is the coupled cluster method, in which the electronic wave function is expressed as a linear combination of Slater determinants and an exponential excitation operator and can give exceptionally accurate results for small to medium-sized molecules [72].

Methods based on MPPT and coupled cluster cannot calculate excited states unless extensions to the theories are used, for example the Algebraic Diagrammatic Construction [73] and equations-of-motion coupled cluster [74] methods for MPPT and coupled cluster respectively. However, CI-based methods can do this simply by taking eigenvalues from states other than the ground state. However in the case of truncated CI a drawback is that the correlation of the ground state is generally better described than that of the excited states under consideration. In other words, the description of the excited states is imbalanced.

2.4.1.2 Multiconfigurational Self-Consistent Field

Related to CI, the MCSCF method is a form of truncated CI expansion where both the orbitals and the expansion coefficients are variationally minimised with respect to the energy [8]. Such an approach is useful in cases where the static correlation is significant in a system and therefore HF (or indeed any single-reference method) is insufficient to describe the required chemistry. MCSCF accounts for static correlation by including more electronic configurations. Like CI, a linear combination of Slater determinants is used as the electronic wave function ansatz,

$$|\Psi^{\mathrm{e}}\rangle = \sum_{n} c_n |\Psi_n\rangle, \tag{2.26}$$

with the key difference from CI being that here, the orbitals are optimised as well as the c_n expansion coefficients. In this way, the methodology can be thought of as a simultaneous CI and SCF calculation. The truncation schemes used also differ from typical CI truncation methods. The most important example is the complete active space (CAS) SCF method in which a user-chosen set of electrons and orbitals (occupied or virtual) are set aside and allowed to be optimised; all other electrons and orbitals are unperturbed. This set of optimised orbitals is called the active space, and full optimisation of the orbitals and expansion coefficients is carried out for all permutations of the active electrons and orbitals. Such a method is not a black-box approach, and detailed knowledge of the problem at hand is required in order to make the best choice of electrons and orbitals to include in the active space. For example in calculating a potential energy curve, any orbitals whose character changes across the course of the coordinate should be included. While not black-box, guidelines have been suggested for the sensible choice of an active space [75]. The method is designed to capture the most important contributions of static electronic correlation without the computational expense of FCI, allowing the study of far larger systems than FCI can realistically accommodate. With a judicious choice in the active space, a computational chemist can use this versatile method in many chemical contexts, including the description of transition states, bond breakage

and open-shell systems.

The CASSCF method still succumbs eventually to the problems of computational scaling [76]: the number of Slater determinants in a CASSCF calculation increases factorially with the number of electrons and orbitals in the active space. With current processing power, CASSCF calculations typically reach their limit at around 16-18 orbitals included in the active space. But the method has proved extremely versatile in the description of photochemical dynamics; it can easily be extended to describe excited states in so-called state-averaged (SA)-CASSCF, where a single set of compromise orbitals is used to simultaneously describe all of the chosen excited states (which may differ in spin multiplicity). Each state is typically given equal weight in the orbital optimisation, meaning that all states are treated in a balanced fashion unlike truncated CI-based methods. This is a key requirement in the accurate treatment of excited state dynamics.

2.4.2 Multireference approaches

CASSCF does not include a description of dynamic correlation. For this, computational chemists must turn to post-CASSCF methods which generally use multiple reference wave functions from which to generate excitations. Such methods are hierarchical extensions to the single-reference methods described above with the most popular being multireference configuration interaction (MRCI) and multireference perturbation theory (MRPT) [77].

2.4.2.1 Multireference configuration interaction

The MRCI method is a natural extension of CASSCF. Instead of one reference determinant (usually corresponding to the HF ground state) in CASSCF, in MRCI theory excitations are generated from several reference determinants using chosen excitation operators, such as the inclusion of single and double excitations as familiar from CISD, and applying them to each of the reference determinants to generate an extremely large expansion of the wave function. This approach can give very accurate results, but is again

limited by the computational expense required to treat such a large span of determinants. Like other truncated CI methods, it is also not size-extensive [78], hindering its application to many-atom systems.

MRCI is notable in its simplicity, but there are pitfalls which much be avoided. Without careful accountancy of the chosen reference functions, it is easy to double-count determinants as some reference functions will almost inevitably already be related to each other by a particular excitation. A further potential problem lies with the Slater determinants themselves, which are typically not spin symmetry-adapted; in other words, they are not eigenfunctions of spin operators. Since this is a necessary condition of the total wave function, complex transformations and expansions of the Slater determinants must be carried out [78]. A solution to this issue is to use symmetry-adapted linear combinations of Slater determinants, i.e. mathematically equivalent constructs termed configuration state functions (CSFs) which expand the MRCI wave function as,

$$|\Psi^{\mathrm{e}}\rangle = \sum_n c_n |\phi_n\rangle = \sum_n c_n \sum_m a_{nm} |\psi_{nm}\rangle, \tag{2.27}$$

where $|\phi_n\rangle$ is a CSF with symmetry-constrained coefficients a_{nm} and c_n are the usual expansion coefficients. In one sense this reformulation complicates the process because in doing so the Slater-Condon rules [79, 80] no longer apply. However, it still saves computational time relative to the necessary Slater determinant expansion.

Other approaches have been developed to widen the scope of MRCI computations. A common implementation is internally-contracted MRCI [81], where contraction coefficients in the expansion of CSFs (or Slater determinants) are taken from a preceding MCSCF calculation without further optimisation. While reducing the size of the expansion, this approach gives a set of configurations with complicated structure [82], but is still by now a well-established approach.

2.4.2.2 Multireference perturbation theory

If MRCI is the multireference extension to CI methods, MRPT does likewise for approaches based on perturbation. Variations of MRPT have been developed based on the wide array of $\hat{H}_0$ partition schemes available, but the most common is probably complete active space perturbation theory second order (CASPT2) [83, 84]. In this method, a CASSCF wave function is taken as the starting point and acted upon by a zero-th order Hamiltonian (which reduces to the MP2 Hamiltonian for a closed-shell reference state [83]). The CASPT2 method has been extended to describe excited states in two different ways. Firstly, there is the single-state method where the second order energy is calculated on a state-by-state basis. A major downside in this method, particularly for dynamics applications, is that it can lead to nonsensical double curve-crossings when there should be avoided crossings [85]. A second approach which circumvents this issue is multi-state (MS) CASPT2 [86], in which multiple electronic states are coupled together at the second-order level using an effective Hamiltonian. This method is generally not much more expensive than an equivalent series of single-state calculations [86]. However, it has been noted that MS-CASPT2 still occasionally does not give a smooth description of the PES in the vicinity of CoIns [87]. An extension to CASPT2 was proposed, with the rather unwieldy title of extended multi-configuration quasi-degenerate second-order perturbation theory (XMCQDPT2). Thankfully, its practical implementation in a CASPT2 context was shortened to merely XMS-CASPT2 [88]. XMS-CASPT2 wave functions are invariant to unitary rotation of the reference wave functions, giving smoother potentials in regions of dynamical interest (namely state crossings and CoIns) [89].

Nowadays, CASPT2 and its multistate derivatives are extremely commonly employed to calculate ground and excited state. Roland Lindh called them the "gold standard" in describing many photochemically-relevant problems [90]. It is not without limits, however. These lie in both computational resources (like any CAS-based method, CASPT2 is limited by the size of the chosen active space) and methodology; a frequently encountered issue is

that of "intruder states", configurations which are not included in the defined reference space but nonetheless have energies close to the reference energy. This is troublesome because such configurations lead to small denominators in the equations defining the second order energy, causing it to over-contribute and rendering the premise of perturbation theory (i.e. a large zeroth order term plus a small correction) redundant. An effective but somewhat blunt technique for dealing with intruder states is the introduction of level shifts [91, 92] which shift the energy of the intruder states up by a constant value (usually $\sim$0.3 a.u) to keep them out of the way of the configuration space.

2.5 Quantum molecular dynamics

With multi-state electronic energies, nuclear gradients, nonadiabatic couplings, and spin-orbit interactions, there are in principle all the ingredients required to describe a static molecule in its chemical and geometrical context. To calculate how these properties (and thus the progress of a chemical reaction) evolve in time, quantum molecular dynamics (QMD) is required. There is great utility in the use of QMD approaches to study photochemical processes, where two or more potential energy surfaces and the coupling between them must be described as the reaction evolves in time. Different QMD methods fall into a number of families based on their approaches in how the electronic properties such as energies, gradients and couplings are dealt with (pre-computed for fitted potential energy surfaces over all necessary phase space, or generated "*on-the-fly*" as the dynamics progresses) and how the nuclear motion is treated (classically, semi-classically, or fully quantum). This two-dimensional spectrum generates an array of approaches suited to studying systems of different scope and computational complexity. PES-fitting methods were the norm until the mid-2000s and are still in regular use today. When using QMD methods predicated on PES-fitting, the dynamically-relevant regions of the potential energy surface manifold

must be elucidated, and the shapes of those potentials and the couplings between them calculated in advance using *ab initio* electronic structure methods. These quantities must then be fitted as a function of the nuclear positions before dynamics can be simulated. These methods can be exact in diatomics and in principle triatomics, but this is difficult for polyatomic systems. Therefore, such approaches allow for restricted-dimensionality studies of a given chemical reaction; useful to reduce computational expense with larger molecules where nuclear motion is known to evolve primarily along a small number of degrees of freedom. However, the precomputing of PESs and couplings between the states is intensive: one must strive to achieve balance between over-calculating the PESs (computing regions which will never be explored dynamically) or over-simplifying the problem by restricting the direction dynamics can take and thereby missing out on some unexpected but relevant dynamical motion. Within this regime, the gold standard is to use approaches which treat the nuclear motion in a fully quantum fashion. The most well known of these methods is the Multiconfigurational Time-Dependent Hartree (MCTDH) approach [93, 94] (thoroughly reviewed in Ref. [95]). A variant of Time-dependent Hartree method where the wave function is described as a Hartree product of single-dimensional functions in a mean-field scheme, MCTDH makes use of a multiconfigurational ansatz for the wave function leading to numerically exact solutions. Here, the time-dependent Schrödinger equation (TDSE) is solved variationally.

The clear advantage of fully quantum propagation of the nuclei is that strictly quantum phenomena such as wave function interference, tunnelling, and coherence can be described. When tied to optimal PES from suitable levels of electronic structure theory, such approaches are the best that can be achieved in the theoretical regime. However, as is typical in computational chemistry, such accuracy comes at a cost — in this case, the exponential scaling of the grid as the dimensionality of the system under study increases. Methods like MCTDH reduce this scaling with a time-dependent set of basis functions.

While MCTDH is highly efficient in its scaling relative to other fully

	Category	**Trajectory type**	**Notes**
MCTDH [93]	Surfaces	n/a	Fully quantum treatment of nuclei
G-MCTDH [96]	"*on-the-fly*"	Travelling Gaussian	Variational equations of motion, "*on-the-fly*" implementation of MCTDH
FMS [97]	"*on-the-fly*"	Travelling Gaussian	Newtonian nuclear dynamics
vMCG [98]	"*on-the-fly*"	Travelling Gaussian	Trajectories follow time-dependent variational parameters
MCE [99]	"*on-the-fly*"	Travelling Gaussian	Trajectories follow a mean-field approximation of the potentials
Surface-Hopping [100]	"*on-the-fly*"	Classical trajectories	Newtonian nuclear dynamics, stochastic algorithm for nonadiabatic coupling

TABLE 2.1: A selection of methods for the simulation of nonadiabatic dynamics. These approaches differ primarily in their description of nuclear motion, ranging from the fully quantum treatment of MCTDH to the fully classical representation in surface-hopping.

quantum propagation methods [95], its computational burden is still significant. Methods have been developed to reduce this expense while still retaining the quantum nature of the problem by approximating the description of nuclear motion as ensembles of travelling, localised Gaussian basis functions. Examples include the Full Multiple Spawning (FMS) method of Martinez and co-workers [97, 101–106], the variational Multiconfigurational Gaussian (vMCG) dynamics by Worth and colleagues [98, 107–111] and its variant G-MCTDH [96], and the Multiconfigurational Ehrenfest (MCE) approach of Shalashilin [112–114]. Methods of this kind lend themselves to "*on-the-fly*" implementations, which avert the potential pitfalls and bottlenecks of PES-fitting methods by calculating the potential energy surfaces and couplings as the dynamics evolve; thus only dynamically important regions are computed — no computational expense is wasted on computing the energies and couplings between the electronic states at geometries never visited by the nuclear trajectory or wavepacket. However, the advantage of precomputed surfaces, in that they need only be computed once before being used in conjunction with a variety of methods, is lost.

In FMS, the configurations (denoted basis functions) and their momenta follow classical trajectories in a Newtonian sense. The basis functions move in response to the topology of the PES landscape, and dependent on the strength of coupling between electronic states at the particular molecular geometry, new basis functions ("children") may be spawned by the "parent"

basis function on the coupled surface. The child basis function then begins propagating in its own right. As time progresses, many basis functions may be spawned to represent the delocalisation of the wavepacket over the course of the process being simulated. However, quantum tunnelling is typically not accounted for without *ad hoc* algorithms to spawn basis functions where classical trajectories would normally be forbidden to do so. When implemented "*on-the-fly*" by introducing the saddle-point approximation for integral calculation, FMS is called *ab initio* Multiple Spawning (AIMS) [103].

Basis functions in vMCG follow the time-dependent variational principle [115] applied to Gaussian basis function parameters, as opposed to Newtonian trajectories; in other words, more "quantum" trajectories which naturally allow the wavepacket to explore classically-forbidden regions and displace the basis functions to give an optimised description of the wave function. The number of basis functions is kept constant, i.e. no spawning takes place.

In the Multiconfigurational Ehrenfest (MCE) method of Shalashilin [99, 114], basis functions travel according to a mean-field ansatz, resulting in equations of motion which can also be solved while retaining quantum character in that they can inherently access classically-forbidden regions of the potential. MCE can also work directly using saddle-point approximations as in AIMS [116]. Further approximations can be applied to the treatment of nuclear motion, for example in the popular surface-hopping approach (described in more detail in the following section), where the nuclei are treated classically and trajectories are localised to one electronic state only at each time step. General categories of QMD methods are summarised in Table 2.1.

2.5.1 Surface-hopping

First reported some five decades ago [117, 118], a popular and perhaps more intuitive alternative to the mean-field ansatz of methods such as MCE is that of surface-hopping (SH). In this method, a swarm of independent nuclear trajectories are propagated according to Newton's equations of motion, with forces calculated from electronic properties (energies and gradients) themselves generated from PESs calculated by some well-chosen

electronic structure method. In short, nuclei are treated classically while electrons are treated by quantum mechanics within the confines of electronic structure theory. Trajectories are fully localised to a particular electronic state α at time t, but by some scheme are allowed to jump or "hop" from state α to another state β in stochastic fashion based on the strength of coupling (be it nonadiabatic or spin-orbit based) between α and β. Energy conservation is enforced on each individual trajectory, typically by a rescaling of the nuclear velocities after a hopping event. Many flavours and modifications of the surface-hopping algorithm exist. Some examples can be found in Refs. [100, 119–124] and references therein. Some of these simply assume that the probability of transition between states α and β is unity if the energetic gap is smaller than a predetermined threshold [125], while more sophisticated methods take into account the NACMEs and/or SOC explicitly [123]. Of these, the most popular is Tully's Fewest Switches Surface-Hopping (FSSH) [100]. The aim of FSSH is to distribute trajectories among the electronic states in such a way as to correctly reflect the populations of those states using the minimal number of surface hops between each time step. By the nature of FSSH (and surface-hopping in general), transfers between electronic states occur instantaneously. This is not the case in reality, but is justified in that a sufficiently large ensemble of trajectories will be seen to transfer smoothly from one state to another, with some trajectories hopping early, and some hopping later. In this way, the aim of FSSH is to approximate the behaviour of a quantum wavepacket. A specific review of FSSH can be found in Ref. [126].

When driven by a suitable electronic structure engine, which may be *ab initio* [127], density functional-based [128] or semi-empirical in nature [129], surface-hopping typically gives at least quantitative results when compared to experiment or more fully quantum methods in cases where specific quantum effects do not dominate the dynamics [126, 130, 131], with trends in lifetimes and quantum yields in qualitative agreement or better. The work in this thesis is carried out using surface-hopping as implemented in the SHARC package. As such, a general overview of surface-hopping methods and the FSSH algorithm is left to the references in the previous paragraphs,

while the SHARC approach is discussed in more detail below. The method is not without criticism; it is not *ab initio* in origin, and there are questions over its description of decoherence and initial conditions.

2.5.1.1 Initial conditions and decoherence

On a more direct technical level than the big picture of the method's lack of *ab initio* origin are the treatment of initial conditions and decoherence. In surface-hopping, trajectories at time zero are localised to a chosen electronic exited state before commencement of the dynamics. However, in time-resolved photochemical experiments, the reaction under study is initiated by a pump pulse with finite temporal and energetic resolution, often leading to the population of other excited states in proportions dictated by the relevant transition dipole moments, the polarisation of the pump pulse, and the orientation of each molecule in the sample. This inevitably affects the progress of dynamics — clearly, the life of a trajectory is dominated by the electronic states it occupies, and therefore ideally this must be taken into account when choosing the initially occupied state in each trajectory, as well as the nuclear positions and momenta. Also, in a well-behaved simulation, one should find that the off-diagonal terms, which represent the overlap of wavepackets on different states of the electronic density matrix,

$$\sigma = \begin{bmatrix} c_1 c_1^* & c_1 c_2^* \\ c_2 c_1^* & c_2 c_2^* \end{bmatrix}, \tag{2.28}$$

where c_α are the electronic amplitudes, should be zero if those wavepackets are non-overlapping. This is not necessarily the case in FSSH and may lead to erroneous state lifetimes [132–136]. However, decoherence correction schemes have been proposed in the context of surface-hopping [137–143], as have methods for initial conditions sampling, typically based on a Wigner distribution [144] from the ground state vibrational frequencies to give a set of nuclear positions and momenta from which trajectories are launched.

True statistical convergence in surface-hopping can be difficult to achieve depending on the probability of the occurrence of a particular nonadiabatic

event — for a probability of $10^{-}2$, between three and five thousand trajectories are required, with this number rising to 10^8 in the case of weakly-coupled states [145]. Clearly, calculating this number of trajectories for any realistic case is not feasible. As such, the quantitative accuracy of surface-hopping will always be limited by the number of trajectories in the ensemble. However, the validity of a particular surface-hopping simulation can be assessed by user-defined convergence metrics relevant to a specific problem [146].

Generally speaking however, methods based on surface-hopping have seen success due to its conceptually intuitive nature in a classical ball-and-surface thought process, relative simplicity of implementation even in an "*on-the-fly*" setup, and ease of parallelisation due to the independent nature of the trajectory swarm. The method can be applied to small and medium-sized systems in full dimensionality, widening the pool of interesting chemical problems which can be studied with it. It is versatile in that it can be coupled to many electronic structure methods from *ab initio*, through density functional-based, to semi-empirical force fields depending on the requirements of a particular problem. While not without fault (chiefly the lack of account of purely quantum phenomena), surface-hopping is an extremely useful approach in studying many relevant dynamical phenomena where both nonadiabatic and spin-orbit effects are important, when its limitations are taken into account. Thus is was chosen for the work at hand. Further critical appraisals of surface-hopping methods are found in Refs. [109, 147–153].

2.5.1.2 Surface-hopping in the SHARC implementation

Surface Hopping including Arbitrary Couplings (SHARC) is an *ab initio* molecular dynamics method which in principle takes into account any form of coupling between electronic states. Most useful for our purposes are nonadiabatic coupling and spin-orbit coupling, but any other kind of coupling one wishes to model can be included, for example an external laser field. Based on the semi-classical FSSH approach of Tully [100], the SHARC

method accounts for these "arbitrary" couplings *via* a reformulation of surface-hopping in terms of unitary transformation matrix. The following description of the SHARC methodology largely follows Ref. [154].

In SHARC, each nuclear trajectory is propagated in the usual scheme of Newton's equations combined with the Velocity-Verlet algorithm [155, 156]. The motion of nuclear coordinates $\vec{R}(t)$ is guided by the gradient of the potential,

$$\vec{R}(t+\Delta t) = \vec{R}(t) + \vec{v}(t)\Delta t + \frac{1}{2M}V(t)\Delta t^2, \tag{2.29}$$

where M is the mass of the nuclei. The velocity is updated using the gradients of the potential at times t and $t+\Delta t$,

$$\vec{v}(t+\Delta t) = \vec{v}(t) + \frac{1}{2M}\Delta_{\vec{R}}V(t)\Delta t + \frac{1}{2M}\Delta_{\vec{R}}V(t+\Delta t)\Delta t, \tag{2.30}$$

Electrons, however, are treated quantum mechanically. Nuclear trajectories are defined by their positions $\vec{R}(t)$ and velocities $\vec{v}(t)$ and evolve along potential energy surfaces calculated from quantum chemistry. The electronic wave function depends directly on electronic coordinates $\vec{r}$ and parametrically on the nuclear coordinates $\vec{R}(t)$. The electronic wave function is defined as $|\Psi(\vec{R}(t),\vec{r},t)\rangle$. The evolution of the classical nuclear trajectories is governed by the expectation value of an effective Hamiltonian,

$$V(t) = \langle\Psi(\vec{R}(t),\vec{r},t)|\hat{H}_{\text{eff}}(R(\vec{t}),\vec{r})|\Psi(\vec{R}(t),\vec{r},t)\rangle, \tag{2.31}$$

where $\hat{H}_{\text{eff}}$ deals with energetic terms in the picture of the BOA.

The potentials which govern the behaviour of the electronic wavepacket (and thus ultimately the nuclear motion) are determined from the time-dependent Schrödinger equation,

$$\imath\hbar\frac{\partial}{\partial t}|\Psi(\vec{R}(t),\vec{r},t)\rangle = \hat{H}_{\text{eff}}(\vec{R}(t),\vec{r})|\Psi(\vec{R}(t),\vec{r},t)\rangle. \tag{2.32}$$

To make the solution of this equation tractable, the wavepacket is expanded as a linear combination of basis functions at different nuclear coordinates $\vec{R}(t)$,

$$|\Psi(\vec{R}(t),\vec{r},t)\rangle = \sum_{\alpha} c_{\alpha}(t)|\phi_{\alpha}(\vec{R}(t),\vec{r})\rangle, \tag{2.33}$$

with coefficients whose time-dependence is given by,

$$\frac{\partial}{\partial t}c_{\beta}(t) = -\sum_{\alpha}\left(\frac{\imath}{\hbar}H_{\beta\alpha}(\vec{R}(t)) + K_{\beta\alpha}(\vec{R}(t))\right)c_{\alpha}(t), \tag{2.34}$$

where,

$$\begin{aligned} H_{\beta\alpha}(\vec{R}(t)) &= \langle\phi_{\beta}[\vec{R}(t),\vec{r},t)(|\hat{H}_{\text{eff}}(\vec{R}(t),\vec{r})|\phi_{\alpha}(\vec{R}(t),\vec{r},t)\rangle \\ K_{\beta\alpha}(\vec{R}(t)) &= \langle\phi_{\beta}(\vec{R}(t),\vec{r},t)|\frac{\partial}{\partial t}|\phi_{\alpha}(\vec{R}(t),\vec{r},t)\rangle, \end{aligned} \tag{2.35}$$

$H_{\beta\alpha}(\vec{R}(t))$ describes the diabatic Hamiltonian. The diagonal elements of the diabatic Hamiltonian give the potential energies, the off-diagonal elements are the diabatic couplings between those potentials, and $K_{\beta\alpha}(\vec{R}(t))$ represents how the electronic basis functions change with time. This is equivalent to the variation of the basis functions with nuclear coordinates multiplied by the velocity, shown below,

$$K_{\beta\alpha}(\vec{R}(t)) = \langle\phi_{\beta}(\vec{R}(t);\vec{r},t)|\frac{d}{d\vec{R}(t)}|\phi_{\alpha}(\vec{R}(t);\vec{r},t)\rangle\vec{v}(t), \tag{2.36}$$

which is solved using a standard fourth order Runge-Kutta algorithm [157].

In terms of the precise form of the electronic basis functions, typically they are eigenfunctions of the TISE for each set of nuclear coordinates chosen in the expansion. The reason for this is that, in short, doing so gives a H_{eff} which generates the adiabatic energies of the different electronic states on its diagonal,

$$H_{\beta\alpha} = V_{\alpha}(\vec{R}(t))\delta_{\beta\alpha}, \tag{2.37}$$

and $K_{\beta\alpha}(\vec{R}(t))$ giving the NACMEs.

However, this method is based on classical trajectories, which cannot be delocalised across many electronic states, so trajectories are restricted to a specific state during a each time step in their propagation and allowed to "hop" from one state to another in the spirit of Tully's FSSH [100] fashion as discussed before. In SHARC the hopping probability is defined as,

$$P_{\beta\alpha} = \frac{2\mathbf{R}\left(c_\beta^*(t)c_\alpha(t)\left[\frac{\imath}{\hbar}H_{\beta\alpha}(\vec{R}(t)) + K_{\beta\alpha}(\vec{R}(t))\right]\right)}{c_\beta^*(t)c_\beta(t)}\Delta t, \tag{2.38}$$

and so depends on the expansion coefficients of the electronic basis functions which construct the electronic wavepacket, the time dependence of those basis functions and the nonadiabatic couplings through $K_{\beta\alpha}$, and the potentials through $H_{\beta\alpha}$.

Surface-hopping is not invariant to the choice of electronic basis function, unlike contexts where the nuclei are fully quantum. SHARC makes use of several representations of the electronic basis functions, each of which give H_{β_α} and K_{β_α} different properties. Firstly, there is the Molecular Coulomb Hamiltonian (MCH), which contains no external fields or relativistic effects but only accounts for the kinetic energies of the electrons and their Coulombic interactions. MCH states are typically aligned with "adiabatic" states in quantum chemistry: in other words, H_{β_α} is diagonal while K_{β_α} gives the nonadiabatic coupling only. Typical quantum chemistry codes are implemented to work with MCH states, so the "*on-the-fly*" dynamics are also propagated in the MCH representation. The novelty of the SHARC method is the inclusion of other kinds of coupling between electronic states. Most relevant for this work is SOC, which enables ISC to take place, but interaction with laser fields can also be accounted for. This is done in SHARC by including extra terms in the potential part of the Hamiltonian, inducing a new non-diagonal matrix,

$$H_{\beta\alpha}^{\mathrm{d}}(\vec{R}(t),t) = H_{\beta\alpha}(\vec{R}(t)) - \vec{m}u_{\beta\alpha}(\vec{R}(t))\vec{\epsilon}(t) + \hat{H}_{\beta\alpha}^{SO}(\vec{R}(t)), \tag{2.39}$$

where $\vec{mu}_{\beta\alpha}(\vec{R}(t))$ and $\hat{H}^{SO}_{\beta\alpha}(\vec{R}(t))$ are the dipole moment and relativistic SOC between states β and α.

This Hamiltonian contains off-diagonal elements which in principle can have significant magnitude at distances far from CoIns (especially terms describing SOC). As well as the corresponding equations being difficult to solve, such elements could be responsible for spurious surface hops at physically unlikely geometries. In SHARC this problem is precluded by translating the coupling elements to the $K(\vec{R}(t))$ matrix. In the diabatic approach, the Hamiltonian $H^{\mathrm{d}}(\vec{R}(t))$ is diagonalised and the $K(\vec{R}(t))$ is recalculated to give localised couplings in regions where the electronic states are closer together, reducing the likelihood of these unphysical jumps. The basis of electronic wave functions $|\phi^{\mathrm{d}}(\vec{R}(t);\vec{r})\rangle$ is recast as a linear combination,

$$|\phi^{a}_{\beta}(\vec{R}(t);\vec{r},t)\rangle = \sum_{\alpha} U_{\beta\alpha}(\vec{R}(t),t)|\phi^{\alpha}_{d}(\vec{R}(t);\vec{r})\rangle, \tag{2.40}$$

where $U_{\beta\alpha}(\vec{R}(t),t)$ is a unitary transform matrix which, at every time step, diagonalises the Hamiltonian $H^{\mathrm{d}}(\vec{R}(t),t)$ (i.e. casting it into the so-called diagonal representation). Once this is done the elements of the Hamiltonian become,

$$H^{a}_{\beta\alpha}(\vec{R}(t),t) = V^{a}_{\alpha}(\vec{R}(t),t)\delta_{\beta\alpha}, \tag{2.41}$$

where $V^{a}_{\alpha}(\vec{R}(t),t)$ are the diagonal elements of $H^{a}(\vec{R}(t),t)$. NACMEs are calculated from the derivatives of $|\phi^{a}(\vec{R}(t);r,t)\rangle$,

$$\begin{aligned} K^{a}_{\beta\alpha}p(\vec{R}(t),t) =& \langle\phi^{a*}_{\beta}(\vec{R}(t),\vec{r},t)|\frac{\partial}{\partial t}|\phi^{a}_{\alpha}(\vec{R}(t),\vec{r},t)\rangle \\ =& K^{\phi}_{\beta\alpha}(\vec{R}(t),t) + K^{U}_{\beta\alpha}(\vec{R}(t),t), \end{aligned} \tag{2.42}$$

where $K^{\phi}_{\beta\alpha}(\vec{R}(t),t)$ and $K^{U}_{\beta\alpha}(\vec{R}(t),t)$ are the nonadiabatic terms in the original basis $|\phi^{\mathrm{d}}(\vec{R}(t);\vec{r})\rangle$ and those induced by the rotation matrix $U(\vec{R}(t),t)$. The first term rotates the original nonadiabatic term into the new basis,

$$K^{\phi}_{\beta\alpha}(\vec{R}(t),t) = \sum_{\lambda\gamma} U^{*}_{\lambda\beta}(\vec{R}(t),t) K_{\lambda\beta}(\vec{R}(t)) U_{\gamma\alpha}(\vec{R}(t),t)$$
$$= \vec{v}(t) U^{*}_{\lambda\beta}(\vec{R}(t),t) \langle \phi_\alpha \gamma^d(\vec{R}(t) l\vec{r}) \nabla_{\vec{R}} \vec{R} | \phi_\alpha \gamma^d(\vec{R}(t) l\vec{r}) \rangle U_{\gamma\alpha}(\vec{R}(t),t)|, \tag{2.43}$$

and the second term from the variation of the rotation matrix,

$$\begin{aligned} K^{U}_{\beta\alpha}(\vec{R}(t),t) &= \sum_{\lambda} U^{*}_{\lambda\beta}(\vec{R}(t),t) \frac{\partial}{\partial t} U_{\lambda\alpha}(\vec{R}(t),t) \\ &= \vec{v}(t) \sum_{\lambda} U^{*}_{\lambda\alpha}(\vec{R}(t),t) \nabla_{\vec{R}} U_{\lambda\alpha}(\vec{R}(t),t). \end{aligned} \tag{2.44}$$

New potentials $V^a(\vec{R}(t),r)$ and nonadiabatic couplings $K^a(\vec{R}(t),t)$ are generated by diagonalising the matrix $H^{\mathrm{d}}(\vec{R}(t),t)$ at distances $\vec{R}(t) + \Delta\vec{R}$ and $\vec{R}(t) - \Delta\vec{R}$. This scheme allows the determination of the gradients of the potential and the $U(\vec{R}(t),t)$ matrix. These gradients are used in equations (2.34) and (2.38) to propagate nonadiabatic dynamics.

A common alternative to the use of full nonadiabatic couplings in QMD are wave function overlaps [158]. The implementation of this in SHARC is outlined in Appendix B.

Much of the work of this thesis is done using surface-hopping as implemented in SHARC version 1 (**S**urface-**h**opping including **ar**bitrary **c**ouplings) [154, 159, 160]. It should be noted that version 2.0 has recently been implemented [161, 162], and the approach has been expanded to include linear vibronic coupling models [163].

The SHARC approach was the first method based on surface hopping to account for ISC in dynamical processes. ISC plays a crucial role in much of the dynamics studied in this work, all shall be shown in the following chapters.

Chapter 3

Photodissociation dynamics of the $1\,^1B_2$ state of CS_2

3.1 Introduction

The molecule at the centre of most of the work in this thesis is CS_2. A structurally simple, second-row analogue of carbon dioxide, CS_2 nonetheless exhibits significant interest due to the complexity of the photodissociation it undergoes upon UV excitation, which takes places on a complex manifold of coupled singlet and triplet states mediated *via* strong spin-orbit coupling.

Over the following chapters, it will be demonstrated that a combination of the high density of singlet and triplet electronic states in the Franck-Condon region of UV excitation, coupled through strong nonadiabatic and spin-orbit coupling (the latter mediated by the presence of the relatively heavy sulfur atoms), leads to a complex interplay of electronic and nuclear motion which has been the subject of experimental interest in both the frequency and time domain [165–174]. Despite this intense study, the reaction dynamics of this system have proved difficult to fully elucidate due to the ultrafast nature of the dynamics and the high ionisation potentials of the products and intermediate species, limiting the results of photoelectron studies to mostly sporadic points along the reaction coordinate.

The state most commonly populated in such pump-probe experiments is the B_2 (Σ_u^+) state, around which lies a number of other degenerate and near-degenerate electronic states at linear geometries. This closely-spaced manifold of electronic states is what facilitates rapid population transfer in

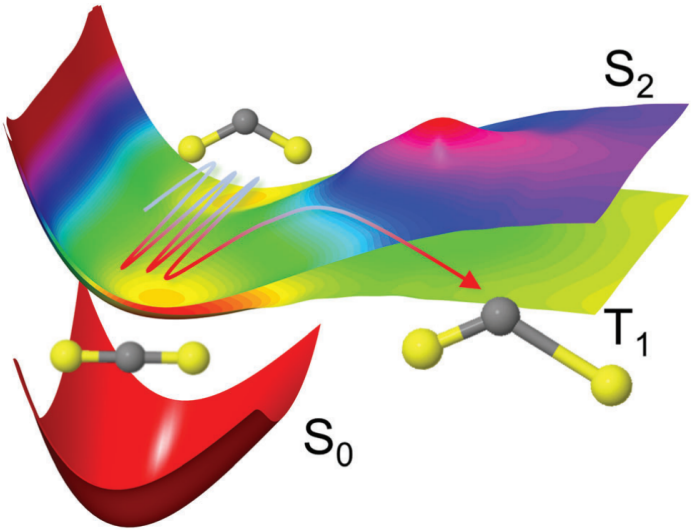

FIGURE 3.1: A schematic representation of CS_2 photodissociation, showing a small subset of potential energy surfaces. A UV photon excites a CS_2 molecule from S_0 to S_2, after which the molecule may dissociate by the spin-allowed singlet channel, or undergo ISC and dissociate *via* the spin-forbidden triplet channel. Taken from Ref. [164]

the early stages of the dynamics. Experimental observations demonstrate that this mixing of electronic states leads to dissociation of a sulfur atom, leaving a ground state ($X\,^1\Sigma^+$) CS fragment. The C-S bond dissociates homolytically along either the spin-allowed singlet or spin-forbidden triplet channels (shown schematically in Fig. 3.1), producing the neutral atom in the ^{1}D or ^{3}P state respectively,

$$CS_2 + h\nu(200\text{ nm}) \rightarrow \begin{cases} CS(X\,^1\Sigma^+) + S(^1D_2), \\ CS(X\,^1\Sigma^+) + S(^3P_j). \end{cases}$$

Both of these pathways lead to lower asymptotic limits than their respective heterolytic counterparts and are therefore favoured with respect to pathways producing, for example, CS^+ and S^-.

While the exact branching ratio of these two channels has not been settled conclusively, it is clear that the spin-forbidden pathway dominates [166, 175, 176], emphasising the importance of spin-orbit coupling to the dissociation mechanism.

Given the level of experimental attention given to this molecule, there has been limited *ab initio* study of the dynamics of this system. At the time the work described in this chapter was carried out, there were no simulations which accounted for spin-orbit coupling paramount to the dissociation dynamics. The only previous simulations accounted for the singlet states only, studying the effect of nonadiabatic coupling on photoelectron angular distributions obtained after UV excitation at 201 nm [177]. In that study, it is posited that the photoangular distribution provides evidence that spin-orbit coupling has limited impact on the early time dynamics. In the experimental observations detailed, a low-energy pump was used, limiting the observation window to only the singlet states, with triplet state dynamics inferred. No account is made within either the experimental or theoretical data of the impact of the close-lying triplet manifold of states.

This chapter describes efforts to combine new TR-PES experiments, featuring a multiphoton probe, with dynamical computations using the surface-hopping method as implemented in the SHARC package [154, 159] to study the effect of spin-orbit coupling on the initial stages of dynamics in the molecule. The TR-PES spectra show large amplitude fluctuations in the electron kinetic energy (almost 3 eV in 40 fs) as the molecule undergoes bending vibrations. This motion, and the subsequent dynamics, is explained by comparison to the dynamics simulations.

At first examination, the theoretical and experimental results present an encouraging match. However, upon further inspection it turns out the comparison is not valid — put plainly, the experiments and the simulations did not consider excitation to the same state of the molecule. The origin of this error, traced back to misbehaviour of electronic structure calculations in high-symmetry point groups and the lack of a standardised electronic state labelling convention in the literature, are discussed in detail in section 3.3.6.

3.2 Methodology

The aim of this project was to marry new time-resolved photoelectron experiments carried out by collaborators in the group of Dr. Russell Minns, (University of Southampton), featuring a multiphoton ionisation probe, to the first *ab initio* quantum dynamics simulations to account for spin-orbit coupling. In preparation for this, the electronic and geometric structure of CS_2 was optimised, and the largest feasible active spaces chosen for subsequent calculations of one-dimensional potential energy cuts and full dynamics simulations with the SA-CASSCF method. It should be noted that it is the high symmetry of CS_2 which allows the use of the full valence space for the geometry optimisations in this case; with resources on hand, this was not the case for full dynamics simulations where symmetry is broken.

Following an exploration of the static electronic structure of the molecule, dynamics simulations were carried out with the surface-hopping approach (see Chapter 2) as implemented in SHARC — **S**urface **H**opping including **Ar**bitrary **C**ouplings [154, 159] — integrated with the electronic structure programme MOLPRO [178].

3.3 Results and discussion

3.3.1 Electronic structure calculations

Ab initio electronic structure calculations were performed using the MOLPRO 2012.1 [178] suite of programs. Table 3.1 shows the results of simple geometry optimisations as predicted by a variety of electronic structure methods and basis sets. In the CASSCF calculation, a full valence active space of 16 electrons in 12 orbitals is used (denoted (16,12)). The CASSCF wave function is used as a reference function for MRCI in which core electrons are not correlated and the presented energy is from a single-point calculation at the optimised geometry of the preceding CASSCF. In these instances, full-valence MRCI generally predicts a molecular energy lying between that predicted by MP3 and MP4. The Hartree-Fock method continually underestimates R_{CS} due to its ill-treatment of electron correlation. This size of

the discrepancy relative to the CASSCF(16,12) decreases as the size of the basis increases, ranging from 0.041 Å with STO-3G to 0.030 Å with aug-cc-pvQZ. The MP*N* results, while showing an encouraging downward trend in terms of energy, demonstrate oscillations in the predicted R_{CS} resulting from the perturbative nature of the method. The performance of coupled-cluster methods varies between the extremes of large and small basis sets. With STO-3G, it is comfortably out-performed by CASSCF and MRCI, using deviation from calculated SCF energy as a benchmark. This is remedied immediately upon increase to 3-21G, and continues through to the end of the series of basis sets tested, although never beating the minimum energy predicted by MP4. With the triple-zeta Pople and all of the Dunning basis sets, MP4 predicts a longer R_{CS} by 0.011 Å.

The experimental bond length for CS_2 is 1.554 Å, which is most closely reached by the HF/aug-cc-pvDZ and MP3/6-31+G* methods. However, these should be treated with caution, as there is no consistent trend in the behaviour as basis size increases; the error in the HF predicted bond distance gets greater with larger Dunning basis sets, and the MP*N* methods oscillate rather than converging smoothly. Somewhat surprisingly, for basis sets larger than 3-21G, the CCSD predicted bond length is consistently closer to the experimental distance than that predicted by the more expensive CCSD(T) method, although both of the coupled-cluster methods see reduced errors in predicted bond distance with larger basis sets. The full-valence CASSCF method also approaches the experimental distance more closely as the size of the basis set increases, using both the Pople and Dunning families of basis sets.

Based on these calculations, the reference geometry taken forward into the calculation of potential energy surfaces (both angular and radial) was $R_{CS} = 1.569$ Å as calculated by the CAS(16,12)/aug-cc-pvQZ method, the best of the variational methods tested. Unfortunately, such a large active space is unsuitable for full dynamics calculations due to computational expense — the (16,12) space comprising some 30901 determinants in the D_2h point group, the highest point symmetry treated by MOLPRO, and 245025 determinants with symmetry turned off as is done in the dynamics code.

Method	*E (a.u)*	*E-ESCF (a.u.)*	R_{CS} *Å*	*E (a.u)*	*E-ESCF (a.u.)*	R_{CS} *Å*
	STO-3G			**3-21G**		
HF	-823.723986	0.000000	1.532	-828.756904	0.000000	1.579
MP2	-823.894171	-0.170185	1.571	-828.984960	-0.228055	1.612
MP3	-823.879905	-0.155919	1.553	-828.974223	-0.217319	1.597
MP4	-823.911971	-0.187985	1.588	-829.010896	-0.253991	1.634
CCSD	-823.886560	-0.162574	1.562	-828.984985	-0.228081	1.608
CCSD(T)	-823.902420	-0.178434	1.571	-829.000189	-0.243285	1.617
CASSCF	-823.904028	-0.180042	1.573	-828.913966	-0.157061	1.619
MRCI	-823.904028	-0.180042	-	-828.998432	-0.241527	-
	6-31G			**6-31+G***		
HF	-832.789645	0.000000	1.584	-832.882806	0.000000	1.544
MP2	-833.013223	-0.223578	1.618	-833.262419	-0.379613	1.563
MP3	-833.001194	-0.211548	1.603	-833.270075	-0.387269	1.553
MP4	-833.039359	-0.249714	1.642	-833.307904	-0.425098	1.578
CCSD	-833.012750	-0.223104	1.615	-833.275605	-0.392799	1.559
CCSD(T)	-833.027911	-0.238266	1.624	-833.299082	-0.416276	1.567
CASSCF	-832.950101	-0.160456	1.623	-833.023931	-0.141125	1.576
MRCI	-833.026278	-0.236633	-	-833.274422	-0.391616	-
	6-311+G*			**cc-pvDZ**		
HF	-832.939151	0.000000	1.543	-832.926009	0.000000	1.552
MP2	-833.338802	-0.399651	1.562	-833.320042	-0.394034	1.576
MP3	-833.344097	-0.404945	1.552	-833.326443	-0.400434	1.566
MP4	-833.384707	-0.445556	1.577	-833.363136	-0.437127	1.591
CCSD	-833.349954	-0.410802	1.558	-833.331053	-0.405044	1.572
CCSD(T)	-833.375125	-0.435974	1.566	-833.354281	-0.428272	1.580
CASSCF	-833.080283	-0.141132	1.575	-833.067271	-0.141263	1.583
MRCI	-833.347577	-0.408425	-	-833.327488	-0.401479	-
	aug-cc-pvDZ			**cc-pvTZ**		
HF	-832.930821	0.000000	1.553	-832.967079	0.000000	1.542
MP2	-833.343544	-0.412723	1.579	-833.461212	-0.494133	1.562
MP3	-833.350682	-0.419861	1.569	-833.472901	-0.505823	1.552
MP4	-833.388953	-0.458132	1.595	-833.518148	-0.551069	1.576
CCSD	-833.353828	-0.423007	1.575	-833.472704	-0.505625	1.557
CCSD(T)	-833.380040	-0.449219	1.584	-833.507611	-0.540532	1.565
CASSCF	-833.071188	-0.140367	1.584	-833.106008	-0.138929	1.572
MRCI	-833.346509	-0.415688	-	-833.456594	-0.489515	-
	aug-cc-pvTZ			**aug-cc-pvQZ**		
HF	-832.967872	0.000000	1.542	-832.978635	0.000000	1.539
MP2	-833.470395	-0.502523	1.562	-833.513939	-0.535304	1.558
MP3	-833.481786	-0.513914	1.552	-833.521803	-0.543168	1.547
MP4	-833.527706	-0.559834	1.577	-833.568814	-0.590179	1.571
CCSD	-833.480755	-0.512883	1.557	-833.518777	-0.540142	1.552
CCSD(T)	-833.517006	-0.549134	1.565	-833.557660	-0.579024	1.560
CASSCF	-833.106711	-0.138839	1.572	-833.116973	-0.138338	1.569
MRCI	-833.463377	-0.495505	-	-833.498449	-0.519813	-

TABLE 3.1: Energies and selected optimised geometric parameters of CS_2 calculated using the HF, MP2,MP3, MP4, CCSD, CCSD(T) CASSCF and MRCI electronic structure methods with seven basis sets in the range STO-3G to aug-cc-pvQZ, where $E - E_{SCF}$ is the difference from the Hartree-Fock energy, R_{CS} is the C-S bond length and Θ_{SCS} is the S-C-S bond angle. Multireference methods make use of a full valence (16,12) active space. The MRCI calculations are done at the respective optimised CASSCF geometry.

Thus, potential energy curves calculated at the CASSCF(16,12) level will be used as a benchmark to compare with the largest feasible active space, which turns out to be an (8,6) space comprising of a relatively painless 225 determinants and featuring the sulfur atom lone pair HOMOs, the σ bonding MO degenerate pair and and π^* LUMO degenerate pair, shown in Fig. 3.2.

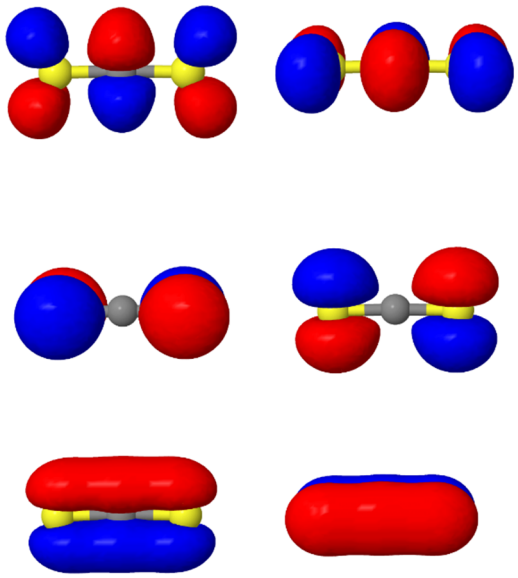

FIGURE 3.2: Orbitals in the (8,6) active space for CS_2, consisting of the HOMO (sulfur lone pairs), HOMO-1 (σ bonding) and LUMO (π antibonding) degenerate pairs of molecular orbitals. Calculated at the HF/aug-cc-pvTZ level, isovalue = 0.05. The orbitals were rendered in Jmol [179].

3.3.2 Potential energy curves

One-dimensional potential energy cuts of angular (both R_{CS} fixed, Θ_{SCS} varied) and radial (one R_{CS} and Θ_{SCS} fixed, the other R_{CS} varied) surfaces have

been calculated at the SA8-CAS(8,6)-SCF/6-31G* level. These are shown in Fig. 3.3, where panels A and B show radial cuts with fixed bond coordinate $R_{CS} = 1.569$ Å and fixed angles Θ_{SCS} at 180° and 120° respectively, and panel C has both R_{CS} bonds fixed at 1.569 Å.

What is immediately obvious is that the potential energy landscape in this manifold of states is extremely crowded. Upon photoexcitation to the S_2 ($^1B_2$) state from the linear ground state geometry, any wavepacket beginning its dynamical journey is immediately confronted by a number of degenerate or near-degenerate states in the Franck-Condon region, coupled strongly to the bright state by either internal conversion or intersystem crossing. In the angular picture these potential energy cuts behave well, demonstrating clearly the density of states and showing that all of the excited states have non-linear minimum energy geometries. However, the same cannot be said for the radial cuts, where the most noticeable drawback is that the (8,6) active space does not describe the region of bond breaking properly between approximately 2.3—2.5 Å. There are discontinuities here due to the exclusion of other orbitals whose character varies along this coordinate (this is addressed in further simulations in Chapter 6). This is not seen in analogous cuts calculated at the benchmark SA8-CAS(16,12)-SCF/aug-cc-pvTZ level of theory shown in Fig. 3.4, where radial behaviour is smooth and steepness of the potentials in the radial well is not as harsh. These potentials agree broadly with previous *ab initio* calculations [180–184]. It should be emphasised, however, that the (8,6) space does an admirable job reproducing the benchmark angular potentials.

Thus the picture one may draw from these static cuts consists of excitation to the bright state, followed by rapid redistribution of population among nearby strongly-coupled singlet and triplet states and structural relaxation towards bent geometries. Dissociation will primarily take place *via* the lower energy triplet dissociation pathway mediated by spin-orbit coupling, with some spirited competition from the higher energy singlet route. In terms of how this is modelled by the (8,6) levels of theory, one may expect initial vibrational bound dynamics to be simulated accurately due to the closely-matching description of the angular potentials to the benchmark

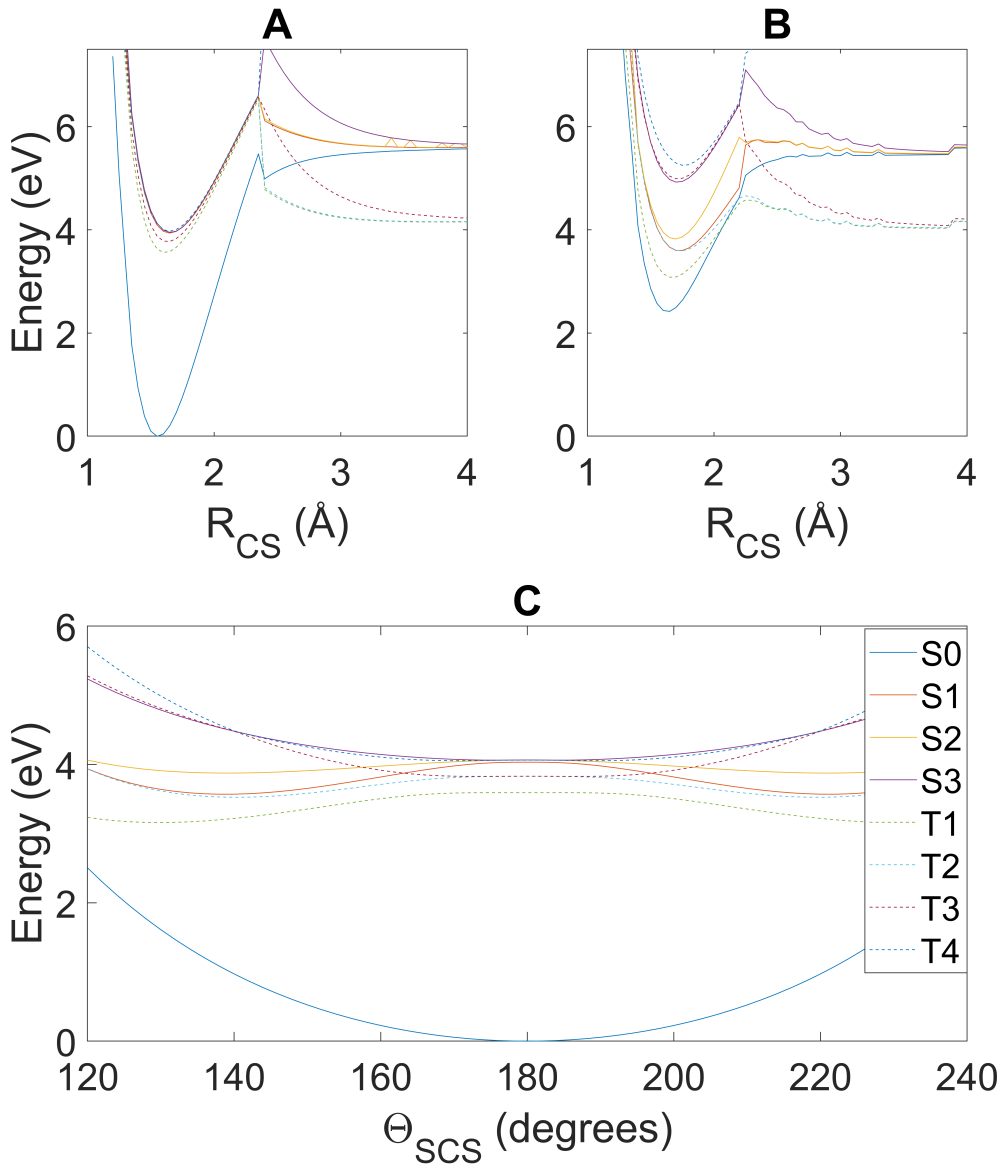

FIGURE 3.3: PECs calculated for CS_2 at the SA8-CAS(8,6)-SCF/6-31G* level of theory. **A** and **B** are calculated as a function of one R_{CS} distance, with Θ_{SCS} fixed at at 180° and 120° respectively. Panel **C** shows PECs as a function of varied Θ_{SCS} with both R_{CS} fixed at equilibrium values.

analogues. However, the description of the dissociation is expected to be less satisfactory; the higher barriers will frustrate the attempts of wavepacket motion to fully dissociate and lead to a lower overall dissociated fraction of

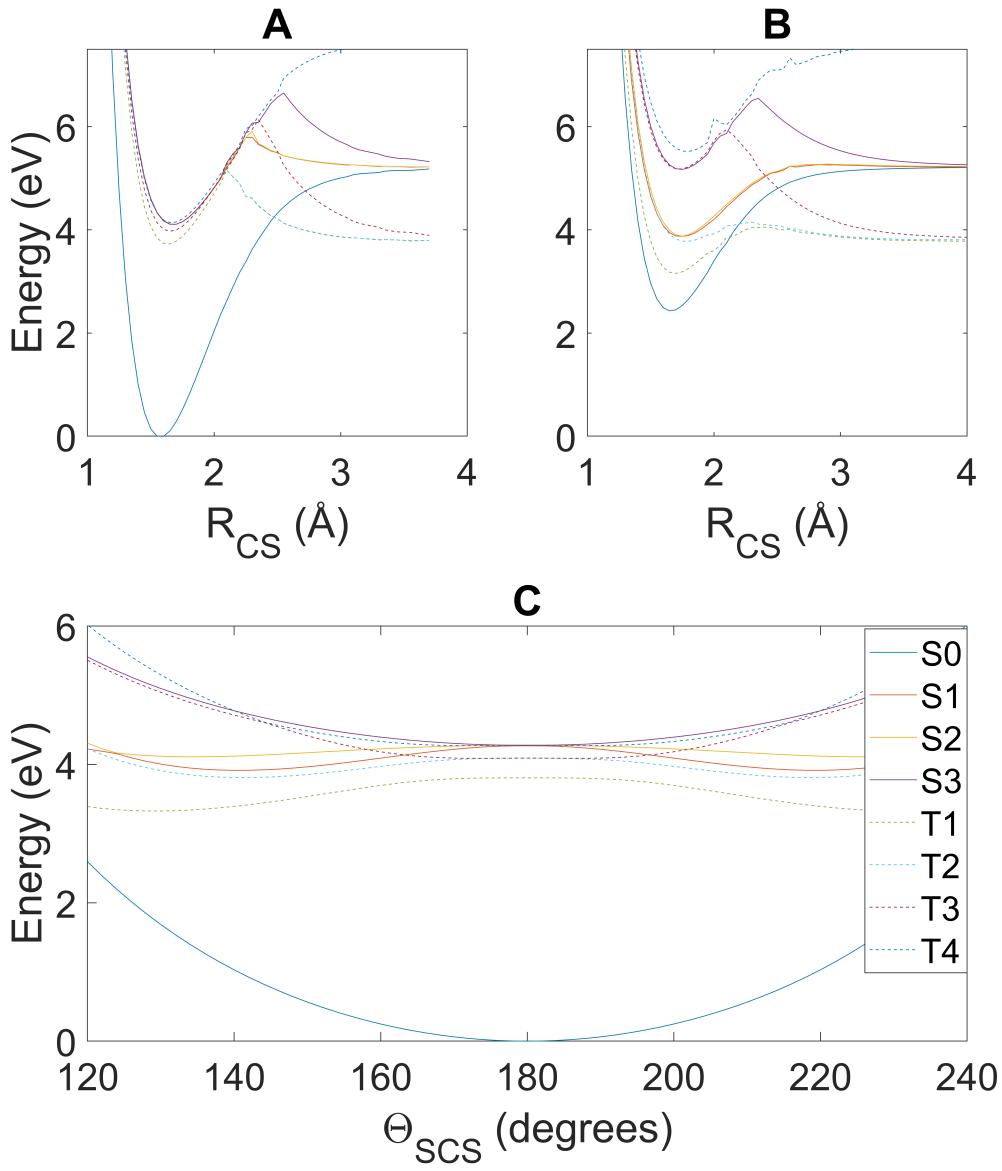

FIGURE 3.4: PECs calculated for CS_2 at the SA8-CAS(16,12)-SCF/aug-cc-pvTZ level of theory. **A** and **B** are calculated as a function of one R_{CS} distance, with Θ_{SCS} fixed at at 180° and 120° respectively. Panel **C** shows PECs as a function of varied Θ_{SCS} with both R_{CS} fixed at equilibrium values.

what is observed in experiment.

State	Energy (eV)	Oscillator strength
S_1	3.821	0
S_2	3.836	0.004282
S_3	3.836	0
S_4	6.430	0.000834

TABLE 3.2: Vertical excitation energies ($\triangle E = E(S_i) - E(S_0)$) and oscillator strengths from the ground state to the first four excited singlet states of CS_2, calculated using SA5-CAS(16,12)-SCF/aug-cc-pvQZ with CASPT2 corrections to the energies. The excitation energies are calculated at the equilibrium geometry (Θ_{SCS}=180° and R_{CS}=1.569 Å), while oscillator strengths are calculated at Θ_{SCS}=160° since transitions are very weak in the linear geometry.

Vertical excitation energies and oscillator strengths for the first four excited singlet states are given in Table 3.2, calculated at the SA5-CAS(16,12)-SCF/aug-cc-pvQZ with CASPT2 corrections. Transition dipole moments are extremely weak due to symmetry considerations in the optimised ground state linear geometry; indeed, all of them to the states considered are zero. The oscillator strengths shown here are calculated at $\Theta_{SCS} = 160°$, predicting that the dominant transition by an order of magnitude is to S_2 ($^1B_2$).

3.3.3 Surface-Hopping dynamics

Dynamics calculations were carried out using surface-hopping implemented in SHARC, which treats nuclear motion classically, but nonadiabatic effects and spin-orbit coupling [160] are included. In contrast to previous singlet-only simulations [177], the dynamics are propagated on the four lowest singlet and triplet electronic states. To keep the simulations computationally feasible, the electronic structure calculations were performed at the SA8-CAS(8,6)/6-31G* level. The differences to the CAS(16,12)/aug-cc-pvTZ level calculations are minor at small and large bond lengths, but at intermediate distances the smaller active space gives rise to elevated barriers to dissociation, that lead to transient trapping of population in the T_2 state.

3.3.3.1 Initial condition selection

Initial positions were generated from a Wigner distribution based on the ground state CAS(8,6)/6-31G* vibrational frequencies and optimised geometry of CS_2. The Wigner distribution is a quasiprobability distribution, a quantum phase space analogue of the classical harmonic oscillator whose goal is to link the wave function with phase space. In order to create an initial condition $(\mathbf{R}, \mathbf{v})$ consisting of nuclear positions and momenta, the following scheme is observed [185, 186]. Firstly, $\mathbf{R}_0 = \mathbf{R}_{eq}$ and $\mathbf{v}_0 = 0$. For each normal mode i, two random numbers P_i and Q_i are generated from the interval $[-3, 3]$. The ground state quantum Wigner distribution value is calculated

$$W_i = \exp -(P_i^2 + Q_i^2). \tag{3.1}$$

Then, W_i is compared to a third random number r_1 in the range $[0, 1]$. If $W_i > r_i$, P_i and Q_i are accepted and the coordinates and velocities for this condition are updated,

$$\mathbf{R}_i = \mathbf{R}_{i-1} + \frac{Q}{\sqrt{2v_i}}\mathbf{n}_i, \tag{3.2}$$

$$\mathbf{v}_i = \mathbf{v}_{i-1} + \frac{P\sqrt{v_i}}{\sqrt{2}}\mathbf{n}_i, \tag{3.3}$$

where $\mathbf{n}_i$ is the normal mode vector and $\mathbf{v}_i$ are the vibrational frequencies. This procedure is repeated for all normal modes. The harmonic potential energy is given as

$$E_{pot} = \frac{1}{2}\sum_i v_i Q_i^2. \tag{3.4}$$

In order to better match the experimental kinetic energy in the system, the Wigner-selected initial velocities were overwritten with a new selection, randomly generated such that the total kinetic energy in the system approximated the leftover energy from the 200 nm (6.20 eV) pump pulse as per the scheme,

$$v = \sqrt{2E/m_a} \begin{bmatrix} \cos\Theta \sin\Phi \\ \sin\Theta \sin\Phi \\ \cos\Phi \end{bmatrix}. \tag{3.5}$$

Thus the selected velocities depend on two randomly chosen numbers Θ and Φ, and the mass of the atom.

Initial states were selected in probabilistic fashion taking into account the oscillator strengths and transition dipole moments of all excited states, calculated at each initial geometry. For each initial condition, the maximum value p_{max} of

$$p_{k,\alpha} = \frac{f^{osc}_{k,\alpha}}{E^2_{k,\alpha}}, \tag{3.6}$$

is found, where $E_{k,\alpha}$ and $f^{osc}_{k,\alpha}$ are the excitation energies and oscillator strengths of initial condition k and excited electronic state α. Following this, a random number $r_{k,\alpha} \in [0..1]$ is generated. If the following condition is met,

$$r_{k,\alpha} < \frac{p_{k,\alpha}}{p_{max}}, \tag{3.7}$$

then the particular excited state α is selected as an initial state. Such a scheme is taken from Ref. [187].

Following this protocol, 85% of trajectories began in the $B\ ^1B_2$ state. A total of 369 trajectories were launched, of which 197 reached 500 fs and 114 reached 1000 fs, using a time step of 0.5 fs. The reasons that some trajectories failed to reach 1000 fs are related to the electronic structure calculations and include numerical problems such as excessive gradients in the CI or failure in convergence of the MCSCF calculations.

3.3.3.2 Nuclear motion

The simulations provide results in two major domains; electronic state populations and nuclear motion.The latter will be discussed first.

Excitation of CS_2 triggers vibrational motion in the molecule, as can be seen in Fig. 3.5, which shows the average molecular geometry as a function

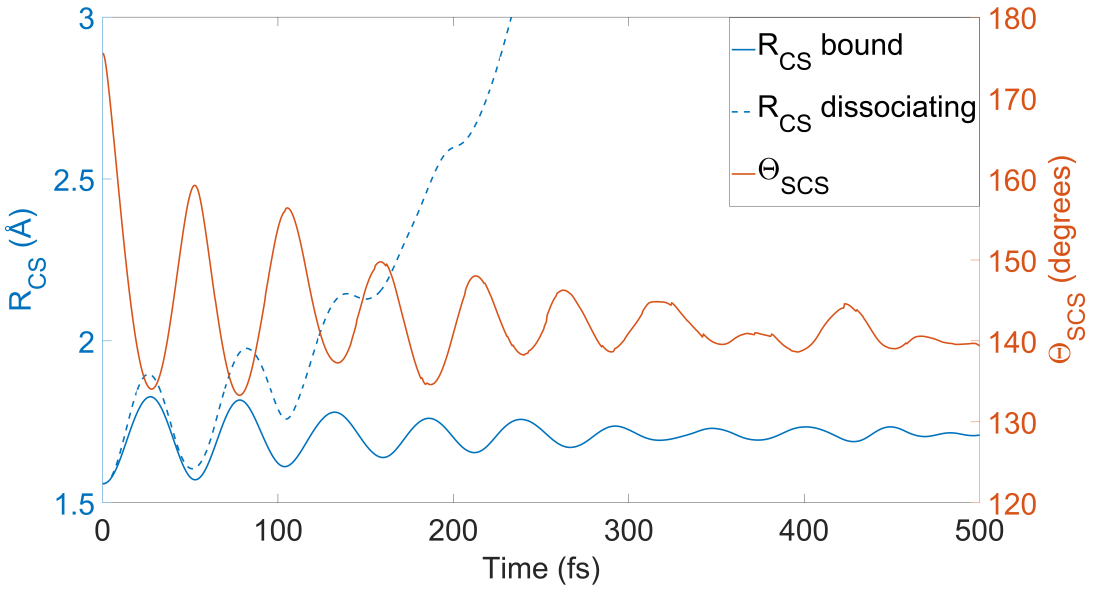

FIGURE 3.5: Structural evolution as a function of time, shown by the average R_{CS} of bound and dissociating trajectories, and the average Θ_{CS} of bound trajectories.

of the C-S bond lengths, R_{CS}, and the bending angle, Θ_{SCS}. The bond length is split into contributions from bound and dissociating trajectories, where the point of dissociation is defined as the minimum distance in the entire ensemble of trajectories from which point dissociation is irreversible — a dynamical definition for dissociation. In this case, the dissociation threshold turns out to be 2.589 Å.

During the first 100 fs the vibrations are dominated by the symmetric stretch, but at later times energy flows into the asymmetric stretch. The frequencies of vibrations are somewhat over-estimated compared to the experimental values (658 cm^{-1} for the symmetric stretch and 397 cm^{-1} for the bending motion [188]), presumably due to slight differences in the *ab initio* potential energy surfaces at the CAS(8,6) level. The total fraction of dissociated molecules in the full set of 369 trajectories is 22%, which constitutes a lower bound since only about a quarter of the trajectories reach 1000 fs. Dissociation occurs predominantly in the triplet states, with 89% of the trajectories that dissociate occurring on the triplet surfaces. The lower degree of dissociation compared to the experiments can be traced to the topology

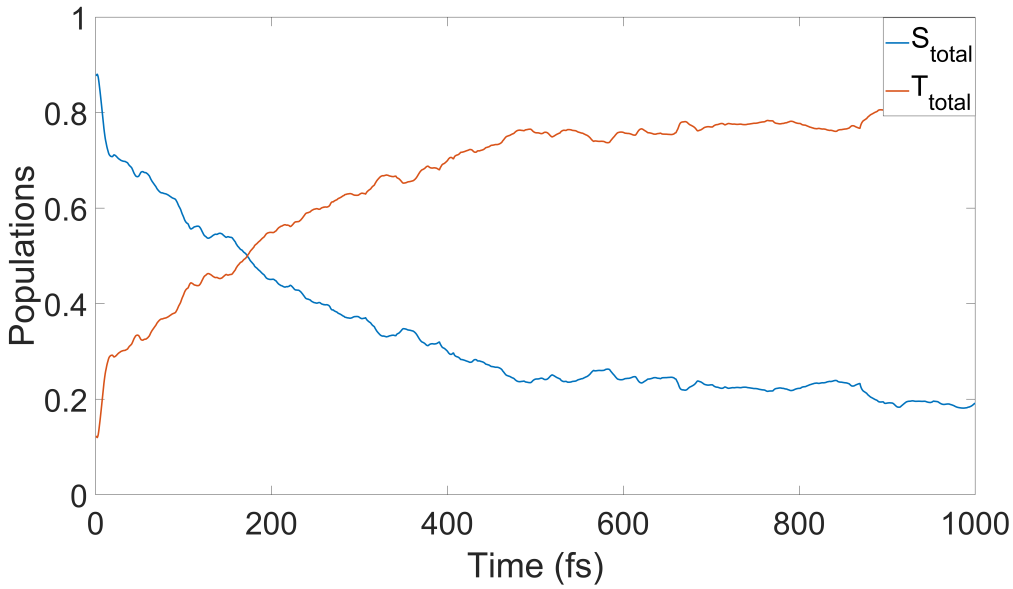

FIGURE 3.6: Total populations of the all MCH singlet and triplet states as a function of time.

of the potential energy surfaces at the level of *ab initio* theory employed in the simulations, as discussed later.

3.3.3.3 Populations

Shown in Fig. 3.6 are the total populations of the singlet and triplet manifolds as a function of time. These populations are calculated as the normalised sum of the absolute squares of the MCH coefficients. Within only a few femtoseconds there is a massive shift in population towards the triplet states — which, as mentioned when the potentials were discussed, may be expected due to the degeneracy and near-degeneracy of a number of states in the Franck-Condon region and the subsequent strong coupling. However, it is clearly the spin-orbit coupling which is dominating here over internal conversion. Following this, there is a period of some 400 fs where the decay in singlet (and commensurate rise in triplet) population is less dramatic and follows a smoother exponential decay, after which point the dynamics begin to settle and populations remain relatively constant, numerical noise notwithstanding.

These populations can be further divided into contributions from the constituent singlet and triplet states. This is shown in Fig. 3.7, whose upper and lower panels detail the populations of the individual singlet and triplet states respectively, and the plots begin to resemble the apocryphal spaghetti monster. The nonadiabatic transfer of population between the singlet states correlates strongly with the bending motion of the molecule, with efficient transfer predominantly occurring close to the linear geometry where states are (near)-degenerate. This gives rise to a periodic beating in both the individual singlet state populations and in the total singlet population. Over time there is a build-up of population in T_2 at t >400 fs, and a subsequent rise of population in T_1 at around t >800 fs, due to population transfer from T_2 to T_1. The build-up in T_1 appears to be an artefact due to the SA8-CAS(8,6)-SCF/6-31G* *ab initio* calculations, which increases the relative barrier height for dissociation on the T_1 and T_2 potentials by ∼1.5 eV, hindering dissociation and leading to the observed accumulation of population in T_2. Consequently, it is reasonable to assume that the population trapped in T_2 in actual fact dissociates, as observed in the experiment. Nevertheless, despite that the simulations underestimate the amount of $t < 1$ ps dissociation *via* the triplet states, the short-time t <400 fs dynamics appears quite reliable.

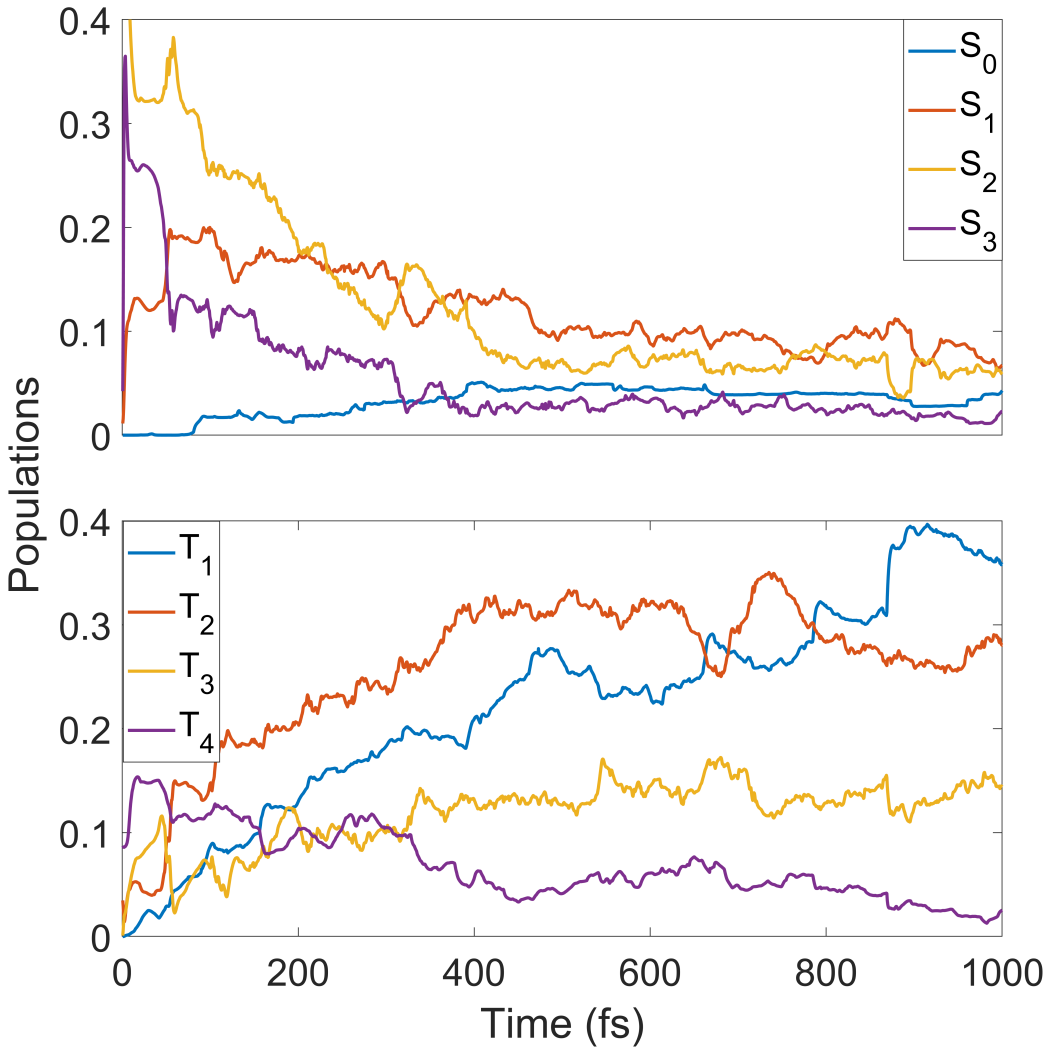

FIGURE 3.7: Populations of the lowest four singlet states (upper) and lowest four triplet states (lower) as a function of time.

3.3.4 Experimental comparison

The experiments detailed here were carried out by the group of Dr. Russell Minns and collaborators at Artemis, Central Laser Facility, see Ref. [34]. Briefly, they used an amplified femtosecond laser system to generate 30 fs pulses of 800 nm light, with a pulse energy of up to 10 mJ at a repetition rate of 1 kHz. The pump pulse was produced by taking the fourth harmonic of the fundamental (800 nm) beam, producing photons of about 200 nm. The

200 nm beam is produced using standard non-linear optics with sequential second, third and fourth harmonic generation in β-barium borate (BBO) giving a pulse energy of $\sim$1 μJ. The 400 nm probe is generated by second harmonic generation of the fundamental laser output, producing approximately 5 μJ per pulse. The pump and probe beams cross at the centre of the interaction region of a velocity-map imaging (VMI) spectrometer [189], where they intersect the CS_2 molecular beam. The pump and probe beams are both linearly polarised in the plane of the VMI detector, perpendicular to the time-of-flight axis.

3.3.4.1 Experimental results

The generated 200 nm pump pulse excites a vibrational wavepacket whose motion is then probed by non-resonant two-photon absorption at 400 nm, providing a total energy of 12.5 eV compared with the ionisation potential of CS_2 of 10.07 eV. The photoelectron signal obtained when the pump and probe pulse are overlapped in time is plotted in Fig. 3.8(a), where three main features around 2.1 eV, 1.4 eV and 0.9 eV electron kinetic energy become obvious. The spacing between the features is similar to that seen in previous single-photon ionisation measurements [165, 169].

The time-dependence of the photoelectron spectrum is shown in Fig. 3.8(b). The three peaks in the spectrum have different appearance times, with those at lower electron kinetic energy appearing after those at higher electron kinetic energy. The low-energy feature rises approximately 35 fs after the highest energy feature at 2.1 eV. This maps the initial bending motion as seen in the calculated dynamic and in previous experimental measurements [168]. As the dynamics continue to evolve, the centre of mass of the photoelectron spectrum shifts to lower electron kinetic energies. To examine these shifts in the electron kinetic energies, the integrated intensities over the features from Fig. 3.8(a) are plotted in Fig. 3.9. There is an obvious difference in lifetime, apparent in the plots, as well as oscillations in intensity which show their peak after time zero. These oscillations are most obvious in the feature centred around 0.9 eV, seen in Fig. 3.9(b), which

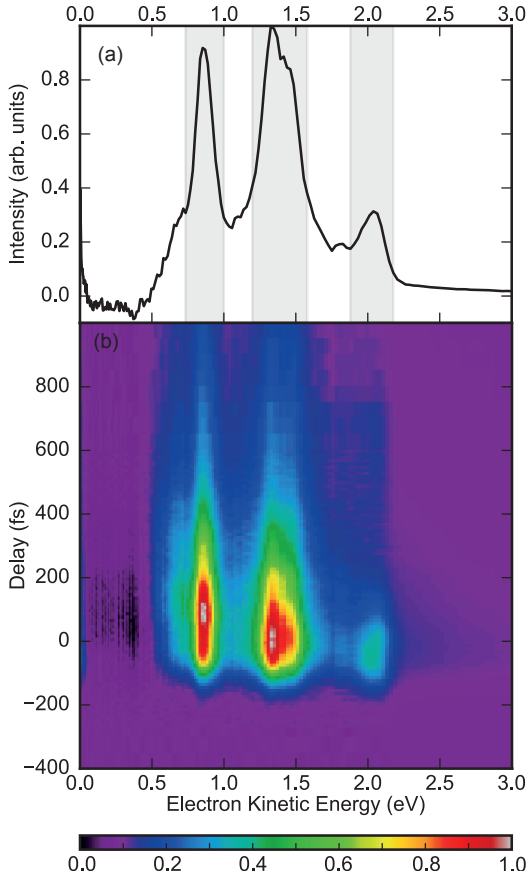

FIGURE 3.8: (a) The photoelectron spectrum generated during the cross-correlation of the pump and probe pulses. The highlighted regions signify those used in the integrated plots shown in Fig. 3.9. (b) The photoelectron spectra as a function of the pump-probe delay time.

has a maximum intensity about ∼200 fs post excitation. None of the transients can be fitted to a simple exponential decay, so here are modulated by at least one oscillating component. The transients are therefore fitted to an exponential decay modulated by either one or two damped oscillations, convoluted with the instrument response function, corresponding to the laser pulse cross-correlation [190],

$$g \otimes \left(A_0 \exp(-\frac{t-t_0}{\tau}) \times \prod^{n} A_n \cos(\omega_n (t-t_0) + \delta_n) \right). \tag{3.8}$$

where A_n are intensity scaling parameters, t_0 is the arrival time of the laser

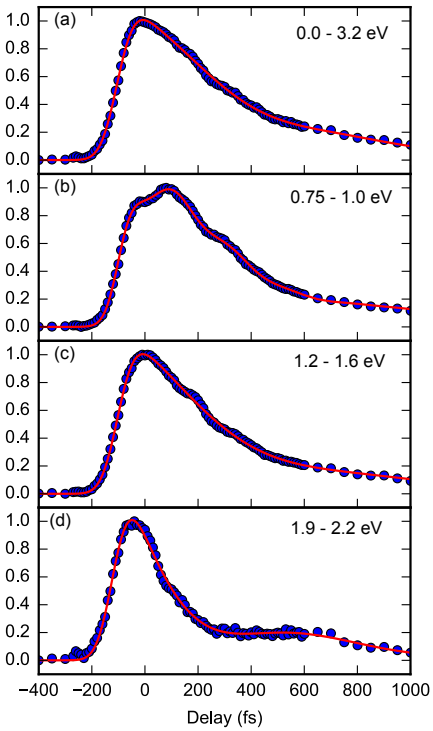

FIGURE 3.9: Total integrated photoelectron intensity (a) and intensity within the shaded areas shown in Fig. 3.8; 0.75 - 1.00 eV (b), 1.20 - 1.60 eV (C) and 1.90 - 2.20 eV (d). Solid lines are added to represent fits to the data. (a,c,d) were fit with a single exponential decay, modulated by a single damped oscillator and convoluted with the instrument response function. However, a second oscillation with a period ∼200 fs is clearly visible in the data. The data in (b) was fitted with two damped oscillating components, which reproduce both observed oscillatory features well.

pulse, τ is the exponential lifetime and ω and δ are the angular frequency and phase of the oscillatory component respectively. Fits are plotted as solid lines in Fig. 3.9. The highest energy feature, from Fig.3.9(d) contains a single oscillation of period ∼0.9 ps, 38 cm^{-1} — this has previously been observed [173, 174] and corresponds to the beat between the ν_1 and ν_2 vibrational modes [172]. This beat is present in each of the other features in the spectrum, alongside a second beat with a shorter period. The effect of this oscillation is most obvious in Fig. 3.9(b). However the assignment of the period of this oscillation is tricky due to mixing with the ∼0.9 ps feature. This leads

to significant margins of error in the assignment of its period, which is extracted as 220 fs. Intriguingly, although observed previously [168], this feature does not correspond to any known vibrational period of the molecule. The calculated fits to experimental data also give a yield in lifetime towards the regions of lower electron kinetic energy; the $1/e$ lifetimes extracted are 401 fs, 452 fs and 457 fs for the peaks at 2.1 eV, 1.4 eV and 0.9 eV respectively.

3.3.5 Discussion

This section details a comparison between the experimental measurements and dynamics simulations. In both regimes, it is clear that the triplet states play a large role in the dynamics from very early times. There is a large transfer of population from the singlet states into the triplet manifold, with over half of the total population in the triplet states within the first 250 fs. This transfer matches well with the experimental decay rate of the singlet population. The calculated bending vibrations of the molecule also correspond well to the observed shift in electron kinetic energy. The wavepacket, after initial excitation, oscillates in the potential well between linear geometries and $\Theta_{SCS} \sim 130^\circ$

Significant population is transferred into the triplet states very rapidly with over 50% of the total population in the triplet states within 250 fs. The overall transfer of population approximately matches the decay rate measured in the experiment. As mentioned above the initial shift in the measured electron kinetic energy maps the initial bending motion of the molecule. As the pump-probe delay increases, the electron kinetic energy shifts towards lower values, such that a longer lifetime for the lower electron kinetic energy regions in the spectrum in Fig. 3.9 is observed. Initial excitation leads to a wavepacket that oscillates between linear geometries to $\Theta_{SCS} < 130^\circ$. As the dynamics proceed, the range of explored bond angles narrows and begins to oscillate around non-linear geometries associated with the spectral feature at the highest electron kinetic energy. The experiment considered here did not have sufficient time resolution to fully resolve the bending motion, but nonetheless the corresponding narrowing and shifting of the electron kinetic energies was observed.

In summary, the *ab initio* surface-hopping simulations and TR-PES measurements both make clear the importance of the triplet states in the early time dynamics and in the branching path of the dissociation mechanism. The features observed in the photoelectron spectrum are mapped directly to aspects of the simulations, namely the shift in electron kinetic energy to the angular range of the bending motion. Oscillations in the photoelectron count are rationalised by the coupling of the close lying singlet and triplet manifolds, facilitating rapid population transfer by IC and ISC on directly comparable timescales.

3.3.6 Post mortem

After publication of this work detailed above, an inconsistency was noticed which had not been uncovered in any preceding dialogue between experimentalist and theoretician.

The simulations consider states within the range of the 6.2 eV (200 nm) pump pulse. According to the high-level CASPT2 calculations detailed in Table 3.2, this included the first four singlet states, S_0 to S_3 in adiabatic notation. The bright state in this range was predicted to be S_2, the first 1^1B_2 state, with $S_4/2^1B_2$ lying about 0.2 eV too high in energy to be accessible. The calculations also predicted that the higher 2^1B_2 had an oscillator strength an order of magnitude lower than 1^1B_2 However, it was since discovered that the results of such MOLPRO calculations may in fact be dependent on which point group the calculations are carried out in.

To demonstrate this, a series of sample calculations have been detailed in Table 3.3. CS_2 is considered at the SA5-CAS(16,12)/6-31+G* level, where the five states are the five singlet states of interest: S_0 to S_4 in C_1 symmetry, $1A'$, $1A''$, $2A'$, $2A''$ and $3A'$ in C_s symmetry, and $1A_1$, $1A_2$, $1B_2$, $2A_2$ and $2B_2$ in C_2v symmetry. Bond lengths are fixed at $R_{CS} = 1.569$ Å, and Θ_{SCS} was chosen to be either 180° or 178° as indicated. For each angle, the results of the three sets of calculations should be formally identical, accounting for a degree of numerical noise.

Firstly, considering the 180° calculations, significant differences become apparent across the point groups. The $2A'$ state is predicted to have zero

				180°				
	C_1			Cs			C_2v	
	E_{excite} (eV)	f		E_{excite} (eV)	f		E_{excite} (eV)	f
S_0	0.000		$1A'$	0.000		$1A_1$	0.000	
S_1	4.266		$1A''$	4.265		$1A_2$	4.163	
S_2	4.270	2.19×10^{-13}	$2A'$	4.271		$2A_2$	4.259	
S_3	4.270		$2A''$	7.313		$1B_2$	6.745	4.71×10^{-4}
S_4	7.346		$3A'$	7.382		$2B_2$	9.045	1.11×10^{-3}
				178°				
	C_1			Cs			C_2v	
	E_{excite} (eV)	f		E_{excite} (eV)	f		E_{excite} (eV)	f
S_0	0.000		$1A'$	0.000		$1A_1$	0.000	
S_1	4.257		$1A''$	4.257		$1A_2$	4.254	
S_2	4.263	3.43×10^{-7}	$2A'$	4.263	3.43×10^{-7}	$1B_2$	4.257	2.30×10^{-7}
S_3	4.264		$2A''$	4.264		$2A_2$	4.258	
S_4	7.409	1.47×10^{-5}	$3A'$	7.409	1.47×10^{-5}	$2B_2$	7.659	1.15

TABLE 3.3: Point group symmetries, excitation energies E_{excite} and oscillator strengths f of the singlet states of interest of CS_2, calculated at the SA5-CAS(16,12)/6-31+G* level of theory. Spin multiplicity subscripts are omitted from symmetry labels.

oscillator strength, compared to S_2 (which admittedly insignificant). The excitation energy of $2A''$ is severely overestimated relative to S_3, but most seriously the C_2v state ordering has qualitatively changed. $2A_2$ appears to have taken the place of $1B_2$, but the excitation energies of both B_2 states is incorrect. Contradicting the trend in Table 3.2, $2B_2$ is predicted to have the larger oscillator strength. However, at $\Theta_{SCS} = 178°$ a semblance of order is restored. There is general consistency across the point groups in the state ordering, excitation energies (with some slight under estimation in the C_2v point group), and trends in oscillator strength, albeit the predicted $2B_2$ oscillator strength is unphysically large.

It is clear that the issue lies with calculations done at a perfectly linear geometry. Such changes across the point groups demonstrates the issue is more fundamental than, for example, a lack of dynamic correlation in the CASSCF method; the calculations should behave similarly regardless of the point group. This points to a failure in the treatment of very high symmetry systems in the underlying electronic structure. This confusion is exacerbated by the lack of a standard system of labelling the electronic states in

CS_2. In [165], it is called S_3, which if counting all states as S_0 to S_N, would correspond to the second A'' state in C_s symmetry, or the second $^1A_2$ state, which seems unlikely. If only counting A' states, S_3 would be the third $^1B_2$ state. In previous singlet state AIMS simulations [177], the state of interest is called S_2, but they only include A' states so their simulations evolve on the third A' state. If A'' states were included, this state would be S_4. Reference [168] does not explicitly define which $^1B_2$ state is excited.

In short, the unreliability of calculations performed in high symmetry point groups at linear geometries allows for the possibility that excitation is in fact to the higher 2^1B_2 state, not the 1^1B_2 state as included in the simulations. Indeed, upon further discussion it was determined that this was the case, despite how well the simulated dynamics matched experimental data. The factors behind this error include the above inconsistencies in electronic structure calculations which were unnoticed at the time, unclear notation in previous literature, similar topologies of the potential energy surfaces at the 1^1B_2 and 2^1B_2 states (as shown in Chapter 4) and indeed mutual misunderstanding between experimental and theoretical collaborators.

A closer look at experimental literature outside of the time-resolved dynamics realm reveals that the only direct experimental studies of the lower $^1B_2$ state, whose spectral absorption peak is in fact four orders of magnitude weaker than the 2^1B_2 state, have focused on photolysis and fluorescence quantum yield studies [191–193], often in the context of atmospheric chemistry.

Therefore, despite the validity of the simulations as an individual demonstration of the importance of SOC in the photodynamics of UV excitation to that particular state, and a testament that such dynamics can indeed be modelled by surface-hopping of this kind, any comparison to this particular experiment is not valid, despite how well-matched the data seems to be. An uncomfortable warning shot then, that even if experimental and theoretical data appear to match clearly, the underlying assumptions must always be challenged and viewed with caution. It should be noted that these electronic structure problems only take effect at perfectly linear $D_\infty h$ geometries treated in high symmetry point groups, and so the simulations themselves

are unaffected given the particular starting state.

However such mistakes are opportunities for further learning. These simulations provide a platform on which to build, and a precursor to mapping the intended dynamics in the upper $^1B_2$ state which involves a more complicated interaction region of a much greater number of states. Electronic structure calculations and simulations pertaining to this process are discussed in the next chapter.

3.4 Conclusion

The work detailed in this chapter primarily consisted of a combined experimental and theoretical study of the photodissociation dynamics of CS_2 upon UV excitation to a $^1B_2$ electronic state. The predicted population dynamics and branching ratio, simulated by the surface-hopping approach, appeared to match extremely well with experimental TR-PES measurements of the dissociation process, emphasising the importance of spin-orbit coupling to a proper description of the dynamics and confirming the dominance of the triplet dissociation channel.

However, it soon became clear that the simulations and the experiment had not considered the same state — dealing with the 1^1B_2 and 2^1B_2 states respectively. A number of factors played into this error, including the erroneous behaviour of electronic structure calculations depending on the point group chosen, with higher symmetries behaving more erratically, and a lack of standard naming conventions in the literature of time-resolved studies of this process.

However, the striking match between experiment and theory suggests that there are similarities between the chemistry of these two excited state regimes. Therefore, these simulations, which nevertheless emphasise the importance of spin-orbit coupling in the dynamics, will be used as a foundation on which to build more rigourous simulations and theoretical study of the 2^1B_2 state. In the following chapter, the error is rectified, with a study of the early stages of dynamics commencing on the higher $^1B_2$ state.

Chapter 4

Extension to the $2\,^1B_2$ state: the limits of surface-hopping

4.1 Introduction

Chapter 3 deals with initial exploration of photodissociation processes in CS_2 in a simplified form — excitation to the first $^1B_2$ state, featuring interaction of four singlet and four triplet states. A formidable computational task, but a simple example compared to most experiments which excite around 200 nm to the second, brighter $^1B_2$ state. The number of states interacting in this region is greatly increased, to 9 singlet and 10 triplet states.

This chapter will discuss simulations of the dissociation of the upper $^1B_2$ state, building on the knowledge acquired by earlier simulations of the eight-state process. Moving to a description involving 19 states, it becomes clear that the limits of "*on-the-fly*" methods are being pushed in terms of sustainable expense. As will be shown, the length of CPU time required for each simulation step (involving the calculation of many energies, gradients, nonadiabatic and SO couplings and so forth) pushes computational expense orders of magnitudes greater to achieve reasonable levels of theory.

4.2 Methodology

Firstly, thorough *ab initio* calculations of the potential energy landscape of CS_2 in this manifold of electronic states shall be detailed. As before, this will involve the comparison of potentials generated by lower levels of theory to

high-level benchmarks in order to inform the choice of the best possible level of theory, limited by computational expense in "*on-the-fly*" dynamics. The simulations are then run, again using the surface-hopping method implemented in SHARC (integrated with MOLPRO) to take into account both nonadiabatic and spin-orbit coupling.

4.3 Results and discussion

4.3.1 Potential energy curves

In this section, the potential energy curves in the angular and radial regimes at the SA19-CASSCF(10,8)/SVP and MRCI(14,10)/aug-cc-pvTZ levels of theory will be compared. The comparison illuminates areas where the predicted dynamics based on the lower level of theory may differ from experiment. The jump in quality between the levels of theory here should be emphasised. On the lower end, there is a reasonably balanced (10,8) active space with all its associated electron-in-orbital permutations, alongside a fairly standard medium-sized double-zeta basis set in the Turbomole SVP. In contrast, the upper level features an active space approaching full-valence in size with two more electron pairs included, the MRCI method which naturally includes even further excitations to capture a higher fraction of electron correlation, and a much larger triple-zeta basis set augmented with diffuse functions to more correctly capture larger orbitals.

Despite this large step in method, for most states the comparison is a favourable one. Excitation energies at equilibrium geometry to each state at each level of theory are summarised in Table 4.1. Firstly looking at the singlet states, at linear geometries the excitation energies correspond well except the $4\,^1A'$ and $5\,^1A'$ states, which are shifted upwards by $\sim$1.2 eV and $\sim$0.6 eV in the lower level of theory. This reflects the larger contribution of extra static and dynamic correlation to these states, a greater fraction of which is captured by the MRCI approach. In the triplet states, the only significant shifts are in the $5\,^3A'$ and $5\,^3A''$ states, again upwards in energy relative to their MRCI counterparts — this time by approximately 1 eV each.

Singlet states			Triplet states		
	CAS(10,8)	MRCI(14,10)		CAS(10,8)	MRCI(14,10)
$1\,^1$A′	0	0	$1\,^3$A′	3.71	3.57
$2\,^1$A′	4.28	4.12	$2\,^3$A′	3.99	3.87
$3\,^1$A′	7.21	6.95	$3\,^3$A′	6.10	5.96
$4\,^1$A′	8.56	7.24	$4\,^3$A′	6.55	6.40
$5\,^1$A″	8.87	8.27	$5\,^3$A′	9.01	8.03
$1\,^1$A″	4.21	4.08	$1\,^3$A″	3.99	3.87
$2\,^1$A″	4.28	4.14	$2\,^3$A″	4.27	4.12
$3\,^1$A″	7.15	6.90	$3\,^3$A″	6.55	6.40
$4\,^1$A″	7.21	6.96	$4\,^3$A″	6.79	6.63
			$5\,^3$A″	9.01	8.04

TABLE 4.1: A summary of predicted excitation energies of the first nine singlet and first 10 triplet states of CS_2 at both levels of theory. These are calculated at $R_{CS_1} = R_{CS_2} = 1.569$ Å and $\Theta_{SCS} = 180°$. There is no change in the ordering of states predicted by the levels of theory.

Generally, these angular curves inform how dynamics would progress at early times before population has had time to cross over barriers to dissociation in either the singlet or triplet channels. Therefore, accurate angular potentials are expected to correlate to accurate early time dynamics. Thus, the lower states shown here at the (10,8) level (up to a range of about 6 eV) should predict bending dynamics accurately. The major deficiency comes as a fault of the $4\,^1A'$ state, which is shifted out of the excitation region, failing to recover predicted conical intersections with the $3\,^1A'$, $3\,^1A''$ and $4\,^1A''$ at geometries near to linear. As well as this, spin-orbit interactions with triplet states at approximately 7 eV would not be described correctly. This presents a severe problem for the prediction of accurate dynamics, where the topology of the other states in the Franck-Condon region is affected by the absence of the $4\,^1A'$ state. One must take this into account when analysing results.

If angular PECs capture the features of early-time dynamics, radial potentials do likewise for long-time dynamics and resultant dissociation. Fig. 4.2 shows such a comparison for $\Theta_{SCS} = 180°{}^*$ (see figure caption) and

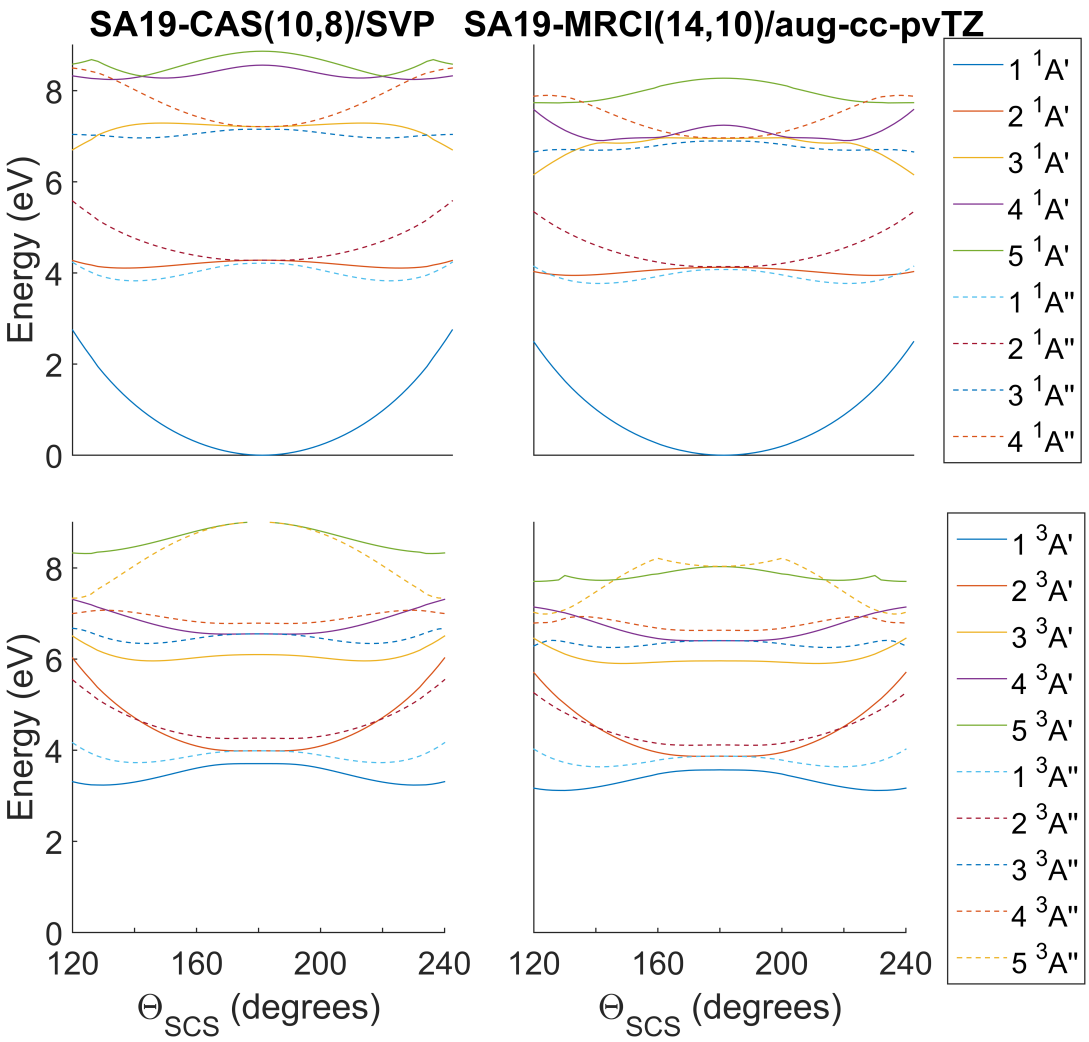

FIGURE 4.1: Angular PECs of CS_2, calculated at the SA19-CASSCF(10,8)/SVP and SA19-MRCI(14,10)/aug-cc-pvTZ levels of theory. The singlet and triplet states are shown in the upper and lower pairs of panels respectively. R_{CS} is fixed at 1.569 Å.

$\Theta_{SCS} = 120^\circ$ at both levels of theory. Again, for the most part the comparison is favourable. However, the same states present problems in the lower level of theory as in the angular potentials — the $4\,^1A'$ and $5\,^1A'$

states being shifted higher in energy at equilibrium geometries. However, it should be noted that barrier heights along these states are replicated faithfully compared to MRCI. A state splitting is neglected in the singlet states at the (10,8) level, where the $5\,^1A'$ and $4\,^1A''$ states are shown to resolve to a slightly higher energy level at long R_{CS} distances. While not ideal, this has little impact on dissociation dynamics, where in a classical sense a trajectory can be considered permanently dissociated once it has crossed the potential barrier — and this splitting occurs after the respective dissociation barriers. No such splitting is lost in the triplet states.

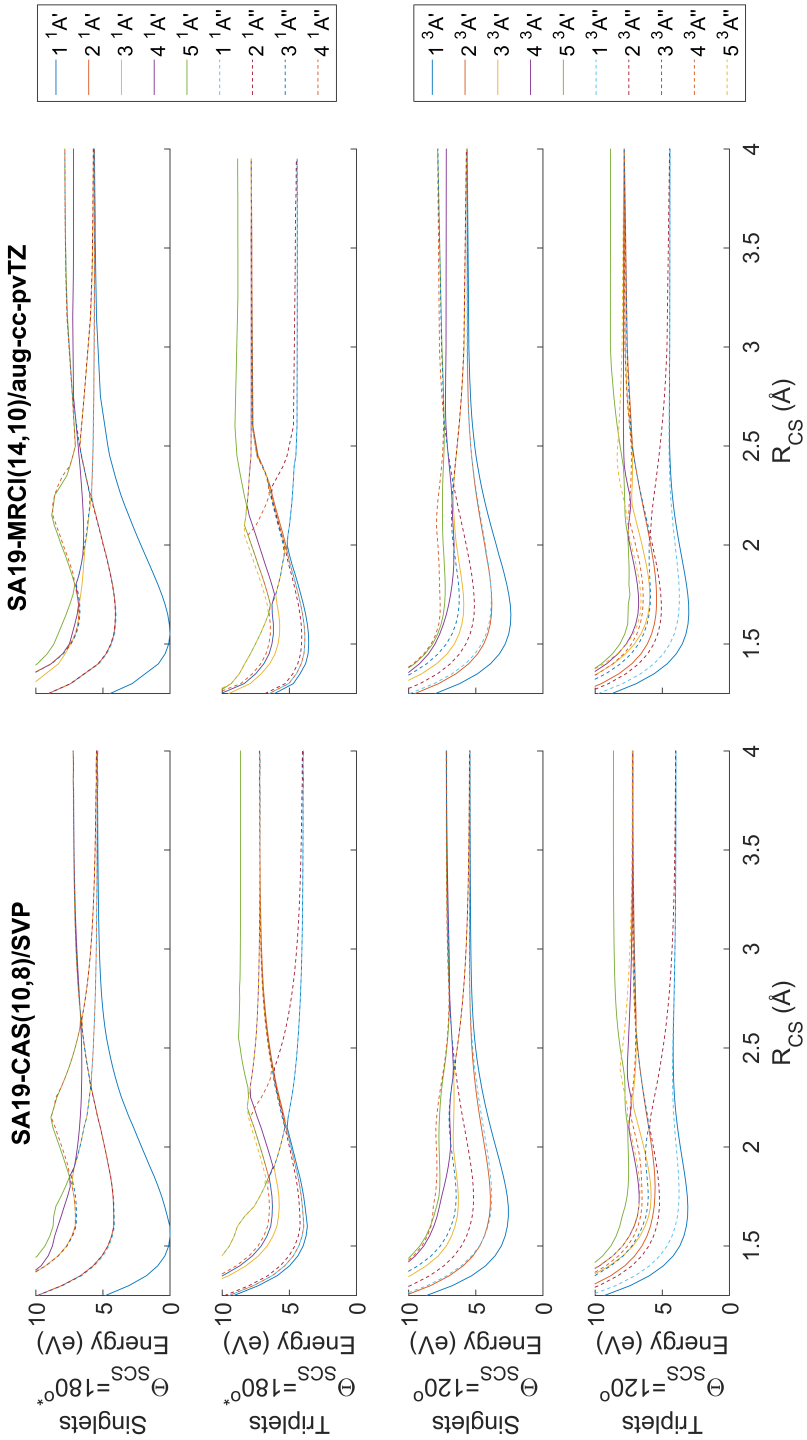

FIGURE 4.2: Radial PECs of CS_2, calculated at the SA19-CASSCF(10,8)/SVP and SA19-MRCI(14,10)/aug-cc-pvTZ levels of theory. One R_{CS} is fixed at 1.569 Åwhile the other is varied * 180° MRCI scans carried out at $\Theta_{SCS} = 178°$ due to increased stability of MOLPRO calculations at just off-linear geometries.

4.3.2 Surface Hopping dynamics

Initial positions were generated from a Wigner distribution based on the ground state CAS(10,8)/SVP vibrational frequencies and optimised geometries of CS_2. As the level of theory here over-estimates the excitation energy to the bright state of interest, the previous scheme of choosing mass-weighted random initial velocities to match the energy gap between the pump pulse (here, still 200 nm) and excitation energy cannot be used. Instead initial velocities were also taken from the Wigner distribution. All trajectories were selected to begin on the $S_4/3^1A''/2^1B_2$ state. In total, the ensemble consisted of 496 trajectories propagated at the SA19-CAS(10,8)/SVP level of theory, with a specified final time of 100 fs and a time step of 0.1 fs (necessary to conserve energy). At this level of theory with this large number of states, it became clear that the numerical stability of the trajectories becomes problematic. As the simulations progressed, trajectories were found to regularly crash mainly due to failure of convergence in the calculation of energy gradients. By the time 100 fs is reached, 33 trajectories remained active. The rate of failure is steady and leads to an increase in noise in reported electronic and structural properties at longer times as the number of contributing trajectories drops. While this gives greater uncertainty in the ensemble populations and geometric parameters at longer times, the large size of the initial ensemble counterweights this over the majority of the timescale covered by the simulations.

4.3.2.1 Nuclear motion

The nuclear motion is shown in Fig. 4.3 as the average R_{CS} bond length and θ_{SCS} angle of all trajectories as a function of time. Like the 1^1B_2 example from before, it is clearly the symmetric stretch mode which is excited in the first instance, with clear oscillations with a period of approximately 50 fs, consistent with those observed in the 1^1B_2 simulations, with rapid damping in amplitude. The angular behaviour is somewhat less well defined, although the ensemble average still drops rapidly to much more acute geometries around 110°. No dissociation is seen in the trajectory ensemble

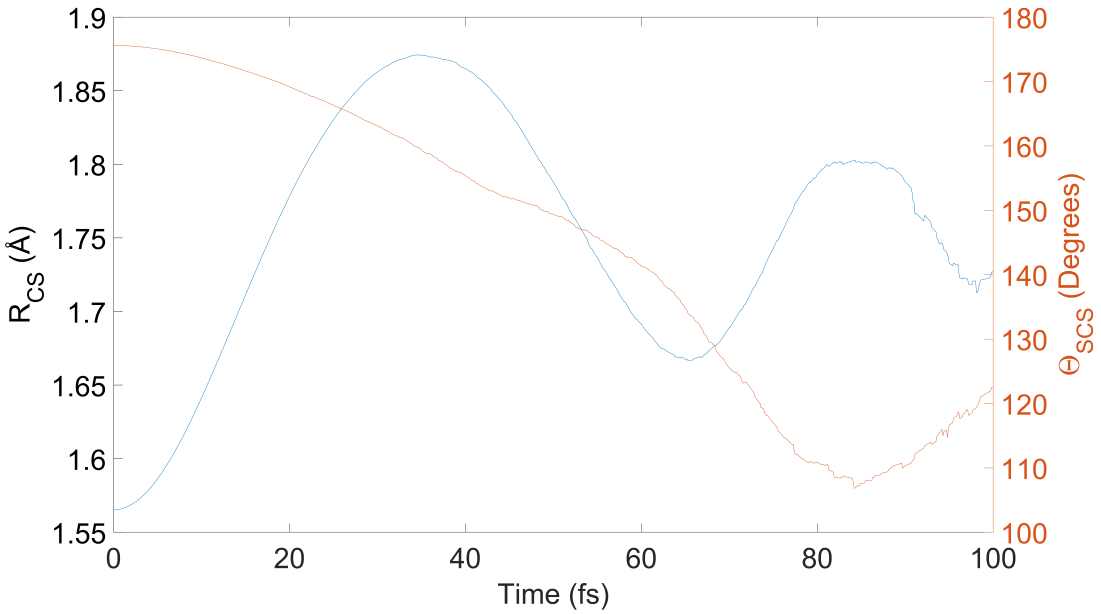

FIGURE 4.3: Average CS_2 bond lengths and angles in the 19-state simulation as a function of time. The reduced number of trajectories contributing at later times leads to the introduction of greater noise; however, it is clear that it is still the symmetric CS_2 stretching mode which is first activated, as seen in the lower state CS_2 dynamics simulations in the previous chapter.

over this early timescale, consistent with experiments which see the onset of dissociation at over the course of a few hundred femtoseconds [33].

These plots are based on an ensemble of 496 trajectories, but the time 100 fs is reached only 33 trajectories were still live, with the rest having crashed due to failures in individual *ab initio* calculations, primarily caused by non-convergence of CASSCF gradient calculations exaggerated by the sheer number of gradients to be calculated in each time step. This is a signature of the complexity and relative instability of the level of theory being employed. Even so, reaching an ensemble this size took months of highly-parallelised CPU time.

4.3.2.2 Populations

Singlet and triplet populations as a function of time are shown in Figs. 4.4 and 4.5. Because of the number of states involved, these are split into sub-figures for convenience (scales not identical). By the definition of the initial conditions in this case, all of the population begins in S_4. The populations remain steady until 30 fs, when there is an initial uptake into S_5 as well as several of the higher-lying triplet states — most notably T_9, whose rise continues to about 40 fs before it gives way to the other triplet states. After these initial exchanges, the clearest feature of the dynamics occurs between 55 and 70 fs with a large transfer of population from S_4 to S_5, with the later state possessing over half of the total population from here until the end of the dynamics. Once this exchange occurs, other singlet states come into play — firstly S_3 (appearing just after the peak of S_5 at about 70 fs), followed sequentially by S_2 and S_1. S_4 also shares an oscillation with S_5 shortly after, at about 75 fs. After this point, S_2 and S_3 oscillate in an contrary motion, with S_1 largely following the same pattern as S_3. Beyond this point, all of the triplet states contribute to a small degree ($< 4\%$) until a comparatively large rise in T_5 over the last 10 seconds of the dynamics, which appears to arise as a result of transfer from T_2 and T_7. These last transfers are sharp, most likely due to the small number of trajectories still active over these times. The light blue dotted line indicates the number of contributing trajectories at each time step.

The most striking feature is a lack of the immediate burst of population exchange between the initially populated states and the triplet states as seen in the previous eight-state simulations, especially considering that the states in question still lie close together in energy in the Franck-Condon region. The dynamics do rationalise to the potentials in that the states to which population is transferred are initially the S_3 and S_5 states either side, followed by transfer to lower singlet states when the molecule bends sufficiently to bring these states into close energetic contact.

The total populations of singlet and triplet states are shown in Fig. 4.6, alongside the analogous curves for the eight-state simulations of the previous chapter (dotted lines). The plot emphasises the stability of the initially

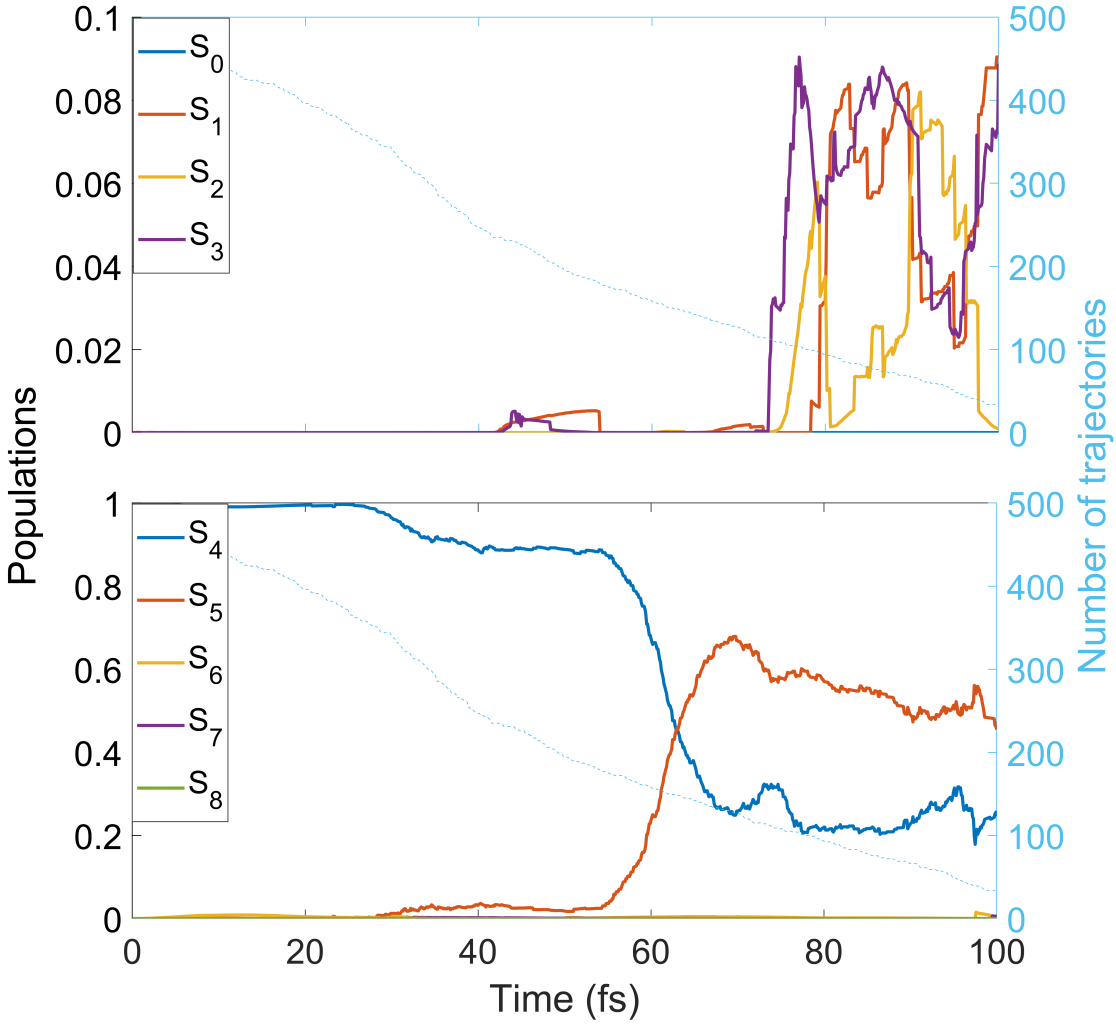

FIGURE 4.4: Singlet state populations as a function of time. Upper panel, states S_0 to S_3. Lower panel, states S_4 to S_8. Population scales are not identical. The dotted line shows the number of contributing trajectories as a function of the simulation time step.

populated singlet states in the 19-state case, before transfer of about ten percent of the population to the triplet states occurs after 24 fs. When this transfer concludes at about 40 fs, the total population in each multiplicity remains steady until a possible smaller rise over the last 10 fs, which may indicate the beginning of another larger transfer. This behaviour is in contrast to the eight-state simulations, where the onset of the transfer is quicker and

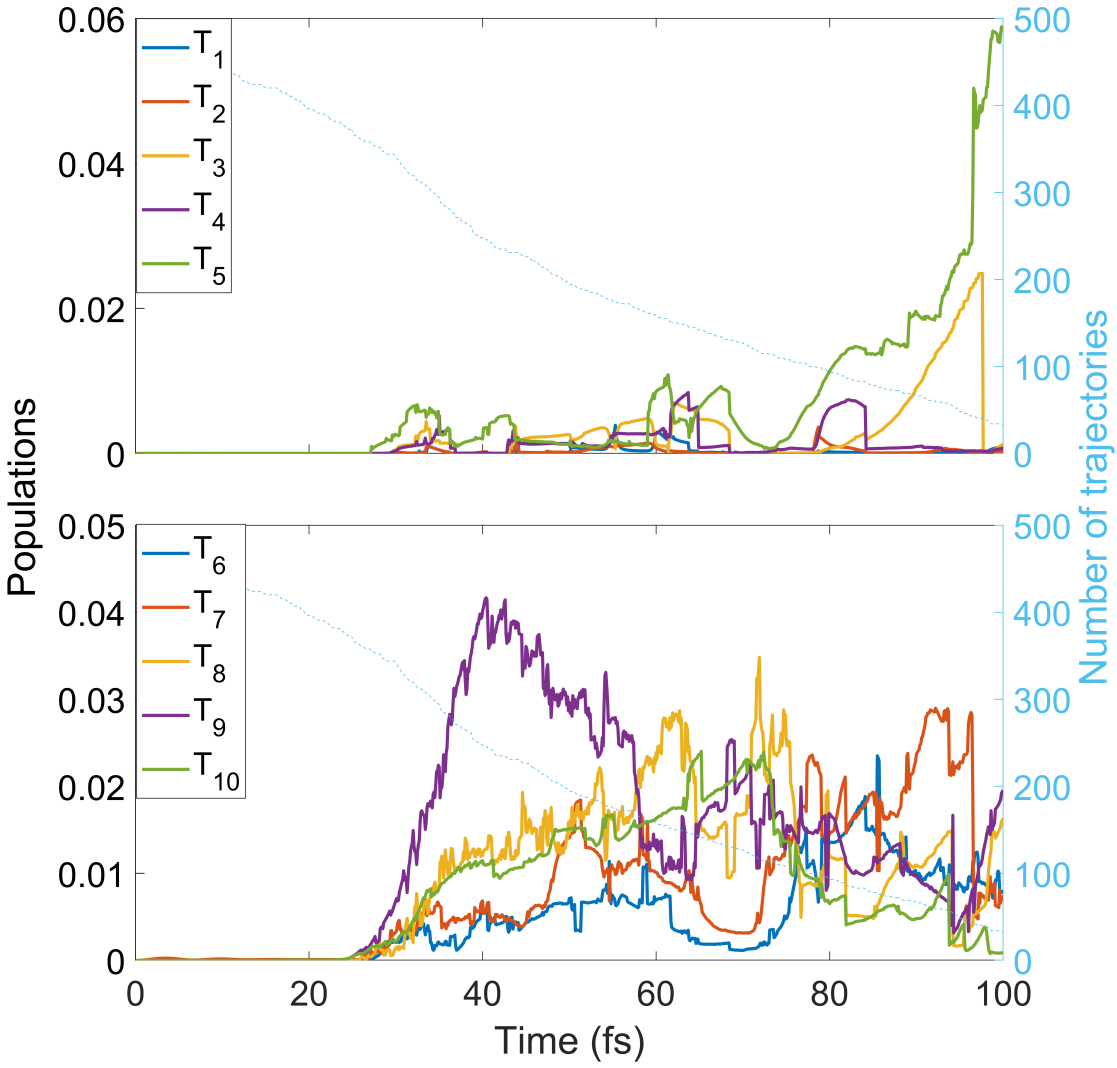

FIGURE 4.5: Triplet state populations as a function of time. Upper panel, states T_1 to T_5. Lower panel, states T_6 to T_{10}. The dotted line shows the number of contributing trajectories as a function of the simulation time step.

the population of triplet states continues to rise after the initial exchange. This intuitively cannot be attributed to the shifting of the $4^1A'$ state out of the excitation region at the SA19-CAS(10,8) level of theory; if anything, the appearance of this state in the Franck-Condon region would be expected to further hinder the impact of SOC by presenting another channel by which population may be transferred away at early times by IC.

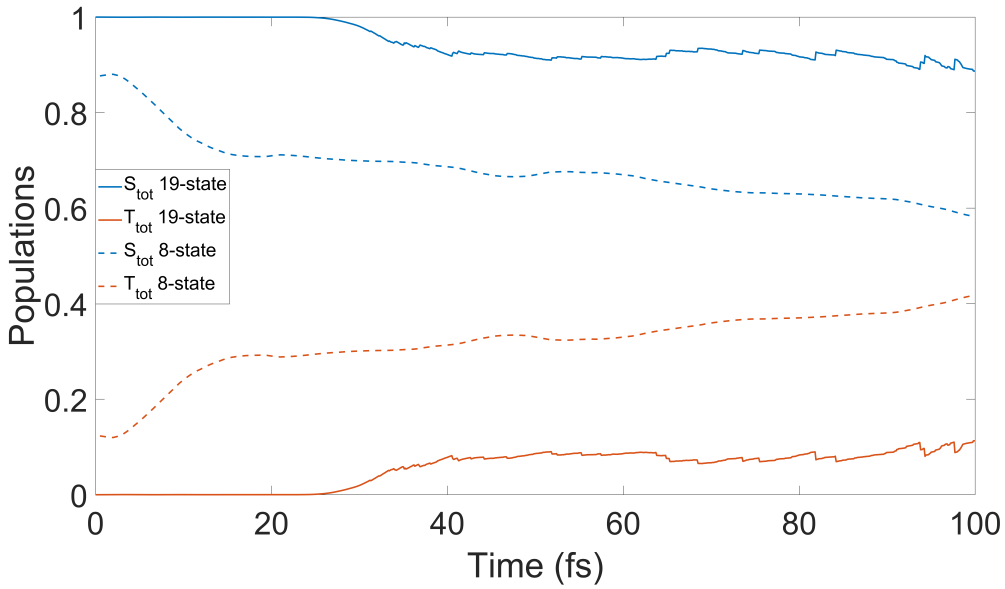

FIGURE 4.6: Total singlet and triplet populations as a function of time for the 19-state (solid lines) and previous eight-state simulations (dotted lines). In the 19-state simulations, the total triplet state curve does not continue to rise after initial population, which also occurs after a longer time.

What is presented here is a complex picture of evolving dynamics across a large number of coupled states. The potential energy landscape is more complicated, but the importance of SOC in the description of the dynamics at this level is still clear, with the triplet states featuring in population exchanges at early times, albeit to a lesser magnitude than in the previous eight-state simulations. In any case, it is clear that this structurally simple system still features markedly complex dynamics which pose a challenge to describe properly, particularly by "*on-the-fly*" methodologies.

4.3.3 Convergence

The convergence of each simulation was measured by the state populations at $t = 100$ fs as a function of all trajectories which reached that time. The mean of all the absolute variances $V(N)$ of the final populations of each state was calculated for random subsets of trajectories for $N \in [1, N_{\text{traj}}]$, with,

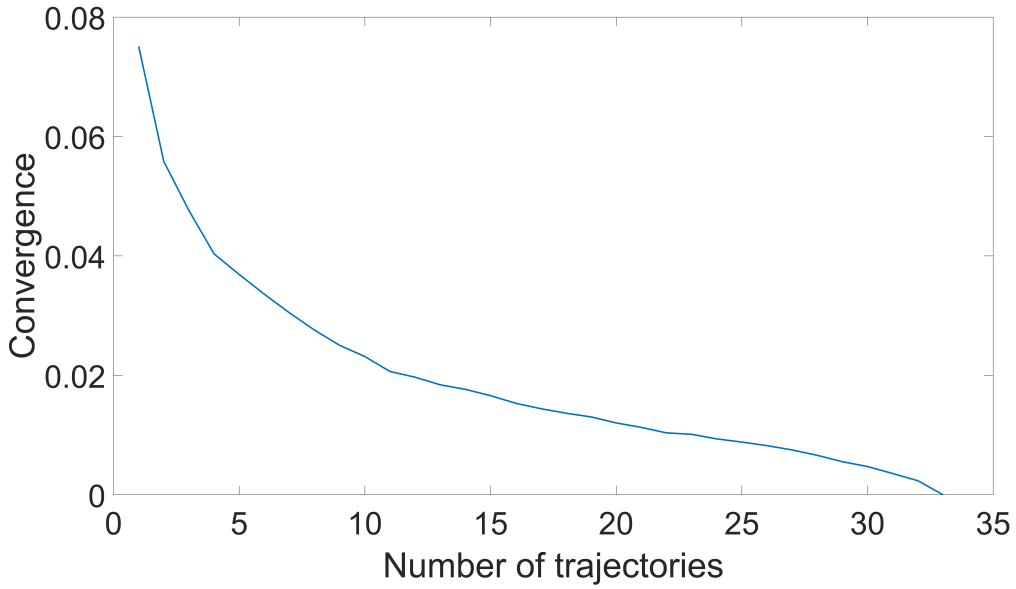

FIGURE 4.7: Convergence plot of the 19-state simulation as a function of the final predicted state populations. The convergence metric is the mean of the absolute variances of all state populations for trajectories which reached $t = 100$ fs. As so few of the trajectories reached this time, the sample size is small; but nonetheless a smooth convergence progression is observed. In each case the random selection and variance calculation was repeated 1000 times and the results averaged.

$$V(N) = \sqrt{(B(N) - \langle B \rangle)^2} \tag{4.1}$$

where $\langle B \rangle$ and $B(N)$ are the final predicted state population and the state populations of a subset consisting of N trajectories respectively. The variance calculation was repeated 1000 times for each N with the N trajectories chosen at random each time, and the result averaged. This procedure generates the plot shown in Fig. 4.7, showing a drop to 3% mean variance in less than 10 trajectories with a smooth exponential-like decrease as the number of included trajectories rises.

4.4 Conclusion

The electronic structure calculations detailed in this chapter lay the foundations and contain initial results of dynamics simulations of the $2\,^1B_2$ state of CS_2. First of all, one-dimensional potential energy curves were calculated as a precursor to the first "*on-the-fly*" surface-hopping simulations of this process, mirroring the methodology of earlier, simplified case. In contrast to the eight-state simulations of the previous chapter, no immediate redistribution of population was observed despite the close-lying nature of the electronic states in the excitation region, although population was observed to transfer to the expected nearby singlet and triplet states after about 30 fs. SOC was still observed to play a notable role in the dynamics even over the relatively short timescale of 100 fs.

From a methodological point of view, this case stretches the applicability of such "*on-the-fly*" methods — the large number of states involved complicates the electronic structure, places a heavy burden on the semi-classical surface-hopping algorithm, and increases both numerical instability and computational expense with the sheer number of energies, gradients and other electronic properties which must be successfully calculated. While a large number of initial conditions were used, the drop to 33 trajectories by 100 fs in indicative of the magnitude of computational effort required which hinders efforts to generate a satisfactory number of "*on-the-fly*" trajectories. This naturally shifts the balance of methodological efficiency towards other approaches, namely the generation of full-dimensional surface. Initial efforts in this direction are discussed in the next chapter.

Chapter 5

Beyond "*on-the-fly*": Trial calculations of CS_2 electronic state surfaces

5.1 Introduction

The 19-state surface-hopping simulations in the previous chapter entail a serious computational endeavour, with each trajectory taking months of CPU time to cover only the first few tens of femtoseconds of the experimental photodissociation dynamics of CS_2. In other words, for this problem the balance of preferred quantum dynamics method has shifted to those based on precomputed surfaces. Compared to grid-based calculations of a wide selection of phase space, "*on-the-fly*" simulations using relatively low to medium levels of theory save time by calculating electronic properties in those regions only visited by a trajectory even if this means repeated sampling of the same region by multiple trajectories. However, with the number of states being considered here at the employed level of CASSCF theory, this advantage no longer holds. Thus one must consider the calculation of full surfaces, driven by the reasoning that the calculation of many points in phase space at this and higher levels of theory will be more efficient than an "*on-the-fly*" trajectory-based method.

While expensive to generate in their own right, this approach offers several advantages, chief among which is access to theoretical methods beyond semi-classical "*on-the-fly*" surface-hopping simulations. Calculations

of fully-dimensional surfaces of the structurally-related CO_2 have been reported by Grebenschikov, identifying seams of conical intersection, state crossings and calculating experimental observables such as the temperature-dependant absorption spectrum [194–197]. While there are many parallels given the similar geometry and electronic structure of CO_2 and CS_2, the latter case is complicated by spin-orbit coupling facilitating ready access to triplet states. This chapter demonstrates early in-roads in the complex process of generating multidimensional surfaces of a triatomic in a "build-from-the-bottom" approach.

Firstly, reduced dimensionality surfaces were generated at very low levels of CASSCF theory ((10,8)/STO-3G), before the level of theory was gradually increased (through (14,10)/STO-3G to (14,10)/6-31+G*). The effect of the increase of level of theory on the stability and smoothness of the surfaces is discussed.

5.2 Methodology

Initial three-dimensional surfaces were tested at exceptionally low-levels of CASSCF *ab initio* theory due to the huge number of points requiring calculation. For these early tests, one bond length was kept fixed while the other bond length and angle were varied in the ranges $R_{CS} = 1 - 4$ Å and $\Theta_{SCS} = 80^\circ - 180^\circ$ in resolutions of $\Delta R = 0.05$ Å and $\Delta\Theta = 2^\circ$. The number of points N_{grid} calculated is trivially a function of these ranges and resolutions,

$$N_{\text{grid}} = \frac{R_{\text{CS}_1\ \text{max}} - R_{\text{CS}_1\ \text{min}}}{\Delta R_1} + \frac{R_{\text{CS}_2\ \text{max}} - R_{\text{CS}_2\ \text{min}}}{\Delta R_2} + \frac{\Theta_{\text{max}} - \Theta_{\text{min}}}{\Delta\Theta} + 1, \tag{5.1}$$

giving some 3111 points for the grid size discussed. If the other bond is varied in the same way, this number increases to over 189,000, emphasising the need to keep dimensionality down, at least in the testing phase. As well as this, fixing one bond length results in the helpful (and not so serendipitous)

co-incidence that the test surfaces are easy to visualise in three dimensions, with co-ordinates of bond length R_{CS}, angle Θ_{SCS}, and energy.

Only four states of A' symmetry are calculated. As well as being an easier computational exercise, the results of such tests may still prove useful in the calculation of singlet-state only dynamics, which because of the symmetry considerations of the nonadiabatic coupling matrix elements are zero between states of A′ and A″ symmetry. This mirrors the approach taken by Wang *et al* in their AIMS simulation of singlet-state photodynamics of CS_2 [198]. Additionally, this provides a reasonable set of test data on which to practice the filtering of points and to ensure all the requisite framework is in place from a logistical point of view to calculate the necessary electronic properties in an easily-accessible format. After the calculation of all of the points, surfaces are generated by linear interpolation to essentially increase the resolution of the grid. There are a number of other approaches to generating surfaces; most common of these are splining, and fitting to an analytical expression shaped by the properties of the molecule.

5.3 Results and discussion

The first simplification made in the early trials described here was to reduce the dimensionality of the problem by keeping one R_{CS} fixed. This not only drastically reduces the number of points to be calculated, but keeps the problem to a three-dimensional one, relatively easy to visualise and plot. The level of theory and number of states were also reduced, considering only the first $4A'$ states of the system (negating the need at this point to calculate spin-orbit coupling).

Thus far, two basis sets and two active spaces within the SA-CASSCF framework have been considered: STO-3G/6-31+G* and (10,8)/(14,10) respectively. This maintains the stable and well-behaved active space from previous surface-hopping simulations, while allowing thousands of points to be calculated in the space of a day or so on a suitable cluster due to the inexpensiveness of each individual calculation. Each calculation included the state-averaged energies of the first four singlet A′ states. The range of points

calculated was from 80° to 180° in 2° steps, and from 1.00 Å to 4.00 Å in steps of 0.05 Å at each angle considered.

5.3.1 STO-3G (10,8) surfaces

Fig. 5.1 presents visualisations of the surfaces for each state, plotted from the raw data from the calculations, with energies zeroed to the $1A'$ global minimum. Linear interpolation was performed on the points, generating data on a finer grid by repeatedly halving the intervals k times in each dimension ($k = 3$ in this case), giving 2^{k-1} interpolated points between sample values. The mean CPU time for each calculation at this level was approximately 6.2 seconds, leading to a serial compute time of just over five and a half hours. Running in parallel on a reasonably-sized cluster naturally reduced this greatly. While the level of theory here is low in terms of basis set, the active space is suitable for describing the short-range potentials of these states. Thus the general topology of the surfaces should be expected to be reasonably accurate, if not quantitative, which will be discussed mainly in terms of the predicted minimum energy and saddle points. The familiar single well of the ground state, the repulsive barrier and a dissociation barrier just over 6 eV are seen. There is the beginnings of another minima lying just outside of the range of points here at $\Theta_{SCS} = 80°$ and $R_{CS} = 1.85$ Å, reminiscent of an analogous structure observed in the ground state potential energy surface of CO_2 [194]. The second state features a clear off-linear minimum (as do the rest of the excited states) at $\Theta_{SCS} = 138°$ and $R_{CS} = 1.70$ Å, as well as two spurious minima both located well past the dissociation barrier. The structure of $3A'$ is more complicated, with an "outer" global minimum at $\Theta_{SCS} = 100°$ and $R_{CS} = 1.80$ Å and an "inner" local minimum at $\Theta_{SCS} = 152°$ and $R_{CS} = 2.20$ Å. Disregarding a spurious minimum at $R_{CS} = 4.00$ Å, the remainder of the reported points comprise two along the $\Theta_{SCS} = 180°$ axis (which in reality corresponds more closely to first order saddle points) and a second likely spurious minimum at $\Theta_{SCS} = 170°$ and $R_{CS} = 2.25$ Å. The surfaces are not perfectly smooth at this level of theory (nor are they at the other levels considered) as a result of occasional poor convergence of individual CASSCF calculations. In a production run,

this raw data would be further processed and subject to smoothing algorithms. This becomes more obvious in the $4A'$ state, which again features intriguing structure. The global minimum is reported at $\Theta_{SCS} = 180^\circ$ and $R_{CS} = 2.30$ Å. There is a less well-defined region of local minimum energy between $\Theta_{SCS} = 110^\circ - 130^\circ$ and $R_{CS} = 1.70 - 2.50$ Å, with a further saddle point at linear geometry with $R_{CS} = 1.80$ Å. All reported minima of each state are collected in Table 5.1.

While of limited use in terms of quantitative predictions, these trial calculations give a relatively quick idea of what to expect when moving to higher levels of theory before the outlay of significant computational expense.

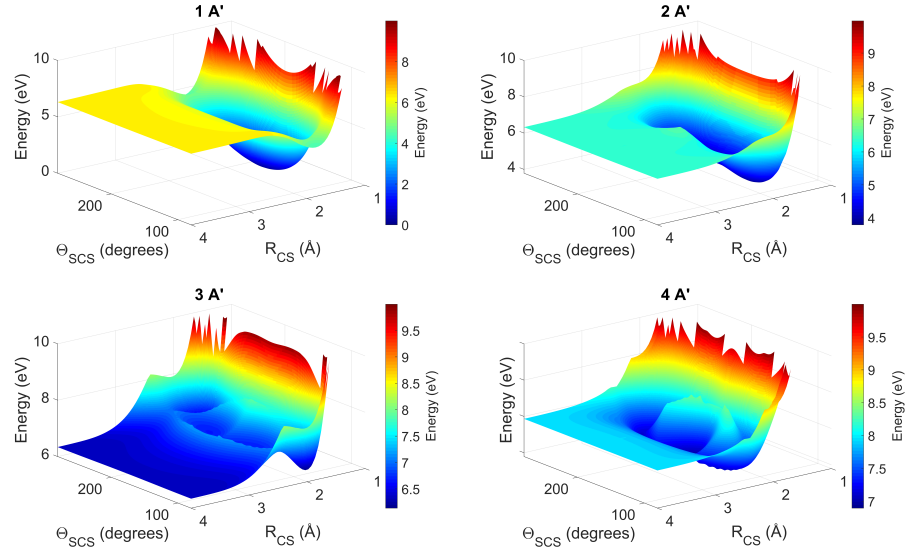

(A) 3D

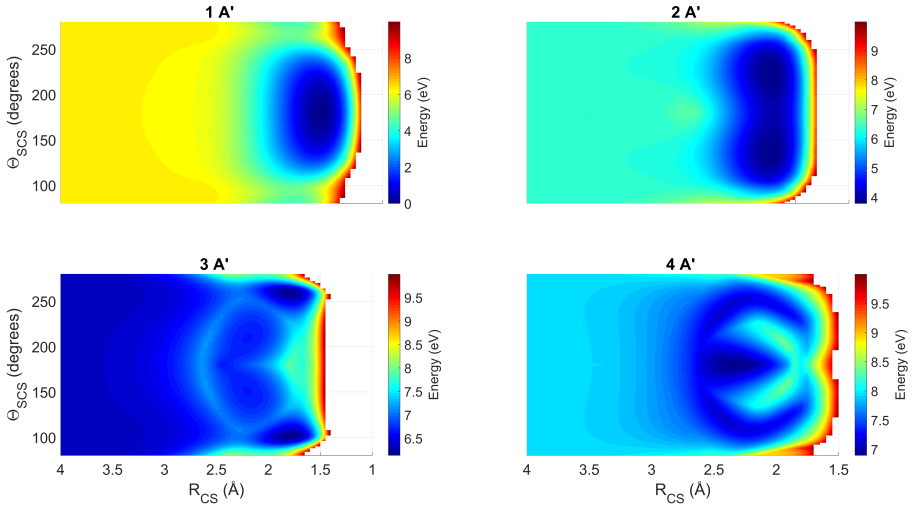

(B) Bird's eye

FIGURE 5.1: Three-dimensional visualisations of the potential energy surfaces of the first four $^1A'$ states of CS_2 calculated in the range $R_{CS} = 1.0 : 4.0$ and $\Theta_{RCS} = 80° : 180°$ at the SA4-CAS(10,8)/STO-3G level of theory. The other R_{CS} bond is fixed at 1.569 Å.

	Θ_{SCS} **(degrees)**	R_{CS} **(Å)**	**Energy (eV)**
$1A'$	180	1.55	0.000
	80	1.85	4.350
$2A'$	138	1.70	3.787
	148	3.25	6.304
	180	3.40	6.302
$3A'$	100	1.80	6.134
	94	4.00	6.337
	180	2.45	6.666
	152	2.20	6.670
	170	2.35	6.719
	180	1.70	7.734
$4A'$	180	2.30	6.895
	118	2.40	7.082
	126	2.45	7.084
	114	2.35	7.088
	134	2.50	7.113
	110	2.30	7.116
	144	2.55	7.153
	110	2.10	7.191
	112	2.05	7.203
	160	2.60	7.211
	116	2.00	7.215
	118	1.95	7.227
	122	1.90	7.241
	128	1.85	7.265
	132	1.80	7.342
	80	4.00	7.934
	180	1.80	7.997

TABLE 5.1: Recorded local minima on the SA4-CAS(10,8)/STO-3G potential energy surfaces of the first four $^1A'$ electronic states of CS_2. Equivalent minima with $\Theta_{SCS} > 180^\circ$ are excluded.

5.3.2 STO-3G (14,10) surfaces

The size of the active space was increased significantly while keeping the basis set the same to see what differences this induces. Immediately, the first cases of outright failure can be seen in some CASSCF points, left blank in the potential energy plots in Fig. 5.2. However, these are limited in number. Encouragingly there are no major changes in surface topology as a result of the bigger active space; indeed, the surfaces change very little save for a slight increase in bumpiness in terms of the number of reported minima (many of which are located well past the dissociation barrier) seen in Table 5.2, suggesting that the extra static correlation accounted for in this active space does not play a big role in describing these states (this does not exclude their importance in higher lying singlet or triplet states).

A more quantitative illustration of the differences in the two levels of theory comes from the calculation of difference plots, which are presented in Fig. 5.3 as a simple subtraction of the larger active space surfaces minus the smaller. While the colour range may be striking at first glance, a look at the breadth of the scale indicates that the surfaces generally fall within +0.1 and -0.8 eV, and for the most part the largest differences are found in the regimes of the repulsive wall and asymptotic limits. For example in the $1A'$ surface, there is a region just in front of the minimum well predicted to be $\sim$0.05 eV higher in the (10,8) calculation than the (14,10) calculation, while the asymptotic limit is predicted to lie $\sim$0.1 eV higher with the (14,10) active space. However the most severe differences are in the steepness of the repulsive wall, as is the case in the rest of the excited states. Stripping out these relative extremes, the dynamically interesting regions of the potentials match extremely well.

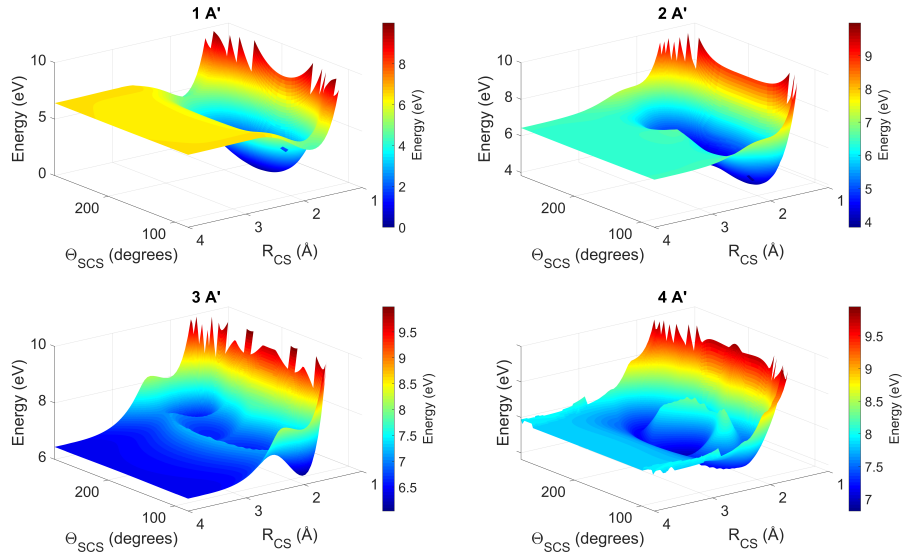

(A) 3D

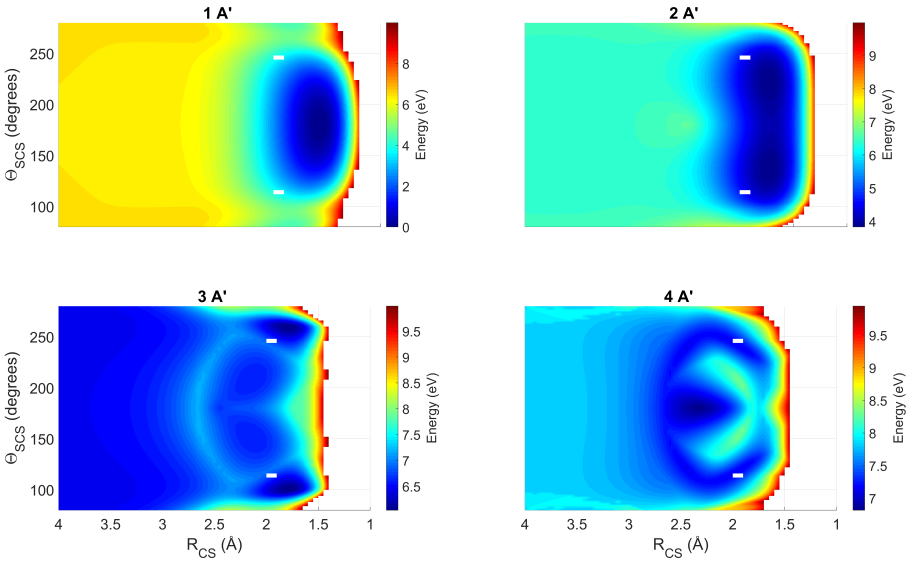

(B) Bird's eye

FIGURE 5.2: Three-dimensional visualisations of the potential energy surfaces of the first four $^1A'$ states of CS_2 calculated in the range $R_{CS} = 1.0 : 4.0$ and $\Theta_{RCS} = 80° : 180°$ at the SA4-CAS(14,10)/STO-3G level of theory. The other R_{CS} bond is fixed at 1.569 Å.

	Θ_{SCS} **(degrees)**	R_{CS} **(Å)**	**Energy (eV)**
$1A'$	180	1.55	0.000
	80	1.85	4.369
	82	4.00	6.415
	80	3.85	6.418
	82	3.75	6.418
	80	2.90	6.463
$2A'$	138	1.70	3.829
	180	3.40	6.405
	148	3.25	6.405
	82	4.00	6.428
	80	3.85	6.430
	82	3.75	6.430
$3A'$	100	1.80	6.036
	102	1.75	6.047
	98	4.00	6.438
	82	4.00	6.438
	96	3.90	6.439
	90	4.00	6.440
	92	4.00	6.440
	80	3.85	6.441
	96	3.70	6.443
	82	3.75	6.443
	152	2.15	6.593
	180	2.45	6.683
$4A'$	180	2.30	6.816
	122	2.45	7.127
	128	2.50	7.134
	116	2.40	7.134
	122	1.90	7.153
	118	1.95	7.153
	112	2.35	7.155
	136	2.55	7.155
	116	2.00	7.158
	124	1.85	7.162
	112	2.05	7.162
	110	2.10	7.166
	108	2.15	7.174
	128	1.80	7.186
	146	2.60	7.187
	162	2.65	7.225
	132	1.75	7.256
	82	4.00	7.828
	80	3.85	7.828
	82	3.75	7.828
	82	3.60	7.830
	80	3.65	7.831

TABLE 5.2: Recorded local minima on the SA4-CAS(14,10)/STO-3G potential energy surfaces of the first four $^1A'$ electronic states of CS_2. Equivalent minima with $\Theta_{SCS} > 180^\circ$ are excluded.

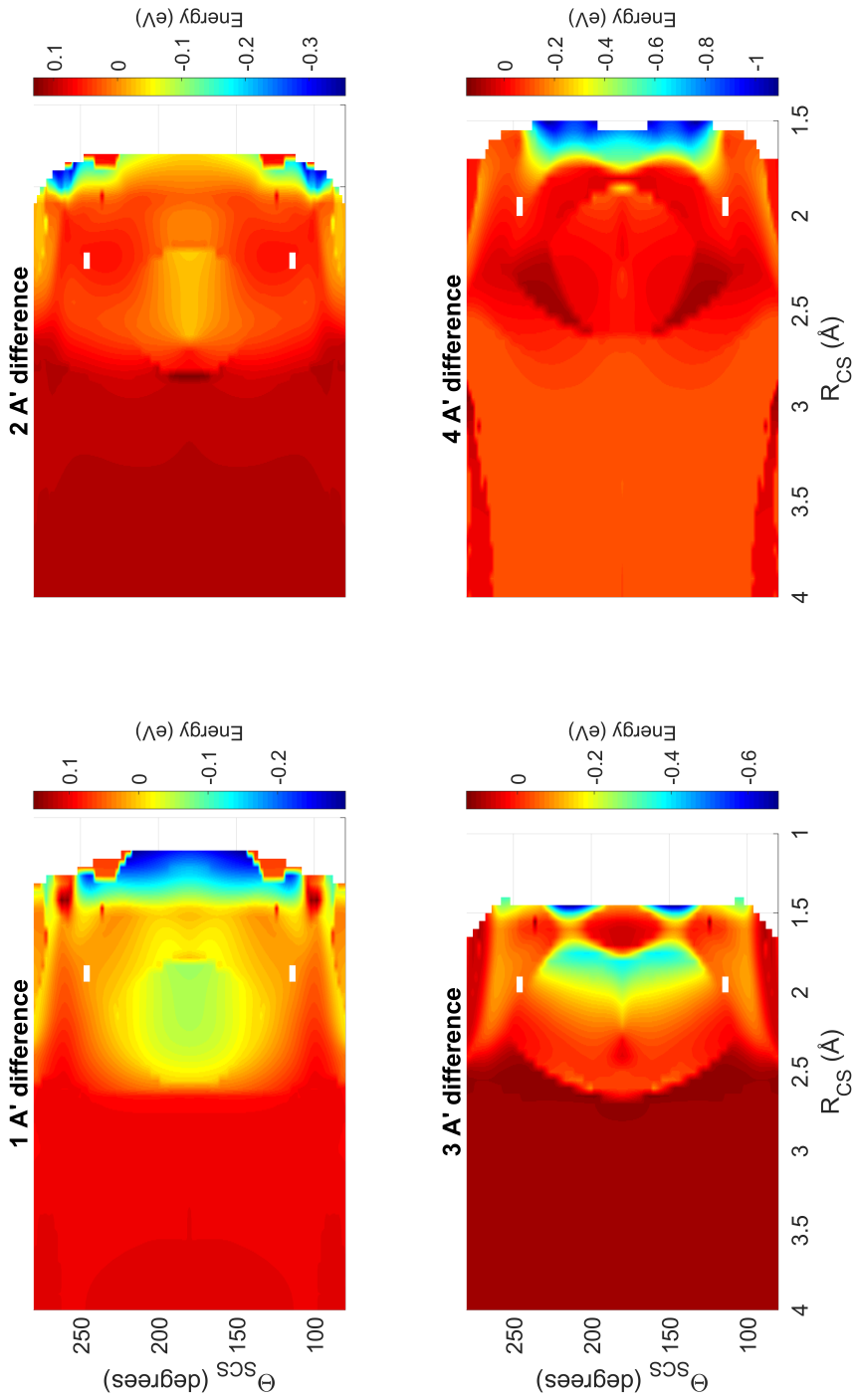

FIGURE 5.3: Difference plots between the calculated surfaces at the SA4-CAS(14,10) and SA4-CAS(10,8) levels with the STO-3G basis set. These surfaces are a simple subtraction, the (14,10) case minus the (10,8) case.

5.3.3 6-31+G*(10,8) surfaces

The next stage was to upgrade the calculations to include a much more reasonable basis set. The choice here was the well-established Pople double-zeta 6-31+G*, featuring diffuse and polarisation functions on heavy atoms. Such a basis set is amenable to further expansion in cardinality as required for greater accuracy. With this upgrade, the increase in computational expense was fairly modest, up to just under 25 hours for a serial run. This merely reflects that the main burden of the calculation lies in the size of the active space. Plots of the calculated surfaces at this level are shown in Fig. 5.4, which show the by now familiar topological features. Again, there has been no significant shift in the locations of key points on the surface. There are fewer reported stationary points here (shown in Table 5.3) than in the (14,10)/STO-3G case, indicating that the increased complexity brought in by the larger active space is the main contributor to surface roughness. Intriguingly here, the $1A'$ global minimum is reported to lie just off-linear at $\Theta_{SCS} = 178^\circ$ — this is clearly erroneous, and can be traced to the resolution of the calculations and the fixed C-S bond length of 1.569 Å, which may not correspond exactly to the predicted minimum bond length at this still relatively low level of theory.

Again, direct difference plots are shown in Fig. 5.5, here between the 6-31+G* and STO-3G generated surfaced with the (10,8) active space. Differences here are naturally greater than shown in previous plots; this merely emphasises the large increase in quality of the basis set allowing calculated energies to get significantly closer to the variational minimum. Taking the ground state as an example, the change in basis set lowers the barrier to dissociation by the order of 1 eV.

	Θ_{SCS} **(degrees)**	R_{CS} **(Å)**	**Energy (eV)**
	178	1.60	0.000
	80	1.85	4.105
	82	1.80	4.110
	156	2.75	4.745
	180	2.80	4.749
$1A'$	138	2.70	4.785
	120	2.65	4.891
	82	2.45	4.958
	80	2.50	4.979
	110	2.60	4.991
	80	2.80	5.155
	132	1.70	3.759
$2A'$	180	3.90	5.003
	120	2.65	5.128
	110	2.60	5.159
	98	4.00	5.048
$3A'$	104	1.75	5.655
	180	2.30	5.822
	178	1.70	6.926
	180	2.30	6.452
	136	2.45	6.539
	128	2.40	6.543
	148	2.50	6.552
	122	2.35	6.564
	118	2.30	6.599
	114	2.25	6.634
	124	1.90	6.649
$4A'$	118	2.00	6.657
	120	1.95	6.658
	116	2.05	6.663
	128	1.85	6.678
	132	1.80	6.785
	122	4.00	7.148
	80	2.75	7.421
	166	1.55	7.805

TABLE 5.3: Recorded local minima on the SA4-CAS(10,8)/6-31+G* potential energy surfaces of the first four $^1A'$ electronic states of CS_2. Equivalent minima with $\Theta_{SCS} > 180^\circ$ are excluded.

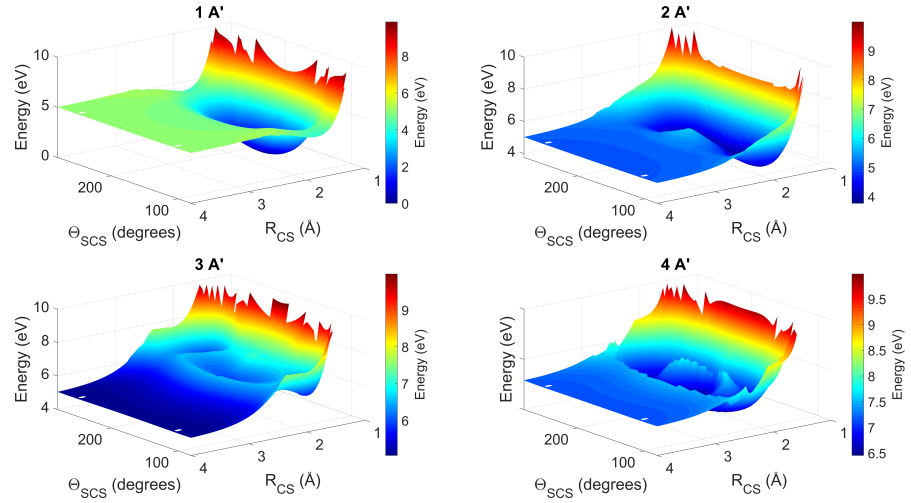

(A) 3D

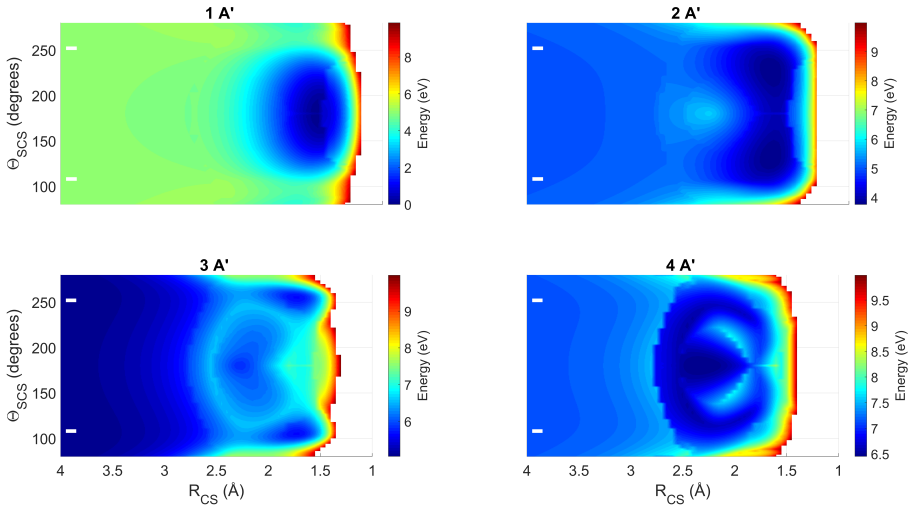

(B) Bird's eye

FIGURE 5.4: Three-dimensional visualisations of the potential energy surfaces of the first four $^1A'$ states of CS_2 calculated in the range $R_{CS} = 1.0 : 4.0$ and $\Theta_{RCS} = 80^\circ : 180^\circ$ at the SA4-CAS(10,8)/6-31+G* level of theory. The other R_{CS} bond is fixed at 1.569 Å.

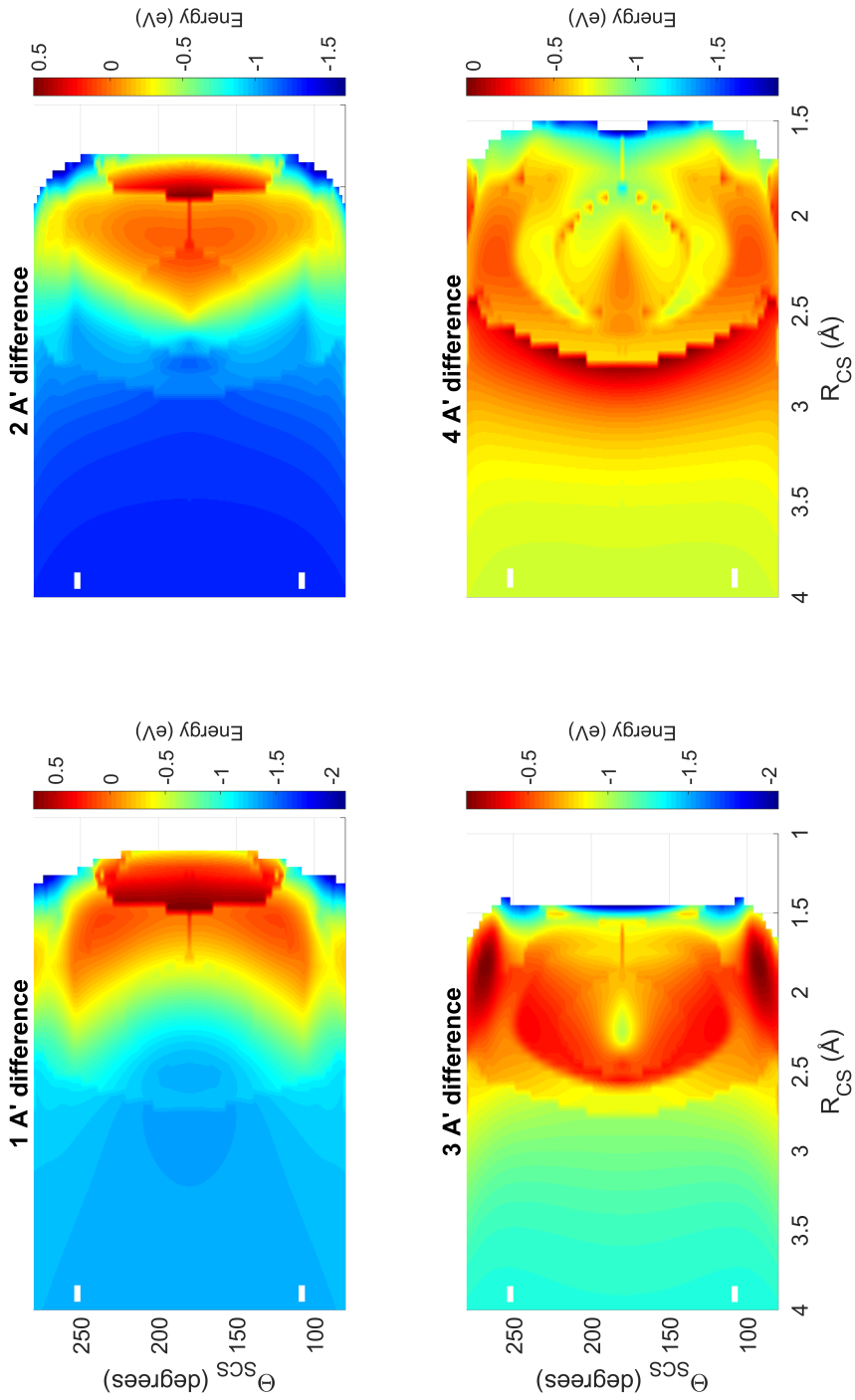

FIGURE 5.5: Difference plots between the calculated surfaces at the SA4-CAS(10,8)/6-31+G* and SA4-CAS(10,8)/STO-3G levels of theory. These surfaces are a simple subtraction, the 6-31+G* case minus the STO-3G case. One R_{CS} bond is fixed at 1.569 Å.

5.3.4 6-31+G* (14,10) surfaces

Finally, the discussion is completed by examining surfaces calculated with both the larger basis set and enlarged active space. The time for a serial run here is increased to 32 hours. Analogous surface plots as before are presented in Figs. 5.6 (surfaces) and 5.7. There are a number of striking features which emerge when one combines the increase in active space with the increase in basis set. Firstly, the increased complexity in the calculation leads to notably more points of failure. Fortunately these mostly occur at extreme geometries; either beyond the dissociation barrier or high up the repulsive wall and could be removed by more rigorous interpolation. The combination of larger active space and basis set still recovers all the required features of these surfaces, but leads to a great increase in the reported number of stationary points, shown in Table 5.4. Difference plots between these surfaces and the (10,8)/6-31+G* surfaces are shown in Fig. 5.7. For the first three states, the only significant differences lie in the repulsive wall, with the dissociation barrier height in the first also having raised slightly around the $\Theta_{SCS} = 180^\circ$ axis, and in all four states with sharper rises in the "wings" at $\Theta_{SCS} = 80^\circ$.

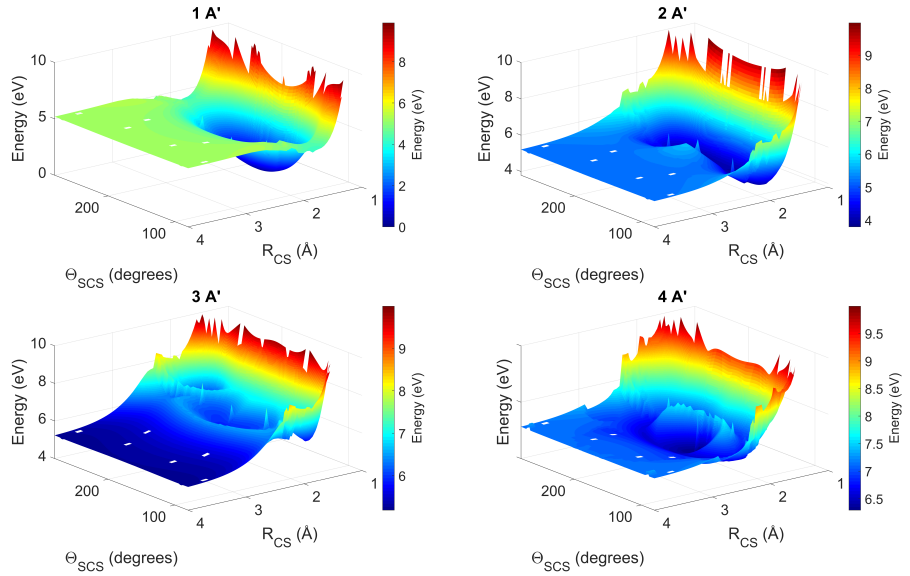

(A) 3D

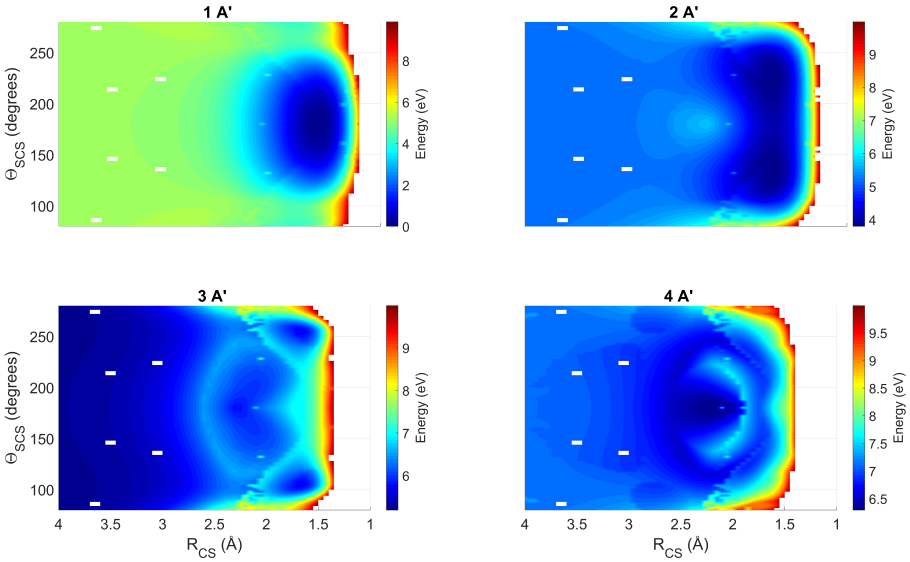

(B) Bird's eye

FIGURE 5.6: Three-dimensional visualisations of the potential energy surfaces of the first four $^1A'$ states of CS_2 calculated in the range $R_{CS} = 1.0 : 4.0$ and $\Theta_{RCS} = 80° : 180°$ at the SA4-CAS(14,10)/6-31+G* level of theory. The other R_{CS} bond is fixed at 1.569 Å.

	Θ_{SCS} (degrees)	R_{CS} (Å)	Energy (eV)
$1A'$	180	1.55	0.000
	180	2.15	2.832
	80	1.85	4.074
	80	2.00	4.205
	86	2.00	4.379
	90	1.95	4.422
	86	2.10	4.545
	98	2.05	4.581
	94	2.05	4.598
	100	2.10	4.638
	84	2.20	4.668
	102	2.15	4.700
	82	2.25	4.700
	80	2.30	4.730
	90	2.25	4.881
	92	4.00	5.149
$2A'$	142	1.75	3.795
	132	1.70	3.799
	148	1.70	3.815
	138	1.80	3.829
	132	1.85	3.885
	128	1.90	3.976
	126	1.95	4.084
	102	2.15	4.956
	100	2.10	5.036
	98	2.05	5.124
	92	4.00	5.160
	180	3.90	5.176
	168	4.00	5.177
	162	4.00	5.178
	160	3.90	5.178
	146	3.75	5.181
	136	3.00	5.216
	134	2.85	5.219
	126	2.85	5.221
	106	2.70	5.274
	106	2.85	5.279
	104	2.90	5.285
	104	2.65	5.287
	94	2.05	5.397
	90	1.95	5.564
	92	2.15	5.602
	90	2.10	5.689
	86	2.00	5.961
	84	2.20	6.116
	80	2.10	6.595

	Θ_{SCS} (degrees)	R_{CS} (Å)	Energy (eV)
$3A'$	92	4.00	5.186
	100	4.00	5.224
	164	4.00	5.251
	170	4.00	5.252
	104	1.70	5.718
	106	1.65	5.719
	180	2.30	5.764
	98	2.05	6.125
	100	2.10	6.158
	134	2.05	6.198
	106	2.10	6.216
	102	2.15	6.226
	130	2.05	6.259
	112	2.05	6.315
	94	2.05	6.371
	122	2.10	6.400
	92	2.15	6.599
	90	1.95	6.808
	180	1.70	6.957
	86	2.00	7.269
	84	2.20	7.384
	80	2.00	7.542
	82	1.85	7.716
$4A'$	180	2.20	6.292
	180	2.05	6.342
	142	2.50	6.513
	156	2.55	6.514
	134	2.45	6.518
	126	2.40	6.545
	120	2.00	6.576
	116	2.05	6.580
	122	2.35	6.582
	116	2.30	6.601
	124	1.95	6.626
	128	1.90	6.678
	132	1.85	6.721
	138	1.80	6.807
	124	1.85	6.814
	128	1.80	6.822
	142	1.75	6.829
	120	1.90	6.841
	126	2.85	6.849
	134	1.75	6.866
	148	1.70	6.887
	106	2.75	6.892
	116	1.95	6.906
	138	1.70	6.938
	168	4.00	7.105
	88	4.00	7.124
	94	2.10	7.206
	92	2.15	7.242
	84	2.20	7.641
	90	1.95	7.780
	86	2.00	8.042
	80	2.10	8.396
	82	1.85	8.613
	84	1.75	9.064

TABLE 5.4: Recorded local minima on the SA4-CAS(14,10)/6-31+G* potential energy surfaces of the first four $^1A'$ electronic states of CS_2. Equivalent minima with $\Theta_{SCS} > 180^\circ$ are excluded.

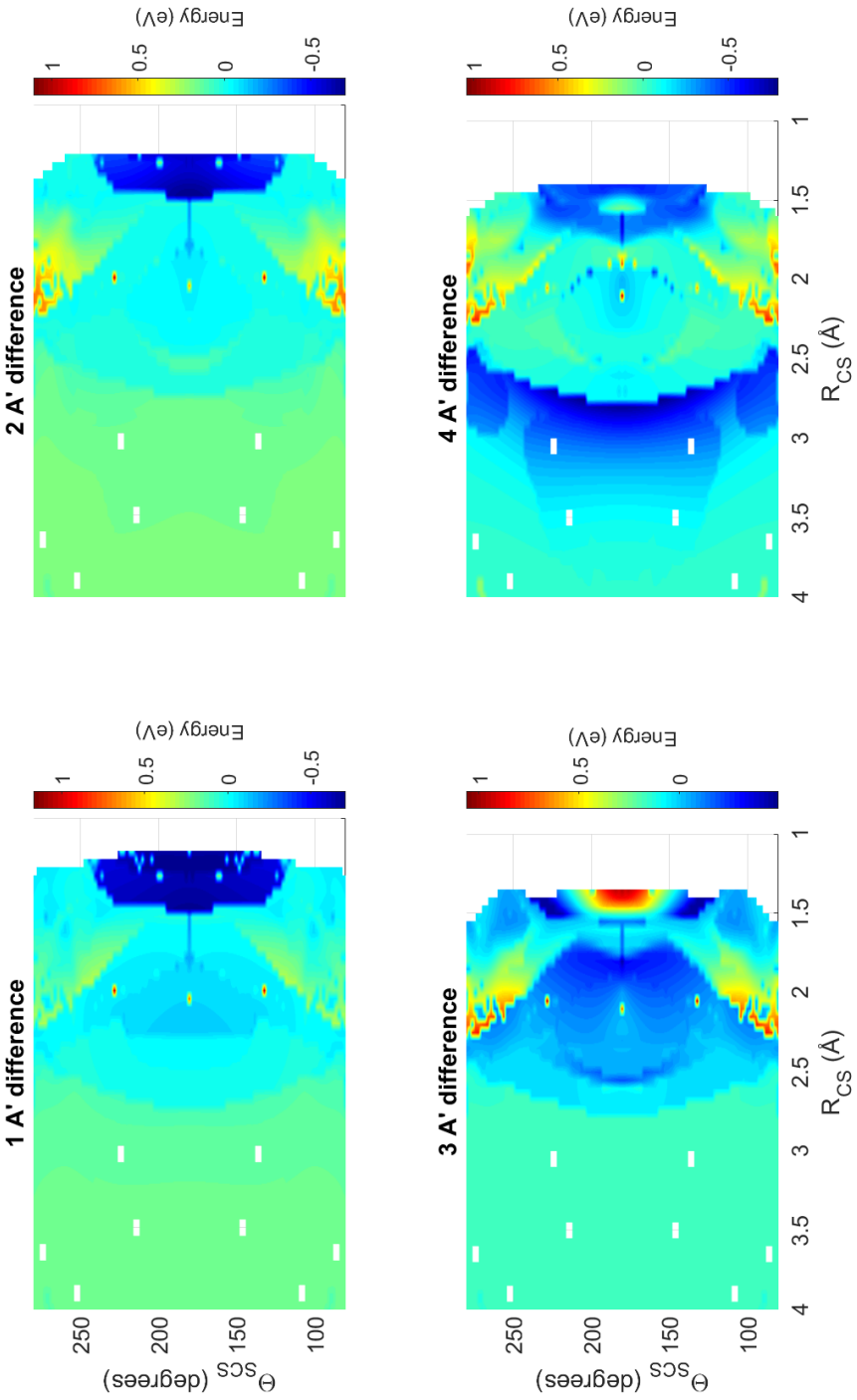

FIGURE 5.7: Difference plots between the calculated surfaces at the SA4-CAS(14,10) and SA4-CAS(10,8) level with the 6-31+G* basis set. These surfaces are a simple subtraction, the larger active space minus the smaller one. One R_{CS} bond is fixed at 1.569 Å.

5.4 Conclusions and outlook

From the previous chapter, it is clear the *ab initio* complexity of the photodynamics of CS_2 from the 2^1B_2 state stretches the applicability of such "*on-the-fly*" methods — the large number of states involved complicates the electronic structure, places a heavy burden on the semi-classical surface-hopping algorithm, and increases both numerical instability and computational expense with the sheer number of energies, gradients and other electronic properties which must be successfully calculated in each time step. Thus, another approach was considered — precomputation of surfaces. While allowing the use of higher-level methods (intended to be MRCI with the (14,10) active space in this case) due to each point only requiring a single computation, this is still an enormous endeavour requiring the careful choice of the level of theory and sensitivity in the range of points and properties calculated. To this end, a number of small-scale trials have taken place at reduced levels of theory and complexity, namely the STO-3G and 6-31+G* basis sets with the (10,8) and (14,10) active spaces, examining the first four singlet states. While no qualitative change in topology is observed as one ascends from (10,8)/STO-3G to (14,10)/6-31+G*, these simple tests serve their purpose in demonstrating increasing instability in the range of points calculated, with sporadic failures of points (either calculations outright crashing or converging to discontinuous energies) increasing in density with the level of theory. However, such issues can be overcome with a judicious choice of interpolation and filtering. More positively, however, these issues do not preclude the possibility of further improvements to higher levels of theory. One envisages a gradual continuation of these testing process, with the addition of more states, the calculation of spin-orbit coupling, and finally an upgrade to MRCI rather than CASSCF.

Once a set of data points are generated from electronic structure, the PES must be fitted in some fashion to the data points. Two categories of methods have traditionally been used for this purpose; global multivariate approaches ensure the functional form reproduces all data points with zero fitting error, with the energies of geometries not found in the data set recovered by interpolation (for example, splining [199, 200] and moving least

squares interpolation [201]), while quasi-interpolation schemes do not require that each data point lies exactly on the surface but attempts to minimise the fitting error.

However, newer approaches to the fitting of PESs is to use artificial neural networks (ANNs). While not new in themselves [202], their application to PES fitting is relatively novel [203–208]. In this context, the ANN converts an input signal (the molecular geometry) into an output (energy, NACME or other desired electronic parameter) through a series of "hidden" layers of neurons in which each neuron, represented by a non-linear function, has a weight optimised from a set of training data (the *ab initio* energies from a data set). A schematic of a four-dimensional ANN of this kind is shown in Fig. 5.8, in which each layer of neurons represent a particular degree of freedom. Further details on how values are ascribed to particular neurons may be found in references e.g. [208, 209]. Once optimised, the trained ANN may be used to predict PES topology at points not included in the training data set. Thus, ANNs are useful tools to provide the surfaces required in many QMD methods.

While grid-based methods as exemplified in this chapter can act as the input data source for a particular neural network, in principle one could use the data from existing CS_2 surface-hopping simulations, which in the case of SHARC includes the MCH state energies of each time step for all trajectories. Using this data from a large sample pool of the 19 state trajectories would automatically cover a large portion of phase space, particularly relevant to early-time dynamics, needing only supplemented by further grid-based calculations at dissociated geometries. The choice of phase space points could be taken from the eight-state simulations in Chapter 3, but these would need to be recalculated with the full 19 states. Using phase space points sampled from trajectories and feeding these into an ANN presents an intriguing and possibly more efficient method to obtaining full dimensional surfaces for CS_2 which the author, colleagues and collaborators [209, 210] are keen to explore further.

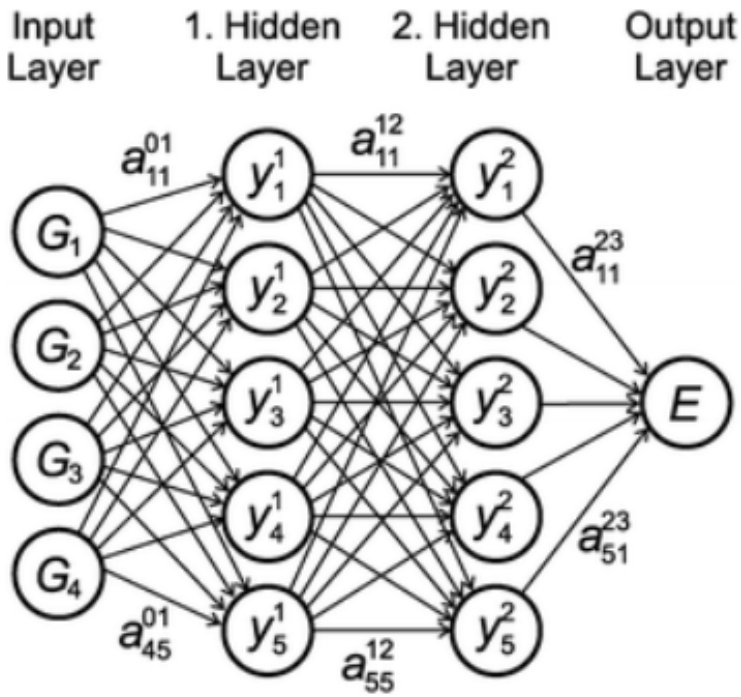

FIGURE 5.8: A schematic representation of a four-dimensional "feed-forward" neural network relating atomic co-ordinates (G_1 to G_4) and energy E. The neurons are arranged in layers; input, two hidden, and output. The neurons are connected by weight parameters a^{kl}_{ij}. Taken from Ref. [208].

Chapter 6

Correlation between electronic structure calculations and dynamics simulations: the 1^1B_2 state revisited

6.1 Introduction

While of limited use in terms of experimental comparison, the simulations carried out at the SA8-CAS(8,6)/6-31G* level of theory in Chapter 3 gave insight into the interplay between competing singlet and triplet dissociation pathways in this region of the potential energy manifold, and how this competition manifested itself in terms of the coupling between nuclear and electronic motion. These results allowed broad conclusions to be drawn about the various stages of the dissociation mechanism — namely excitation, population redistribution, and preferential dissociation at acute angles along the triplet channel. However, it was clear that while the chosen level of theory described the initial vibrational dynamics well, there were clear deficiencies in the description of the bond-breaking region. So while the calculations of early time dynamics were reliable, questions remained over how this deficiency affected the dissociation dynamics.

To answer this question, it was necessary to run simulations at a higher level of *ab initio* electronic structure theory [164]. Primarily this involved increasing the active space of the SA-CASSCF level to such an extent as to

match high level benchmark calculations as closely as possible in the depiction of the dissociation barrier. Ideally, every other simulation parameter would be kept identical in order to limit responsibility for any resultant changes in dynamics to the active space alone. However, the increase in computational expense from a larger active space in this case necessitated the introduction of other approximations, most critically in the nonadiabatic coupling scheme used; here, wave function overlaps are utilised instead of expensive full nonadiabatic couplings. As a result, the previous SA8-CAS(8,6)/6-31G* simulations were re-run using overlaps, and with the SVP basis as used in the higher-level (10,8) simulations. This ensures any change in results comes from the active space alone. The parameters of each simulation are discussed in more detail below.

By this comparison, there is opportunity to analyse how the change in level of theory affects the predicted dynamics, and answer the question of whether the conclusions from previous simulations are validated by higher level calculations.

6.2 Methodology

Potential energy curves in both the angular and radial regimes were calculated at the levels of theory of the simulations: SA8-CAS(8,6)/SVP and SA8-CAS(10,8)/SVP respectively. These are compared alongside high level reference calculations accounting for dynamic correlation, calculated at the SA8-MRCI(14,10)/aug-cc-pvTZ level. Following this, the set up parameters of the two simulations (herein referred to as **A** and **B**) are discussed and the results compared in terms of predicted population dynamics, nuclear motion and dissociation mechanism.

6.3 Results and discussion

6.3.1 Potential energy curves

To get an idea of the performance of each level of theory, it is instructive to examine one-dimensional potential energy cuts along coordinates of interest, as shown in Figs. 6.2 and 6.3 calculated at the SA8-(8,6)/SVP, SA8-CAS(10,8)/SVP and reference SA8-MRCI(14,10)/aug-cc-pvTZ levels of theory. The SVP basis set was used here in the simulations instead of 6-31G* as previous; SVP is a more recent basis set of the Turbomole family [211] and reproduces the HF orbital ordering of 6-31G*. Common to both active spaces are the degenerate sulfur lone pair HOMOs, the σ bonding MOs and the π^* LUMO pair. The (10,8) active space features an additional electron pair in the second-highest occupied MO (HOMO-1), and a σ^* antibonding virtual MO. In total the (8,6) active space comprises 345 determinants (225 singlet, 120 triplet) and (10,8) 5096 determinants (3136 singlet, 1960 triplet), illustrating the factorial scaling of computational cost with the size of the active space in CASSCF calculations. Fig. 6.1 shows both of these active spaces alongside the (14,10) active space used in the benchmark using MRCI(14,10)/aug-cc-pvTZ calculations. While the latter is too expensive a level of theory on which to run the "*on-the-fly*" dynamics, such curves serve as a useful reference with which to compare the lower levels of theory.

The included adiabatic electronic states can be labelled according to their adiabatic ordering (S_0, S_1 *etc.* for the singlets and T_1, T_2 *etc.* for the triplets), but also according to the symmetry labels in the linear and bent geometries as summarised in Table 6.1.

Fig. 6.2 shows the potentials along the Θ_{SCS} bending coordinate. Reminiscent of the simulations in Chapter 3, both the (8,6) and (10,8) levels of theory replicate the angular potentials of the benchmark MRCI(14,10) calculations rather well, with the predicted vertical $S_2 \leftarrow S_0$ excitation energy 4.16 eV for (8,6), 4.29 eV for (10,8), and 4.12 eV for MRCI(14,10). In this regard, the stories presented by the (8,6) and (10,8) levels of theory used in simulations **A** and **B** are consistent, and their angular potentials show comparatively small quantitative differences. Therefore, it is to be expected that

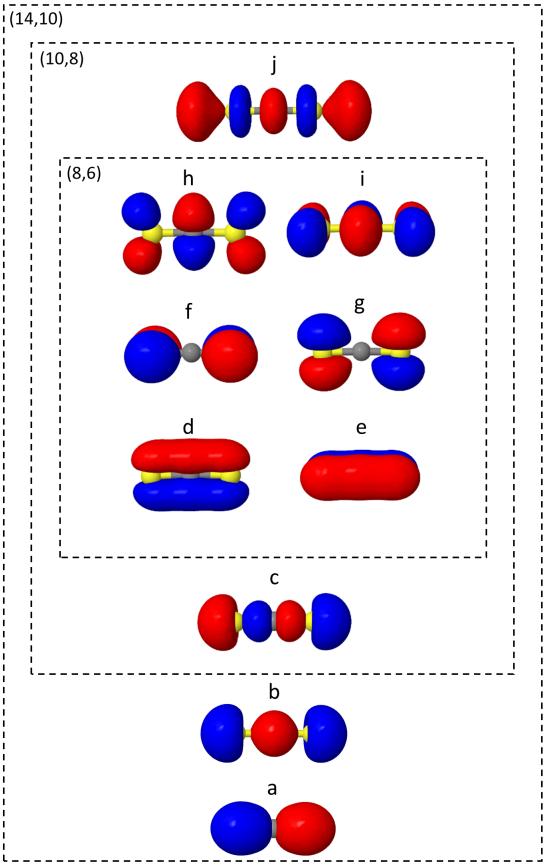

FIGURE 6.1: Molecular orbitals (MOs) included in the active spaces (8,6), (10,8), and (14,10), corresponding to simulation **A** (*d*-*i*, inner rectangle), simulation **B** (*c*-*j*, centre rectangle), and the reference calculations (*a*-*j*, outer rectangle). The innermost (8,6) MOs (*d*-*i*) include the degenerate sulfur lone pair HOMOs, the σ bonding MOs and a π^* LUMO pair. The (10,8) active space includes a further two MOs (*c* and *j*) that correspond to an additional electron pair found in the next-highest occupied MO and a σ^* antibonding virtual MO. Finally, in (14,10) two occupied orbitals (*a* and *b*) are added.

both simulations will give similar descriptions of the early time dynamics.

Fig. 6.3 shows the radial potential energy curves along the R_{CS} stretch coordinate corresponding to dissociation of one sulfur. In contrast to the angular curves, the active space must accurately describe not just the reactant but also the products while accounting for the electron correlation

Point group:	$\mathbf{C}_1$	$\mathbf{C}_s$	$\mathbf{C}_{2v}$	$\mathbf{D}_{\infty h}$
State/notation:	S_0	^{1}A′	^{1}A$_1$	$^1\Sigma_g^+$
	S_1	^{1}A″	^{1}A$_2$	$^1\Sigma_u^-$
	S_2	^{1}A′	^{1}B$_2$	$^1\Delta_u$
	S_3	^{1}A″	^{1}A$_2$	$^1\Delta_u$
	T_1	^{3}A′	^{3}B$_2$	$^3\Sigma_u^+$
	T_2	^{3}A″	^{3}A$_2$	$^3\Delta_u$
	T_3	$^3A'$	^{3}B$_2$	$^3\Delta_u$
	T_4	^{3}A″	^{3}A$_2$	$^3\Sigma_u^-$

TABLE 6.1: Symmetry labels and correlations for the four lowest energy singlet and triplet states of CS_2 at linear geometry in the C_1, C_s, C_{2v} and $D_{\infty h}$ point groups (which are used to classify the electronic states). The C_1 point group has no symmetry and simply corresponds to the energy ordering of the adiabatic singlet and triplet states. Assignments in the $D_{\infty h}$ point group are taken from Ref. [181].

during bond breaking. The deficiencies in the (8,6) active space used in simulation **A** are again present as discontinuities and severe exaggerations of the barrier height towards dissociation. This is particularly prevalent in the highest state considered, T_4; however, the barrier of this state is energetically inaccessible during the simulations. Also noteworthy are unphysical undulations in the potential energy curves beyond the barrier in the smaller (8,6) calculations at $\Theta_{SCS} = 120^\circ$. However, because these lie beyond the barrier they have no effect of the assignment of a dissociation event as singlet or triplet. The potential wells for the (8,6) calculations have sharper gradients along the stretch coordinate than in (10,8), so one may expect the vibrational motion to be faster in simulation **A**. Overall, the radial potential energy curves are much smoother in the (10,8) calculations (i.e. simulation **B**), with no discontinuities and close match to the MRCI(14,10) reference potentials. Simulation **B** is therefore expected to give a more accurate representation of the dissociation dynamics of the system.

As discussed previously, in the linear ground state equilibrium $D_{\infty h}$ geometry, the dipole transition moments to many excited states are zero due to symmetry. However, the system exhibits strong couplings and the transition moments change rapidly as the geometry is perturbed. To demonstrate

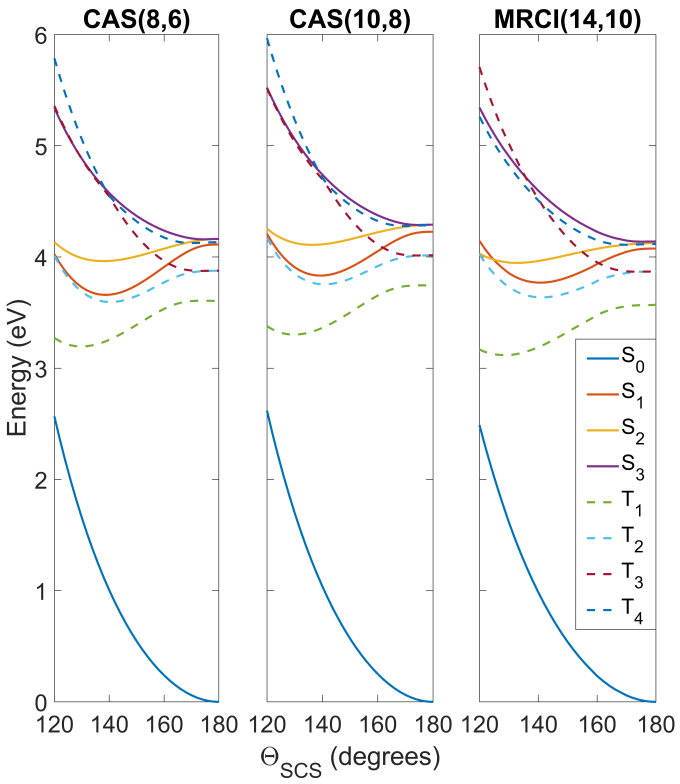

FIGURE 6.2: Potential energy curves as a function of the Θ_{SCS} bending coordinate, calculated at the SA8-CAS(8,6)/SVP (simulation **A**), SA8-CAS(10,8)/SVP (simulation **B**), and MRCI(14,10)/aug-cc-pvTZ (reference) levels of theory, shown in the left, centre and right panels. Bond lengths are fixed at the CASSCF(16,12)/aug-cc-pvQZ optimised value of 1.569 Å. For compactness, only the range $120° \leq \Theta_{SCS} \leq 180°$ is shown as the curves are symmetric about the linear geometry at $\Theta_{SCS}=180°$.

this, Table 6.2 shows oscillator strengths at $\Theta_{SCS}=170°$ and excitation energies at each level of theory considered. Since the simulations use stochastic initial conditions taken from the Wigner distribution, this effect is accounted for.

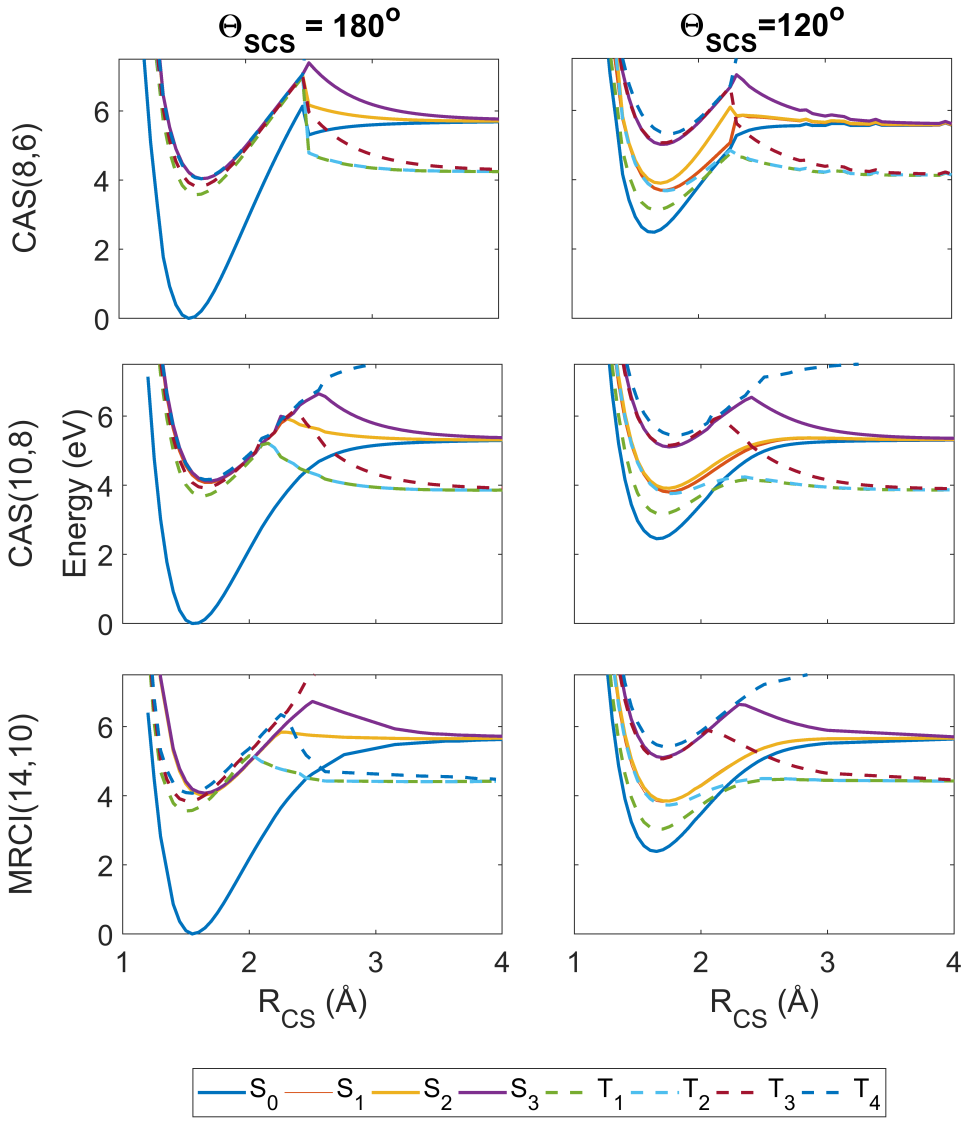

FIGURE 6.3: Potential energy curves as a function of the R_{CS} stretch coordinate, with the second bond length fixed at $R_{CS} = 1.569$ Å and the angle Θ_{SCS} fixed at linear 180° (left column) and bent 120° (right column), with calculations at the SA8-CAS(8,6)/SVP (simulation **A**), SA8-CAS(10,8)/SVP (simulation **B**), and MRCI(14,10)/aug-cc-pvTZ (reference) level shown in the top, middle and bottom rows.

	CAS(8,6)		**CAS(10,8)**		**MRCI(14,10)**	
	ΔE (eV)	f_{ij} ($\times 10^{-4}$)	ΔE (eV)	f_{ij} ($\times 10^{-4}$)	ΔE (eV)	f_{ij} ($\times 10^{-4}$)
$S_1 \leftarrow S_0$	4.11	0	4.23	5.89×10^{-4}	4.08	0
$S_2 \leftarrow S_0$	4.16	1.38	4.29	1.70	4.12	2.13
$S_3 \leftarrow S_0$	4.16	0	4.29	2.48×10^{-2}	4.14	0

TABLE 6.2: Predicted oscillator strengths f_{ij} at bent geometry with $\Theta_{SCS} = 170°$ and excitation energies ΔE at linear geometry with $\Theta_{SCS} = 180°$ for the three lowest excited singlet states, calculated at SA8-CAS(8,6)/SVP (simulation **A**), SA8-CAS(10,8)/SVP (simulation **B)** and MRCI(14,10)/aug-cc-pvTZ (reference) level of theory (taken from Ref. [33]). In all cases the molecule has the equilibrium bond length $R_{CS} = 1.569$ Å.

Simulation:	**A**	**B**
Active space	(8,6)	(10,8)
Basis set	SVP	SVP
Coupling approach	Overlaps	Overlaps
Number of trajectories	571	1024
Surface hopping algorithm	SHARC	SHARC
$\Delta\, t$ (fs)	0.5	0.5
Initial E_k (eV)	2.5	2.5

TABLE 6.3: Electronic structure and simulation setup parameters of simulations **A** and **B**.

6.3.2 Surface Hopping dynamics

The key parameters of simulations **A** and **B** are shown in Table 6.3. To circumvent the severe computational bottleneck imposed by the calculation of full nonadiabatic coupling matrix elements (NACMEs), wave function overlaps were used. These can be generated by an efficient code integrated in the SHARC package [212] and offer a faster alternative to full NACME calculation while offering stable numerical propagation of the wave function. It is this choice which made simulation **B** feasible, allowing the jump to larger active space (with its associated higher quality potentials) without exceeding the limits of acceptable computational expense.

For each simulation, trajectories were run for 1 ps with a time step of 0.5 fs. After a surface hop, velocities were rescaled to adjust the kinetic

energy in order to conserve the total energy, and a decoherence correction is applied [213]. Initial positions were taken from a Wigner distribution, and initial momenta were assigned to each atom such that the total kinetic energy per molecule approximates the excess kinetic energy from excitation by excitation by a 200 nm pump pulse to the S_2 state, using an in-built algorithm in SHARC. In reality such a pulse would access higher-lying electronic states of CS_2 that are not included in the current simulations, but here the excess energy serves to ensure that the total energy in the system is sufficient to allow barrier crossing. Initial occupied electronic states are assigned to each trajectory by a probabilistic scheme accounting for the excitation energies and oscillator strengths at each initial position, again using a built-in algorithm in SHARC originally taken from Ref. [214]. By this scheme, normalised populations at time zero for states S_0 to S_3 are $< 10^{-8}/0.0105/0.8535/0.0915$ for simulation **A** and $< 10^{-7}/0.0176/0.7258/0.0885$ for simulation **B**. Initial triplet populations (T_1 to T_4) are $< 10^{-5}/0.0249/0.0013/0.0182$ and $< 10^{-4}$ $/0.0271/0.0025/0.1384$ for simulations **A** and **B** respectively.

In simulation **A**, 500 initial conditions were generated from the Wigner distribution, from which 573 trajectories were launched (an initial condition may be used to launch trajectories on more than one state due to the probabilistic selection of initial states). Trajectories that failed to reach $t_{max} = 1$ ps, for instance due to convergence problems of the CASSCF electronic structure calculations at a particular time step, were treated in the following manner. If prematurely-terminated trajectories had dissociated before the point of failure, the dissociating sulfur atom was propagated to t_{max} at the average velocity between the point of dissociation and the last successful time step, with the last recorded MCH state taken as final (since surface hops within a particular spin multiplicity beyond dissociation have no meaningful effect on the branching ratio). Trajectories that had not dissociated before failure were discarded. By this procedure, 571 successful trajectories were obtained.

In simulation **B**, a larger set of 1000 initial conditions were generated

from the Wigner distribution to compensate for more frequent CASSCF failures due to the larger active space. A restart procedure was applied to trajectories which fail to reach 1 ps as follows:

1. Re-running the point-of-failure time step with internal orbital optimisation in the CASSCF step turned off, and turning it back on if the step was successful.

2. Failing that, if the trajectory was dissociative (defined as one bond being 3 Å or longer), that bond is extended by a small percentage (1%, 2% or 5% depending on the severity of the case) and continued from the new coordinates.

Following these steps, the same assumptions in terms of propagation of the dissociated sulfur atom and its MCH state as in simulation **A** were applied. Since the restart procedure inevitably reduces the quality of trajectories to which it is applied, the whole dataset was scanned for trajectories exhibiting discontinuous behaviour, such as unphysically large jumps in bond length during a single time step (seen most prevalently where step 2 of the above procedure was applied to trajectories with already large C-S distances). Such trajectories, comprising approximately 8% of the bunch, were filtered out, resulting in no qualitative change in the final results. Because the restart procedure applied only to trajectories past the dissociation barrier, it had no effect on the final singlet/triplet branching ratio or pre-barrier dynamics. These procedures gave a total of 1024 trajectories for simulation **B**.

6.3.2.1 Populations

The total singlet and triplet populations from each simulation are plotted in Fig. 6.4. Like before, there is a near-immediate decay in the singlet population, the extent of which is greater in simulation **A**. By 1 ps, the singlet/triplet fraction for simulation **A** is 0.25/0.75 compared to 0.32/0.68 in simulation **B**, although the curves have not plateaued by this time.

A more mechanistic picture of the dynamics, where the singlet and triplet populations are categorised as bound or dissociated, is shown in Fig. 6.5.

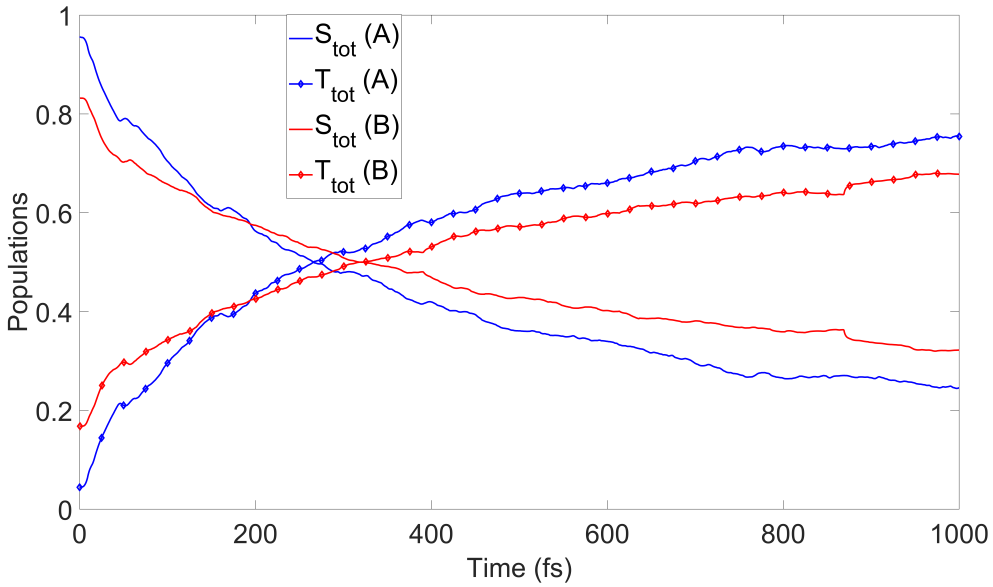

FIGURE 6.4: Total singlet and triplet populations as a function of time, defined as as the sum of the squares the MCH state coefficients, for simulations **A** and **B**.

The dynamic definitions of dissociation threshold here fall out as 2.73 Å and 2.96 Å in simulations **A** and **B** respectively. The decay of the bound singlet population follows a similar profile in both simulations, decaying exponentially to 15-20% of the total population by the end of the simulated dynamics. For each simulation, the other curves are qualitatively similar but significantly differ in magnitude. The rapid transfer of population into bound triplet at very early times is common to both simulations, but in simulation **A** the rise continues until about 500 fs, where it settles near 50% of the population. The behaviour in simulation **B** is in contrast; here, after the initial rise population is efficiently transferred into both of the dissociation channels, of which the singlet channel opens notably quicker that the triplet pathway. In simulation **A**, it is instead the triplet channel which dominates from the earliest dissociation at 50 fs. By the end of the dynamics in both simulations, the triplet channel has become the dominant dissociation pathway.

Therefore, there is a clear mapping between the topology of the potential energy cuts discussed earlier. The higher barriers and steeper potentials in

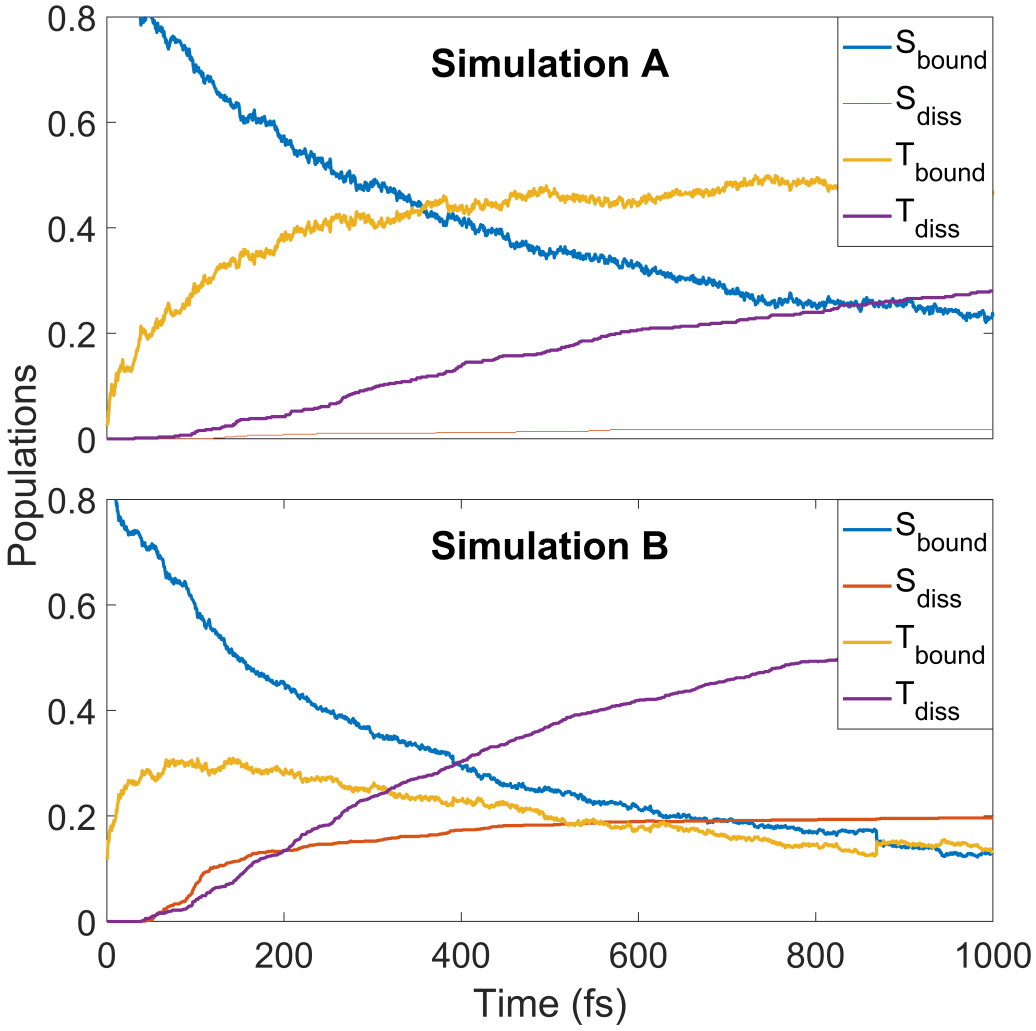

FIGURE 6.5: Populations of singlet and triplet states in simulation **A** (upper panel) and **B** (lower panel), separated into contributions from bound and dissociated trajectories.

simulation **A** lead to a trapping of population in the triplet states causing the dissociation to be frustrated, evidenced by the final reported dissociation fractions of the entire trajectory ensembles (1.8% singlet and 28% triplet in **A**, and 20% singlet and 54% triplet in **B** and branching ratios (singlet:triplet ratio 1:15.6 for **A** and 1:2.8 for **B**). The larger dissociation barriers featured in simulation **A** impact both the overall proportion of the trajectories which dissociate and emphasise the role of the triplet channel as the more accessible route to dissociation in this system.

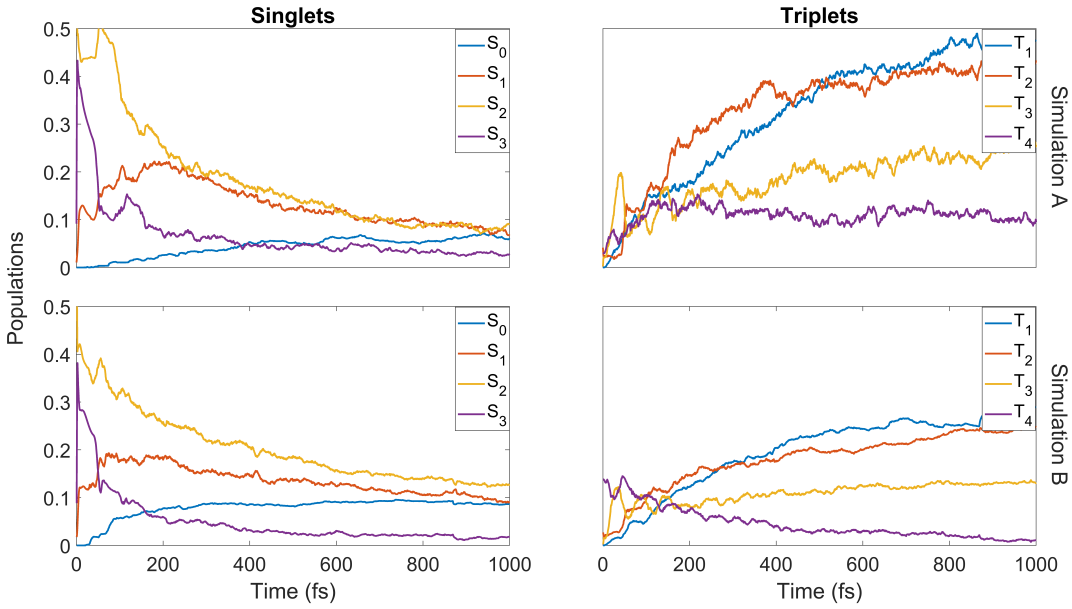

FIGURE 6.6: State-resolved populations as a function of time for each of the simulations. The rows refer to simulation **A** and **B** (upper and lower respectively) and the columns to singlet and triplet states (left and right respectively).

Further insight can be gained by examining the state-by-state populations as shown in Fig. 6.6. In both **A** and **B**, most trajectories naturally begin in the S_2 state. This does not last long: the immediate population redistribution upon commencement of the dynamics leaves this state with less than 50% population within 50 fs in both simulations. The population mainly moves into S_3 and S_1, after which the former state quickly loses its accrued population while S_1 continues a slight rise until $\sim$200 fs. After this point, states S_{1-3} all decay smoothly. Meanwhile, the ground state population begins to rise as the first trajectories decay into this state. The S_0 rise is slow in **A**, taking 600 fs to reach a plateau at about 7% of the population. In simulation **B**, the initial rise is over the first 30 fs, followed by a short plateau before a second rise levelling out at about 9% of the population. After the halfway point in the simulated dynamics, all notable activity in the singlet states has ceased. This is most obvious in **A**, while there is still some slow decay in S_1 and S_2 at later times in simulation **B**.

More specifically, some distinct fluctuations are visible in the populations in both simulations, most notably an increase in S_2 population in the interval 40 to 75 fs. Examination of net flux of surface hops (where flux is simply defined as the difference between the number of hops to and from the state of interest) involving S_2 in this period reveal that the net population gain is due to an influx of hops from S_3 alongside a small contribution from T_3 (specifically, 93% and 7% respectively in simulation **B**). Looking at the individual triplet state populations one sees that these states also play a strong role in the early redistribution of population, reinforcing the importance of spin-orbit coupling in the early-time dynamics of the system. Other features that emerge in the first 100 fs are early out-of-phase oscillations between T_3 and T_4, the secondary role of T_3 (whose dissociation barrier is energetically greater than that of T_1 and T_2), the near-commensurate rise in T_1 and T_2 (clearer in simulation **B**) reflecting the closely-spaced nature of the respective potential energy surfaces of those states, and the steady hold of population in T_4, whose high barrier to dissociation allows this state to act as a wavepacket reservoir before the stored population eventually leaks elsewhere. Hops into T_3 over the first 50 fs mainly come from S_3 and T_4 (55% and 37% of net flux respectively in simulation **B**). The hopping analysis explains why S_3, after gaining so much population in the immediate redistribution *via* internal conversion, decays as rapidly as it does: population first transfers *via* ISC to T_3 until $\sim$50 fs, followed by IC to S_2 up to $\sim$75 fs. This analysis shows clearly the direct competition between internal conversion and intersystem crossing characteristic of the dynamics of the system.

To emphasise the immediacy of the initial exchange of population, for a random subset of 250 trajectories from simulation **B**, dynamics were rerun over the first 10 fs with a reduced time step of 0.1 fs. The resulting populations are shown in Fig. 6.7. Compared with the simulation **B** plots in Fig. 6.6, the singlet and triplet state populations give the same qualitative (albeit noisier) behaviour, assuring that this effect is largely independent of time step.

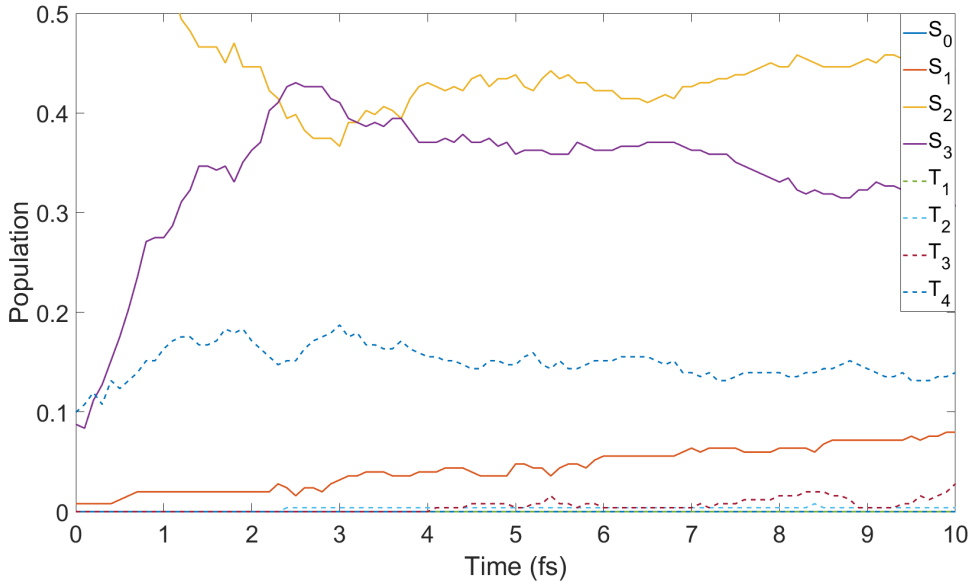

FIGURE 6.7: Populations over the first 10 fs of a random subset of 250 trajectories from simulation **B**, run with a shorter time step of 0.1 fs.

6.3.2.2 Nuclear motion

Shown in Fig. 6.8 are the average CS bond lengths separated into contributions from bound and dissociated trajectories, and the average Θ_{SCS} angle for the bound trajectories in each simulation. Again, a number of features are common to both simulations. Initially it is the symmetric stretch that is excited, with the clear oscillations dispersing after 300 fs. The impact of the higher dissociation barrier on the predicted dynamics in simulation **A** manifests itself by the two clear oscillations seen in the bound R_{CS} curve, compared to only one in simulation **B**, reflecting the difficulty trajectories have in getting over the barrier in **A**. A similar effect is seen in the average angle in that it is slower to damp in **A** than **B**.

In Fig. 6.9, snapshots of the nuclear densities associated with the sulfur atoms are shown at a series of time points (0, 50, 100 and 1000 fs) for each simulation, representing different stages of the reaction. These were calculated by projecting the internal coordinates onto the $(x, y > 0)$ plane with the carbon atom (whose probability density was neglected) centred at the

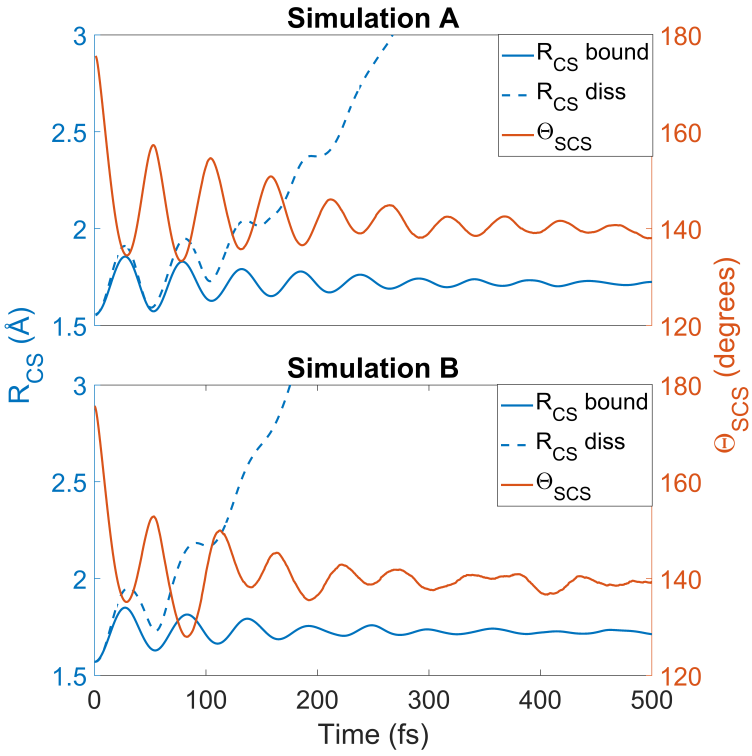

FIGURE 6.8: Average R_{CS} for bound and dissociated molecules and average Θ_{SCS} for bound molecules, calculated for simulation **A** (upper) and **B** (lower) as a function of time. The average bound geometry is calculated for all molecules up until they dissociate (i.e. CS fragments are excluded). A trajectory is designated as dissociated when one R_{CS} exceeds the minimum distance from which dissociation is irreversible in each simulation.

origin. For the sulfur atoms, this was calculated as,

$$P(x,y) = \left(N_{\text{traj}}\right)^{-1} \sum_{i=1}^{N_{\text{traj}}} \sum_{j=1}^{N_S} \left(\frac{\gamma}{\pi}\right) \exp\left(-\gamma\left[(x,y) - \vec{q}_{ij}\right]^2\right), \tag{6.1}$$

where $\vec{q}_{ij}$ are the coordinates of sulfur atom j in trajectory i projected onto the $(x, y > 0)$ plane, γ is a Gaussian width parameter equal to $1/(2\sigma^2)$ where

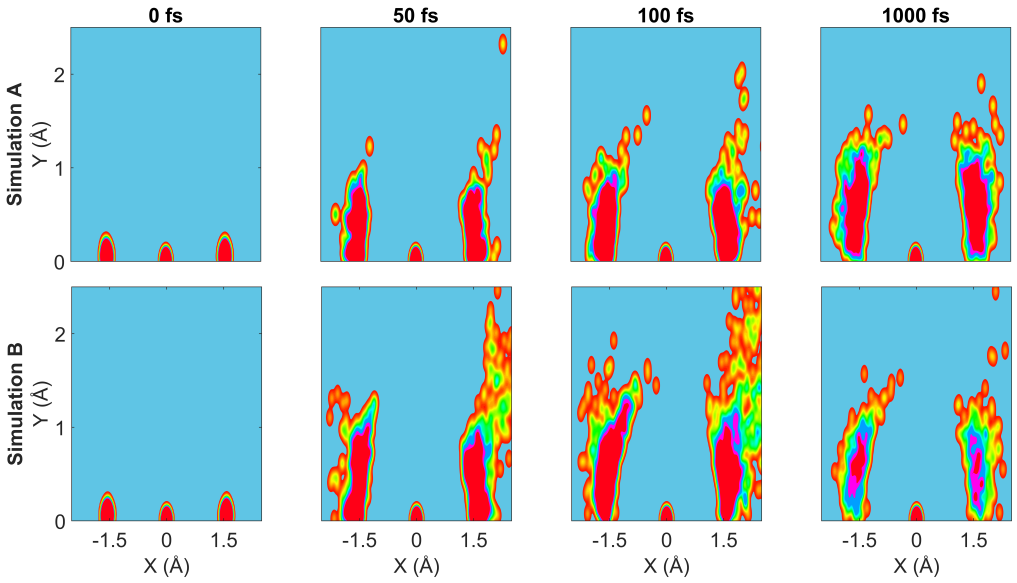

FIGURE 6.9: Nuclear probability density snapshots at selected time points in each simulation. These are generated by projecting the nuclear coordinates onto the XY plane and calculating the subsequent atomic densities, with the carbon atom fixed at the origin. Top row: simulation **A**, bottom row: simulation **B**.

$\sigma = 0.05$, N_S is the number of sulfur atoms and N_{traj} is the number of trajectories. The probability density $P(x, y)$ corresponds to a convolution of the classical coordinates of the sulfur atoms with a normalised Gaussian function. This provides a simple way of visualising the dispersion of the nuclear motion as the dynamics unfolds, while separating out electronic effects. At time zero all atoms are clearly localised around the equilibrium geometry, taking into account the spread of the Wigner distribution of initial positions for the trajectory ensemble. By 50 fs the dissociation pathway has clearly opened, notably to a significantly greater extent in simulation **B** (albeit the bound portion of the wavepacket is approximately the same shape in both simulations). The vibrational wavepacket spreads rapidly, covering the range $\Theta_{SCS} = 180°$ to $120°$. This theme continues in the two remaining snapshots, with the extent of dissociation clearly growing at 100 fs before greatly reducing by the end of the simulations at 1000 fs, reflecting

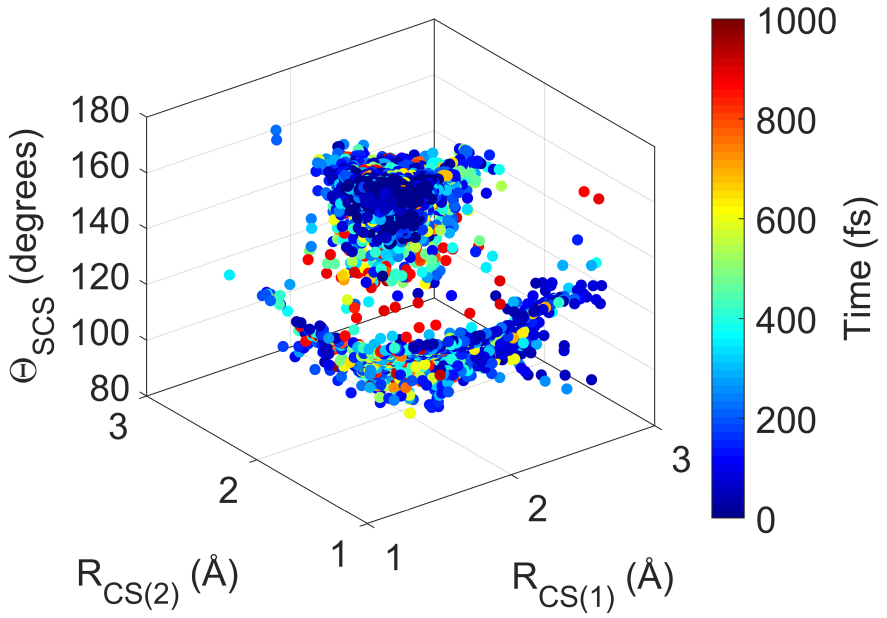

FIGURE 6.10: Four-dimensional plots of surface hops between states of singlet multiplicity only (i.e. IC). Each point represents a hop between electronic states, with the molecular geometry represented by its position and the time by its colour.

the evolution of the populations in Fig. 6.5). By 1000 fs the dissociative pathway has completely stalled in **A**; this is not the case in simulation **B** where the dissociation of the sulfur atom is clearly still ongoing.

Figs. 6.10 to 6.12 visualise individual surface-hopping events in simulation **B** in terms of their molecular geometry and the time of occurrence. Each data point represents an individual surface hop, defined by each of the two CS bond lengths, the angle Θ_{SCS}, and the time of occurrence. The three panels respectively show all hops within singlet states, triplet states, and between singlet and triplet states. The resultant clusters of data points provide evidence of the correlation between nonadiabatic and spin-orbit coupling effects and the molecular geometry, as well as the evolution of the dynamics. Common to each plot is a dense cluster centred around early times around equilibrium geometry, representative of the rapid internal conversion and intersystem crossing at early times and the concurrent competition between these two distinct processes. This feature is naturally less pronounced in the

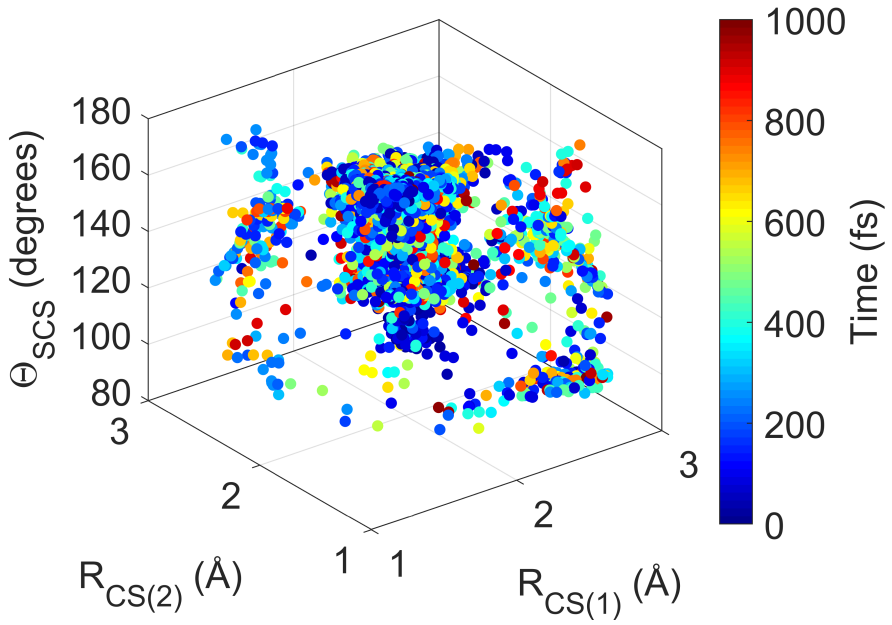

FIGURE 6.11: Four-dimensional plots of surface hops between states of triplet multiplicity only (i.e. IC). Each point represents a hop between electronic states, with the molecular geometry represented by its position and the time by its colour.

plot of triplet-triplet hops only, as nonadiabatic hops within the triplet manifold must be preceded by a intersystem crossing into that manifold (barring the small number of trajectories that originate in a triplet state). There is an additional well-defined cluster in the singlet-to-singlet panel corresponding to one elongated C-S bond and a narrow distribution of acute bending angles, reflective of the other main region where the different singlet electronic states come closer together in energy as they approach and exceed the barrier crossing region. This is seen to be broadly symmetric across both bonds. A similar effect is seen in the triplet-to-triplet panel, but here it is not nearly as restricted in terms of angular range due to the smaller variation of energy spacing with bending angle in the triplet states. The spin-orbit coupling (intersystem crossing) surface hops in the singlet-triplet panel are in contrast far more tightly clustered in the Franck-Condon region because trajectories spending time is this region are constantly exposed to singlet and triplet states lying close to each other.

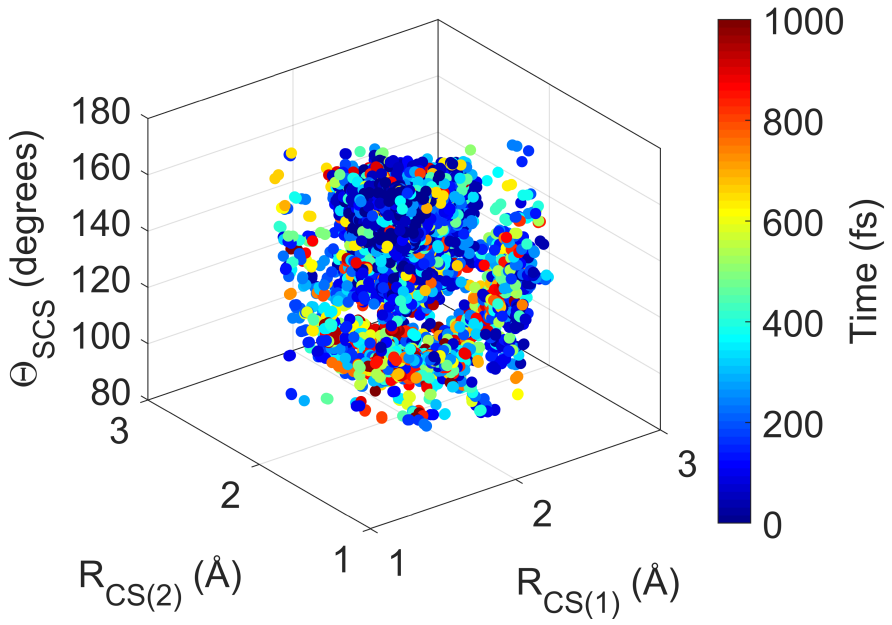

FIGURE 6.12: Four-dimensional plots of surface hops between states of singlet and triplet multiplicity (i.e. ISC). Each point represents a hop between electronic states, with the molecular geometry represented by its position and the time by its colour.

6.3.3 Branching ratios, convergence, and timings

The final branching ratio between singlet and triplet dissociation, perhaps the key metric of the simulations, is given in Table 6.4. Both simulations show the same qualitative trend in that the triplet pathway is the dominant dissociation channel due to its lower barrier to dissociation and the support of spin-orbit coupling in the system. This ratio is exaggerated in simulation **A** as a consequence of the overestimation of the barriers to dissociation in

Simulation	**S branch**	**T branch**
A	0.059	0.941
B	0.267	0.733

TABLE 6.4: Branching ratio of singlet to triplet state dissociated sulfur atoms at the end of the simulation at 1 ps, for simulations **A** and **B**.

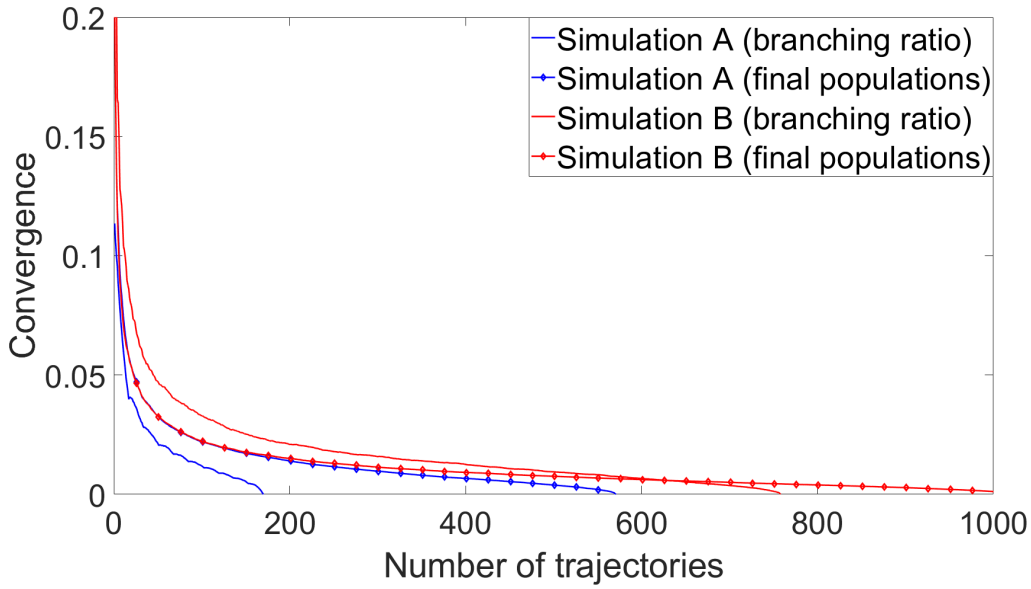

FIGURE 6.13: Convergence plots of each simulation as a function of the branching ratio and the final predicted state populations. In the former case, convergence is defined as absolute variance from the final predicted branching ratio of a random subset of dissociated trajectories as a function of the number of trajectories selected. In the latter case, the convergence metric is the mean of the absolute variances of all state populations at $t = 1$ ps. In each case the random selection and variance calculation was repeated 1000 times and the results averaged.

the singlet states.

To measure convergence of each simulation, two measures were used; the branching ratio as a function of the number of dissociated trajectories, and the state populations at $t = 1$ ps as a function of all trajectories. For each metric, the absolute variance $V(N)$ (or the mean of all the $V(N)$ in the case of final state populations) was calculated for random subsets of trajectories for $N \in [1, N_{\text{traj}}]$, with,

$$V(N) = \sqrt{(B(N) - \langle B \rangle)^2} \tag{6.2}$$

where $\langle B \rangle$ and $B(N)$ are the final predicted branching ratio/state populations and the branching ratio/state populations of a subset consisting of N trajectories respectively. The variance calculation is repeated 1000 times for

Wall clock time (s)	**(8,6)/overlap**	**(8,6)/NACME**	**(10,8)/overlap**	**(10,8)/NACME**
Integrals	0.696	0.701	0.749	0.813
CASSCF	1.620	1.620	3.942	3.942
Gradients	2.689	2.476	14.037	11.905
Spin-orbit coupling	3.379	3.347	7.449	7.831
NACMEs	-	2.318	-	14.365
WF overlaps	1.017	-	1.152	-
Total *ab initio* time	28.970	51.791	126.470	276.625

TABLE 6.5: Example timing information illustrating the difference in computational expense for the different simulations. These are based on the reported per-time step compute times of four 100 fs trajectories with identical initial conditions and parameters as shown. The total *ab initio* time accounts for the fact that each substep requires multiple integral, gradient and NACME computations. In NACME simulations no separate CASSCF-only calculation is carried out, but this value can be approximated by the corresponding overlap simulation.

each N with the N trajectories chosen at random each time, and the result is averaged. This procedure generates the plots shown in Fig. 6.13. For the branching ratio, convergence is faster in simulation **A** with the variance halving from its initial value in only $\sim$10 trajectories. Convergence is much smoother in simulation **B**, decreasing rapidly in a similar number of trajectories as the first simulation. A similar trend is seen in terms of population convergence with simulation **A** converging in fewer trajectories than in simulation **B**. In this case both curves decrease very smoothly.

Example timing information between the two simulations is shown in Table 6.5. For simplicity, these are based on four representative trajectories[1]. with identical initial conditions, run with either the (8,6) or (10,8) active spaces and either the overlap or NACME coupling schemes. Whilst merely illustrative, these give approximate measures as to the growth in expense from method to method. Changing the coupling scheme from overlaps to NACMEs increases per-time step expense by 78% and 119% for the (8,6) and (10,8) active spaces respectively, while increasing the active space from (8,6) to (10,8) increases expense by 337% and 434% for overlap and NACME

[1]These were run on independent compute nodes at the ECDF HPC (64 GB RAM, Intel® Xeon® processor E5-2630 v3, 2.4 GHz).

simulations respectively. Accounting for the fact that multiple NACMEs and gradients were calculated at each step, it is those components which contribute the most to total compute time.

6.4 Conclusion

In this chapter, two different simulations of the photodissociation dynamics of the 1^1B_2 state of CS_2 have been compared. The simulations consist of ensembles of surface-hopping trajectories evolving on potential energy surfaces generated "*on-the-fly*" as implemented in SHARC [154, 159], with electronic structure calculations at the SA-CASSCF level in MOLPRO [215]. The key difference between the simulations lies in the choice of active space, (8,6) versus (10,8), and the impact this has on the dynamical outcomes has been examined. The simulations run using the smaller active space shows frustrated dissociation due to the excessively high potential barriers generated by the more limited active space, whose orbitals do not describe the bond-breaking regime of the potential energy landscape adequately. The larger active space, where the addition of only two extra orbitals (one occupied, one virtual) eliminates this deficiency. Further improvements could be made with an even larger active space and the inclusion of dynamic correlation as exemplified by the reference *ab initio* potential energy curves calculated at the MRCI(14,10)/aug-cc-pvTZ level. However, the computational cost would be too large if the goal was to include both nonadiabatic and spin-orbit coupling in the "*on-the-fly*" dynamics at this level.

An important observation is that examination of potential energy curves along key coordinates provides a reasonably reliable prediction of the nature and shortcomings of the dynamics in systems whose potential energy landscape contains distinct topological features such as dissociation barriers, especially if more accurate potential energy curves are available for reference. Therefore, it is often valuable to include such representative potential energy curves alongside published simulations, preferably accompanied by accurate reference calculations. The observed correlation between potential energy surfaces and dynamics is not surprising, but intriguingly, it

could be argued that lower-level *ab initio* calculations can still produce dynamics that yields qualitative insights into the photochemistry, especially if the shortcomings of the electronic structure calculations have been properly assessed and are considered during the analysis — but careful attention must be paid to the subtle effects which may be lost, for example in this case the switch in order between the rise of each dissociation channel. Of particular highlight are the spatio-temporal mapping of the nonadiabatic transitions, corresponding to internal conversion, as well as the singlet-triplet spin-orbit coupled transitions, corresponding to intersystem crossing, which emphasise the direct competition between IC and ISC. This picture is in contrast to that presented by the typical Jablonski diagram as discussed in Chapter 1, which represents conventional thinking by showing these processes as sequential. Observations of this kind are typically hard to disentangle from the abundant data produced by the simulations. It is worth emphasising that even in a structurally simple molecule such as CS_2, remarkable complexity lies hidden in the interplay between spin-orbit-coupled electronic states and nuclear motion, a topic on which there remains much work to be done in terms of trajectory-based dynamics simulation methods.

Here marks the end of the exploration of the photodynamics of CS_2. The discussion now moves on to a different class of molecule; trimethylamine, a tertiary aliphatic amine (TAA).

Chapter 7

Rydberg state photodynamics of trimethylamine

7.1 Introduction

In this chapter focus is on the role of Rydberg states in photochemistry and their interaction with valence states. Atomic Rydberg orbitals are extremely diffuse orbitals whose energies can be predicted by the Rydberg formula, which was originally derived [216] to describe the spectral lines of the hydrogen atom with the form,

$$\frac{1}{\lambda} = R_H \left(\frac{1}{n_1^2} - \frac{1}{n_2^2} \right) \tag{7.1}$$

where λ is the wavelength of light emitted in a vacuum, R_H is the Rydberg constant, and n_1 and n_2 are the principle quantum numbers of the occupied orbitals before and after excitation respectively. For fixed values of n_1 and n_2 running from $n_1 + 1$ to ∞, converging series are generated — for example the famous Lyman, Balmer, and Paschen series in hydrogen for $n_1 = 1$, 2, and 3. In molecules, sufficiently high principle quantum numbers give rise to states of Rydberg character which can be described by a similar formula,

$$E_{\text{ex}} = E_{\text{ion}} - \frac{\text{R}}{(n - \delta)^2} \tag{7.2}$$

where E_{ex} is the excitation energy, E_{ion} is the ionisation potential, R is the Rydberg constant in appropriate units, n is the principle quantum number

and δ is the quantum defect parameter which accounts for any penetration of the Rydberg electron to the atomic or molecular ionic core.

In molecules, Rydberg states are typically found only at sufficiently large principle quantum numbers such that the molecule resembles an ionic core, with the excited electron occupying a diffuse orbital with a high probability of being found far from the nuclei. These orbitals resemble hydrogenic orbitals in shape. The energy levels of these states follow Rydberg series converging on the respective ionisation limit. The diffusivity of Rydberg states sets them apart from valence states, which are spatially localised around the nuclei and generally lower in energy. The interaction between valence and Rydberg states is interesting from both an experimental and theoretical viewpoint [217, 218], affecting the spectroscopic and dynamical behaviour in such systems, whose electronic structure is typically extremely complicated to describe accurately [219]. While typically in the context of small organic open or closed-shell species, similar effects are also seen in larger molecules, for example Rydberg series in C_{60} [220] and its related superatomic molecular orbitals (SAMOs) [221–223].

Amine-like moieties are frequent in natural and biological applications such as amino acids and the DNA bases, where they display resistance to photodamage when excited by UV light [224]. Therefore, an understanding of how the excess energy is redistributed in these and related systems is crucial. A general class of these compounds, the tertiary aliphatic amines (TAAs), possess the general characteristic that their Rydberg states are low-lying in energy [225]. Indeed, there are typically no valence states below the Rydberg series; the lowest manifolds of singlet states are Rydberg in character, separated energetically from states of pure valence character at equilibrium geometry, with Rydberg-valence mixing occurring along particular reaction coordinates where σ^* character develops [218, 226–228]. These systems have been examined experimentally by time-resolved photoelectron spectroscopy (TR-PES) [229–240], time-resolved mass spectrometry (TR-MS) [241] and time-resolved X-ray diffraction (TR-XRD) [242, 243], in many cases

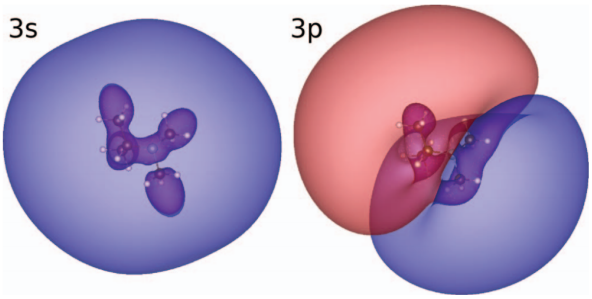

FIGURE 7.1: Visualisation of the 3*s* and 3*p* Rydberg states of *N*,*N*-dimethylisopropylamine (DMIPA) molecule, where the isosurfaces correspond to 0.0001 $Å^{-3/2}$. Taken from Ref. [246].

backed by extensive high-level *ab initio* calculations featuring characterisation of the relevant regions of phase space and reaction coordinates of interest to determine the change in character of the electronic states, using e.g. time-dependent density functional theory and equations-of-motion coupled cluster in combination with large triple zeta basis sets.

These studies generally conclude that the lifetime of the 3*s* excited state depends on the level of substitution at the nitrogen centre, with many-picosecond scale lifetimes in tertiary systems [229–231, 234, 237–239, 241, 243–245], generally decreasing with secondary and primary amines to as low as sub 1 ps [232–236, 239]. Such dynamics studies have recently been extended to biologically-related amide systems [240].

In the case of TAAs, excitations of approximately 6 eV are generally observed to occur from the lone pair of the nitrogen atom into the 3*p* manifold, followed by fast internal conversion to the 3*s* state. More generally, non-radiative relaxation has been suggested to be the principal relaxation pathway at excitation wavelengths above 200 nm (6.2 eV) [247–249]. In the case of *N*,*N*-dimethylisopropylamine [229], time constants of 701 fs and 87.9 ps were observed for depopulation of the 3*p* manifold and the 3*s* state respectively, while in *N*,*N*-dimethylphenethylamine, the population transfer from the 3*p* states to 3*s* occurs in 149 fs after 208 nm excitation, with exponential decay of the 3*s* state in 1.3 ps and 5.6 ps [241]. A further study of three TAAs (*N*-methylpyrrolidine, *N*,*N*-dimethylpropylamine and

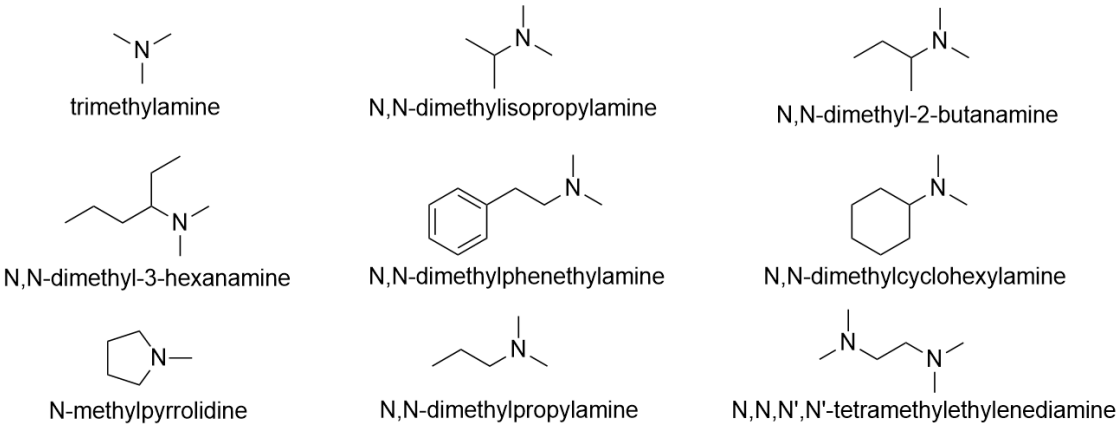

FIGURE 7.2: Schematic structures of a selection of TAAs which have been subject to recent experimental time-resolved dynamics studies [229, 230, 237, 238, 241, 243, 245, 250, 251]. Each of these systems feature low-lying Rydberg states which feature extensively in their ultrafast dynamics.

N,*N*-dimethylisopropylamine) after excitation at 200 nm backed by extensive theoretical calculations again showed ultrafast internal conversion between the 3*p* manifold and the 3*s* Rydberg state [237]. The effect of structural rigidity was studied in the bicyclic system 1-aza-bicyclo[2.2.2]octane (ABCO, or quinuclidine) after excitation at 201 nm, showing that despite the lack of freedom for the nitrogen atom to planarise, rapid 3*p*-3*s* conversion still occurs in less than one picosecond [238], while the lifetime of the 3*s* state is enhanced further to more than 10 ns. TR-PES has been used to uncover ultrafast internal conversion between other TAAs such as *N*,*N*-dimethyl-2-butanamine and *N*,*N*-dimethyl-3-hexanamine [250]. The ultrafast dynamics of Rydberg-excited *N*,*N*,*N*′,*N*′-tetramethylethylenediamine [251] have also been studied by Rydberg fingerprint spectroscopy [252] coupled with computational simulations. Internal conversion between the 3*p* and 3*s* states was again observed to be rapid.

In the case of TMA, ultrafast interconversion has previously been observed by resonance-enhanced multiphoton ionisation PES experiments between the $3p_z$ and $3p_{xy}$ states in 539 fs, with further relaxation from $3p_{xy}$ to the 3*s* state seen within 2.9 ps [230], and fast (640 fs) and slow (74 ps) methyl fragmentation pathways seen after 200 nm excitation [243]. Excitation at

209 nm in the same system was seen to elicit a decay with a 200 fs time constant to 3*s* [231], and a recent study examined the energy dependence of the photodissociation dynamics of the system [245] over the range 200-224 nm, observing no change in the product state distribution of methyl products over this range, suggested to be due to the different time scales of the 3*p* to 3*s* conversion and methyl dissociation.

Therefore, despite variation in precise time constants and lifetimes of the 3*p* and 3*s* excited states in different experiments, a common strand is clear; rapid conversion of population within the 3*p* manifold and to the 3*s* state. The rest of this chapter focuses on the ultrafast dynamics of trimethylamine, and the rapid dissociation mechanism described in [243]. This system offers a combination of early-time electron dynamics *via* the 3*p* to 3*s* interconversion and later time nuclear dynamics *via* the dissociation of a methyl fragment. UV excitation again takes place from the HOMO, corresponding to the lone pair on the nitrogen atom, and thus excitation from this orbital is suspected to promote planarisation of the molecule about the nitrogen.

7.2 Methodology

The approach for TMA was similar to the one followed for CS_2 in previous chapters; evaluation of the electronic structure of the molecule at equilibrium geometry, followed by calculation of potential energy cuts that give preliminary indications of the dynamics and the level of theory as appropriate for the subsequent simulations. Firstly, a number of levels of theory were considered in calculations of the static molecule — as will be shown, TMA proves a tricky case in getting the precise ordering of the 3*s* and 3*p* states correct.

Two sets of simulations were then considered. The first of these accounts for only the lowest 5 singlet states, i.e. the S_0 ground state and the 3*s* and $3p_{xyz}$ Rydberg states. These are compared to further simulations including the next singlet state, S_5, which is shown in potentials to interact in the Frank-Condon region (it is the highest state which does so) and is therefore included for completeness.

7.3 Results and discussion

7.3.1 Electronic structure

Table 7.1 details a series of geometry optimisations of TMA using a number of common electronic structure methods over a series of basis sets of increasing size. The methods included are HF, MP2, CCSD, CASSCF, and MRCI (the latter being single-point calculations at the geometry of the preceding CASSCF). The starting point of the multireference methods is a (2,5) active space consisting of the nitrogen lone pair HOMO and the 3*s* and $3p_{xyz}$ Rydberg orbitals as used in Ref. [238]. HF predicts the shortest R_{CN} bond length and most acute Θ_{CNC} irrespective of basis set due to neglect of electron correlation and exaggerated prediction of the nitrogen lone pair repulsion. CASSCF captures a little of the correlation energy, enough to significantly lengthen the N-C bond in each case relative to HF, but only a small amount relative to MRCI, the perturbative MP2, and coupled-cluster optimisations (the latter giving the greatest reduction in molecular energy with any basis set).

Table 7.2 reports excitation energies for the first five excited singlet states of TMA across a matrix of basis sets at the SA6-CAS(2,6), SA6-MRCI(2,6) and multistate (MS) CASPT2 levels alongside experimental results for excitation to the 3*s* and $3p_z$. In each case, the excitation energies are calculated using the corresponding optimised CASSCF ground state geometry. In the variant of MS-CASPT2 used here, all states are treated together with the same number of contracted reference states. A level shift of 0.3 a.u. is employed. In order to include the sixth (3*d*) state, the (2,5) active space is insufficient as it yields an energy for the 3*d* state that is several electronvolts too high. Instead, a slightly expanded (2,6) active is used which gives physically more reliable results. No higher singlet states were included because test calculations with a variety of active spaces demonstrated that no other singlet states fell near the experimental pump range.

Surprisingly, at the CASSCF level it is the smallest basis set (6-31+G*) which best matches the experimental results, although still underestimates

Method	*E (a.u)*	*E-E_{SCF} (a.u.)*	*R_{NC} (Å)*	*Θ_{CNC} (degrees)*
		STO-3G		
HF	-171.1919224	0	1.485	110.284
MP2	-171.4001714	-0.20824903	1.515	107.799
CCSD	-171.4709184	-0.27899601	1.527	107.284
CASSCF	-171.2101724	-0.01825003	1.488	109.292
MRCI	-171.4399571	-0.24803476	-	-
		3-21G		
HF	-172.3102696	0	1.464	113.037
MP2	-172.6937726	-0.38350302	1.489	110.804
CCSD	-172.7426699	-0.43240027	1.491	110.908
CASSCF	-172.3225301	-0.01226043	1.465	112.726
MRCI	-172.6905348	-0.38026513	-	-
		6-31G		
HF	-173.1897009	0	1.452	114.228
MP2	-173.5767408	-0.38703994	1.479	112.387
CCSD	-173.6265819	-0.43688102	1.480	112.463
CASSCF	-173.2028598	-0.01315889	1.453	113.889
MRCI	-173.5714301	-0.38172916	-	-
		6-31+G*		
HF	-173.272094	0	1.446	111.894
MP2	-173.8331883	-0.56109431	1.457	110.793
CCSD	-173.8841067	-0.61201272	1.459	110.943
CASSCF	-173.2954346	-0.02334061	1.448	111.596
MRCI	-173.8022377	-0.53014375	-	-
		6-311+G*		
HF	-173.3061128	0	1.444	111.953
MP2	-173.9019108	-0.59579793	1.454	110.631
CCSD	-173.9516405	-0.64552762	1.457	110.853
CASSCF	-173.3303375	-0.02422467	1.447	111.632
MRCI	-173.8630497	-0.55693684	-	-
		aug-cc-pvDZ		
HF	-173.2909488	0	1.448	111.740
MP2	-173.9317497	-0.64080094	1.462	109.841
CCSD	-173.9864682	-0.6955194	1.464	110.146
CASSCF	-173.3151359	-0.02418709	1.450	111.444
MRCI	-173.8843116	-0.59336286	-	-
		aug-cc-pvTZ		
HF	-173.3360395	0	1.443	112.010
MP2	-174.1010207	-0.76498122	1.452	109.953
CCSD	-	-	-	-
CASSCF	-173.3629813	-0.02694182	1.447	111.589
MRCI	-174.0254966	-0.68945716		

TABLE 7.1: Energies and selected optimised geometric parameters of TMA calculated using the HF, MP2, CCSD, CASSCF and MRCI electronic structure methods with seven basis sets in the range STO-3G to aug-cc-pvTZ, where $E - E_{SCF}$ is the difference from the Hartree-Fock energy, R_{NC} is the N-C bond length and θ_{CNC} is the C-N-C bond angle. Multireference methods make use of a (2,5) active space. The MRCI calculations are done at the respective optimised CASSCF geometry.

	CASSCF				
	6-31+G*	6-311+G*	aug-cc-pvDZ	d-aug-cc-pvDZ	Experimental [230]
$3s$	4.011	3.778	3.217	3.161	5.460
$3p_z$	4.487	4.339	3.823	3.584	6.229
$3p_{xy}$	4.634	4.463	3.774	3.654	
$3d$	5.360	5.267	4.459	4.251	
	MRCI				
	6-31+G*	6-311+G*	aug-cc-pvDZ	d-aug-cc-pvDZ	
$3s$	5.203	5.027	4.701	-	5.460
$3p_z$	5.826	5.726	5.421	-	6.229
$3p_{xy}$	5.951	5.823	5.380	-	
$3d$	6.603	6.534	6.070	-	
	MS-CASPT2				
	6-31+G*	6-311+G*	aug-cc-pvDZ	d-aug-cc-pvDZ	
$3s$	6.426	6.378	6.063	5.642	5.460
$3p_z$	7.154	7.178	6.847	6.277	6.229
$3p_{xy}$	7.284	7.275	6.824	6.329	
$3d$	7.866	7.905	7.516	6.891	

TABLE 7.2: Excitation energies to each excited state at the predicted CASSCF ground state minimum energy geometries for each basis set, compared with experimental values for excitation to the $3s$ and $3p_z$ state.

them by about 1.4 eV for the $3s$ and 1.2 eV for the $3p_z$. The poorest performing are the Dunning basis sets; aug-cc-pvDZ orders the $3p_z$ and $3p_{xy}$ states incorrectly, as well as underestimating the excitation energies by over 2 eV. The addition of extra diffuse functions in the d-aug-cc-pvDZ restores the correct ordering but further underestimates the excitation energies.

The MRCI and MS-CASPT2 methods significantly alter the picture. The results with MRCI and both Pople basis sets keep the same state ordering and bring the excitations much more into line with the experimental values, although curiously double-zeta 6-31+G* still outperforms the triple-zeta 6-311+G*. With aug-cc-pvDZ there is also significant improvement, with increases of more than 1.4 eV to the excitation energies predicted at the CASSCF level. The excitation energies are still underestimated overall but the additional dynamic correlation clearly does a great deal to reduce the difference with experiment.

	CASSCF			
	6-31+G*	6-311+G*	aug-cc-pvDZ	d-aug-cc-pvDZ
$3p_z - 3s$	0.476	0.561	0.606	0.423
$3p_{xy} - 3p_{xy}$	0.147	0.124	-0.049	0.07
$3d - 3p_{xy}$	0.726	0.804	0.685	0.597
	MRCI			
	6-31+G*	6-311+G*	aug-cc-pvDZ	d-aug-cc-pvDZ
$3p_z - 3s$	0.623	0.699	0.720	-
$3p_{xy} - 3p_{xy}$	0.125	0.097	-0.041	-
$3d - 3p_{xy}$	0.652	0.711	0.690	-
	MS-CASPT2			
	6-31+G*	6-311+G*	aug-cc-pvDZ	d-aug-cc-pvDZ
$3p_z - 3s$	0.728	0.800	0.784	0.635
$3p_{xy} - 3p_{xy}$	0.130	0.097	-0.023	0.052
$3d - 3p_{xy}$	0.582	0.630	0.692	0.562

TABLE 7.3: Separations between the excitation energies reported in Table 7.2. Clearly there is a significant difference in the absolute excitation energies calculated by multireference approaches, but more crucial for dynamics is the relative separation of the excited states which remains similar between the levels of theory.

Conversely, with MS-CASPT2 the excitation energies are overestimated by approximately 1 eV in both Pople basis sets. Here, it is the Dunning basis sets which perform better — aug-cc-pvDZ is brought to within 0.6 eV of the experimental energies, and the best result of all the methods shown here is seen with the d-aug-cc-pvDZ. Here, the 3*s* excitation is overestimated by only 0.2 eV while the $3p_z$ result is correct to a tenth of an electronvolt.

Clearly, dynamic correlation is significant in the prediction of absolute excitation energies, which could be further improved by the addition of specialised Rydberg functions (for example based on Kaufmann exponents [253]). But the MRCI and MS-CASPT2 methods here are generally too expensive for "*on-the-fly*" dynamics. More important in benchmarking for the most useful method is the relative separation between the excited states, where most of the interesting dynamics takes place. Table 7.3 shows this separation of the levels of theory considered. These remain broadly similar between all these levels of theory. The CASSCF methods underestimate the

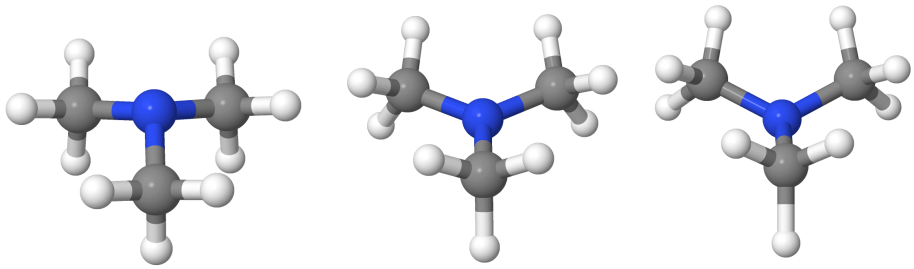

FIGURE 7.3: A ball and stick representation of the umbrella normal mode of TMA. From left to right, structures represent the ground state equilibrium structure, the planar geometry about the nitrogen atom, and the outer turning point of the mode.

$3s \rightarrow 3p_z$ gap by between 0.16 eV to 0.34 eV compared to the experimental value of 0.796 eV. For MRCI, this range is between 0.07 eV to 0.15 eV, and for MS-CASPT2 is between 0.15 eV to 0.13 eV. While the multireference methods are clearly superior in this regard, as expected, the performance of CASSCF is not far behind. To further establish the merits of each method, the differences in the levels of theory are now further examined by the calculation of potentials along the relevant vibrational and radial coordinates for the CASSCF and MS-CASPT2 methods.

7.3.2 Potential energy curves

The first set of potentials examined are the those along the vibrational mode corresponding to pyramidalisation, the motion of which is shown schematically in Fig. 7.3. As well as aiding the benchmarking levels of theory, this serves as an illustration of the approximate expected early-time dynamics. A number of basis sets have been tested at the state-averaged CASSCF level. These potentials are shown in Fig. 7.4.

To give a unique coordinate path against which each method could be compared, the ground state CAS(2,5)/6-31+G* geometry and frequencies

were used to create a series of displacements along the appropriate vibrational mode (specifically, the fourth mode at $\nu = 398\,\mathrm{cm}^{-1}$) in both the forward and reverse direction. Initially, five states (S_0, $3s$, $3p_{xyz}$) were included in the state averaging and subsequent MS-CASPT2 corrections using the (2,5) active space as in section 7.3.1. However, it was later decided to include the next highest singlet state ($3d$), to study its interaction with the lower lying states. The basis sets tested were the 6-31+G* and 6-311+G* double-zeta and triple-zeta Pople basis sets respectively, as well as the Dunning aug-cc-pvDZ and d-aug-cc-pvDZ basis sets. Here the states are labelled S_0 to S_5 rather than symmetry labels. This is because the symmetry labels are only applicable at certain geometries; the character of each of these states varies along the given reaction coordinate and such labelling becomes misleading.

Because these potentials are generated from a vibrational mode where all the atoms move to some degree, the motion cannot be fully defined by a single internal coordinate. Instead the motion is captured by defining a pyramidalisation angle Θ_{pyram}; that is, 90° minus the angle between an N-C bond and the plane formed by the three carbon atoms. In a perfectly symmetric system, the magnitude of Θ_{pyram} is independent of the choice of N-C bond. This is not quite the case here where numerical noise leads to slight misalignments of equivalent atoms relative to each other. Thus the average of all possible Θ_{pyram} at each geometry is considered (however, in this case the individual values vary only in the second decimal place of a degree).

One striking feature of these potentials is the unintuitive lack of symmetry at $\Theta_{\mathrm{pyram}} = 0°$. The reason for this becomes clear looking at the stereochemistry of the structures generated by this method of repeated normal mode displacements from the equilibrium structure, shown in Fig 7.3. At the outer turning point, the two "upper" hydrogen atoms of each methyl group repel each other sterically; this is in contradiction to the inner turning point, where only the single "lower" hydrogen atoms on methyl will come close in phase space. This is why the potentials are asymmetric about the planar geometry in Fig. 7.4.

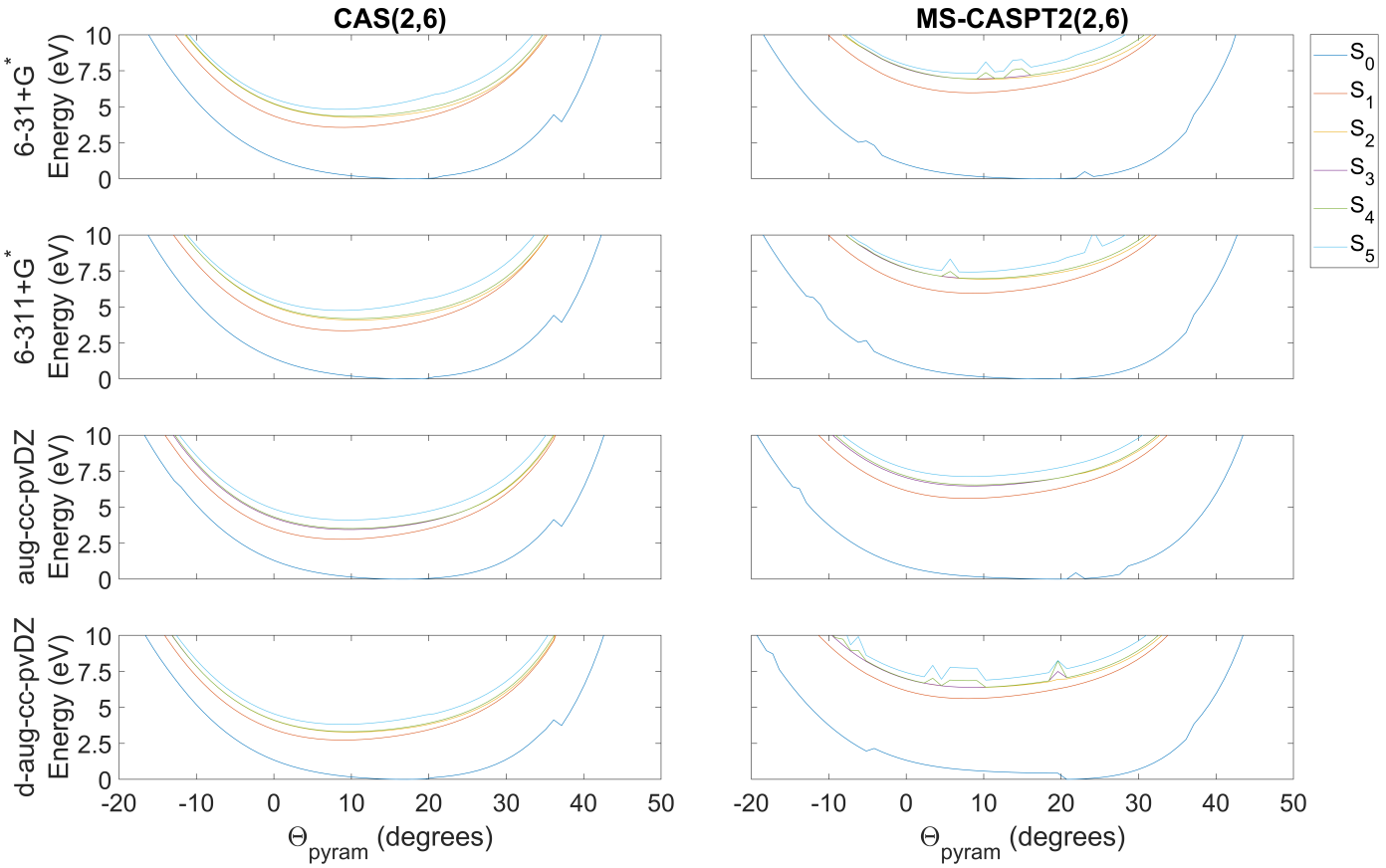

FIGURE 7.4: Normal mode PECs of TMA, calculated at the SA6-CASSCF(2,6) (left column) and MS-CASPT2 (right column) levels with the 6-31+G*, 6-311+G*, aug-cc-pvDZ and d-aug-cc-pvDZ basis sets in order from the top row to the bottom row. These cuts represent geometries along the $\nu = 398\,\mathrm{cm}^{-1}$ umbrella mode, defined by the average pyramidalisation angle between the nitrogen atom and the plane formed by the three carbon atoms (see discussion in text).

The structure here, on each carbon atom, shows two hydrogen atoms pointed upwards while only one pointed downwards. Thus the motion towards the outer turning points of the mode is necessarily asymmetric. However, one should note that the methyl groups can easily rotate around the N-C bond during the dynamics.

At the CASSCF level, the potentials give broadly similar topologies in the resultant curves, which for the most part behave smoothly save for slight discontinuities in all basis sets at approximately $\Theta_{\text{pyram}} = 37°$. There is no obvious error in the *ab initio* calculations at this geometry, with the calculations converging smoothly. However, the fact the discontinuity is present with all basis sets implies a discrepancy in the active space, mostly likely the active space changing due to the geometry (unlike in the SHARC simulations, orbitals are not carried forward from the previous time step to be used as input for the subsequent CASSCF). This fault is minor and only affects the ground state at a region far energetically from other states. The CASPT2 corrections eliminate this fault, but at the cost of inducing others; generally seen however at isolated points rather than as a permanent shift past a certain pyramidalisation angle, except for in the d-aug-cc-pvDZ curves. This aside, the dynamic correlation clearly has a notable effect on the absolute separation of the excited states from the ground state, bringing the curves significantly closer to experimental results. That said, the relative separation between each of the excited states, crucial for the dynamics, remains broadly similar in going from CASSCF to CASPT2.

Over timescales on the order of picoseconds, it is known that a methyl fragment may dissociate along a repulsive σ^* state leaving behind a dimethyl radical in each case [243]. To examine the prospect of this occurring on the short timescales covered by the simulations, potentials were calculated along this coordinate. Taking the CAS(2,5)/6-31+G* equilibrium geometry as a starting point, one of the N-C bond lengths was varied while all other coordinates were kept frozen. Again, six singlet states were included, and the calculations were carried out with the same variety of basis sets as in the normal mode potentials above as well as at the MS-CASPT2 level for each. These potentials are shown in Fig. 7.5. The most obvious feature of

the curves is analogous to the previous vibrational curves — the absolute separation of the ground and excited states clearly depends greatly on dynamic correlation. Also, the MS-CASPT2 curves again feature a number of sporadic discontinuities which may be related to the multistate nature of the MS-CASPT2 corrections, although these are almost absent in the 6-31+G* and d-aug-pv-ccDZ curves. Over short ranges (approximately 1-1.75 Å) the relative separations of the excited states remains similar as has been seen before. In these curves the dissociative σ state is seen as a progression of conical intersections of the $3p$ manifold with the $3s$ state, then the $3s$ state with the ground state. Dependent on the level of theory, the positions of latter conical intersection shifts, generally to greater N-C distances and most prominently in the d-aug-cc-pvDZ curves. The $3p$ to $3s$ conical intersection is generally seen not to shift significantly.

Finally, calculated oscillator strengths at the SA6-CAS(2,6)/6-31+G* and MS-CASPT2(2,6)/d-aug-cc-pvDZ levels for the respective equilibrium geometries are shown in Table 7.4. These values show the same trends for each method in that the dominant transitions are to the $3p_z$ states, in each case an order of magnitude larger than those to the $3p_{xy}$ states (which are approximately equal in value).

Analysis of the performance of each basis set at the CASSCF level of theory compared with multireference counterparts in the calculation of excitation energies, and vibrational and radial potential energy curves resulted in the choice of the CAS(2,6)/6-31+G* as the level at which to run dynamics simulations. This basis set counter-intuitively outperformed its triple-zeta analogue and the Dunning basis sets at the CASSCF level, and is also the least expensive of the basis sets trialled. The relative separations between the excited states remain similar between the CASSCF and MS-CASPT2 methods, and although ideally dynamics would be simulated using a method accounting for dynamical correlation, this level should still return qualitatively accurate simulated early time dynamics for the photoexcitation of TMA.

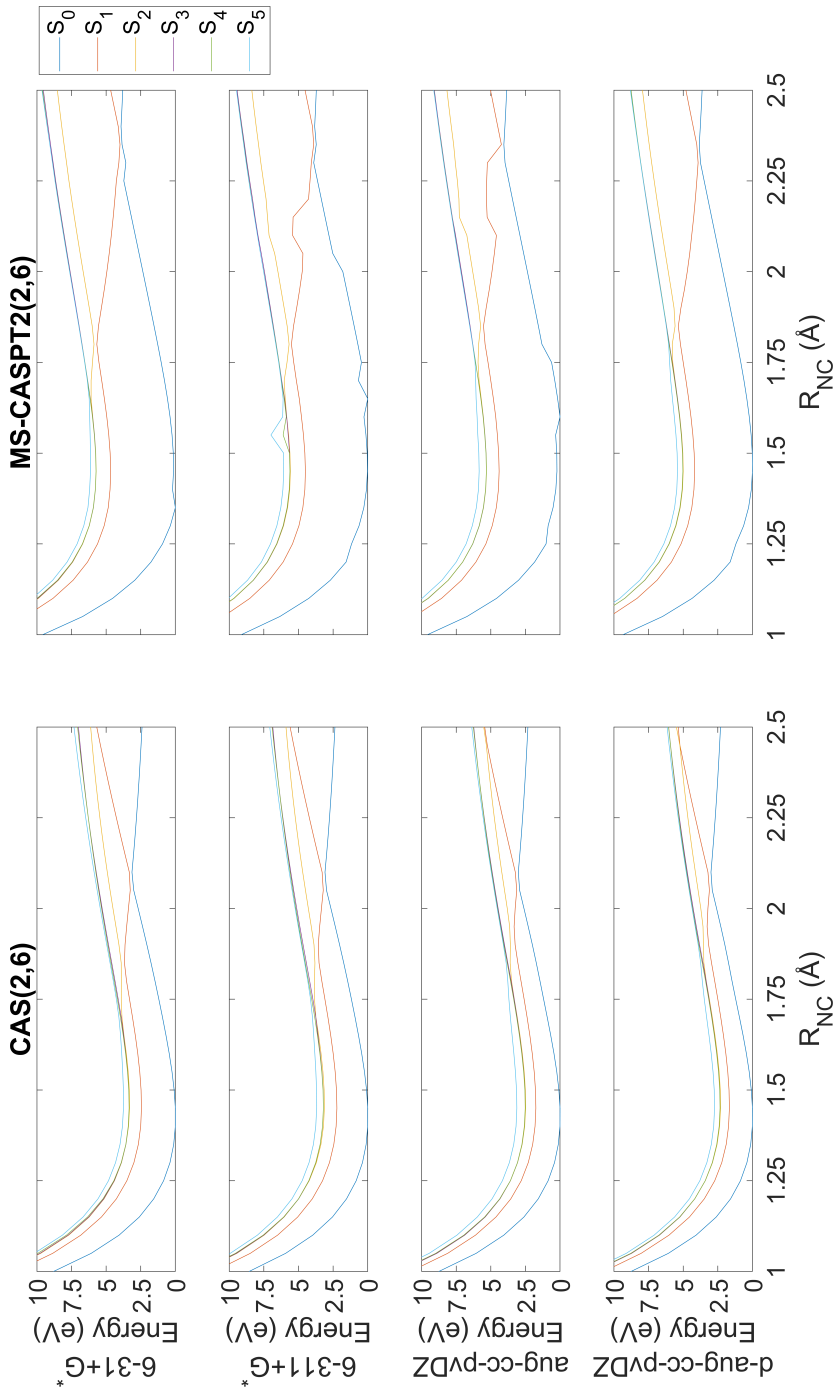

FIGURE 7.5: Radial PECs of TMA, calculated at the SA6-CASSCF(2,6) (left column) and MS-CASPT2 (right column) levels with the 6-31+G*, 6-311+G*, aug-cc-pvDZ and d-aug-cc-pvDZ basis sets in order from the top row to the bottom row. These cuts represent geometries along the R_{NC} stretching coordinate.

	CASSCF	MS-CASPT2
$3p_z$	0.142	0.0302
$3p_x$	0.019	0.0014
$3p_y$	0.019	0.0014

TABLE 7.4: Calculated oscillator strengths to members of the $3p$ Rydberg manifold of states at the SA6-CAS(2,6)/6-31+G* and MS-CASPT2(2,6)/d-aug-cc-pvDZ levels of theory. The dominant transitions in each case are to the $3p_z$ state.

7.3.3 Surface Hopping dynamics

Two sets of simulations have been performed covering the first 2500 fs of the dynamics with a time step of 0.1 fs. The first of these simulations includes the lowest five singlet states (the ground, $3s$, and $3p$ manifold). A second set of simulations was run to assess the impact of the $3d$ state on the dynamics and whether this would increase the likelihood of early time dissociation.

7.3.3.1 Initial condition selection

A collection of starting geometries (100 in the five-state simulations, 200 in the six-state simulations) was taken from the Wigner distribution of the ground state vibrational frequencies calculated at the CAS(2,5)/6-31+G* level of theory. Energy was distributed randomly (weighted by mass), such that each molecule had 0.5 eV of kinetic energy ascribed to it, approximately matching the experimental conditions of a 200 nm (6.20 eV) pump pulse. From each starting geometry, oscillator strengths and excitation energies were calculated for each of the included exited states. The same stochastic procedure as used in Chapters 3, 4 and 5 is used to generate trajectories beginning on each of the excited states. For the purposes of the simulations, trajectories beginning on either the $3s$ state or the sixth state (tentatively labelled $3d$) were filtered out — those states are unlikely to be populated by the experimental pump pulse due to its narrow bandwidth (less than 1.8 nm or $\sim$0.05 eV at full-width half-maximum). This gave a total of 178 five state trajectories and 306 six state trajectories. The populations of each state at

	Five state	Six state
S_0	0	0
$3s$	0	0
$3p_1$	0.52	0.65
$3p_2$	0.22	0.22
$3p_3$	0.24	0.14
$3d$	n/a	0

TABLE 7.5: Initial populations of the electronic singlet states of TMA in the five state and six-state simulations. The majority of population begins in the $3p_1$ state, with the rest split more evenly between the remaining two P Rydbergs.

time zero are shown in Table 7.5, with over half of the population beginning in the $3p_1$ state (implying correspondence with the $3p_z$ state at these geometries).

7.3.3.2 Populations

Populations for each of the electronic states included in the simulations as a function of time are shown in Fig. 7.6. In both cases, more than half of the population initially begins in the $3p_1$ state, but over the first few tens of femtoseconds there is a shift into the two other components of the the $3p$ manifold. This drop is much greater in the six-state simulation, with the $3p_1$ population dropping by over 20% compared to approximately 10% in the five-state simulation. This difference is accounted for by the faster initial rise of population in the $3s$ and additional transfer into the $3d$ state. After this initial motion, they $3p$ manifold of states begin a rapid oscillation between each other. One may attribute this simply to noise, but the effect is not significantly lessened by the inclusion of many more trajectories in the six-state simulation. Over the 2500 fs, in both cases the population of the $3p$ manifold as a whole gradually decreases, an effect which is more noticeable in the six-state simulation.

In the five-state simulation, the $3s$ state benefits only very slightly from the early population exchange, before remaining steady for about 500 fs before a gradual rise to a plateau at approximately 10% of the population from 700 fs onwards. While this is going on, very little population makes its way

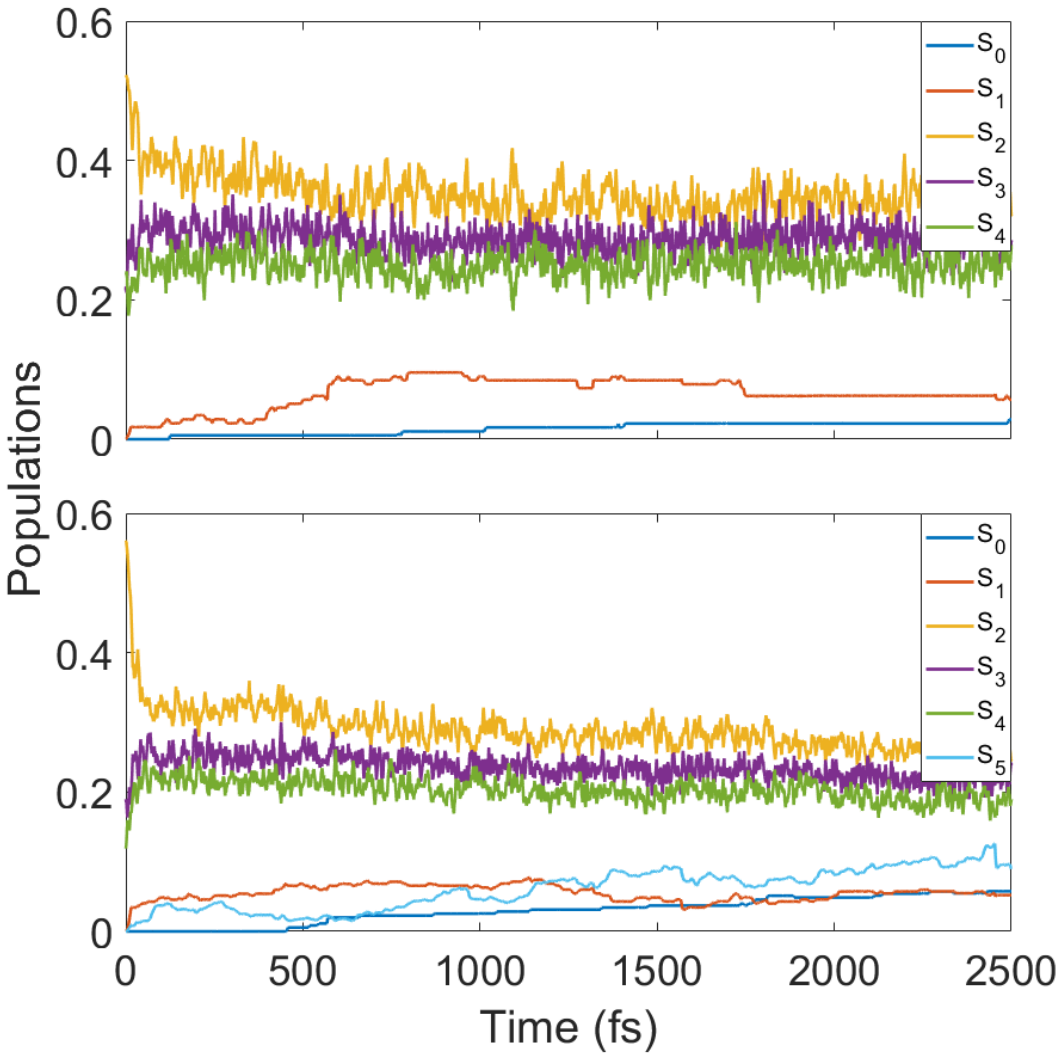

FIGURE 7.6: Populations as a function of time for each electronic state in the TMA five-state simulation (top) and six-state simulation (bottom). The five-state simulation was carried out at the SA5-CAS(2,5)/6-31+G* level, and the six-state simulation at the SA6-CAS(2,6)/6-31+G* level.

back into the ground state. In the six-state simulation, the 3*s* state follows similar behaviour initially in that it has a rapid rise, but it sticks to the initial plateau it reaches for a much greater time — there is no secondary rise around 700 fs. The ground state does not gain population until much later (500 fs), but does so to a greater extent than in the five-state simulation.

The 3*d* state is significantly involved, sequentially gaining and losing population from very early times with an overall gradual rise as the dynamics progresses, such that by the end of the simulation it holds the greatest population outside of any state outside the 3*p* manifold. In this sense, it competes with the 3*s* state for population transfer from the $3p_{xyz}$ manifold and acts as a kind of population reservoir.

7.3.3.3 Nuclear motion

Fig. 7.7 represents the progression of nuclear motion in both sets of simulations by three geometric coordinates. These are the average of all N-C bond lengths (i.e. three per molecule), the average of those which remain bound for the duration of the simulations, and the average of all possible pyramidalisation angles, defined in the same way as for the vibrational potential energy curves presented earlier.

Overall, both simulations appear to give extremely similar behaviour; there are clear coherent oscillations in all of these modes, suggesting excitation of the symmetric N-C stretch and umbrella modes. These oscillations occur with approximately the same frequency and cover the same range of magnitude. Over the timescale of about 500 fs these oscillations decohere, settling around equilibrium values of approximately 1.47 Å for the bound N-C bond length and 0° for the pyramidalisation angle, expected by the fact that an electron has been removed from the nitrogen lone pair, reducing the lone pair repulsion. Dissociation (simply defined as an $R_{\mathrm{NC}} > 2 \times 1.448$Å , i.e. greater than twice the calculated equilibrium R_{NC} at the CAS(2,6)/6-31+G* level of theory) is slightly faster in its onset in the six-state simulation, but not by a great margin, and the contribution of the N-C bond lengths of dissociating trajectories to the overall average gives the same profile in each case. This begs the question as to what effect, if any, the addition of the 3*d* state has on the evolution of the nuclear motion.

This is tentatively answered by examining the absolute dissociation fractions in each case. In the five-state simulation, methyl groups dissociated in two trajectories out of the ensemble of 178, leaving a dimethylamine radical. Poor statistics notwithstanding, this gives a dissociation fraction of only

1.12% over the course of the simulation. In the six-state simulation, this almost doubles to 1.96% (six trajectories out of an ensemble of 306). While lower than experimental estimates for early-time dissociation ($\sim$10 %), this nonetheless emphasises that methyl dissociation is a relatively rare process over the first two picoseconds of the dynamics, and the addition of the sixth state does play a noticeable role in facilitating the dissociation that does occur. Even more notably, if one includes trajectories which begin on the $3d$ state as part of the overall ensemble, the dissociation rate rises significantly to 4.32% (15 trajectories in an ensemble of 347). The inclusion of the $3d$ state is therefore shown to influence the dissociation pathway, which intuitively seems likely to occur along the σ^* pathway shown in Fig. 7.5 by the conical intersections with states in the $3p$ Rydberg manifold leading to a progression down the diabatic state to dissociation.

In Fig. 7.8, snapshots of trajectory probability densities associated with the average pyramidalisation angle Θ_{pyram} and R_{NC} are shown at a series of time points (0, 50, 100 and 500 fs) for each simulation, representing the progression of the dynamics. Here, the densities represent the probability of finding a trajectory with a particular Θ_{pyram} and R_{NC}. For each trajectory, this is calculated as,

$$P(x,y) = \left(N_{\text{traj}}\right)^{-1} \sum_{i=1}^{N_{\text{traj}}} \left(\frac{\gamma}{\pi}\right) \exp\left(-\gamma \left[(x,y) - \vec{q}_j\right]^2\right), \tag{7.3}$$

where $\vec{q}_j$ are the Θ_{pyram} and R_{NC} of trajectory j, γ is a Gaussian width parameter equal to $1/(2\sigma^2)$ where $\sigma = 0.05$, and N_{traj} is the number of trajectories in the ensemble. The probability density $P(x,y)$ corresponds to a convolution of the classical coordinates of each trajectory on this grid with a normalised Gaussian function. This provides a simple way of visualising the dispersion of the nuclear motion as the dynamics unfolds, while separating out electronic effects.

At the commencement of the simulations, the wavepacket is localised nicely around the equilibrium geometry, corresponding to the instantaneous projection of the ground state ensemble onto the excited states and taking into account the spread of the Wigner distribution of initial positions for the

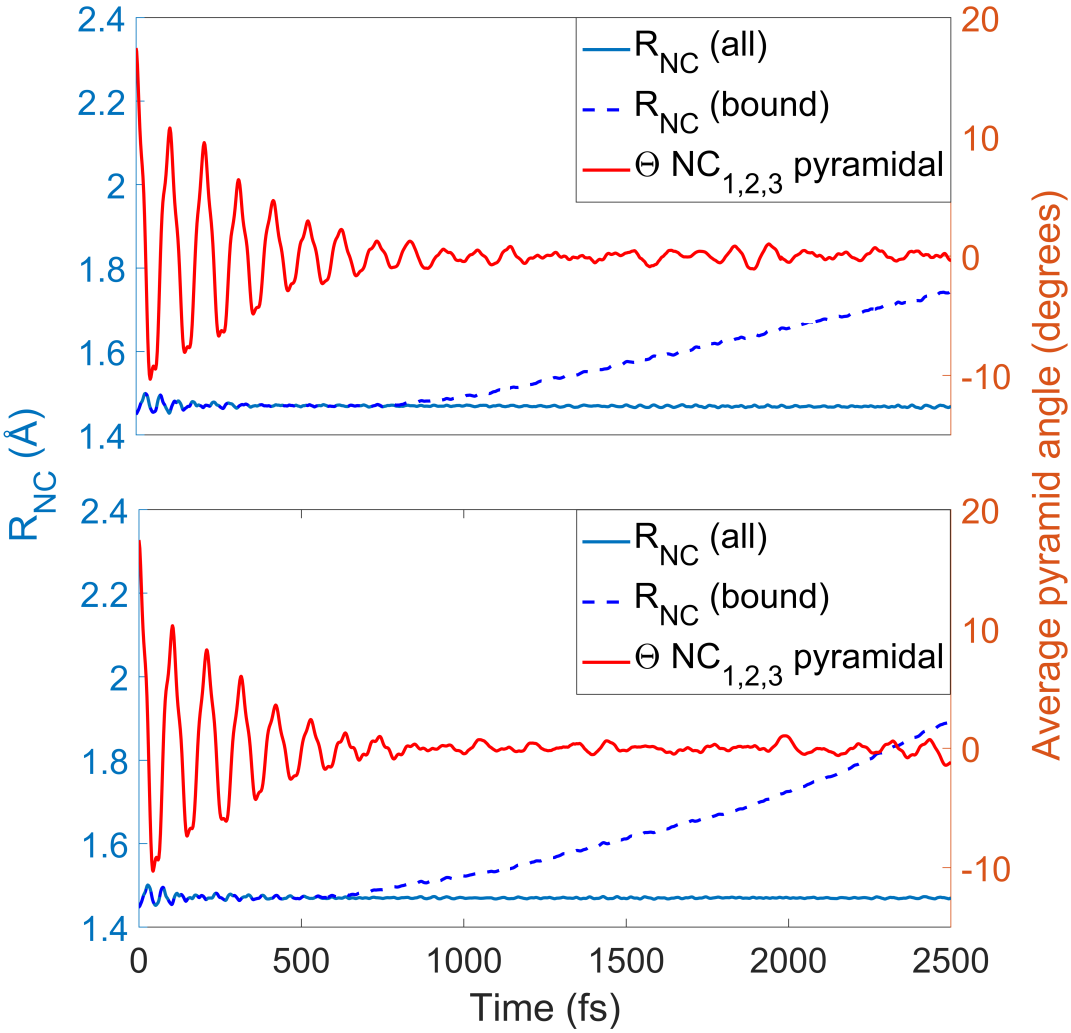

FIGURE 7.7: A comparison of key internal geometrical parameters as a function of time in the five-state simulations (upper) and six-state simulations (lower). R_{NC} is a simple average of all three N-C bond lengths over all trajectories, including the limited number which dissociate in the timescale covered here. R_{NC} (bound) excludes dissociating bonds from this average. Lastly, shown in red is the average of all possible Θ_{pyram} permutations.

trajectory ensemble.

The 50 fs frame shows the wavepacket approaching the outer turning point of the umbrella mode with the spread of R_{NC} remaining narrow. By

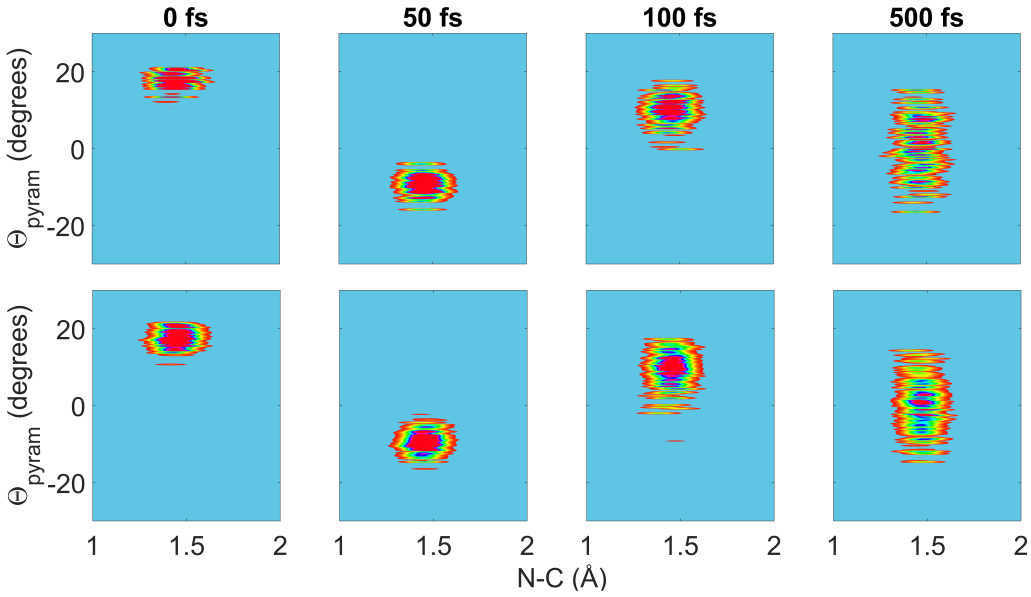

FIGURE 7.8: Probability density snapshots at selected time points in each TMA simulation. These are generated as a function of the average pyramidalisation angle Θ_{pyram} and R_{NC} in each simulation, with the density representing the probability of finding a trajectory with a particular Θ_{pyram} and R_{NC}. Top row: five-state simulation, bottom row: six-state simulation.

the return of the wavepacket to the point of origin by 100 fs, some delocalisation has begun to take place across a range of Θ_{pyram} from approximately 0° to 21°. By 500 fs, this spread is across the whole range of accessed Θ_{pyram}, and the effect of the excitation of the electron from the lone pair of the nitrogen atom is made clear; the electron, now localised largely to extremely specially diffuse Rydberg orbitals, activates the umbrella mode as the system seeks to reduce its energy by adopting geometries closer to planar about the nitrogen. This behaviour occurs almost identically in both simulations.

The behaviour of the dimethylamine (DMA) fragments after dissociation is shown in Fig. 7.9. In the plot, the average R_{NC} distance and average Θ_{CNC} is plotted as a function of time for the dimethyl fragments. For each individual trajectory, no bond distances or angles before the point of dissociation are taken into account. During the last 500 fs of the dynamics, the R_{NC} values oscillate in a narrow range of 1.43 to 1.51 Å, while in the same

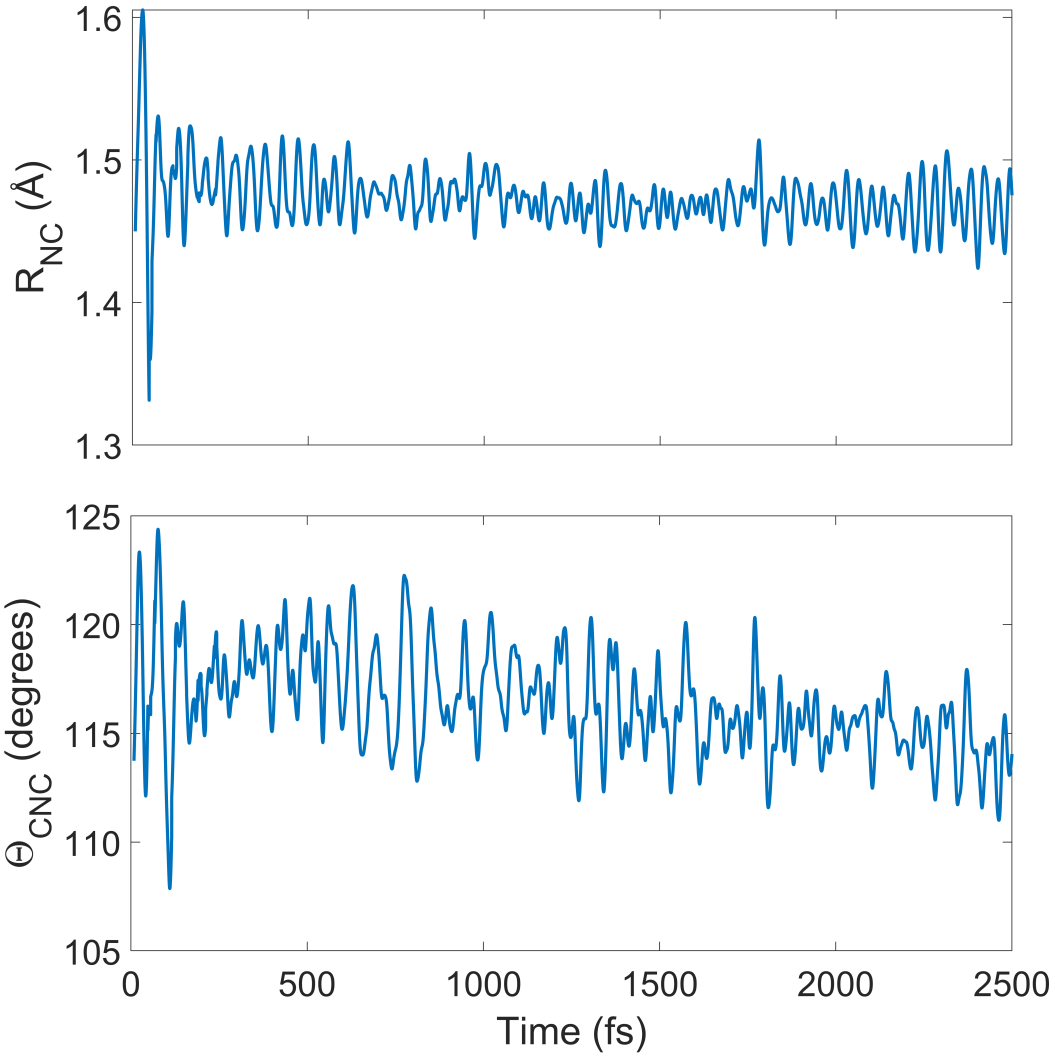

FIGURE 7.9: Average R_{NC} and Θ_{CNC} of dimethyl fragments after dissociation events in the six-state simulations as a function of time. No bond distances or angles from trajectories before the onset of dissociation are included in the averaging.

time the Θ_{CNC} values fluctuate between 110° to 118°. This is in excellent agreement with the experimental values presented in Ref. [243] of 1.45 ± 0.02 Å and 118° ± 4°.

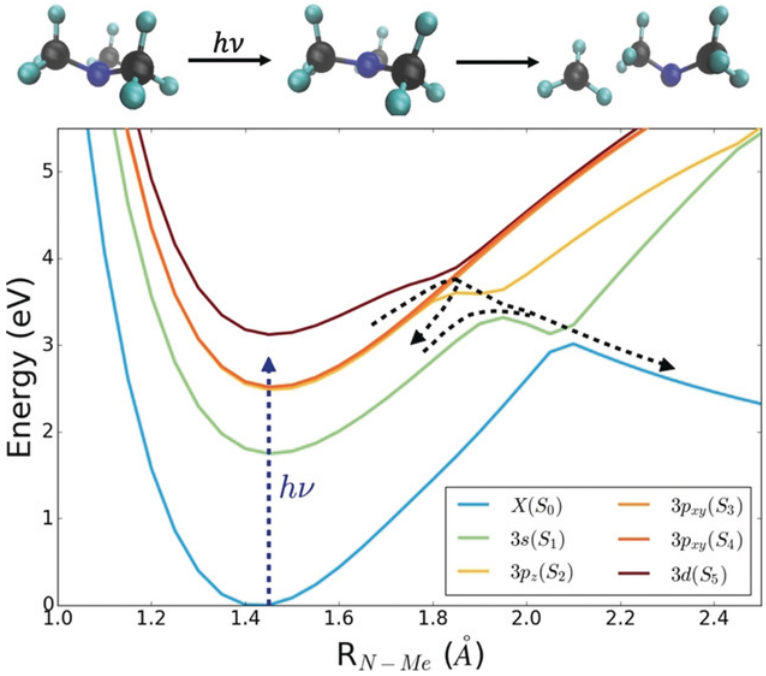

FIGURE 7.10: Radial curves calculated at the SA6-CAS(2,6)/6-31+G* level, beginning from the minimum 3*s* state geometry (approximately planar about the nitrogen atom). The black dashed arrows refer to potential dissociation pathways; either straight down the diabatic state (the so-called ladder mechanism) or trapping in potential wells prior to eventual dissociation. Taken from Ref. [243]

7.3.3.4 Dissociation mechanism

The precise mechanism by which dissociation occurs warrants further investigation. In an intuitive picture of a "ladder" mechanism, once a trajectory has reached the 3*d* state (the top of the ladder), one would expect a smooth progression of a trajectory down the electronic states through each conical intersection out to dissociation. This would be reflected by a downward stepwise motion of the population curve for the trajectory from the 3*d* state down to the ground state. Alternatively, branching may occur at each conical intersection, leading to temporary trapping of population in one or more potential wells before dissociation eventually occurs. These two possible mechanisms are shown by black dashed arrows in Fig. 7.10. In order to

see which mechanism is more prevalent, Fig. 7.11 shows the classically occupied electronic states as a function of time for the six dissociating trajectories which did not begin in the 3*d* state. Alongside this, the kinetic energy of the trajectory is shown, with the time of dissociation and the mean total energy printed in the right hand side of each panel. The rapid ladder mechanism occurs in two of the six trajectories shown in the figure (top row, right hand side and bottom row, right hand side). In the other cases, the 3*d* state is either not reached at all during the progression of the trajectory, or a surface hop out of that state occurred some time before the onset of dissociation. Thus while the ladder mechanism is seen to occur, it is not the only dissociation mechanism — the other cases see the trajectory caught oscillating in the 3*p* or 3*s* Rydberg states before eventually overcoming the barrier. However, even in cases where the ladder mechanism appears to be active, the energy change is not continuous during the dissociation process. Every case sees a sharp spike in the kinetic energy at the time the ground state is reached and immediately afterwards. In other words, whatever mechanism precedes the arrival of the trajectory in the ground state, the energy gap between this and the preceding 3*s* state is significant at the time of dissociation. Clearly, the dissociation channel does not facilitate these states coming close together in energy (despite what is intuited from the potentials in Fig. 7.5), which may explain why dissociation is a relatively rare event over these timescales in this system. This effect is emphasised when one recalls that at the CASSCF level, the excited states are inherently predicted to lie closer in energy to the ground state; therefore if dynamics were run at a post-CASSCF level, one might expect to see an even greater jump in energy between the 3*s* and ground states.

In Fig. 7.12, the discussion is expanded to those dissociating trajectories which did originate in the 3*d* state. As noted before, trajectories beginning in the 3*d* are more likely to dissociate (leading to a total dissociation rate of 15 in 347 trajectories, or 9 in 41 of the 3*d*-originating ensemble). Clearly, beginning in the 3*d* state greatly improves the chances of dissociation occurring over this timescale. However, this does not lead to a consistent manifestation of the ladder mechanism; like before, it occurs in some instances — top

row, middle column, and middle row, right hand column. Being generous, perhaps the middle row, middle column and the bottom row, middle column could be included. In the other cases, the trajectory leaves the 3*d* state well before dissociation takes place, and in a number of cases never returns to that state after initially hopping into the 3*p* manifold. However, of those which do follow the ladder mechanism there are two cases where the dissociation is exceptionally rapid once the 3*d* state is reached (top row, middle column and middle row, right column), confirming that such a mechanism for rapid progression through the states without spending any significant time in the 3*p* or 3*s* states does exist. In the other cases, some tens of femtoseconds is spent in each of the lower electronic states as the dissociation progresses. What is also crucial to the increased dissociation in this subset of trajectories is the fact that they possess greater total energy because the amount of kinetic energy in each system at time zero is consistent (and trajectories beginning in 3*d* inherently possess greater potential energy). As the total energy is conserved, potential energy is converted into more kinetic energy as the trajectory descends down the states. Therefore, even if a trajectory fails to progress smoothly down the ladder and gets stuck in one or more potential wells, it will have enough newly converted kinetic energy to increase the likelihood of over-the-barrier dissociation on this timescale. The distribution of kinetic energy in the system clearly plays a more dominant role in the dissociation dynamics, and that encountering the 3*d* state in and of itself does not necessarily facilitate a smooth ladder-type dissociation.

Thus, the picture is one of competitive mechanisms even within the fast dissociation channel; on one hand, a dissociating trajectory may successfully navigate all conical intersections on its way down the diabatic state to dissociation, or it may become trapped in one or more potential wells on the way down and experience a kind of hindered dissociation, with trajectories featuring a greater conversion of potential energy into kinetic energy most likely to escape those potential wells and complete their dissociation.

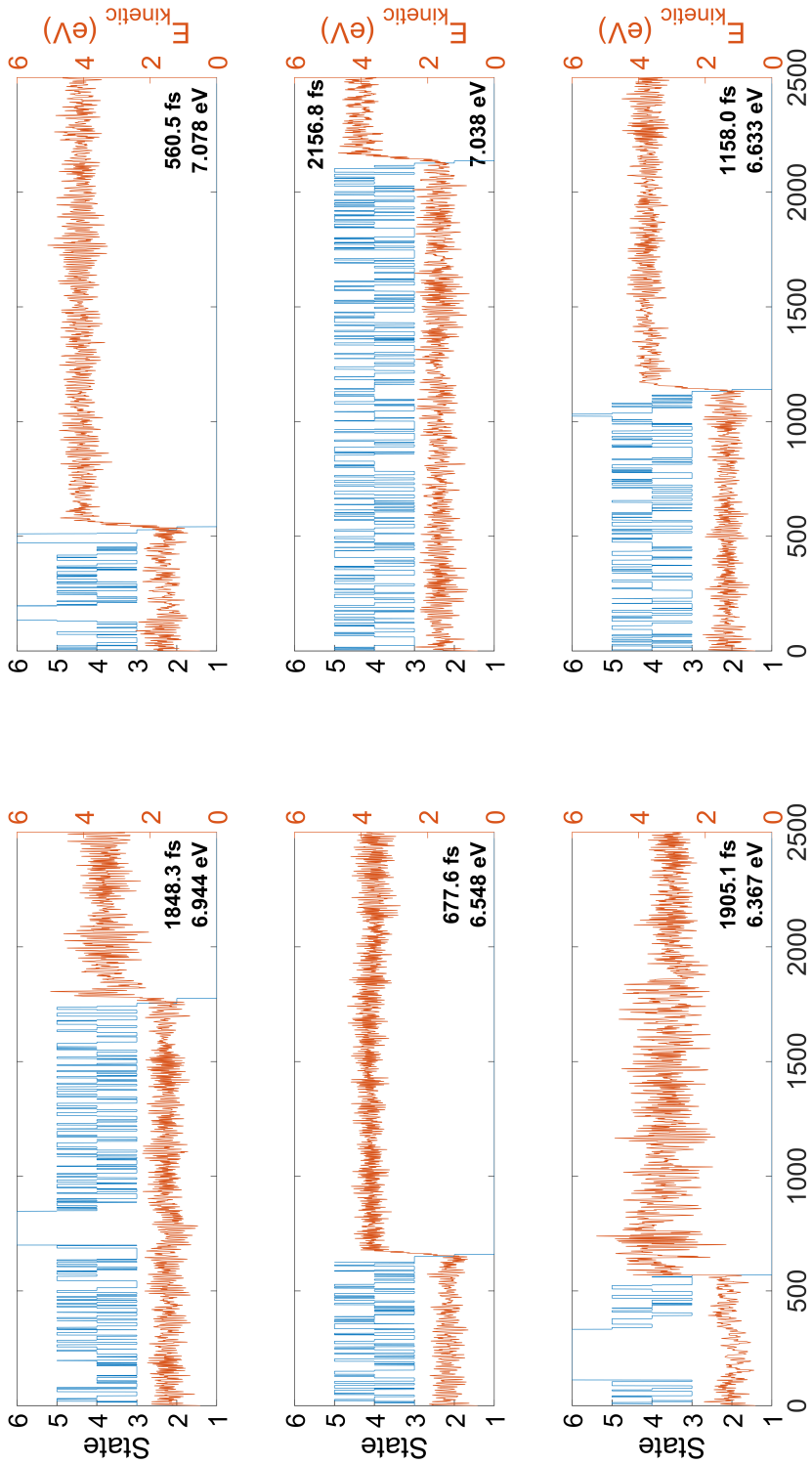

FIGURE 7.11: The localised classical state assigned to each dissociating trajectory as a function of time, alongside the kinetic energy. These are the dissociating trajectories which did not originate in the 3*d* state, comprising six dissociation events out of an ensemble of 306 trajectories. Also shown in the right hand side of each panel are the time step at which dissociation occurred, and the mean total energy of each trajectory.

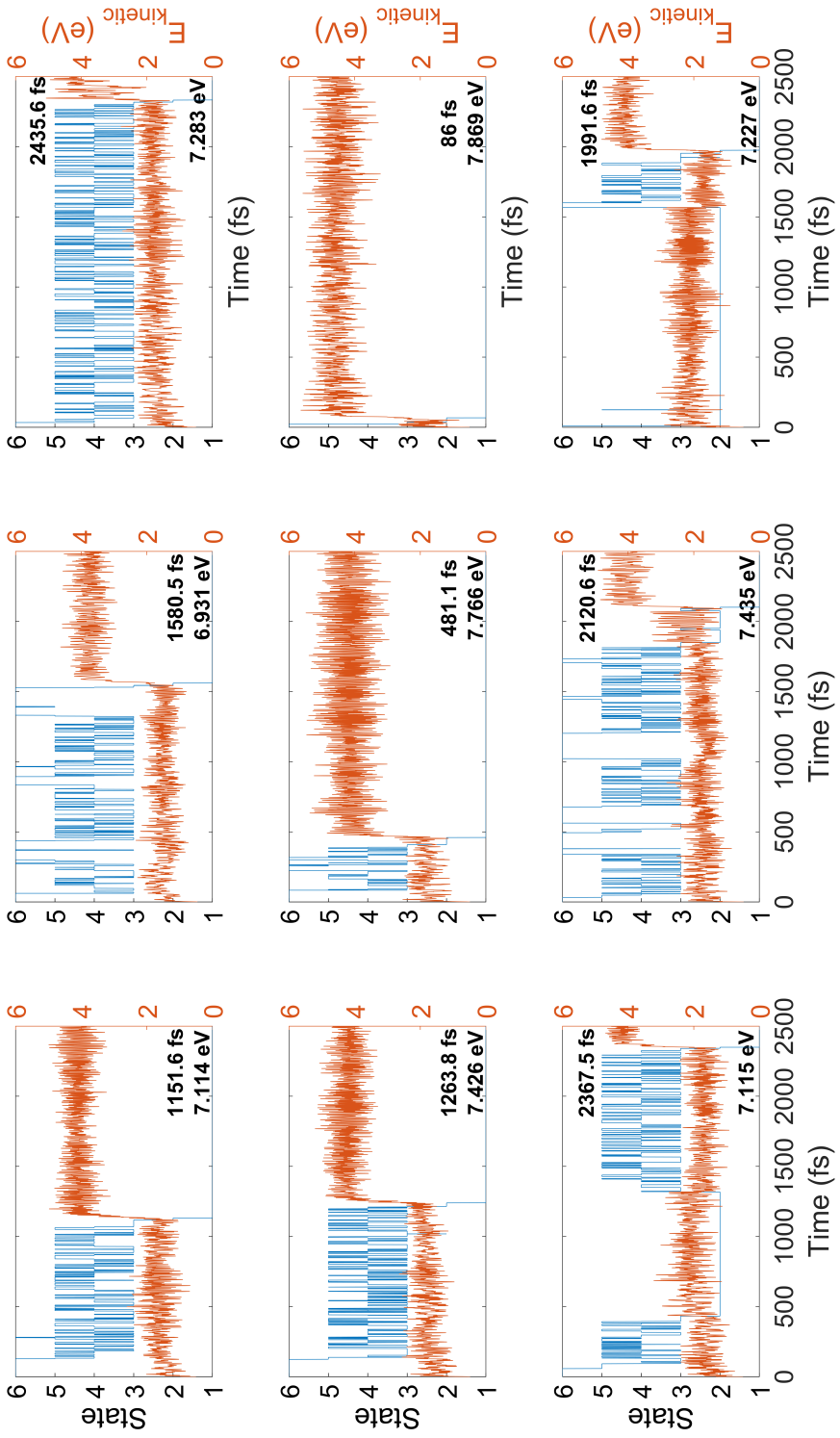

FIGURE 7.12: The localised classical state assigned to each dissociating trajectory as a function of time, alongside the kinetic energy. These are the dissociating trajectories which originated in the $3d$ state, comprising nine dissociation events out of an ensemble of 41 trajectories. Also shown in the right hand side of each panel are the time step at which dissociation occurred, and the mean total energy of each trajectory.

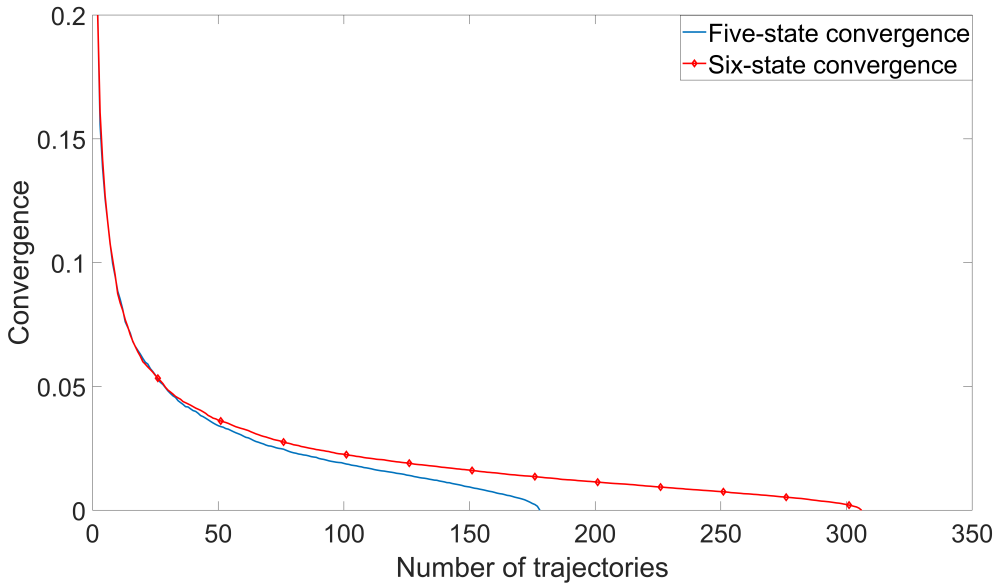

FIGURE 7.13: Convergence plots of each simulation as a function of the final state populations. The convergence metric is the mean of the absolute variances of all state populations at $t = 2500$ fs. In each case the random selection and variance calculation was repeated 1000 times and the results averaged.

7.3.3.5 Convergence

The convergence of each simulation was measured by the state populations at $t = 2500$ fs as a function of all trajectories. The mean of all the absolute variances $V(N)$ of the final populations of each state was calculated for random subsets of trajectories for $N \in [1, N_{\text{traj}}]$, with,

$$V(N) = \sqrt{(B(N) - \langle B \rangle)^2} \tag{7.4}$$

where $\langle B \rangle$ and $B(N)$ are the final predicted state population and the branching ratio/state populations of a subset consisting of N trajectories respectively. The variance calculation was repeated 1000 times for each N with the N trajectories chosen at random each time, and the result averaged. This procedure generates the plots shown in Fig. 7.13, which shown a rapid and smooth convergence for both sets of simulations in a comparatively small

number of trajectories; a reduction to 4% average variance in under 50 trajectories.

7.4 Conclusion

This chapter has dealt with *ab initio* calculations of static TMA, and 1D potential energy cuts along the umbrella vibrational normal mode and the N-C fragmentation pathway. This was in anticipation of "*on-the-fly*" surface-hopping simulations of the photodynamics of the system after excitation into the 3*p* manifold of low-lying Rydberg states; a use of the methodology in a system not complicated by spin-orbit coupling. The simulations showed the expected interplay between the closely-lying 3*p* states, with slower decay to the 3*s* state. The effect of the next highest electronic state, labelled 3*d*, was examined by re-running simulations which included this state, and while limited impact was seen in the progression of the ensemble populations and nuclear motion, the inclusion of this state had a strong impact on overall dissociation of methyl radicals over early times, especially if trajectories which began on the 3*d* state were included. The addition of this latter state highlights its importance in facilitating the fast dissociation mechanism, whatever precise form that mechanism takes — smooth progression down the ladder of states, or trapping in one or more potential wells.

What is also reinforced is the utility in the examination of potential energy curves along the dominant reaction coordinate. This was discussed fully in Chapter 6, but here is shown another example of simplifying a multidimensional process down to a small number of key coordinates, and the relevance of those coordinates accounting for much of the ensuing simulated dynamics.

It should be noted that surface-hopping is most ideally suited to situations with clearly localised conical intersections, while the potential landscape of TMA features largely parallel surfaces with extended regions of strong coupling. Despite this, the method still shows the Rydberg state interactions and gives insight into the dissociation mechanism. However, a

wavepacket-based method such as AI-MCE [112–114] or AIMS [103] may give an improved description of the dynamics.

The electronic structure calculations and simulations detailed in this chapter stand side-by-side with experimental TR-XRD studies carried out by collaborators at the X-FEL at LCLS, Stanford, which examined the dissociation process over short and longer timescales as detailed in Ref. [243]. The simulations successfully describe the fast dissociation channel and shine a light on this complex process in terms of both the internal electronic motion between the Rydberg states and the evolution of the nuclear geometry, with the predicted behaviour of the DMA radical fragments accurately matching that of the experiment.

Chapter 8

Conclusions and outlook

The overall aim of the work undertaken in this project was to study the photochemistry of interesting small gas-phase molecular systems using computational tools. The methodology to achieve this involved the use of *ab initio* methods, primarily based on the CASSCF approach, to investigate the electronic structure of the systems in question and examine relevant reaction coordinates along the potential energy landscapes in each case before running "*on-the-fly*" simulations using the SHARC surface-hopping code. This was applied to two systems; work on CS_2 comprises the bulk of the work here, with TMA the focus of the final results chapter.

With CS_2, the aim was to describe the impact of spin-orbit coupling on the photodissociation dynamics of this structurally simple system which nonetheless features complex underlying dynamics which evolve on multiple coupled electronic states. The structure was optimised and radial and angular potential energy curves of the states though to be involved were calculated. Simulations were ran for excitation primarily to the 1^1B_2 state and initially appeared to match well with experimental time-resolved photoelectron spectroscopy methods in terms of population decay and rise, most clearly in terms of loss of population from the singlet states to the triplet states. However, further examination revealed that the simulations did not populate the same state that was excited in the experiments, due to a number of factors including misbehaviour of the electronic structure calculations at high-symmetry geometries which gave misleading implications as to which states lay within the excitation level. Candidly, the dialogue between theoretician and experimentalist should have been more thorough to

avoid such an exercise. However, the simulations still indicated the feasibility of using the SHARC method to simulate the spin-orbit coupled dynamics of a small system with a significant number of states. The SOC was shown to be non-negligible and have significant impact at early times in the interaction of all the states with each other and flow of population between them.

In Chapter 4 the aim was to expand the simulations to the experimentally-excited 2^1B_2 state. This proved to be a monumental computational exercise. Highly accurate MRCI calculations with a large active space were carried out over the radial and angular coordinates with an expanded ensemble of 19 interacting electronic states (10 singlet and 9 triplet) to generate the requisite potential energy curves. Simulations were carried out at the reduced CASSCF(10,8) level, with computational time limiting the simulations to only the first 100 fs of the dynamics. This was all that was achievable when each 0.1 fs time step took several hours of CPU time. While disappointing in that the experimental times at which dissociation is known to occur were not reached, this still allowed study of the effect of SOC at early times in the experimental system. While not as dramatic as in the earlier CS_2 simulations, the triplet states still had a part to play with non-negligible portions of the population leaking onto a number of coupled triplet states. But this endeavour marked the end of the use of "*on-the-fly*" methods for this system — the cost is simply too great. Instead, efforts turned to the generation of fully-dimensional surfaces, or more accurately inroads to that end. This was approached in a bottom-up approach, beginning with a limited number of singlet states and slowly raising the level of theory in order to see what problems this brought. It was seen that even modest gains in the level of theory brought a much greater level of roughness to the surfaces and highlighted the need for robust smoothing and filtering of the data in order for it to be used as the basis in fully quantum methods such as MCTDH. The possibility of using artificial neural networks to fit the surfaces was briefly discussed, as this would present an intriguing and scientifically useful ultimate aim in the pursuit of accurate descriptions of the photodynamics of this system. Finally on CS_2, in Chapter 6 a comparison was made between

two sets of simulations on the lower set of states carried out at different levels of theory. The aim here was to see the impact of modest changes to levels of theory on the ultimate results of the simulations and to examine the veracity of cheaper lower-level simulations in terms of generating meaningful results. Overall, it was found that indeed the cheaper simulations still gave qualitatively correct results, especially using *a priori* knowledge of the flaws of that level of theory by examining the potential energy curves along key reaction coordinates in advance.

Lastly, Chapter 7 discussed simulations of the early time photodynamics of trimethylamine, a system with low lying Rydberg states. The simulations showed the interplay between the 3*s* and 3*p* Rydberg manifolds, and a comparison was made with simulations featuring an extra higher lying state (3*d*) which was shown to have significant impact on the available dissociation pathway of a methyl fragment — while rapid dissociation is not guaranteed after a trajectory reaches this state, its inclusion greatly enhanced the rate of dissociation. The behaviour of the remaining dimethylamine fragments was in excellent agreement with complementary time-resolved X-ray diffraction experiments.

In terms of outlook, the future is promising. The CS_2 work has a clear goal of migration to methods based on precomputed surfaces coupled to fitting by artificial neural networks. This work is ongoing with collaborators. In the realm of TAAs, there is ongoing work to study further systems including the novel use of "*on-the-fly*" trajectories to generate pools of sample structures of *N*-methylmorpholine, used for the fitting of TR-XRD patterns for comparison with experiment. This approach has shown great utility in regimes where the dynamics occur on timescales simply too long to simulate, and the pool of structures can be fitted to time points well beyond the end of the dynamics.

The above represent promising and exciting directions in which this work will go, the foundations of which the author is pleased to have played his part in laying.

Appendix A

Hartree-Fock theory, basis sets and nuclear properties

The following paragraphs give a brief overview of the basic concepts of electronic structure theory which underpin much of the work in previous chapters. For a more exhaustive discussion of these concepts, a great variety of textbooks and study material may be consulted e.g. Refs. [8, 254–262].

A.1 Hartree-Fock theory

A.1.1 Spin orbitals

The electronic wave function is constructed from one-electron wave functions called orbitals. A spatial orbital $\phi_i(r)$ is a function of the coordinates $\vec{r}$ whose square modulus $|\phi_i(\vec{r})|^2 dr$ gives the probability density of finding an electron in the region dr. In *ab initio* calculations, these spacial orbitals are constructed from a basis set of functions resembling atomic orbitals (see section A.2) and the number of orbitals generated is equal to the number of functions in the basis set. From each spatial orbital two spin orbitals may be generated by applying the spin functions,

$$\begin{aligned} \langle \alpha | \alpha \rangle &= \langle \beta | \beta \rangle = 1 \\ \langle \alpha | \beta \rangle &= \langle \beta | \alpha \rangle = 0. \end{aligned} \tag{A.1}$$

These sets of spin orbitals, denoted χ, describe the electron in terms of both spatial and spin coordinates,

$$\chi(x) = \begin{cases} \phi(\vec{r})\alpha(\omega) \\ \phi(\vec{r})\beta(\omega). \end{cases} \tag{A.2}$$

A.1.2 Hartree products

HF theory begins with a simplified system of non-interacting electrons with a Hamiltonian of the form,

$$\hat{H} = \sum_{i=1}^{N} h(i), \tag{A.3}$$

where $h(i)$ is the one-electron operator describing the kinetic and potential energies of the i-th electron. In the limit of no electron correlation, this would be the full Hamiltonian. $h(i)$ has a set of eigenfunctions which are assumed to be the spin orbitals χ_j,

$$h(i)\chi_j(x_i) = \epsilon_j\chi_j(x_i), \tag{A.4}$$

giving one-electron energies ϵ_j. Because $\hat{H}$ is a sum of one-electron Hamiltonians, a wave function comprising of a product of spin orbitals for each electron is an eigenfunction of $\hat{H}$,

$$\hat{H}\Psi^{\mathrm{HP}} = E\Psi^{\mathrm{HP}}, \tag{A.5}$$

where E is simply the sum of the energies of each spin orbital. Such a wave function is termed a Hartree product (HP). However, such a Hartree product does not take into account the indistinguishability of electrons, i.e. the following condition is not met,

$$\Psi(x_1, ...x_i, ..., x_j, ..., x_N) = -\Psi(x_1, ...x_j, ..., x_i, ..., x_N), \tag{A.6}$$

and so Hartree products do not satisfy the Pauli principle. HF theory circumvents this problem by using a mathematical construct called a Slater determinant [79] as the central wave function ansatz.

A.1.3 Slater determinants

A Slater determinant is a linear combination of Hartree products,

$$\Psi(x_1, x_2) = \frac{1}{\sqrt{2}} \left(\chi_i(x_1)\chi_j(x_2) - \chi_j(x_1)\chi_i(x_2) \right), \tag{A.7}$$

where $\frac{1}{\sqrt{2}}$ is a normalising constant. This wave function obeys the Pauli principle ($\Psi(x_1, x_2) = -\Psi(x_2, x_1)$) and vanishes if electrons occupy the same spin orbital ($i = j$). For a larger N-electron system, such a construction is more easily written as,

$$\Psi(x_1, x_2, ..., x_N) = -(N!)^{\frac{1}{2}} \begin{vmatrix} \chi_i(x_1) & \chi_j(x_1) & ... & \chi_k(x_1) \\ \chi_i(x_2) & \chi_j(x_2) & ... & \chi_k(x_2) \\ ... & ... & & ... \\ \chi_i(x_N) & \chi_j(x_1) & ... & \chi_k(x_N) \end{vmatrix}, \tag{A.8}$$

or even more briefly,

$$|\Psi\rangle = |x_1, x_2, ..., x_N\rangle. \tag{A.9}$$

This determinant accounts for antisymmetry and Pauli exclusion in that interchange of a row or column (equivalent to the interchange of electron coordinates) changes the sign of the determinant and identical rows or columns (equivalent to two electrons occupying the same spin orbital) reduce the determinant to zero. Slater determinants account for so-called exchange correlation, a quantum mechanical effect arising from the motion of electrons with parallel spins.

A cornerstone of HF theory is the variational principle, which states that for any trial wave function $|\Psi_{\text{trial}}\rangle$ subject to boundary conditions, the expectation value for the resulting energy will never be lower than the true energy E_{exact}. Mathematically,

$$E = \frac{\langle \Psi_{\text{trial}} | \hat{H} | \Psi_{\text{trial}} \rangle}{\langle \Psi_{\text{trial}} | \Psi_{\text{trial}} \rangle} \geq E_{\text{exact}}, \tag{A.10}$$

where the denominator is unity if the chosen wave functions are orthonormal. In HF theory the energy is minimised by varying the spin orbitals of $|\Psi\rangle$, resulting in the Hartree-Fock equation,

$$f(i)\chi(x_1) = \epsilon_j \chi(x_i), \tag{A.11}$$

where $f(i)$ is the one-electron Fock operator,

$$f(i) = -\frac{1}{2}\nabla_i^2 - \sum_{A=1}^{M} \frac{Z_A}{r_{iA}} + v^{HF}(i), \tag{A.12}$$

and $v^{HF}(i)$ is the average potential felt by the i-th electron due to the mean-field projected by the other $N-1$ electrons. This expression also contains a term for the quantum mechanical exchange interaction.

This potential depends on the spin orbitals of the other electrons. In other words, the Fock operator depends on its own eigenfunctions. Thus, a non-linear iterative method is required to solve the Hartree-Fock equation. This procedure, termed the self-consistent field (SCF) method, involves the following steps:

- An initial guess set of spin orbitals is used as the starting point
- Using these, v^{HF} for each electron is calculated
- The Hartree-Fock equation is solved to generate a new set of spin orbitals
- The procedure is repeated until self-consistency within a chosen tolerance is achieved

Solution of the Hartree-Fock equation gives a set of orthonormal Hartree-Fock spin orbitals χ_k, each with individual orbital energies ϵ_k. The Slater determinant where the N lowest energy spin orbitals are occupied is the Hartree-Fock ground state wave function — the best variational approximation to the ground state of the system within the constraint of having a single determinant. The remaining orbitals are the so-called virtual orbitals. In practice, the potentially infinite number of solutions to the Hartree-Fock

equation is curtailed by introducing a finite set of spatial basis functions, which are substituted into the Hartree-Fock equation to obtain a matrix eigenvalue problem (the Roothaan-Hall equations).

A.2 Basis sets

The following section discusses the mathematical form of the orbitals themselves from which the wave functions are built.

A.2.1 Slater-type and Gaussian-type orbitals

In 1930 John C. Slater proposed analytical wave functions for all atoms [263], whose radial parts have the form,

$$\phi = r^{n^*-1} \exp\left(-\frac{Z-s}{n^*}\right), \tag{A.13}$$

where Z is the atomic charge, s is a screening constant, and n^* is the effective quantum number. These Slater-type orbitals (STOs) can be written as,

$$\phi^{STO} = N r^{n^*-1} e^{-\eta r}, \tag{A.14}$$

where $r = |r - R_A|$ and N is a normalising constant. Two decades later, S. F. Boys proposed the use of Gaussian-type functions as the radial parts of atomic basis functions [264]. These Gaussian-type orbitals (GTOs) have the form,

$$\phi^{GTO} = C^G e^{-\alpha r^2}. \tag{A.15}$$

In practice, the main differences between STOs and GTOs are seen at $r = 0$ and large r. In the former case the derivative of the exponential term in an STO $\left[\frac{d}{dr}e^{-\eta r}\right]$ is non-zero, while for a GTO $\left[\frac{d}{dr}e^{-\alpha r^2}\right]$ is equal to zero. In the latter case, as $r \to \infty$ the GTO decays faster than the STO due to the square term. GTOs do not generally represent the behaviour of an atomic orbital as well as an STO due to to the lack of a cusp at $r = 0$ and because they decay too early. However, due to the Gaussian product rule it is computationally

less expensive to sum multiple so-called Gaussian primitives to produce a contraction accurately reflecting a real atomic orbital than it is to take a smaller number of STOs to achieve the same effect. Gaussian contractions can be expressed,

$$\Phi = \sum_{s=1}^{n_k} \mu_s \phi_s^{GTO}, \tag{A.16}$$

with contraction size n_k and expansion coefficients μ_s, both of which are predefined in standard libraries of basis sets. In turn, each spatial orbital is constructed as a linear combination of basis functions,

$$\psi(r) = \sum_{k=1}^{N_{BF}} M_k \phi_k^{BF}, \tag{A.17}$$

again with expansion coefficients M_k.

In practice, the Gaussian primitives may come in spherical or Cartesian forms. The former, centred at r_0 from the origin, look like

$$g(r) = N Y_m^l(\theta, \phi)(r - r_o)^n e^{-\gamma(r-r_0)^2}. \tag{A.18}$$

Here Y_m^l is a spherical harmonic, θ and ϕ are the polar and azimuthal angles, and l, m, and n are the polar, azimuthal and radial quantum numbers. A Cartesian GTO centred at $r_0 = (x_0, y_0, z_0)$ is expressed as

$$g(r) = N(x - x_0)^l (y - y_0)^m (z - z_0)^n e^{-\gamma(r-r_0)^2}, \tag{A.19}$$

with normalisation constant N and orbital angular momentum numbers l, m, and n.

A.2.1.1 Common families of basis sets

The smallest possible basis sets used in quantum chemistry consisted of one function to describe each atomic orbital required. Sets of this type are referred to as minimal, and are most commonly notated as STO-NG, where N

is an integer referring to the number of Gaussian (despite the name) primitives contracted into a single basis function. Whilst computationally inexpensive, such basis sets are rarely adequate for the generation of meaningful results. A number of families of larger basis sets have become popular over recent decades. Two of the most common are the Pople and Dunning basis sets, briefly detailed below as examples alongside the more recent Turbomole family of basis sets.

A.2.1.1.1 Pople basis sets Among the first families of basis sets to become popular for routine quantum chemistry calculations, the basis sets (from the group of John A. Pople, joint recipient of the 1998 Nobel Prize in chemistry) are typically notated in the style **X-YZ**G. Core orbitals are described by one basis function each; a contraction of X Gaussian primitives. Valence orbitals are each described by two basis functions; the first a contraction of Y primitives, and the second a contraction of Z primitives. Such a basis set is termed double-zeta as two functions are used to describe each valence orbital, but extensions to triple-zeta or or greater are common. Additionally, sets of diffuse and polarisation functions are indicated by + and * respectively; diffuse functions better describe regions where an electron is far from the nucleus, and polarisation functions describe the change in the shape of atomic orbitals as they are perturbed by regions of charge. Typically, a single + or * sign indicates these functions are added to all non-hydrogen atoms, while ++ or ** indicates these functions are added to hydrogen atoms as well. For example in the 6-311++G** basis set the valence orbitals are described by three basis functions, consisting of contractions of 6, 3 and 1 Gaussian primitives. The core orbitals are described by a single Gaussian contraction of 6 primitives and polarisation and diffuse functions are placed on all atoms.

A.2.1.1.2 Dunning basis sets Another popular group of basis sets are the so-called correlation-consistent basis sets published by the group of Thom H. Dunning Jr. These basis sets are designed to converge systematically to the complete basis set limit as the cardinality increases. Such basis sets are

notated cc-pvNZ where N is a letter or integer referring to the cardinality of the basis set. "cc" stands for correlation-consistent. The prefix aug, standing for augmented, refers to the addition of diffuse functions to the basis set. For example, the aug-cc-pvTZ basis set is of triple-zeta quality and features additional diffuse functions.

A.2.1.1.3 Turbomole basis sets The Turbomole family of basis sets [211, 265, 266] form a set of segmented contracted basis sets for the atoms hydrogen to radon, parametrised by a test set of 300 conditions (atoms in various common oxidation states) and designed to give similar errors across the periodic table for a given basis set.

There are many other basis sets in use today, and new basis sets continue to be actively developed. These three groups merely serve as archetypal examples.

A.3 Electronic properties

For dynamics purposes, calculating only the energy of a system at a given geometry is not sufficient. Other properties of the system must be calculated at each time step in order to predict how the system will respond to the potential energy landscape. Fortunately, the wave function inherently contains all possible information about the system; all experimental observables and calculable properties. The most pertinent of these to quantum dynamics methods are discussed below.

A.3.1 Nuclear gradients

Both the first derivative (nuclear gradient) and second derivative (the Hessian) with respect to the nuclear co-ordinates are useful quantities in characterising the nature of particular points on the PES, most importantly local and global minima (stable structures) and maxima (transition states). In a classical sense, the nuclear gradients also provide the driving force for how the nuclei move.

Nuclear gradients have been calculated analytically since the early days of computational quantum chemistry [267, 268] and are nowadays available for all of the most common electronic structure approaches [269] including SA-CASSCF [270], MRCI [271], CASPT2 [272] and XMS-CASPT2 [88]. For variational methods, these approaches are based on the Hellman-Feynman theorem [273] which states that,

$$\boldsymbol{\nabla}\langle\Psi^e|\hat{H}|\Psi^e\rangle = \langle\Psi^e|\boldsymbol{\nabla}\hat{H}^e|\Psi^e\rangle. \tag{A.20}$$

In other words, the derivative of the energy equals the expectation value of $\boldsymbol{\nabla}\hat{H}$. This does not hold for non-variational methods, in which some system of linear equations must be solved (this is sometimes termed orbital response [274]) — the case in excited state methods which use a common set of orbitals to describe all states (i.e. SA-CASSCF and MRCI), because the orbitals are not variationally optimised for each state. Where analytical methods fail, numerical approaches based on finite differences may suffice, albeit necessitating a deal of patience on behalf of the user.

A.3.2 Transition dipole moments

Dipole moments are critical in governing how a molecule will respond to perturbation by an electromagnetic field, the pertinent example here being the photon of light which initiates a photochemical reaction.

The permanent or static dipole moment μ, a measure of charge distribution in the absence of such perturbation, can be calculated as the expectation value of the dipole operator,

$$\mu = \langle\Psi^e| - e\hat{r}|\Psi^e\rangle, \tag{A.21}$$

which is straightforward to calculate for variational methods. A related quantity is the transition dipole moment (TDM) (μ_x, μ_y, μ_z), a vector which ultimately quantifies the likelihood of transition between a particular pair of states. If a photon of light whose polarisation axis aligns with a strong TDM between states α and β, and the Frank-Condon overlap is good, electronic

transition is much more likely to occur. The TDMs for the x, y, and z directions may be generalised to an overall transition probability (the oscillator strength) by,

$$\mathrm{Osc}_{\alpha\beta} = \frac{2}{3}(E_\beta - E_\alpha)(\mu_x^2 + \mu_y^2 + \mu_z^2). \tag{A.22}$$

A.3.2.1 Spin-orbit coupling

A starting point for the inclusion of relativistic effects such as SOC in electronic structure theory is the Dirac equation [275],

$$\left(\beta mc^2 + c\left(\sum_{n=1}^{3}\alpha_n p_n\right)\right)\Psi(r,t) = \imath\hbar\frac{\partial}{\partial t}\Psi(r,t), \tag{A.23}$$

where β and α are 4×4 Hermitian matrices which mutually anticommute and have squares equal to the identity matrix, p_n corresponds to the components of the momentum operator of the Schrödinger equation. However, this equation deals with only a single particle of mass m. This expression has not at present been generalised to a many-body system [276], so approximations must be invoked to solve it. An important example is the Breit equation [277],

$$\left[\sum_i \hat{h}_i^D + \sum_{i<j}\left(\frac{1}{r_{ij}} - \hat{B}_{ij}\right)\right]|\Psi^e\rangle = \imath\hbar\frac{\partial}{\partial t}|\Psi^e\rangle. \tag{A.24}$$

At first glance, it is a clear relative of the TDSE, reproduced below for convenience,

$$\imath\hbar\frac{\partial}{\partial t}|\Psi(\vec{R},\vec{r},t)\rangle = \hat{H}(\vec{R},\vec{r},t)|\Psi(\vec{R},\vec{r},t)\rangle. \tag{A.25}$$

The Breit equation (A.24) contains the one-electron Dirac operator $\hat{h}_i^D$ which describes the relativistic kinetic energy of the i-th electron and its potential interaction with the nuclei, $1/r_{ij}$ is the Coulombic repulsion between the i-th and j-th electron, and finally the Breit term $\hat{B}_{ij}$ which accounts for special relativity (practically, that the Coulomb interaction is not actually instant across the distance r_{ij}. This is termed "electron retardation" by Breit

[278]). The collection of operators on the left hand side of Eq. A.24 is today known as the Dirac-Coulomb-Breit Hamiltonian. The wave function in this equation is a four-dimensional quantity called a spinor; two of its components are each given to describing spin up and spin down electrons (arising naturally here, rather than an external correction as in the Schrödinger equation through the addition of Pauli exclusion).

The equations of Dirac and Breit have solutions which give negative energies (often assigned to positrons, with mixed success [279]) and are unsuitable to variational electronic structure methods. In order to make them so, techniques have been developed to block diagonalise the Hamiltonian to remove these negative energy solutions, which has the effect of removing two of the components in the Breit wave function. In practical quantum chemistry, possibly the most popular of these approaches is the Douglas-Kroll-Hess (DKH) transformation [280–282].

The Dirac-Coulomb-Breit Hamiltonian is not merely a theoretical construct; its components can be ascribed physical meaning. Most relevant here is the SOC term which must be accounted for to fully describe systems in which the spin-orbit interaction is strong. The SOC operator [277, 278] can be given the following form,

$$\begin{aligned}\hat{H}_{\mathrm{BP}}^{\mathrm{SOC}} &= \frac{1}{2c^2}\left(\sum_i\sum_A \frac{Z_A}{r_{iA}^3}\left(\hat{r}_{iA}\times\hat{p}_i\right)\cdot\hat{s}_i - \sum_{j\neq i}\frac{1}{r_{ij}^3}\left(\hat{r}_{ij}\times\hat{p}_i\right)\cdot\left(\hat{s}_i+2\hat{s}_j\right)\right)\\ &= \sum_i \hat{H}^{\mathrm{SOC}}(i) + \sum_{j\neq i}\hat{H}^{\mathrm{SOC}}(i,j),\end{aligned} \tag{A.26}$$

which includes the speed of light c, the orbital angular momentum $\hat{r}_{iA}\times\hat{p}_i$, and $\hat{s}$ is the spin angular momentum. The first term in the large brackets acts over individual electrons (the one-electron term) and the second deals with the interaction of spin with same-orbit and different-orbit electrons. It is clear that the strength of this Hamiltonian is dependent on nuclear charge Z_a, and inversely dependent on the cube of the distance between two interacting particles r_{iA} or r_{ij}. In these respects, this equation is similar to Eq.

2.18. While tractable for light systems [283], almost in the spirit of electronic structure theory this term is too expensive to calculate in realistic examples due to the two-electron term. It is typically replaced by a mean-field operator [284, 285] evocative of the treatment of electron correlation in the HF method. Practically, efficient methods for calculating spin-orbit coupling have been implemented for both MCSCF and internally-contracted MRCI [283] approaches.

Appendix B

Wave function overlaps

B.1 Wave function overlaps

Within the SHARC package, the facility exists to use wave function overlaps instead of expensive nonadiabatic couplings in the calculation of nonadiabatic interaction terms via a computationally-efficient algorithm. In general, the use of wave function overlaps in this way is well-established in the study of nonadiabatic dynamics as an alternative to the calculation of full nonadiabatic couplings [158]. At its simplest, overlaps are represented as a scalar product of CI vectors to give a measure of change in the character of the wave function [286–288]. More sophisticated implementations are available for a number of types of wave function, including those of multireference character [289, 290].

Here, the task is to compute the following the overlap matrix **S**, containing elements,

$$S_{IJ} = \langle \Psi_I | \Psi'_J \rangle. \tag{B.1}$$

As a first step, the two sets of electronic wave functions $|\Psi_I\rangle$ and $|\Psi'_J\rangle$ are expanded into Slater determinants,

$$|\Psi_I\rangle = \sum_{k=1}^{n_{\mathrm{CI}}} d_{Ik} |\Phi_k\rangle \tag{B.2}$$

$$|\Psi'_J\rangle = \sum_{l=1}^{n'_{\mathrm{CI}}} d'_{Jl} |\Phi'_l\rangle, \tag{B.3}$$

where d_{IK} and d'_{JI} are the CI coefficients which form the CI vectors for each state, and n_{CI} and n'_{CI} are the number of elements in those vectors. Substitution of these terms into equation B.1 gives,

$$S_{IJ} = d_{lk} d'_{Jl} \langle \Phi_l | \Phi'_J \rangle, \tag{B.4}$$

which sums over the Slater determinant overlaps.

To determine the overlap between an individual pair of Slater determinants, a matrix is generated containing all mutual orbital overlaps and its determinant calculated. The matrix is block diagonal due to the vanishing contribution of orbitals of differing spin. Its component blocks can be solved separately. Overlap matrix elements S_{IK} are not necessarily unique to the pair of Slater determinants generating it; they are the same for determinants with the same spin occupation pattern. This repetition is a source of efficiency in the algorithm as such terms do not need to be recomputed.

The nonadiabatic coupling vector between states I and J is defined,

$$h_{IJ}(\vec{R}) = \langle \Psi_I(\vec{R}) | \nabla \Psi_J(\vec{R}) \rangle, \tag{B.5}$$

which can be rewritten as,

$$h_{IJ}(\vec{R}) = \nabla' \langle \Psi_I(\vec{R}) | \Psi_J(\vec{R}') \rangle |_{\vec{R}'=\vec{R}} = \nabla' S_{IJ}(\vec{R}, \vec{R}') |_{\vec{R}'=\vec{R}}, \tag{B.6}$$

where ∇' is the gradient vector with respect to the $\vec{R}'$ nuclear co-ordinates. Using the following general definition of a derivative,

$$f'(x) = \lim_{h \to 0} \frac{f(x+h) - f(x)}{h}, \tag{B.7}$$

the fact that $S_{IJ} = 0$ if $R = R'$, and the chain rule, the following can be derived,

$$\lim_{t \to 0} \frac{S_{IJ}(\vec{R}, \vec{R} + t\vec{R}_D)}{t} = h_{IJ}(\vec{R}) \cdot \vec{R}_D, \tag{B.8}$$

where $\vec{R}_D$ is a displacement vector. Using a discrete value of t and setting $\Delta\vec{R} = t\vec{R}_D$, this reduces to,

$$S_{IJ}(\vec{R}, \vec{R} + \Delta\vec{R}) \approx h_{IJ}(\vec{R}) \cdot \Delta\vec{R}, \tag{B.9}$$

and the link between wave function overlaps and nonadiabatic coupling is established. A fuller description of the theory and implementation of wave function overlaps in SHARC can be found in Ref. [212], from which the above extremely brief overview is taken.

Bibliography

[1] A. H. Zewail. *Femtochemistry: ultrafast dynamics of the chemical bond*. Vol. 1. World Scientific, 1994.

[2] V. Gold. *The Compendium of Chemical Terminology*. Blackwell Science, 1987.

[3] R. G. Gould. "The LASER, light amplification by stimulated emission of radiation". *The Ann Arbor conference on optical pumping, the University of Michigan*. Vol. 15. 1959, 128.

[4] B. A. Lengyel. *Lasers: generation of light by stimulated emission*. John Wiley & Sons, 1962.

[5] R. D. Miller. *Annu. Rev. Phys. Chem.* **65**, 583 (2014).

[6] R. D. Miller. *Science* **343**, 1108 (2014).

[7] A. H. Zewail. *Angew. Chem. Int. Ed.* **39**, 2586 (2000).

[8] F. Jensen. *Introduction to Computational Chemistry*. 2nd Edition. JW, 2011.

[9] G. E. Moore. *Proc. IEEE* **86**, 82 (1998).

[10] T. Goto. *Pure Appl. Chem.* **17**, 421 (1968).

[11] H. Gaffron and E. W. Fager. *Ann. Rev. Plant. Physiol.* **2**, 87 (1951).

[12] F. Collins. *Biol. Rev.* **29**, 453 (1954).

[13] G. M. Wahl and A. M. Carr. *Nat. Cell Biol.* **3**, E277 (2001).

[14] R. B. Woodward and R. Hoffmann. *J. Am. Chem. Soc.* **87**, 395 (1965).

[15] E. E. Coyle and M. Oelgemöller. *Photochem. Photobiol. Sci.* **7**, 1313 (2008).

[16] T. V. Grotthaus. *Ostwald's Klassiker der exakten Wissenschaften* **152** (1820).

[17] A. Cox and T. J. Kemp. *Introductory photochemistry*. New York, McGraw-Hill, 1971.

[18] R. S. Fisher. *Photophysical characterisation of novel fluorescent base analogues*. The University of Edinburgh, 2018.

[19] A. Jablonski. *Z. Phys.* **96**, 236 (1935).

[20] L. Cederbaum, D. Yarkony, and H Köppel. *Born-Oppenheimer Approximation and Beyond*, 6 (2004).

[21] G. A. Worth and L. S. Cederbaum. *Annu. Rev. Phys. Chem.* **55**, 127 (2004).

[22] W. Domcke, D. R. Yarkony, and H. Köppel. *Conical intersections: theory, computation and experiment*. Vol. 17. World Scientific, 2011.

[23] W. Domcke and D. R. Yarkony. *Ann. Rev. Phys. Chem.* **63**, 325 (2012).

[24] R. Squibb, M. Sapunar, A Ponzi, R Richter, A Kivimäki, O Plekan, P Finetti, N Sisourat, V Zhaunerchyk, T Marchenko, L Journal, R Guillemin, R Cucini, M Coreno, C Grazioli, M Di fraia, C Callegari, K. C. Prince, P Decleva, M Simon, J. H. D. Eland, N Došlić, R Feifel, and M. N. Piancastelli. *Nat. Commun.* **9**, 63 (2018).

[25] E. Muybridge. *Animals in motion*. Courier Corporation, 2012.

[26] A. Ashkin, S. Chu, J. Bjorkholm, A. Cable, and J. Gordon. *Phys. Rev. Lett* **24**, 156 (1970).

[27] J. Van Houten. *J. Chem. Educ* **78**, 1570 (2001).

[28] V. Ramamurthy and N. J. Turro. *Chem. Rev.* **93**, 1 (1993).

[29] J. S. Baskin and A. H. Zewail. *J. Chem. Educ.* **78**, 737 (2001).

[30] G. Cerullo, C. Manzoni, L. Lüer, and D. Polli. *Photochem. Photobiol. Sci.* **6**, 135 (2007).

[31] K. Reid. *Annu. Rev. Phys. Chem.* **54**, 397 (2003).

[32] H. H. Fielding and G. A. Worth. *Chem. Soc. Rev.* **47**, 309 (2018).

[33] A. D. Smith, E. M. Warne, D. Bellshaw, D. A. Horke, M. Tudorovskya, E. Springate, A. J. H. Jones, C. Cacho, R. T. Chapman, A. Kirrander, and R. S. Minns. *Phys. Rev. Lett.* **120**, 183003 (2018).

[34] D. Bellshaw, D. A. Horke, A. D. Smith, H. M. Watts, E. Jager, E. Springate, O. Alexander, C. Cacho, R. T. Chapman, A. Kirrander, and R. S. Minns. *Chem. Phys. Lett.* **683**, 383 (2017).

[35] B. Patterson and R. Abela. *Phys. Chem. Chem. Phys.* **12**, 5647 (2010).

[36] A. A. Ischenko, P. M. Weber, and R. D. Miller. *Chem. Rev.* **117**, 11066 (2017).

[37] W. Ackermann, G. Asova, V. Ayvazyan, A. Azima, N. Baboi, J. Bähr, V. Balandin, B. Beutner, A. Brandt, and A. Bolzmann. *Nat. Photonics* **1**, 336 (2007).

[38] J. B. Murphy and C. Pellegrini. *Nucl. Instrum. Methods Phys. Res. A* **237**, 159 (1985).

[39] Y. S. Derbenev, A. Kondratenko, and E. Saldin. *Nucl. Instrum. Methods Phys. Res.* **193**, 415 (1982).

[40] Z. Huang and K.-J. Kim. *Phys. Rev. Accel. Beams.* **10** (2007).

[41] M. Cornacchia and H. Winick. *Technological challenges of third-generation synchrotron radiation sources*. Tech. rep. Stanford Linear Accelerator Center, Menlo Park, CA (USA), 1990.

[42] R. D. Miller, R. Ernstorfer, M. Harb, M. Gao, C. T. Hebeisen, H. Jean-Ruel, C. Lu, G. Moriena, and G. Sciaini. *Acta Cryst. A* **66**, 137 (2010).

[43] M. Chergui and A. H. Zewail. *ChemPhysChem* **10**, 28 (2009).

[44] V. Ayvazyan, N. Baboi, J. Bähr, V. Balandin, b. Beutner, A. Brandt, I. Bohnet, A. Bolzmann, R. Brinkmann, O. Brovko, *et al. Eur. Phys. J. D* **37**, 297 (2006).

[45] V. Lyamayev, Y. Ovcharenko, R. Katzy, M. Devetta, L. Bruder, A. LaForge, M. Mudrich, U. Person, F. Stienkemeier, M. Krikunova, T. Möller, P. Piseri, L. Avaldi, M. Coreno, P. O'Keeffe, P. Bolognesi, M. Alagia, A. Kivimäki, M. Di Fraia, N. B. Brauer, M. Drabbels, T. Mazza, S. Stranges, P. Finetti, C. Grazioli, O. Plekan, R. Richter, K. C. Prince, and C. Callegari. *J. Phys. B* **46**, 164007 (2013).

[46] J. Arthur, P. Anfinrud, P. Audebert, *et al. Linac Coherent Light Source (LCLS) Conceptual Design Report*. Tech. rep. Accessed: 18-06-2019.

[47] M. Yabashi, H. Tanaka, T. Tanaka, H. Tomizawa, T. Togashi, M. Nagasono, T. Ishikawa, J. Harries, Y. Hikosaka, and A. Hishikawa. *J. Phys. B* **46**, 164001 (2013).

[48] M. Altarelli, R. Brinkmann, M. Chergui, W. Decking, B. Dobson, S. Düsterer, G. Grübel, W. Graeff, H. Graafsma, J. Hajdu, *et al. Technical Design Report, DESY* **97**, 1 (2006).

[49] E.-S. Kim and M. Yoon. *IEEE Trans. Nuc. Sci* **56**, 3597 (2009).

[50] R. Ganter. *SwissFEL-Conceptual design report*. Tech. rep. Paul Scherrer Institute (PSI), 2010.

[51] E. Schrödinger. *Phys. Rev.* **28**, 1049 (1926).

[52] M. Born and R. J. Oppenheimer. *Ann. Phys* **84**, 457 (1927).

[53] M. Born and K. Huang. *Dynamical theory of crystal lattices*. Clarendon press, 1954.

[54] L. J. Butler. *Annu. Rev. Phys. Chem.* **49**, 125 (1998).

[55] T. Van Voorhis, T. Kowalczyk, B. Kaduk, L.-P. Wang, C.-L. Cheng, and Q. Wu. *Annual review of physical chemistry* **61**, 149 (2010).

[56] F. Gadea and M. Pelissier. *The Journal of Chemical Physics* **93**, 545 (1990).

[57] H. Nakamura. *International Reviews in Physical Chemistry* **10**, 123 (1991).

[58] M. Baer. *Molecular Physics* **40**, 1011 (1980).

[59] T. Pacher, L. Cederbaum, and H. Köppel. *Advances in chemical physics* **84**, 293 (1993).

[60] R. S. Mulliken. *Journal of the American Chemical Society* **74**, 811 (1952).

[61] N. S. Hush. *Progress in inorganic chemistry*, 391 (1967).

[62] H. Nakamura and D. G. Truhlar. *The Journal of Chemical Physics* **115**, 10353 (2001).

[63] B. A. Hess. *Relativistic effects in heavy-element chemistry and physics*. Wiley, 2003.

[64] P. Pyykko and J. P. Desclaux. *Acc. Chem. Res.* **12**, 276 (1979).

[65] S. Rose, I. Grant, and N. Pyper. *J. Phys. B* **11**, 1171 (1978).

[66] P. Pyykkö. "Relativistic quantum chemistry". *Advances in quantum chemistry*. **11**. Elsevier, 1978, 353.

[67] N. Christensen, S. Satpathy, and Z. Pawlowska. *Phys. Rev. B* **34**, 5977 (1986).

[68] P. Pyykko. *Chem. Rev.* **88**, 563 (1988).

[69] R. J. Bartlett. *Annu. Rev. Phys. Chem.* **32**, 359 (1981).

[70] J. W. Hollett and P. M. Gill. *J. Chem. Phys.* **134**, 114111 (2011).

[71] C. Møller and M. S. Plesset. *Phys. Rev.* **46**, 0618 (1934).

[72] I. Shavitt and R. J. Bartlett. *Many-body methods in chemistry and physics: MBPT and coupled-cluster theory*. Cambridge University Press, 2009.

[73] A. Dreuw and M. Wormit. *WIRES Comput. Mol. Sci.* **5**, 82 (2015).

[74] J. F. Stanton and R. J. Bartlett. *J. Chem. Phys.* **98**, 7029 (1993).

[75] V. Veryazov, P. Å. Malmqvist, and B. O. Roos. *Int. J. Quantum Chem.* **111**, 3329 (2011).

[76] J. Olsen. *Int. J. Quantum Chem.* **111**, 3267 (2011).

[77] D. I. Lyakh, M. Musiał, V. F. Lotrich, and R. J. Bartlett. *Chem. Rev.* **112**, 182 (2011).

[78] P. G. Szalay, T. Müller, G. Gidofalvi, H. Lischka, and R. Shepard. *Chem. Rev.* **112**, 108 (2011).

[79] J. C. Slater. *Phys. Rev.* **34**, 1293 (1929).

[80] E. Condon. *Phys. Rev.* **36**, 1121 (1930).

[81] H.-J. Werner and P. J. Knowles. *J. Chem. Phys.* **89**, 5803 (1988).

[82] P. E. Siegbahn and M. Svensson. *Int. J. Quantum Chem.* **41**, 153 (1992).

[83] K. Andersson, P. A. Malmqvist, B. O. Roos, A. J. Sadlej, and K. Wolinski. *J. Phys. Chem.* **94**, 5483 (1990).

[84] K. Andersson, P.-Å. Malmqvist, and B. O. Roos. *J. Chem. Phys.* **96**, 1218 (1992).

[85] J.-P. Malrieu, J.-L. Heully, and A. Zaitsevskii. *Theor. Chem. Acc.* **90**, 167 (1995).

[86] J. Finley, P.-Å. Malmqvist, B. O. Roos, and L. Serrano-Andrés. *Chem. Phys. Lett.* **288**, 299 (1998).

[87] A. A. Granovsky. *J. Chem. Phys.* **134**, 214113 (2011).

[88] T. Shiozaki, W. Győrffy, P. Celani, and H.-J. Werner. *J. Chem. Phys.* **135**, 081106 (2011).

[89] S. Sen and I. Schapiro. *Mol. Phys.* 1 (2018).

[90] D. Roca-Sanjuán, F. Aquilante, and R. Lindh. *WIRES Comput. Mol. Sci.* **2**, 585 (2012).

[91] B. O. Roos and K. Andersson. *Chem. Phys. Lett.* **245**, 215 (1995).

[92] B. O. Roos, K. Andersson, M. P. Fülscher, L. Serrano-Andrés, K. Pierloot, M. Merchán, and V. Molina. *J. Mol. Struct* **388**, 257 (1996).

[93] H.-D. Meyer, U. Manthe, and L. S. Cederbaum. *Chem. Phys. Lett.* **165**, 73 (1990).

[94] U. Manthe, H.-D. Meyer, and L. S. Cederbaum. *J. Chem. Phys.* **97**, 3199 (1992).

[95] M. H. Beck, A. Jäckle, G. Worth, and H.-D. Meyer. *Physics reports* **324**, 1 (2000).

[96] S. Römer, M. Ruckenbauer, and I. Burghardt. *J. Chem. Phys.* **138**, 064106 (2013).

[97] T. Martinez, M. Ben-Nun, and R. Levine. *J. Phys. Chem. A* **101**, 6389 (1997).

[98] G. Worth, M. Robb, and I. Burghardt. *Faraday Discussions* **127**, 307 (2004).

[99] D. V. Shalashilin. *J. Chem. Phys.* **130**, 244101 (2009).

[100] J. C. Tully. *J. Chem. Phys.* **93**, 1061 (1990).

[101] M. Ben-Nun and T. J. Martinez. *J. Chem. Phys.* **108**, 7244 (1998).

[102] M. Ben-Nun and T. J. Martinez. *J. Phys. Chem. A* **103**, 10517 (1999).

[103] M. Ben-Nun, J. Quenneville, and T. J. Martinez. *J. Phys. Chem. A* **104**, 5161 (2000).

[104] M. Ben-Nun and T. J. Martinez. *J. Chem. Phys.* **112**, 6113 (2000).

[105] M. Ben-Nun and T. J. Martinez. *Adv. Chem. Phys* **121**, 439 (2002).

[106] B. G. Levine, J. D. Coe, A. M. Virshup, and T. J. Martinez. *Chem. Phys.* **347**, 3 (2008).

[107] B. Lasorne, M. J. Bearpark, M. A. Robb, and G. A. Worth. *Chem. Phys. Lett.* **432**, 604 (2006).

[108] B. Lasorne, M. Robb, and G. Worth. *Phys. Chem. Chem. Phys.* **9**, 3210 (2007).

[109] G. Worth, M. Robb, and B. Lasorne. *Mol. Phys.* **106**, 2077 (2008).

[110] B. Lasorne, G. A. Worth, and M. A. Robb. *WIRES Comput. Mol. Sci.* **1**, 460 (2011).

[111] D. Mendive-Tapia, B. Lasorne, G. A. Worth, M. A. Robb, and M. J. Bearpark. *J. Chem. Phys.* **137**, 22A548 (2012).

[112] K. Saita and D. V. Shalashilin. *J. Chem. Phys.* **137** (2012).

[113] D. V. Shalashilin. *Faraday Discussions* **153**, 105 (2011).

[114] D. V. Shalashilin. *J. Chem. Phys.* **132**, 244111 (2010).

[115] A. McLachlan. *Mol. Phys.* **8**, 39 (1964).

[116] K. Saita, M. G. Nix, and D. V. Shalashilin. *Phys. Chem. Chem. Phys.* **15**, 16227 (2013).

[117] A. Bjerre and E. Nikitin. *Chem. Phys. Lett.* **1**, 179 (1967).

[118] J. C. Tully and R. K. Preston. *J. Chem. Phys.* **55**, 562 (1971).

[119] O. V. Prezhdo and P. J. Rossky. *J. Chem. Phys.* **107**, 825 (1997).

[120] C. Zhu, H. Kamisaka, and H. Nakamura. *J. Chem. Phys.* **115**, 11036 (2001).

[121] A. W. Jasper, S. N. Stechmann, and D. G. Truhlar. *J. Chem. Phys.* **116**, 5424 (2002).

[122] A. W. Jasper and D. G. Truhlar. *Chem. Phys. Lett.* **369**, 60 (2003).

[123] E. Fabiano, G. Groenhof, and W. Thiel. *Chem. Phys.* **351**, 111 (2008).

[124] A. K. Belyaev, C. Lasser, and G. Trigila. *J. Chem. Phys.* **140**, 224108 (2014).

[125] S. Hayashi, E. Tajkhorshid, and K. Schulten. *Biophys. J.* **96**, 403 (2009).

[126] G. Granucci and M. Persico. *J. Chem. Phys.* **126**, 134114 (2007).

[127] M. Barbatti, M. Ruckenbauer, F. Plasser, J. Pittner, G. Granucci, M. Persico, and H. Lischka. *WIRES Comput. Mol. Sci.* **4**, 26 (2014).

[128] E. Tapavicza, I. Tavernelli, and U. Rothlisberger. *Phys. Rev. letters* **98**, 023001 (2007).

[129] E. Fabiano, T. Keal, and W. Thiel. *Chem. Phys.* **349**, 334 (2008).

[130] J. J. Bajo, G. Granucci, and M. Persico. *J. Chem. Phys.* **140**, 044113 (2014).

[131] M. Persico and G. Granucci. *Theor. Chem. Acc* **133**, 1526 (2014).

[132] B. J. Schwartz and P. J. Rossky. *J. Chem. Phys.* **101**, 6902 (1994).

[133] E. R. Bittner and P. J. Rossky. *J. Chem. Phys.* **103**, 8130 (1995).

[134] B. J. Schwartz, E. R. Bittner, O. V. Prezhdo, and P. J. Rossky. *J. Chem. Phys.* **104**, 5942 (1996).

[135] O. V. Prezhdo and P. J. Rossky. *J. Chem. Phys.* **107**, 5863 (1997).

[136] J. E. Subotnik, W. Ouyang, and B. R. Landry. *J. Chem. Phys.* **139**, 211101 (2013).

[137] G. Granucci, M. Persico, and A. Zoccante. *J. Chem. Phys.* **133**, 134111 (2010).

[138] J. E. Subotnik. *J. Phys. Chem. A* **115**, 12083 (2011).

[139] J. E. Subotnik and N. Shenvi. *J. Chem. Phys.* **134**, 244114 (2011).

[140] J. E. Subotnik and N. Shenvi. *J. Chem. Phys.* **134**, 024105 (2011).

[141] N. Shenvi and W. Yang. *J. Chem. Phys.* **137**, 22A528 (2012).

[142] H. M. Jaeger, S. Fischer, and O. V. Prezhdo. *J. Chem. Phys.* **137**, 22A545 (2012).

[143] A. Jain, E. Alguire, and J. E. Subotnik. *J. Chem. Theory Comput.* **12**, 5256 (2016).

[144] E. P. Wigner. "On the quantum correction for thermodynamic equilibrium". *Part I: Physical Chemistry. Part II: Solid State Physics*. Springer, 1997, 110.

[145] S. Nangia, A. W. Jasper, T. F. Miller III, and D. G. Truhlar. *The Journal of chemical physics* **120**, 3586 (2004).

[146] T. Nelson, S. Fernandez-Alberti, V. Chernyak, A. E. Roitberg, and S. Tretiak. *The Journal of chemical physics* **136**, 054108 (2012).

[147] M. D. Hack and D. G. Truhlar. *J. Phys. Chem. A* **104**, 7917 (2000).

[148] S. Bonella, D. Coker, D MacKernan, R Kapral, and G Ciccotti. "Trajectory based simulations of quantum-classical systems". *Energy Transfer Dynamics in Biomaterial Systems*. Springer, 2009, 415.

[149] M. Barbatti. *WIRES Comput. Mol. Sci.* **1**, 620 (2011).

[150] Z. Lan and J. Shao. (2012).

[151] E. Tapavicza, G. D. Bellchambers, J. C. Vincent, and F. Furche. *Phys. Chem. Chem. Phys.* **15**, 18336 (2013).

[152] J. E. Subotnik, A. Jain, B. Landry, A. Petit, W. Ouyang, and N. Bellonzi. *Annu. Rev. Phys. Chem.* **67**, 387 (2016).

[153] J. Peng, Y. Xei, D. Hu, and L. Du Likai. *Acta Phys.-Chim. Sinca*, 0 (2018).

[154] M. Richter, P. Marquetand, J. González-Vázquez, I. Sola, and L. González. *J. Chem. Theory Comput.* **7**, 1253 (2011).

[155] L. Verlet. *Phys. Rev.* **159**, 98 (1967).

[156] L. Verlet. *Phys. Rev.* **165**, 201 (1968).

[157] J. C. Butcher. (1987).

[158] S. Hammes-Schiffer and J. C. Tully. *J. Chem. Phys.* **101**, 4657 (1994).

[159] S. Mai, M. Richter, M. Ruckenbauer, M. Oppel, P. Marquetand, and L. González. *SHARC: Surface Hopping Including Arbitrary Couplings — Program Package for Non-Adiabatic Dynamics*. sharc-md.org. 2014.

[160] S. Mai, P. Marquetand, and L. González. *Int. J. Quantum Chem.* **115**, 1215 (2015).

[161] S. Mai, P. Marquetand, and L. González. *WIRES Comput. Mol. Sci.* e1370 (2018).

[162] S. Mai, M. Richter, M. Heindl, M. F. Menger, A. J. Atkins, M. Ruckenbauer, F. Plasser, M. Oppel, P. Marquetand, and L. González. *SHARC2.0: Surface Hopping Including Arbitrary Couplings — Program Package for Non-Adiabatic Dynamics*. sharc-md.org. 2018.

[163] F. Plasser, S. Gómez, M. F. Menger, S. Mai, and L. González. *Physical Chemistry Chemical Physics* **21**, 57 (2019).

[164] D. Bellshaw, R. S. Minns, and A. Kirrander. *Physical Chemistry Chemical Physics* (2019).

[165] D. Townsend, H. Satzger, T. Ejdrup, A. M. Lee, H. Stapelfeldt, and A. Stolow. *J. Chem. Phys.* **125**, 234302 (2006).

[166] T. N. Kitsopoulos, C. R. Gebhardt, and T. P. Rakitzis. *J. Chem. Phys.* **115**, 9727 (2001).

[167] M. Brouard, E. K. Campbell, R. Cireasa, A. J. Johnsen, and W.-H. Yuen. *J. Chem. Phys.* **136**, 044310 (2012).

[168] R. Spesyvtsev, T. Horio, Y.-I. Suzuki, and T. Suzuki. *J. Chem. Phys.* **142**, 074308 (2015).

[169] C. Z. Bisgaard, O. J. Clarkin, G. Wu, A. M. D. Lee, O. Geßner, C. C. Hayden, and A. Stolow. *Science* **323**, 1464 (2009).

[170] T. Horio, R. Spesyvtsev, and T. Suzuki. *Opt. Express* **21**, 22423 (2013).

[171] T. Horio, R. Spesyvtsev, and T. Suzuki. *Opt. Lett.* **39**, 6021 (2014).

[172] R. J. Hemley, D. G. Leopold, J. L. Roebber, and V. Vaida. *J. Chem. Phys.* **79**, 5219 (1983).

[173] P. Farmanara, V. Stert, and W. Radloff. *J. Chem. Phys.* **111**, 5338 (1999).

[174] P. Hockett, C. Z. Bisgaard, O. J. Clarkin, and A. Stolow. *Nat Phys* **7**, 612 (2011).

[175] I. M. Waller and J. W. Hepburn. *J. Chem. Phys.* **87**, 3261 (1987).

[176] D. Xu, J. Huang, and W. M. Jackson. *J. Chem. Phys.* **120**, 3051 (2004).

[177] K. Wang, V. McKoy, P. Hockett, and M. S. Schuurman. *Phys. Rev. Lett.* **112**, 113007 (2014).

[178] H.-J. Werner, P. J. Knowles, G. Knizia, F. R. Manby, M. Schütz, *et al. MOLPRO, version 2012.1, a package of ab initio programs*. `http://www.molpro.net`. Cardiff, UK, 2012.

[179] A. Herráez. *How to use Jmol to study and present molecular structures*. Vol. 1. Lulu Enterprises, 2008.

[180] D. Tseng and R. Poshusta. *J. Chem. Phys.* **100**, 7481 (1994).

[181] Q. Zhang and P. H. Vaccaro. *J. Phys. Chem.* **99**, 1799 (1995).

[182] S. T. Brown, T. J. Van Huis, B. C. Hoffman, and H. F. Schaefer III. *Mol. Phys.* **96**, 693 (1999).

[183] K. B. Wiberg, Y.-g. Wang, A. E. de Oliveira, S. A. Perera, and P. H. Vaccaro. *J. Phys. Chem. A* **109**, 466 (2005).

[184] A. Mank, C. Starrs, M. Jego, and J. Hepburn. *J. Chem. Phys.* **104**, 3609 (1996).

[185] J. P. Dahl and M. Springborg. *J. Chem. Phys.* **88**, 4535 (1988).

[186] R. Schinke. *Photodissociation dynamics: spectroscopy and fragmentation of small polyatomic molecules*. Cambridge University Press, 1995.

[187] M. Barbatti, G. Granucci, M. Ruckenbauer, F. Plasser, J. Pittner, M. Persico, and H. Lischka. *Max-Planck-Institut fur Kohlenforschung: Mulheim an der Ruhr, Germany* (2011).

[188] T. Shimanouchi and T. Shimanouchi. *Tables of molecular vibrational frequencies*. National Bureau of Standards Washington, DC, 1980.

[189] A. Eppink and D. Parker. *Review of Scientific Instruments* **68**, 3477 (1997).

[190] D. Hanggi and P. W. Carr. *Anal. Chem.* **57**, 2394 (1985).

[191] S. P. McGlynn, J. W. Rabalais, J. R. McDonald, and V. Scherr. *Chem. Rev.* **71**, 73 (1971).

[192] S. Ahmed and V. Kumar. *Pramana* **39**, 367 (1992).

[193] L. M. Goss, G. J. Frost, D. Donaldson, and V. Vaida. *Geophys. Res. Lett.* **22**, 2609 (1995).

[194] S. Y. Grebenshchikov. *Communication: Multistate quantum dynamics of photodissociation of carbon dioxide between 120 nm and 160 nm*. 2012.

[195] S. Y. Grebenshchikov. *J. Chem. Phys.* **138**, 224106 (2013).

[196] S. Y. Grebenshchikov and R. Borrelli. *J. Phys. Chem. letters* **3**, 3223 (2012).

[197] S. Y. Grebenshchikov. *J. CO_2 Utilization* **15**, 32 (2016).

[198] K. Wang, V. McKoy, P. Hockett, and M. S. Schuurman. *Phys. Rev. letters* **112**, 113007 (2014).

[199] W. H. Press, S. A. Teukolsky, W. T. Vetterling, and B. P. Flannery. *Numerical recipes 3rd edition: The art of scientific computing*. Cambridge University Press, 2007.

[200] C. De Boor. *A Practical Guide to Splines. Applied Mathematical Series, revised edition*. 2001.

[201] Y. Guo, A. Kawano, D. L. Thompson, A. F. Wagner, and M. Minkoff. *J. Chem. Phys.* **121**, 5091 (2004).

[202] W. McCulloch. *Bull. Math. Biophys.* **5**, 115 (1943).

[203] J. M. Zurada. *Introduction to artificial neural systems*. Vol. 8. West publishing company St. Paul, 1992.

[204] R. J. Schalkoff. *Artificial neural networks*. Vol. 1. McGraw-Hill New York, 1997.

[205] S. Lorenz, A. Groß, and M. Scheffler. *Chem. Phys. Lett.* **395**, 210 (2004).

[206] B. D. Ripley. *Pattern recognition and neural networks*. Cambridge University Press, 2007.

[207] C. M. Handley and P. L. Popelier. *J. Phys. Chem. A* **114**, 3371 (2010).

[208] J. Behler. *Phys. Chem. Chem. Phys.* **13**, 17930 (2011).

[209] B. Jiang, J. Li, and H. Guo. *Annu. Rev. Phys. Chem.* **35**, 479 (2016).

[210] J. Li and H. Guo. *J. Phys. Chem. A* **120**, 2991 (2015).

[211] A. Schäfer, H. Horn, and R. Ahlrichs. *J. Chem. Phys.* **97**, 2571 (1992).

[212] F. Plasser, M. Ruckenbauer, S. Mai, M. Oppel, P. Marquetand, and L. González. *J. Chem. Theory Comput.* **12**, 1207 (2016).

[213] G. Granucci, M. Persico, and A. Zoccante. *J. Chem. Phys.* **133**, 134111 (2010).

[214] M. Barbatti, M. Ruckenbauer, F. Plasser, J. Pittner, G. Granucci, M. Persico, and H. Lischka. *Wiley Interdiscip. Rev.: Comput. Mol. Science* **4**, 26 (2014).

[215] H.-J. Werner, P. J. Knowles, G. Knizia, F. R. Manby, M. Schütz, P. Celani, T. Korona, R. Lindh, A. Mitrushenkov, G. Rauhut, K. R. Shamasundar, T. B. Adler, R. D. Amos, A. Bernhardsson, A. Berning, D. L. Cooper, M. J. O. Deegan, A. J. Dobbyn, F. Eckert, E. Goll, C. Hampel, A. Hesselmann, G. Hetzer, T. Hrenar, G. Jansen, C. Köppl, Y. Liu, A. W. Lloyd, R. A. Mata, A. J. May, S. J. McNicholas, W. Meyer, M. E. Mura, A. Nicklass, D. P. O'Neill, P. Palmieri, D. Peng, K. Pflüger, R. Pitzer, M. Reiher, T. Shiozaki, H. Stoll, A. J. Stone, R. Tarroni, T. Thorsteinsson, and M. Wang. *MOLPRO, version 2012.1, a package of ab initio programs*. `http://www.molpro.net`. Cardiff, UK, 2012.

[216] J. R. Rydberg. *Kungl. Sv. Vetens. Akad. Handl.* **23** (1890).

[217] R. K. Chaudhuri, A. Mudholkar, K. F. Freed, C. H. Martin, and H. Sun. *J. Chem. Phys.* **106**, 9252 (1997).

[218] H. Reisler and A. I. Krylov. *Annu. Rev. Phys. Chem.* **28**, 267 (2009).

[219] M. Merchán, L. Serrano-Andrés, L. S. Slater, B. O. Roos, R. McDiarmid, and X. Xing. *J. Phys. Chem. A* **103**, 5468 (1999).

[220] M. Boyle, K Hoffmann, C. Schulz, I. Hertel, R. Levine, and E. E. Campbell. *Phys. Rev. Lett.* **87**, 273401 (2001).

[221] J. O. Johansson, G. G. Henderson, F. Remacle, and E. E. Campbell. *Phys. Rev. Lett.* **108**, 173401 (2012).

[222] B. Mignolet, J. O. Johansson, E. E. Campbell, and F. Remacle. *ChemPhysChem* **14**, 3332 (2013).

[223] H. Li, B. Mignolet, Z. Wang, K. Betsch, K. Carnes, I. Ben-Itzhak, C. Cocke, F. Remacle, and M. Kling. *J. Phys. Chem. Lett.* **7**, 4677 (2016).

[224] A. Sobolewski, W. Domcke, C. Dedonder-Lardeux, and C. Jouvet. *Phys. Chem. Chem. Phys.* **4**, 1093 (2002).

[225] M. Robin. *Higher excited states of polyatomic molecules*. Vol. 3. Elsevier, 2012.

[226] G. Gregoire, C. Jouvet, C. Dedonder, and A. Sobolewski. *Chem. Phys.* **324**, 398 (2006).

[227] M. N. Ashfold, G. A. King, D. Murdock, M. G. Nix, T. A. Oliver, and A. G. Sage. *Phys. Chem. Chem. Phys.* **12**, 1218 (2010).

[228] G. M. Roberts and V. G. Stavros. *Chem. Sci.* **5**, 1698 (2014).

[229] J. L. Gosselin, M. P. Minitti, F. M. Rudakov, T. I. Sølling, and P. M. Weber. *J. Phys. Chem. A* **110**, 4251 (2006).

[230] J. D. Cardoza, F. M. Rudakov, and P. M. Weber. *J. Phys. Chem. A* **112**, 10736 (2008).

[231] S. Deb, B. A. Bayes, M. P. Minitti, and P. M. Weber. *J. Phys. Chem. A* **115**, 1804 (2011).

[232] R. Livingstone, O. Schalk, A. E. Boguslavskiy, G. Wu, L Therese Bergendahl, A. Stolow, M. J. Paterson, and D. Townsend. *J. Chem. Phys.* **135**, 194307 (2011).

[233] J. O. Thompson, R. A. Livingstone, and D. Townsend. *J. Chem. Phys.* **139**, 034316 (2013).

[234] J. O. Thompson, L. Saalbach, S. W. Crane, M. J. Paterson, and D. Townsend. *J. Chem. Phys.* **142**, 03B612_1 (2015).

[235] M. M. Zawadzki, J. O. Thompson, E. A. Burgess, M. J. Paterson, and D. Townsend. *Phys. Chem. Chem. Phys.* **17**, 26659 (2015).

[236] L. B. Klein, J. O. Thompson, S. W. Crane, L. Saalbach, T. I. Sølling, M. J. Paterson, and D. Townsend. *Phys. Chem. Chem. Phys.* **18**, 25070 (2016).

[237] J. O. Thompson, L. B. Klein, T. I. Sølling, M. J. Paterson, and D. Townsend. *Chem. Sci.* **7**, 1826 (2016).

[238] L. B. Klein, T. J. Morsing, R. A. Livingstone, D. Townsend, and T. I. Sølling. *Phys. Chem. Chem. Phys.* **18**, 9715 (2016).

[239] M. M. Zawadzki, M. Candelaresi, L. Saalbach, S. W. Crane, M. J. Paterson, and D. Townsend. *Faraday Discussions* **194**, 185 (2016).

[240] M. A. Larsen, T. I. Sølling, R. Forbes, A. E. Boguslavskiy, V. Makhija, K. Veyrinas, R. Lausten, A. Stolow, M. M. Zawadzki, L. Saalbach, N. Kotsina, M. J. Paterson, and D. Townsend. *J. Chem. Phys.* **150**, 054301 (2019).

[241] J. C. Bush, M. P. Minitti, and P. M. Weber. *J. Phys. Chem. A* **114**, 11078 (2010).

[242] H. Yong, N. Zotev, B. Stankus, J. M. Ruddock, D. Bellshaw, S. Boutet, T. J. Lane, M. Liang, S. Carbajo, J. S. Robinson, W. Du, N. Goff, Y. Chang, J. E. Koglin, M. D. J. Waters, T. I. Sølling, M. P. Minitti, A. Kirrander, and P. M. Weber. *J. Phys. Chem. Lett.* **9**, 6556 (2018).

[243] J. M. Ruddock, N. Zotev, B. Stankus, H. Yong, D. Bellshaw, S. Boutet, T. J. Lane, M. Liang, S. Carbajo, W. Du, A. Kirrander, M. P. Minitti, and P. M. Weber. *Angew. Chem. Int. Ed.* (2019).

[244] M. P. Minitti, J. D. Cardoza, and P. M. Weber. *J. Phys. Chem. A* **110**, 10212 (2006).

[245] Y. Onitsuka, Y. Kadowaki, A. Tamakubo, K. Yamasaki, and H. Kohguchi. *Chem. Phys. Lett.* **716**, 28 (2019).

[246] H. Guðmundsdóttir, Y. Zhang, P. M. Weber, and H. Jonsson. *J. Chem. Phys.* **139** (2013).

[247] G. Abbott, C. Cureton, K. Hara, S. Hirayama, and D. Phillips. *J. Photochem.* **9**, 260 (1978).

[248] Y. Matsumi and K. Obi. *Chem. Phys.* **49**, 87 (1980).

[249] C. G. Cureton, K. Hara, D. V. O'Connor, and D. Phillips. *Chem. Phys.* **63**, 31 (1981).

[250] M. P. Minitti and P. M. Weber. *Phys. Rev. Lett.* **98**, 253004 (2007).

[251] X. Cheng, Y. Zhang, S. Deb, M. P. Minitti, Y. Gao, H. Jónsson, and P. M. Weber. *Chem. Sci.* **5**, 4394 (2014).

[252] J. L. Gosselin and P. M. Weber. *J. Phys. Chem. A* **109**, 4899 (2005).

[253] K. Kaufmann, W. Baumeister, and M. Jungen. *J. Phys. B* **22**, 2223 (1989).

[254] J. Simons. *Energetic Principles of Chemical Reactions*. Jones & Bartlett, 1983.

[255] A. Szabo and N. S. Ostlund. *Modern quantum chemistry: introduction to advanced electronic structure theory*. Courier Corporation, 1989.

[256] J. Simons and J. A. Nichols. *Quantum mechanics in chemistry*. Oxford University Press New York, 1997.

[257] J. Simons. *An introduction to theoretical chemistry*. Cambridge University Press, 2003.

[258] R. M. Martin. *Electronic structure: basic theory and practical methods*. Cambridge university press, 2004.

[259] P. W. Atkins, J. De Paula, and J. Keeler. *Atkins' Physical Chemistry*. 2006.

[260] P. Atkins, J. De Paula, and R. Friedman. *Quanta, matter, and change: a molecular approach to physical chemistry*. Oxford University Press, 2009.

[261] H. F. Schaefer. *Methods of electronic structure theory*. Vol. 3. Springer Science & Business Media, 2013.

[262] T. Helgaker, P. Jorgensen, and J. Olsen. *Molecular electronic structure theory*. John Wiley & Sons, 2014.

[263] J. C. Slater. *Phys. Rev.* **36**, 57 (1930).

[264] S. F. Boys. "Electronic wave functions. I. A general method of calculation for the stationary states of any molecular system". *Proc. Royal Soc. Lond. A.* Vol. 200. The Royal Society. 1950, 542.

[265] A. Schäfer, C. Huber, and R. Ahlrichs. *J. Chem. Phys.* **100**, 5829 (1994).

[266] F. Weigend, F. Furche, and R. Ahlrichs. *J. Chem. Phys.* **119**, 12753 (2003).

[267] P. Pulay. *Mol. Phys.* **17**, 197 (1969).

[268] M. Dupuis and H. F. King. *J. Chem. Phys.* **68**, 3998 (1978).

[269] P. Pulay. *Ab Initio Methods in Quantum Chemistry, Part II, edited by KP Lawley* **69**, 241 (2007).

[270] A. A. Granovsky. *J. Chem. Phys.* **143**, 231101 (2015).

[271] H. Lischka, M. Dallos, and R. Shepard. *Mol. Phys.* **100**, 1647 (2002).

[272] M. K. MacLeod and T. Shiozaki. *J. Chem. Phys.* **142**, 051103 (2015).

[273] R. P. Feynman. *Phys. Rev.* **56**, 340 (1939).

[274] J. Stålring, A. Bernhardsson, and R. Lindh. *Mol. Phys.* **99**, 103 (2001).

[275] P. A. M. Dirac. *Proc. R. Soc. Lond. A* **117**, 610 (1928).

[276] C. M. Marian. *WIRES Comput. Mol. Sci.* **2**, 187 (2012).

[277] H. A. Bethe and E. E. Salpeter. *Quantum mechanics of one-and two-electron atoms*. Springer Science & Business Media, 2012.

[278] G. Breit. *Phys. Rev.* **34**, 553 (1929).

[279] K. G. Dyall and K. Fægri Jr. *Introduction to relativistic quantum chemistry*. Oxford University Press, 2007.

[280] B. A. Hess. *Phys. Rev. A* **33**, 3742 (1986).

[281] G. Jansen and B. A. Heß. *Phys. Rev. A* **39**, 6016 (1989).

[282] A. Wolf, M. Reiher, and B. A. Hess. *J. Chem. Phys.* **117**, 9215 (2002).

[283] A. Berning, M. Schweizer, H.-J. Werner, P. J. Knowles, and P. Palmieri. *Mol. Phys.* **98**, 1823 (2000).

[284] B. A. Heß, C. M. Marian, U. Wahlgren, and O. Gropen. *Chem. Phys. Lett.* **251**, 365 (1996).

[285] F. Neese. *J. Chem. Phys.* **122**, 034107 (2005).

[286] G. Groenhof, M. Bouxin-Cademartory, B. Hess, S. P. De Visser, H. J. Berendsen, M. Olivucci, A. E. Mark, and M. A. Robb. *J. Am. Chem. Soc.* **126**, 4228 (2004).

[287] O. Weingart, I. Schapiro, and V. Buss. *J. Phys. Chem. B* **111**, 3782 (2007).

[288] S. Fernandez-Alberti, A. E. Roitberg, T. Nelson, and S. Tretiak. *J. Chem. Phys.* **137**, 014512 (2012).

[289] J. Pittner, H. Lischka, and M. Barbatti. *Chem. Phys.* **356**, 147 (2009).

[290] P.-Å. Malmqvist and B. O. Roos. *Chem. Phys. Lett.* **155**, 189 (1989).